Coupled Experimental Study and Thermodynamic Optimization of the K_2O-Na_2O-CaO-MgO-Al_2O_3-SiO_2 System

Donggeun Kim

Department of Mining and Materials Engineering

McGill University, Montreal, Quebec, Canada

February, 2017

A Thesis Submitted to the Faculty of Graduate and Postdoctoral Studies in Partial Fulfilment of the Requirements for the Degree of Doctor of Philosophy

Abstract

Phase diagram and thermodynamic properties of the K_2O-Na_2O-CaO-MgO-Al_2O_3-SiO_2 system are important in various applications, such as glass/glass-ceramics, biomass combustion, steelmaking, refractory, and geology/mineralogy. In the present work, a critical evaluation and optimization of the phase diagram and thermodynamic properties of this six-component system was performed to develop an accurate thermodynamic database for industrial and academic research. Sub-binary/ternary systems containing K_2O were thermodynamically optimized based on the critical assessment of all experimental data available in the literature, and a consistent set of model parameters of solid and liquid phases describing their Gibbs energies was obtained. Key phase diagram experiments were performed for the K_2O-SiO_2, K_2O-Al_2O_3, and K_2O-MgO systems in order to provide new phase diagram information and resolve the inconsistencies between existing experimental data.

Equilibration/quenching experiments and thermal analyses were performed using K_2O-containing samples sealed in Pt capsules to overcome the experimental difficulties (high hygroscopicity and volatile nature of K_2O) and provide reliable results. In the study of the K_2O-SiO_2 system, the eutectic reaction, Liquid → K_4SiO_4 + K_2SiO_3, was successfully measured at 714 ± 6 °C. In the K_2O-MgO system, the peritectic reaction of Liquid + MgO → K_6MgO_4 was determined to occur at 858 ± 14 °C. These two invariant reactions were determined for the first time. In the K_2O-Al_2O_3 system, the thermal stability of K β″-alumina was confirmed up to 1600 °C from the present experiments, and a large discrepancy in the literature related to the eutectic temperature of Liquid → $KAlO_2$ + β-alumina was resolved.

In the optimization of this study, the Modified Quasichemical Model (MQM) and Compound Energy Formalism (CEF) were used to describe the liquid and solid solutions, respectively, based on the structure of the solutions. In particular, solid solutions were modeled considering their lattice structure, in this way, a proper configurational entropy of the solution could be treated in the thermodynamic calculations. In the study of K_2O-MgO-Al_2O_3 system, for example, a new solid solution model was developed to describe the details of ionic substitutions in non-stoichiometric K β- and β″-alumina solutions. In both K_2O-MgO-SiO_2 and K_2O-Al_2O_3-SiO_2 melt, associates K_2MgSiO_4 and $KAlO_2$ were considered, respectively, to describe the phase diagram, thermodynamic properties and structural data of liquid phase more accurately.

With the model parameters optimized in binary and ternary systems, the phase diagram and thermodynamic properties of higher order systems in the K_2O-Na_2O-CaO-MgO-Al_2O_3-SiO_2 system were well predicted. The database developed in this study is compatible with the FactSage thermodynamic databases and can be used for the prediction of any unexplored thermodynamic properties and phase diagram within the six-component system. Case studies of several industrial applications were also included at the end of this study.

Résumé

Le diagramme de phase et les propriétés thermodynamiques du système K_2O-Na_2O-CaO-MgO-Al_2O_3-SiO_2 sont importants dans diverses applications telles que les verres/vitrocéramiques, la combustion de la biomasse, la sidérurgie, les réfractaires et la géologie/minéralogie. Dans le présent travail, une évaluation critique et une optimisation du diagramme de phase et des propriétés thermodynamiques de ce système à six-composantes ont été réalisés pour développer une base de données thermodynamique précise pour la recherche industrielle et universitaire. Les systèmes sous-binaires / ternaires contenant du K_2O ont été optimisés thermodynamiquement sur la base de l'évaluation critique de toutes les données expérimentales disponibles dans la littérature et un ensemble cohérent de paramètres du modèle des phases solide et liquide décrivant leurs énergies de Gibbs a été obtenu. Des expériences clés de diagrammes de phases ont été réalisées pour les systèmes K_2O-SiO_2, K_2O-Al_2O_3 et K_2O-MgO afin de fournir de nouvelles informations de diagramme de phase et de résoudre les incohérences entre les données expérimentales existantes.

Des expériences d'équilibrage/trempe à froid et des analyses thermiques ont été effectuées en utilisant des échantillons contenant du K_2O scellés dans des capsules de Pt afin de surmonter les difficultés expérimentales (hygroscopicité élevée et nature volatile du K_2O) et fournir des résultats fiables. Dans l'étude du système K_2O-SiO_2, la réaction eutectique, Liquide → K_4SiO_4 + K_2SiO_3, a été mesurée avec succès à 714 ± 6 °C. Dans le système K_2O-MgO, il a été déterminé que la réaction péritectique de Liquide + MgO → K_6MgO_4 se produisait à 858 ± 14 °C. Ces deux réactions invariantes ont été déterminées pour la première fois. Dans le système K_2O-Al_2O_3, la stabilité thermique de l'alumine K β″ a été confirmée jusqu'à 1600 °C à partir des présentes expériences et

une grande divergence dans la littérature concernant la température eutectique de Liquide → $KAlO_2$ + β-alumine a été résolue.

Dans l'optimisation de cette étude, on a utilisé le modèle quasi-chimique modifié (MQM) et le formalisme d'énergie des composés (CEF) pour décrire les solutions liquides et solides, respectivement, en fonction de la structure des solutions. En particulier, les solutions solides ont été modélisées en considérant la structure de leur réseau et de cette façon, une entropie de configuration appropriée de la solution a pu être considérée dans les calculs thermodynamiques. Dans l'étude du système K_2O-MgO-Al_2O_3, par exemple, un nouveau modèle de solution solide a été développé pour décrire les détails des substitutions ioniques dans des solutions de K β- et β″-alumine non stoechiométriques. Dans les liquides K_2O-MgO-SiO_2 et K_2O-Al_2O_3-SiO_2, les paires associées K_2MgSiO_4 et $KAlO_2$ ont été considérés, respectivement, pour décrire le diagramme de phase, les propriétés thermodynamiques et les données structurales de la phase liquide.

Avec les paramètres du modèle optimisés dans les systèmes binaires et ternaires, le diagramme de phase et les propriétés thermodynamiques des systèmes d'ordre supérieur dans le système K_2O-Na_2O-CaO-MgO-Al_2O_3-SiO_2 ont été bien prédits. La base de données développée dans cette étude est compatible avec les bases de données thermodynamiques FactSage et peut être utilisé pour la prédiction de toute propriété thermodynamique inexplorée et de diagrammes de phases dans les systèmes à six-composantes. Des études de cas de plusieurs applications industrielles ont également été incluses à la fin de cette étude.

Acknowledgments

The accomplishment of this dissertation would have been impossible without the help of many people who have contributed in various ways in my life.

I sincerely acknowledge and am deeply grateful for the thorough supervision, enlightening guidance and insightful academic advice I received from my supervisor, Prof. In-Ho Jung. He provides valuable advice and supervision throughout my Ph.D. studies. It has been a great pleasure to work under the guidance of Prof. Jung, not only because of his knowledge, but also his admirable characters.

I would like to thank Dr. Pierre Hudon and Dr. Lang Shi, who helped me on the experimental work. I would also like to thank Dr. Pierre Hudon for translating the abstract to French. Many thanks go to everyone in the Department of Mining and Materials and the McGill High Temperature Thermochemistry Laboratory who has helped me immensely in many ways: some of these include Ms. Barbara Hanley, Dr. Marie-Aline Van Ende, Mr. Bikram Konar, Dr. Elmira Moosavi-Khoonsari, Dr. Junghwan Kim, Mr. Sunyong Kwon, and Mr. Gabriel Garcia Curiel.

I am really grateful to the financial support from Tata Steel Europe, Posco, RIST, Hyundai Steel, Nucor Steel, RioTinto Iron and Titanium, Nippon Steel and Sumitomo Metals Corp., JFE Steel, Voestalpine, RHI, the Natural Sciences and Engineering Research Council of Canada (NSERC), and the McGill Engineering Doctorate Award (MEDA).

Special thanks go to Dr. Tong Wang, who has supported me through my Ph.D. study and brought a lot of happiness, laughter, and love into my life. Most of all, I would like to thank my family, especially my parents and sister, for their unconditional love.

Preface and Contributions of Authors

All the work presented hereafter was performed at the High-Temperature Thermochemistry Laboratory at the Department of Mining and Materials Engineering of McGill University. Five chapters of the present thesis have been or will be submitted for publication:

Chapter 4: Coupled Experimental Study and Thermodynamic Optimization of the K_2O-SiO_2 System by Dong-Geun Kim, Marie-Aline Van Ende, Pierre Hudon and In-Ho Jung, submitted to *Journal of Non-Crystalline Solids*.

Chapter 5: Coupled Experimental Study and Thermodynamic Optimization of the K_2O-MgO and K_2O-MgO-SiO_2 Systems by Dong-Geun Kim, Bikram Konar and In-Ho Jung, submitted to *Metallurgical and Materials Transactions B*.

Chapter 6: Thermodynamic Modeling of the K_2O-Al_2O_3 and K_2O-MgO-Al_2O_3 Systems with Emphasis on β- and β″-Alumina by Dong-Geun Kim, Elmira Moosavi-Khoonsari and In-Ho Jung, to be submitted.

Chapter 7: Thermodynamic Optimization of the K_2O-Al_2O_3-SiO_2 System by Dong-Geun Kim, Bikram Konar and In-Ho Jung, to be submitted.

Chapter 8: Thermodynamic Optimization of the K_2O-CaO-SiO_2 and K_2O-Na_2O-SiO_2 Systems by Dong-Geun Kim and In-Ho Jung, to be submitted.

For the work presented, the author of the thesis is the main investigator, in charge of literature review, concept formation, thermodynamic modeling, and experimental investigations including data collections and characterizations, as well as manuscript preparation. All the work and

manuscripts was performed and written under the supervision and guidance of Prof. In-Ho Jung. For Chapter 4, Dr. Marie-Aline Van Ende guided the optimization and manuscript organization. Dr. Pierre Hudon guided the experimental work in early stages of the research and contributed to the editing of the manuscript. For Chapters 5 and 7, Mr. Bikram Konar assisted in the experimental work and thermodynamic optimization. For Chapter 6, Dr. Elmira Moosavi-Khoonsari was involved in the discussion of thermodynamic models.

Table of Contents

List of Figures

List of Tables

Chapter 1 Introduction

The K_2O-Na_2O-CaO-MgO-Al_2O_3-SiO_2 system is important in various fields. K_2O, Na_2O, CaO, MgO, Al_2O_3, and SiO_2 are the main components for different types of glass-ceramics, glass optical fibers, and high-strength glass products [1-7]. Some compounds in this system, such as K_2CaSiO_4, K_2MgSiO_4, and $K_2MgSi_3O_8$, are considered to be good candidates as fertilizers because of their slow-releasing potential of K, Ca, Mg, and Si for crops [8-10]. Potassium β- and β″-alumina are excellent solid ionic conductors, which make them attractive for energy storage applications [11]. Alkali metal thermal electric converter (AMTEC) made of potassium β- and β″-alumina can be five times more efficient compared to traditional ones in spacecraft. Studying the complex chemical reactions in this system can also help to understand and avoid the premature wear and corrosion of refractories in glass- and iron-making industries caused by K_2O vapor [12-16] and in biomass combustion process caused by K_2O-containing silicate slags [17, 18]. In geological studies, the phase stability and thermodynamic properties of the compounds in this system are essential to understand the complex phase equilibria in the K_2O-Na_2O-CaO-MgO-Al_2O_3-SiO_2 system, which involve many mineralogically important phases, such as kalsilite, leucite, and potash feldspar, etc. [19, 20]. However, the understanding of the phase equilibria and thermodynamic properties of this system is limited in certain compositions and temperature ranges. There are also discrepancies in the experimental data reported in the literature. Experimental difficulties come from the high volatility of K_2O and Na_2O, hygroscopic nature of K_2O, Na_2O, and CaO, high melting points of MgO and Al_2O_3, and the sluggish nature of SiO_2 within the compositions studied in this system.

In thermodynamic optimizations, all the phase diagram and thermodynamic data are critically evaluated and optimized to obtain a set of self-consistent thermodynamic functions to reproduce all available and reliable experimental data. The thermodynamic models employed for the description of solid and liquid solutions are based on the structure of respective solutions to capture the nature of configurational entropy more accurately.

The overall goal of this study is the development of thermodynamic database for the K_2O-Na_2O-CaO-MgO-Al_2O_3-SiO_2 system based on the critical evaluation of the available experimental data and new phase diagram data. The Modified Quasichemical Model (MQM) and the Compound Energy Formalism (CEF) were used to describe the liquid and solid solution phases, respectively. Some solid solutions were also modeled using the MQM as an extension of previous optimization work. Using the newly optimized thermodynamic functions, unexplored phase stability and thermodynamic properties of the system can be accurately predicted in a thermodynamically correct manner.

1.1 Scope of Work

The main goal of this work is to develop a comprehensive, accurate, and self-consistent thermodynamic database for the K_2O-Na_2O-CaO-MgO-Al_2O_3-SiO_2 system, including all the K_2O-containing binary, ternary, and multi-component sub-systems. Key phase diagram experiments were performed followed by phase characterizations to resolve uncertainties in the literature and confirm the results of thermodynamic optimizations. The addition of K_2O in the previous Na_2O-CaO-MgO-Al_2O_3-SiO_2 system were done as listed in Table 1.1. Among all the K_2O-containing sub-systems from the K_2O-Na_2O-CaO-MgO-Al_2O_3-SiO_2 system, K_2O-(SiO_2, MgO, Al_2O_3) binary systems, K_2O-SiO_2-(Na_2O, CaO, MgO, Al_2O_3) and K_2O-MgO-Al_2O_3 ternary systems are

important due to compounds/solid solutions/strong interactions in their liquid solution. Systematic thermodynamic optimizations from lower to higher order systems were performed in this work.

(i) Modeling and new phase diagram experiments: ***bold italic*** in Table 1.1

(ii) Modeling only based on the literature data: *italic* in Table 1.1

(iii) Purely prediction from ideal solution assumption, and prediction from binary systems using proper interpolation technique: normal in Table 1.1

This work is part of a large thermodynamic database development project for the multi-component K_2O-Li_2O-Na_2O-CaO-MnO-MgO-FeO-Fe_2O_3-Al_2O_3-SiO_2-P_2O_5-F-S system, which has been funded by eleven industrial partners worldwide: Tata Steel Europe, POSCO, Nucor Steel, Rio Tinto Iron and Titanium, Hyundai Steel, Nippon Steel and Sumitomo Metals Corp., JFE Steel, Voestalpine, RHI, Schott AG, and the CRD grant from Natural Sciences and Engineering Research Council of Canada (NSERC).

1.2 Organization

The structure of this thesis is as follows:

In Chapter 2, experimental methodologies, including sample preparations, equilibration/quenching experiments, and phases characterizations, are presented. Detailed thermodynamic modeling and optimization approach used in this work are given in Chapter 3. Chapter 4 is about the coupled experimental study and thermodynamic optimization of the K_2O-SiO_2 binary system; Chapter 5 shows the coupled experimental study and thermodynamic optimization of the K_2O-MgO and K_2O-MgO-SiO_2 systems; Chapter 6 presents the thermodynamic modeling of the K_2O-Al_2O_3 and K_2O-MgO-Al_2O_3 systems with emphasis on β- and β'-alumina; Chapter 7 is about the thermodynamic optimization of the K_2O-Al_2O_3-SiO_2 system; Chapter 8 shows the thermodynamic optimization of the K_2O-CaO-SiO_2

and K_2O-Na_2O-SiO_2 systems. Finally, case studies of several industrial applications are included in the appendix of this thesis.

Table 1.1 Sub-systems containing K_2O in the K_2O-Na_2O-CaO-MgO-Al_2O_3-SiO_2 system.

System	Remarks	System	Remarks
K	FToxid [21]	K-N-C-S	Predicted (Appendix I)
K-S	Optimized (Chapter 4)	K-N-M-S	No data (predicted)
K-M	Optimized (Chapter 5)	K-C-M-S	No data (predicted)
K-A	Optimized (Chapter 6)	K-N-C-A	No data (predicted)
K-C	No data (Ideal liquid solution)	K-N-M-A	No data (predicted)
K-N	No data (Ideal liquid solution)	K-C-M-A	No data (predicted)
K-M-S	Optimized (Chapter 5)	K-N-A-S	Predicted (Appendix I)
K-A-S	Optimized (Chapter 7)	K-C-A-S	Predicted (Appendix I)
K-C-S	Optimized (Chapter 8)	K-M-A-S	Predicted (Appendix I)
K-N-S	Optimized (Chapter 8)	K-N-C-M	No data (predicted)
K-M-A	Optimized (Chapter 6)	K-N-C-M-A	No data (predicted)
K-C-A	Optimized (only solids)	K-N-C-M-S	No data (predicted)
K-N-A	No data (Ideal liquid solution)	K-N-C-A-S	Predicted
K-N-C	No data (Ideal liquid solution)	K-N-M-A-S	No data (predicted)
K-N-M	No data (Ideal liquid solution)	K-C-M-A-S	Predicted
K-C-M	No data (Ideal liquid solution)	K-N-C-M-A-S	Predicted (Appendix I)

K: K_2O, N: Na_2O, C: CaO, M: MgO, A: Al_2O_3, S: SiO_2.

References

[1] V. Saraswati, K.V.S.R. Anjaneyulu, Crystallization of mica in the potassium oxide-silicon dioxide-magnesium oxide-magnesium fluoride glass system, Bull. Mater. Sci. 13(4) (1990) 283-91.
[2] C.C. Gonzaga, P.F. Cesar, C.Y. Okada, C. Fredericci, F. Beneduce Neto, H.N. Yoshimura, Mechanical properties and porosity of dental glass-ceramics hot-pressed at different temperatures, Mater. Res. (Sao Carlos, Braz.) 11(3) (2008) 301-306.
[3] L. Song, J. Wu, Z. Li, X. Hao, Y. Yu, Crystallization mechanisms and properties of α-cordierite glass–ceramics from K2O–MgO–Al2O3–SiO2 glasses, Journal of Non-Crystalline Solids 419 (2015) 16-26.
[4] A. Tandia, K.D. Vargheese, J.C. Mauro, A.K. Varshneya, Atomistic understanding of the network dilation anomaly in ion-exchanged glass, Journal of Non-Crystalline Solids 358(2) (2012) 316-320.
[5] Y. Yu, M. Wang, D. Zhang, B. Wang, G. Sant, M. Bauchy, Stretched exponential relaxation of glasses at low temperature, Phys. Rev. Lett. 115(16) (2015) 165901/1-165901/5.

[6] K. Tsujikawa, M. Ohashi, Rayleigh Scattering in K2O–MgO–SiO2 and Na2O–B2O3–SiO2 Glasses, Optical Fiber Technology 6(1) (2000) 74-82.
[7] K. Tsujikawa, M. Ohashi, K. Tajima, Optical properties of multicomponent oxide glasses and glass fibers, Electronics and Communications in Japan (Part I: Communications) 86(12) (2003) 21-35.
[8] X. Ma, H. Ma, J. Yang, Sintering Preparation and Release Properties of K2MgSi3O8 Slow-Release Fertilizer Using Biotite Acid-Leaching Residues as Silicon Source, Industrial & Engineering Chemistry Research 55(41) (2016) 10926-10931.
[9] A.S. Mangrich, L.C. Tessaro, A.D. Anjos, F. Wypych, J.F. Soares, A slow-release K+ fertilizer from residues of the Brazilian oil-shale industry: synthesis of kalsilite-type structures, Environ. Geol. (Berlin, Ger.) 40(8) (2001) 1030-1036.
[10] L.K. Bankole, R.S. Abdul, N.M. Sharif, Crystallization of potassium calcium silicate from modified industrial EAF slag, Adv. Mater. Res. (Durnten-Zurich, Switz.) 620 (2013) 66-71, 7 pp.
[11] M.A.K. Lodhi, P. Vijayaraghavan, A. Daloglu, An overview of advanced space/terrestrial power generation device: AMTEC, J. Power Sources 103(1) (2001) 25-33.
[12] M.D. Allendorf, K.E. Spear, Thermodynamic analysis of silica refractory corrosion in glass-melting furnaces, J. Electrochem. Soc. 148 (2001) B59-B67.
[13] K.E. Spear, M.D. Allendorf, Thermodynamic analysis of alumina refractory corrosion by sodium or potassium hydroxide in glass melting furnaces, J. Electrochem. Soc. 149(12) (2002) B551-B559.
[14] J. Stjernberg, B. Lindblom, J. Wikstroem, M.L. Antti, M. Oden, Microstructural characterization of alkali metal mediated high temperature reactions in mullite based refractories, Ceram. Int. 36(2) (2010) 733-740.
[15] L.A.M. Scudeller, E. Longo, J.A. Varela, Potassium vapor attack in refractories of the alumina-silica system, J. Am. Ceram. Soc. 73(5) (1990) 1413-16.
[16] S.E. McCune, T.P. Greaney, W.C. Allen, R.B. Snow, Reaction between K2O and Al2O3-SiO2 refractories as related to blast-furnace linings, J. Am. Ceram. Soc. 40 (1957) 187-95.
[17] M. Zevenhoven-Onderwater, R. Backman, B.J. Skrifvars, M. Hupa, The ash chemistry in fluidised bed gasification of biomass fuels. Part I: predicting the chemistry of melting ashes and ash-bed material interaction, Fuel 80(10) (2001) 1489-1502.
[18] I.-L. Naezelius, J. Fagerstroem, C. Boman, D. Bostroem, M. Oehman, Slagging in Fixed-Bed Combustion of Phosphorus-Poor Biomass: Critical Ash-Forming Processes and Compositions, Energy Fuels 29(2) (2015) 894-908.
[19] W.A. Deer, R.A. Howie, J. Zussman, An Introduction to the Rock-Forming Minerals, Pearson; 2 edition1996.
[20] E.W. Roedder, The system K2O-MgO-SiO2. I. II, Am. J. Sci. 249 (1951) 81-130,224-48.
[21] C.W. Bale, E. Belisle, P. Chartrand, S.A. Decterov, G. Eriksson, A.E. Gheribi, K. Hack, I.H. Jung, Y.B. Kang, J. Melancon, A.D. Pelton, S. Petersen, C. Robelin, J. Sangster, P. Spencer, M.A. Van Ende, FactSage thermochemical software and databases, 2010-2016, CALPHAD: Comput. Coupling Phase Diagrams Thermochem. 54 (2016) 35-53.

Chapter 2 Key Phase Diagram Experiments

Key phase diagram experiments were conducted to investigate unknown phase diagram regions and resolve discrepancies in the literature of the K_2O-SiO_2, K_2O-MgO, and K_2O-Al_2O_3 systems. The experimental results are critical to restrict the thermodynamic optimizations.

2.1 Starting Materials

Starting materials were prepared using reagent grade K_2CO_3 (99.997 wt. %, Alfa Aesar), SiO_2 (99.995 wt. %, Alfa Aesar), MgO (99.995 wt. %, Alfa Aesar), and Al_2O_3 (99.99 wt. %, Alfa Aesar). Batches of 5 to 10 g of the materials were mixed in an agate mortar for 1 hour. Due to the hygroscopic nature of the starting materials, mixing was performed in isopropyl alcohol (H_2O < 0.02 vol. %) to prevent moisture pickup from air. In order to dry off the alcohol, the mixtures were kept in a drying oven at 120 °C for more than 12 hours and then cooled down to room temperature in a desiccator. To obtain K_2O, which is extremely hygroscopic, the decarbonation of K_2CO_3 ($K_2CO_3 \rightarrow K_2O + CO_2$) was conducted using only the required amount of premixed material just before each experiment. As K_2O is highly volatile, the decarbonation temperature was set to minimize the volatile loss of K_2O according to the preliminary Thermo-Gravimetric Analysis (TGA). The weight of each sample was measured before and after decarbonation to confirm the completion of the decarbonation reaction. Even though the decarbonation was performed below the solidus temperature, a small amount of K_2O loss is inevitable. In the decarbonation temperatures between 600 and 760 °C, vapor pressure of potassium ($\log P_K$(atm)) was measured to be in a range of -22.9 to -16.3 at 40 mol % K_2O and extrapolated to be -15.8 to -9.3 at 67 mol %

K_2O [1]. However, the partial pressure of CO_2 ($\log P_{CO_2}$ (atm)) from the mixtures of K_2CO_3:SiO_2 at 2:1, 1:1, and 1:2 measured to be in the range of -1 to -2 at the same temperature range [2]. After the decarbonation, the sample mixtures were stored in a drying oven to cool them down to 120 °C and subsequently in a desiccator to reach room temperature. Then, the mixtures were crushed and packed into one-side-sealed platinum (Pt) tubes with dimensions of about 12 mm/17mm in length, 3.2 mm in outer diameter and 0.2 mm in wall thickness. The open end of the Pt tubes was gently crimped to remove the air and welded into capsules using an electric arc welder to ensure gas-tight condition. The integrity of the welding was checked with an optical microscope before the main experiments. For thermal analysis experiments of the K_2O-SiO_2 system, two starting compositions were prepared: 40 mol % K_2O/60 mol % SiO_2 and 67 mol % K_2O/33 mol % SiO_2. For thermal analysis and equilibration/quenching experiments on the K_2O-MgO and K_2O-Al_2O_3 systems, one starting composition of 20 mol % K_2O/80 mol % MgO and 35 mol % K_2O/65 mol % Al_2O_3 was used, respectively.

2.2 Thermal Analysis

Differential Scanning Calorimetry (DSC), Differential Thermal Analysis (DTA), and Thermo-Gravimetric Analysis (TGA) measurements were conducted using a Jupiter STA 449 F3 thermal analyzer under an argon flowing atmosphere at a rate of 20 $mL \cdot min^{-1}$. For DSC/TGA, sealed Pt capsules were placed inside a DSC Al_2O_3 crucible with an outer diameter of 6.8 mm and a capacity of 85 μL. For DTA/TGA, a DTA Al_2O_3 crucible with an outer diameter of 8 mm and a height of 23 mm was used. The heating and cooling cycles were performed at a rate of 10 $K \cdot min^{-1}$. TGA was simultaneously performed to confirm that there was no leakage of the sealed capsules during the experiments. Three heating and cooling cycles were run for each sample to obtain reliable and

reproducible results. Temperature and sensitivity calibrations were conducted by measuring the melting temperatures and enthalpies of the following eight reference materials: Indium (In), tin (Sn), bismuth (Bi), zinc (Zn), aluminum (Al), silver (Ag), gold (Au), and nickel (Ni).

2.2.1 Sensitivity Tests for Sealed Pt capsules in Thermal Analysis

The sensitivity of DTA with sealed Pt capsules was confirmed using pure potassium chromate (K_2CrO_4) and diopside ($CaMgSi_2O_6$). The corresponding DTA curves of K_2CrO_4 and $CaMgSi_2O_6$ are depicted in Fig. 2.1 (a) and (b), respectively. A polymorphic transition (α to β) of K_2CrO_4 sample in a sealed Pt capsule was detected at 669.8 °C, which is in good agreement with the reported value of 666 °C [3]. The melting temperature of $CaMgSi_2O_6$ sample in a sealed Pt capsule was measured to be at 1397.1 °C. This value is reasonably close to the reported melting temperature of $CaMgSi_2O_6$ at 1392 °C [3]. This analysis confirms that samples sealed in this type of Pt capsules can be used for DTA experiments without interfering the heat incidents.

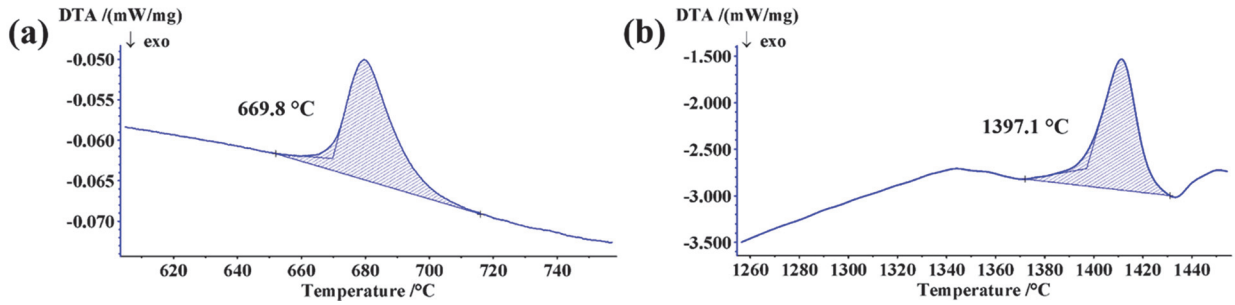

Figure 2.1 DTA results for the samples contained in sealed Pt capsules (a) K_2CrO_4 and (b) $CaMgSi_2O_6$.

2.3 Equilibration/Quenching Method

Equilibration/quenching experiments were conducted on the K_2O-MgO and K_2O-Al_2O_3 samples. A muffle box furnace (ST-1700C, SentroTech, $MoSi_2$ heating elements) was used with a B-type thermocouple ($Pt_{30}Rh$-Pt_6Rh) located at about 10 mm away from the sample. The temperature of the furnace was controlled within ± 1 °C by a PID controller. The temperature of the furnace was calibrated by melting diopside mineral ($CaMgSi_2O_6$, melting point at 1392 °C). For each equilibration experiment, several Pt capsules containing the sample mixtures were placed in a porous Al_2O_3 holder at the hot zone of the furnace. For the K_2O-MgO samples, equilibration experiments were carried out at 700 °C for 167 hours, 800 and 950 °C for 66 hours. For the K_2O-Al_2O_3 samples, equilibration was conducted at 1500 °C for 2 hours and 1600 °C for 1 hour. After the equilibration process, the samples contained in Pt capsules were immediately quenched in cold water, mounted in epoxy resin and polished with lapping oil (water-free lubricant) just before phase characterization to avoid the hydration of K_2O. For the transportation to characterization, the polished samples were put in a glass vial filled with desiccants in a vacuumed desiccator.

2.4 Phase Identification

For the K_2O-SiO_2 samples, Electron Probe Microanalyzer (EPMA) or X-Ray Diffraction (XRD) phase analysis could not be carried out because of the high volume fraction of K_2O. The K_2O/SiO_2 mixtures became fully hydrated during polishing and transportation for such analysis.

For the K_2O-MgO and K_2O-Al_2O_3 samples, phase characterization was conducted using X-ray Diffractometer (Bruker D8 Discover, Madison, WI, Cu *K*α-radiation) equipped with a VANTEC detector. All XRD profiles were identified with the Powder Diffraction Files (PDF) of the

International Centre for Diffraction Data (ICDD) using the DIFFRAC.EVA software package (Bruker AXS, Karlsruhe, Germany, 2000).

EPMA analysis was conducted on the K_2O-Al_2O_3 samples with an accelerating voltage of 8 kV, a beam current of 4nA, a beam size of 20 μm, and ZAF matrix correction. However, due to the extremely volatile nature of K_2O, all the quantitative analysis results showed an average of total 64.9 wt. % counts. Therefore, only micrographs were taken using EPMA to investigate the morphology of the K_2O-Al_2O_3 samples.

References

[1] E.R. Plante, C.D. Olson, T. Negas, Interaction of K2O with slag in open cycle, coal fired MHD, Proc. Sixth Int. Conf. on Magnetohydrodynamic Electrical Power Generation, Washington, DC, June 9-13, CONF750601-P2 (1975) 211-218.
[2] C. Kroger, E. Fingas, Action of quartz and alkali silicates upon alkali carbonates, Z. Anorg. Allg. Chem., 213 (1933) 12-57.
[3] I. Barin, Thermochemical Data of Pure Substances, VCH, 1989.

Chapter 3 Thermodynamic Modeling

Thermodynamic modeling/optimization studies have been advanced since CALPHAD (CALculation of PHAse Diagram or computer coupling of phase diagrams and thermochemistry) method was established [1]. The CALPHAD method, which based on classical thermodynamics, has recognized to be one of the most effective way to predict complex thermochemistry in multi-component systems. Although the first principles calculations based on density functional theory is becoming popular in recent years, the predictability of thermodynamic properties is limited in simple solid phases. The CALPHAD method is still the best approach for developing the multi-component thermodynamic database.

3.1 Principles of Thermodynamic Modeling/Optimization

In the process of thermodynamic modeling/optimization, all phase equilibria and thermodynamic property data are critically evaluated to obtain a set of model equations for all stable phases. The equations are built on thermodynamic principles. Therefore, the thermodynamic properties and phase diagrams can be back-calculated beyond the compositions, temperature ranges of the experimental data used in the optimization. The FactSage^{TM} thermochemical software [2] was used for thermodynamic calculations. With FactSage, the Gibbs energy at a given composition and temperature is calculated using a Gibbs energy minimization routine. Phase diagrams are also reproduced by calculating the chemical potentials of each species and the phase boundaries are drawn at the identical chemical potential.

The procedure of critical evaluation and optimization is explained as following steps.

1) The system of interest is defined.
2) All available literature data are collected:
    a) Phase diagram data (phase diagrams at 1 atm, phase equilibria between solids, liquid, and gas), calorimetric data (heat capacity, heat content, enthalpy of formation, and enthalpy of mixing), vapor pressure data, chemical potential and activity data, etc.
    b) Structural data (crystal system/space group, cationic distributions between sublattices, lattice parameters, etc).
    c) Physical property data (ionic conductivity, viscosity, molar volume, etc).
    d) Phase diagram or thermodynamic property data of higher order systems, which consist of the system of interest in this study. This is because, when there is a lack of data available for the system of interest, information for the lower order sub-systems can be obtained from interpolations of higher order systems.
3) A proper thermodynamic model is selected considering the real structure of each solution phase. This is essential to minimize the number of model parameters, and increase the predictive ability in multi-component systems.
4) The reliability of collected experimental data is assessed. The experimental error limits are checked. When discrepancies are found between the data, their experimental techniques, sample preparation, and analytical methods, etc. must be critically evaluated. Other possible experimental errors, which are not specified, must also be taken into account for the evaluation. Systematic evaluation between multiple systems and preliminary thermodynamic optimizations are often helpful for critical assessment.

5) The model parameters for each phase are optimized based on reliable experimental data to construct the database for a given system. The phase diagram and thermodynamic property data of interest are back-calculated.
6) The reliability of thermodynamic calculations are tested for higher order systems.

3.2 Stoichiometric Compounds

The list of stoichiometric compounds optimized in the present study is as follows:

In the K_2O-SiO_2 system, there are four binary stoichiometric compounds. These compounds are orthosilicate (K_4SiO_4), metasilicate (K_2SiO_3), disilicate (α-, β-, and γ-$K_2Si_2O_5$), tetrasilicate (α- and β-$K_2Si_4O_9$). In the K_2O-MgO system, one binary compound K_6MgO_4 exists. The K_2O-MgO-SiO_2 ternary system consists of four ternary stoichiometric compounds: $K_2MgSi_5O_{12}$, $K_2Mg_5Si_{12}O_{30}$. $K_4Mg_2Si_5O_{14}$, and $K_{10}Mg_5Si_{11}O_{32}$. In the K_2O-MgO-Al_2O_3 system, one ternary compound $KMg_2Al_{15}O_{25}$ exists. The K_2O-Al_2O_3-SiO_2 system consists of two ternary stoichiometric compounds: $KAlSi_2O_6$ and $KAlSi_3O_8$. In the K_2O-CaO-SiO_2 system, 8 stoichiometric compounds are stable: K_2CaSiO_4, $K_2Ca_2Si_2O_7$, $K_4CaSi_3O_9$, $K_8CaSi_{10}O_{25}$, $K_4CaSi_6O_{15}$, $K_2Ca_3Si_6O_{16}$, $K_2Ca_2Si_9O_{21}$, and $K_2Ca_6Si_4O_{15}$.

The Gibbs energy of a stoichiometric compound is described as:

$$G_T^o = \Delta H_{298.15K}^o + \int_{298.15K}^{T} C_P dT - T(S_{298.15K}^o + \int_{298.15K}^{T} C_P/T dT) \quad (1)$$

where $\Delta H_{298.15K}^o$ and $S_{298.15K}^o$ are the standard enthalpy of formation and standard entropy at 298.15 K, respectively; C_P is the heat capacity as a function of temperature; T is the absolute temperature.

If no thermodynamic data of binary and ternary solid compounds were available, the $S^{o}_{298.15K}$ and C_P of compounds were first approximated using the Neumann-Kopp rule (NKR) using the pure substance data of K_2O, Na_2O, CaO, MgO, Al_2O_3, and SiO_2 from the FToxid database [2]. In the NKR, SiO_2 polymorphs were selected based on the structure of each compound. Then, the $\Delta H^{o}_{298.15K}$ of the solid compounds were optimized to reproduce the phase diagram data.

3.3 Liquid Solution

The liquid oxide phase ($KO_{0.5}$-$NaO_{0.5}$-MgO-CaO-$AlO_{1.5}$-SiO_2-$KAlO_2$-$NaAlO_2$-K_2MgSiO_4) was modeled using the MQM considering the $KAlO_2$, $NaAlO_2$, and K_2MgSiO_4 associates. $NaAlO_2$ associate component replacing SiO_2 is already used for the modeling of liquid phase in alkali aluminosilicate systems [3, 4]. $KAlO_2$ and K_2MgSiO_4 associates were considered as charge compensation at high SiO_2 region. The Gibbs energies of the $KAlO_2$ and K_2MgSiO_4 associates in this study were assessed using the thermodynamic property and phase diagram data of the K_2O-Al_2O_3-SiO_2 and K_2O-MgO-SiO_2 systems.

3.3.1 Binary System

The Modified Quasichemical Model (MQM) in the pair approximation [5] was employed to express the Gibbs energy function of the liquid oxide phase. The MQM takes into account the short-range ordering (SRO) of second-nearest-neighbor cations in the oxide melt. The cationic species in the liquid solution are K^+, Na^+, Ca^{2+}, Mg^{2+}, Al^{3+}, $NaAl^{4+}$, KAl^{4+}, K_2MgSi^{8+}, and Si^{4+} depending on the sub-systems, while O^{2-} is a common anion.

The quasichemical reaction considered in the binary oxide melt is:

$$(A-A)+(B-B)=2(A-B);\ \ \Delta g_{A-B} \tag{2}$$

where A and B are the cationic species in the respective solution; $(A-B)$ represents a second-nearest-neighbor pair of A and B cations with a common O^{2-} anion; Δg_{A-B} is the Gibbs energy of the reaction, which is a model parameter. Δg_{A-B} can be expanded as functions of pair fractions and temperature:

$$\Delta g_{A-B}=\Delta g^{o}_{AB}+\sum_{i\geq 1} g^{i0}_{AB}X^{i}_{AA}+\sum_{j\geq 1} g^{0j}_{AB}X^{j}_{BB} \tag{3}$$

where Δg^{o}_{AB}, g^{i0}_{AB}, and g^{0j}_{AB} are parameters as a function of temperature; X_{AA} and X_{BB} are the pair fractions of $(A-A)$ and $(B-B)$, respectively.

The Gibbs energy of the liquid solution is expressed as:

$$G^{sol}=(n_A g^{o}_{A}+n_B g^{o}_{B})-T\Delta S^{conf}+(n_{AB}/2)\Delta g_{A-B} \tag{4}$$

where n_i and g^{o}_{i} are the number of moles and the molar Gibbs energy of pure component *i*, respectively; n_{AB} is the number of moles of $(A-B)$ pairs; ΔS^{conf} is the configurational entropy of the solution expressed as a function of random distribution of quasichemical pairs based on one-dimensional Ising model [6]:

$$\Delta S^{conf}=-R(n_A \ln X_A+n_B \ln X_B)-R[n_{AA}\ln(\frac{X_{AA}}{Y_A^2})+n_{BB}\ln(\frac{X_{BB}}{Y_B^2})+n_{AB}\ln(\frac{X_{AB}}{2Y_AY_B})] \tag{5}$$

where Y_i is the coordination-equivalent fraction of *i*, which has the following relationships:

$$X_A = \frac{n_A}{n_A + n_B} = 1 - X_B \tag{6}$$

$$X_{ij} = \frac{n_{ij}}{n_{AA} + n_{BB} + n_{AB}} \tag{7}$$

$$Y_A = \frac{Z_A n_A}{Z_A n_A + Z_B n_B} = \frac{Z_A X_A}{Z_A X_A + Z_B X_B} = 1 - Y_B \tag{8}$$

$$Y_i = X_{ii} + X_{ij}/2 \tag{9}$$

where Z_A and Z_B are the coordination numbers of A and B, respectively. The coordination numbers are allowed to vary with composition as follows:

$$\frac{1}{Z_A} = \frac{1}{Z_{AA}^A}\left(\frac{2n_{AA}}{2n_{AA} + n_{AB}}\right) + \frac{1}{Z_{AB}^A}\left(\frac{n_{AB}}{2n_{AA} + n_{AB}}\right) \tag{10}$$

Z_{AA}^A and Z_{AB}^A are the coordination numbers of A when all nearest neighbors of an A are As and all nearest neighbors of an A are Bs, respectively; Z_{BB}^B and Z_{BA}^B are defined in a similar manner.

The SRO behavior in liquid solution can be well described by setting the coordination numbers of cations. For example, in the K_2O-SiO_2 system, the coordination numbers of K^+ (Z_{KK}^K), Si^{4+} (Z_{SiSi}^{Si}), and O^{2-} are set to be 0.6887, 2.7549, and 1.3774, respectively. Therefore, a strong SRO in the K_2O-SiO_2 liquid solution is clearly reproduced near the orthosilicate (K_4SiO_4) composition. All coordination numbers employed in this study are consistent with those used in the molten oxide database (FToxid) of the FactSage software [2].

3.3.2 Ternary and Multi-Component Systems

The Gibbs energy of ternary solution can be calculated using a so-called geometric interpolation technique. Symmetric Kohler-type and asymmetric Toop-type interpolation models are commonly used for ternary systems [7]. For example, in the K_2O-MgO-SiO_2 system, Δg_{K-Si} and Δg_{Mg-Si} are very negative (strong SRO behavior) while Δg_{K-Mg} shows ideal solution behavior. Hence, the ternary Gibbs energy was calculated using asymmetric Toop-type interpolation technique with SiO_2 as an asymmetrical component (see Fig. 3.1).

The excess Gibbs energy of the ternary solution at point P in Fig. 3.1 is calculated based on the excess Gibbs energies of sub-binary systems at point a, b, and c. The excess Gibbs energy at the ternary point P using the MQM model can be expressed as below:

$$g_P^E = (X_{12}/2)(\Delta g_{12} - \Delta g_{12}^o) + (X_{13}/2)(\Delta g_{13} - \Delta g_{13}^o) + (X_{23}/2)(\Delta g_{23} - \Delta g_{23}^o) + (ternary\ terms) \tag{11}$$

where X_{ij} are the mole fractions of $(i-j)$ pairs; Δg_{ij} are the binary interaction parameters of $(i-j)$ systems.

In the K_2O-MgO-SiO_2 ternary system, $\Delta g_{K\,Si}$ for the ternary excess Gibbs energy is expressed as:

$$\Delta g_{K\,Si} = \Delta g^o_{K\,Si} + \sum_{(i+j)\geq 1} g^{ij}_{K\,Si} X^i_{Si\,Si} (X_{K\,K} + X_{K\,Mg} + X_{Mg\,Mg})^j$$

$$+ \sum_{\substack{i\geq 0 \\ j\geq 0 \\ k\geq 1}} g^{ijk}_{K\,Si\,(Mg)} X^{\,i}_{Si\,Si} (X_{K\,K} + X_{K\,Mg} + X_{Mg\,Mg})^j \left(\frac{Y_{Mg}}{Y_K + Y_{Mg}}\right)^k \tag{12}$$

and $\Delta g_{Mg\,Si}$ can be expressed in a similar manner as for the $\Delta g_{K\,Si}$.

The $\Delta g_{K\,Mg}$ is given as:

$$\Delta g_{K\,Mg} = \Delta g^{o}_{K\,Mg} + \sum_{(i+j)\geq 1} g^{ij}_{K\,Mg} \left(\frac{X_{K\,K}}{X_{K\,K} + X_{K\,Mg} + X_{Mg\,Mg}}\right)^{i} \left(\frac{X_{Mg\,Mg}}{X_{K\,K} + X_{K\,Mg} + X_{Mg\,Mg}}\right)^{j}$$

$$+ \sum_{\substack{i\geq 0 \\ j\geq 0 \\ k\geq 1}} g^{ijk}_{K\,Mg\,(Si)} \left(\frac{X_{K\,K}}{X_{K\,K} + X_{K\,Mg} + X_{Mg\,Mg}}\right)^{i} \left(\frac{X_{Mg\,Mg}}{X_{K\,K} + X_{K\,Mg} + X_{Mg\,Mg}}\right)^{j} Y^{k}_{Si} \qquad (13)$$

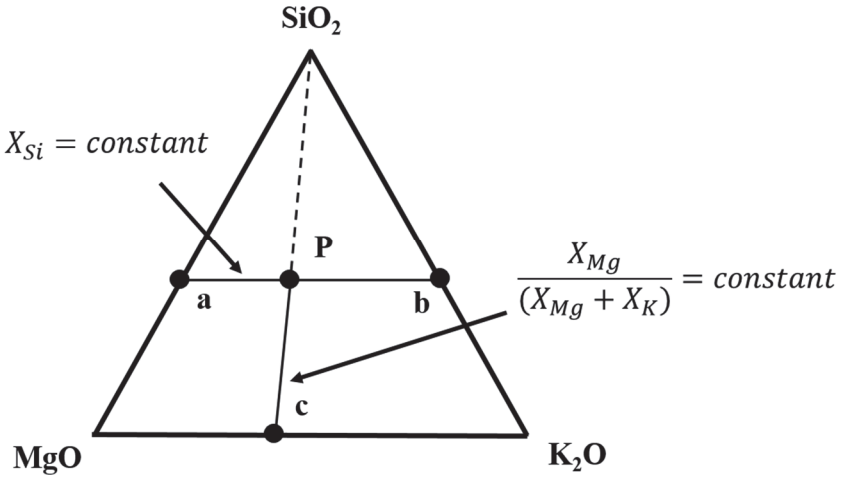

Figure 3.1 Schematic diagram of the Toop-type ternary interpolation technique used for the K_2O-MgO-SiO_2 system.

The details of overall interpolation method are well described in Ref. [8]. The MQM equations for the ternary interpolation models can be found in Ref. [7].

In general, the Gibbs energies of ternary solution can be calculated using the default setting of interpolation models. Two subgroup of components were assumed; acid group (Si^{4+}) and basic group (K^{+}, Na^{+}, Ca^{2+}, Mg^{2+}, Al^{3+}, $NaAl^{4+}$, KAl^{4+}, and K_2MgSi^{8+}). When two basic group

components and one acid group component was mixed, the Toop interpolation technique was used with the acid group component as an asymmetric component. Small ternary model parameters were introduced to reproduce the phase diagram and thermodynamic property data more accurately. The calculations of the quaternary and higher order systems were based on a general and complete extension of the Kohler-Muggianu-Toop formalism to multi-component systems which was developed by Pelton [8].

The structure of the K_2O-SiO_2 melt was predicted from the MQM. Three quasichemical pairs of $K-K$, $K-Si$, and $Si-Si$, which correspond to O^{2-} (free oxygen), O^- (broken oxygen), and O^o (bridged oxygen), respectively, are considered in the calculation. The calculated results at 1000 °C are plotted in Fig. 3.2 along with experimental data. The experimental structural data were measured using infrared (IR) spectroscopy [9], X-ray Photoelectron Spectroscopy (XPS) [10], Raman spectroscopy [11] and Nuclear Magnetic Resonance (NMR) [12-15] techniques. The calculated results from Molecular Dynamics (MD) [16] were also compared in Fig. 3.2. The available literature data are very well reproduced by the present calculations, even though these structural data were not directly considered throughout the process of thermodynamic optimization. Therefore, it can be said that this MQM can accurately describe not only the thermodynamic properties of liquid solution but also the short-range ordering structure of the K_2O-SiO_2 liquid solution. The melt structure of the K_2O-Al_2O_3-SiO_2 and K_2O-Na_2O-SiO_2 systems were also well predicted in this study (see Chapters 7 and 8).

In conclusion, the thermodynamic model used for the liquid solution in the present study, the MQM, adequately represents the actual structure of the molten oxide phase.

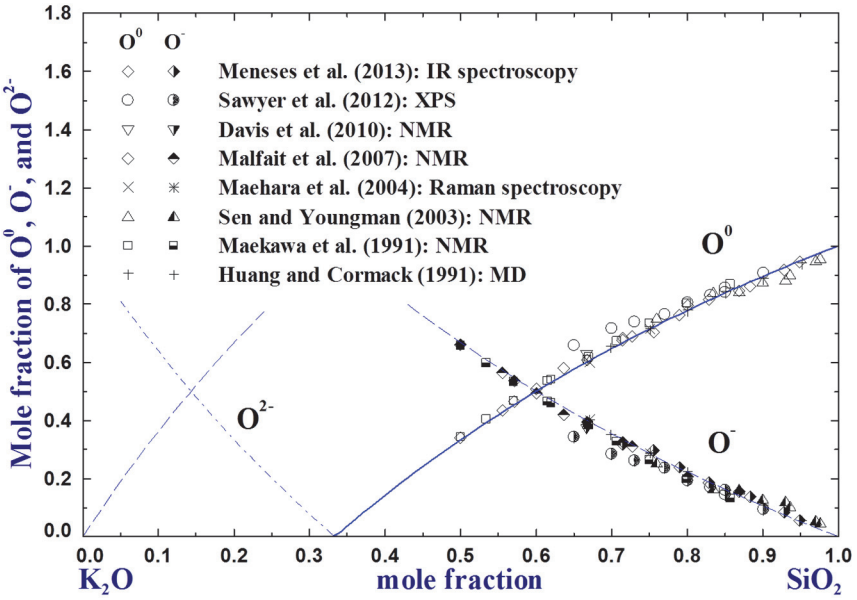

Figure 3.2 Predicted oxygen connectivity in terms of bridged oxygen (O^0), broken oxygen (O^-), and free oxygen (O^{2-}) of the K_2O-SiO_2 melt at 1000 °C in comparison with experimental data [9-16].

3.3.3 Associate Formation

Alkali and alkaline-earth oxides such as K_2O, Na_2O, Li_2O, BaO, and SrO are known to form associates in the SiO_2 melt with Al_2O_3 or Fe_2O_3. For example, the associate formation is based on the charge compensation effect [17] of K^+ ions with Al^{3+} ions to form an associate KAl^{4+} of valance 4^+, as the Si^{4+} ions in the SiO_2 network structure. The associate KAl^{4+} can replace Si^{4+} in the network structure with energetically favorable charge balance. This mechanism applies to other alkali and alkaline-earth oxide components in a similar manner, such as the formations of $NaFe^{4+}$ and $SrAl_2^{8+}$. Both experimental and thermodynamic optimization studies reported the evidence of the associates. Sukenaga *et al*. [18] reported that K^+ ions have strong tendency of associate formation with Al^{3+} ions in silicate system using ^{17}O-solid-state Nuclear Magnetic Resonance

(NMR). Mysen *et al*. [19] observed $NaFe^{4+}$ using Mossbauer and Raman spectroscopy. $NaAlO_2$, $NaFeO_2$, $SrAl_2O_4$, and $BaAl_2O_4$ associate components have already been used for the modeling of the liquid phase [3, 4, 20] under the MQM description. These associate components, which are the separate components in the liquid solution, were necessary to reproduce the phase diagram data. For example, the phase diagram of the K_2O-Al_2O_3-SiO_2 system implies the formation of $KAlO_2$ associate in the SiO_2-rich region (liquidus of SiO_2), which can be analyzed using the so-called limiting slope rule [21]. The limiting slope rule tells the nature of the entropy state of solution with the addition of new components in the solution. In the pseudo-binary section of $KAlO_2$-SiO_2, the slope of the SiO_2 liquidus close to pure SiO_2 ($X_{SiO_2} \rightarrow 1$) shows that K^+ and Al^{3+} enter into the liquid solution as KAl^{4+} associate instead of individuals; the mixing entropy introduced by two individual components are bigger than the associate, so the limiting slope should be steeper than the real experimental slope. The optimized SiO_2 liquidus in the $KAlO_2$-SiO_2 (present study) and the $NaAlO_2$-SiO_2 [3] sections are shown in Fig. 3.3 (a) and (b) as examples for the associate formation.

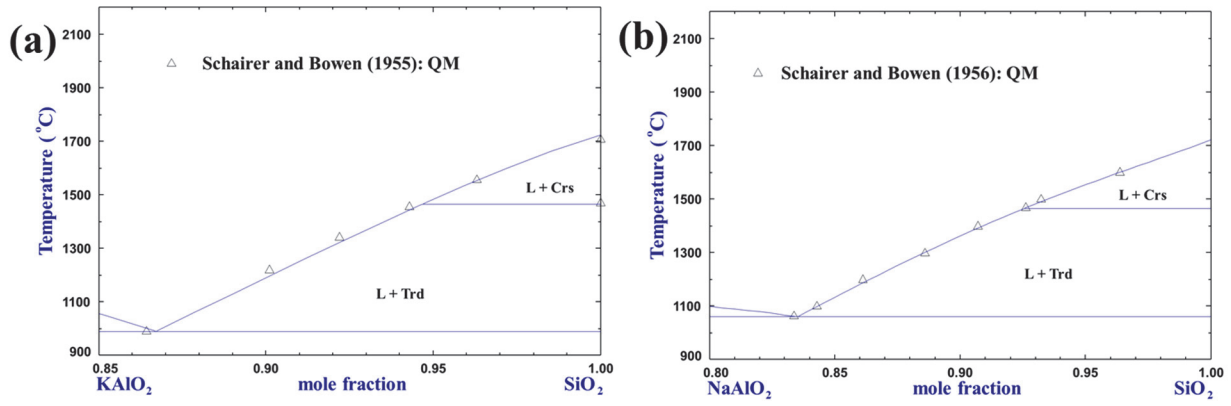

Figure 3.3 Optimized SiO_2 liquidus using the $KAlO_2$ and $NaAlO_2$ associates in (a) the $KAlO_2$-SiO_2 and (b) the $NaAlO_2$-SiO_2 [3] sections.

3.4 Solid Solutions

The high- and low-temperature meta-oxide (KAl^{4+}, $NaAl^{4+}$, $KMg_{0.5}Si_{0.5}^{4+}$, Si^{4+})O_2, β- and β″-alumina ($[K^+,Va]_1^{BR}[K^+,Va]_1^{aBR}[Al^{3+},Mg^{2+}]_2^{Al(2)}[O^{2-},Va]_1^{mO}\,Al_9^{Al(other)}O_{17}$), metasilicate (K_2^{2+} , Na_2^{2+})SiO_3, and disilicate (K_2^{2+} , Na_2^{2+})Si_2O_5 solid solutions were treated within the framework of the Compound Energy Formalism (CEF). Nepheline and kalsilite ($KAlSi^{8+}$, $KMg_{0.5}Si_{1.5}^{8+}$, $VaSi_2^{8+}$)O_4, and feldspar (KSi^{5+}, $NaSi^{5+}$, $CaAl^{5+}$)$AlSi_2O_8$ solid solutions were treated using the MQM. α- and α′-Ca_2SiO_4 solid solutions were optimized using a simple random mixing model.

3.4.1 Meta-Oxide Solid Solution

The dissolution mechanism of SiO_2 into low-temperature K_2MgSiO_4 meta-oxide (KMS) is adopted from Grey *et al*.'s study [22]. In fact, this is the only comprehensive crystal structure study for the meta-oxide solid solution which revealed the dissolution mechanism of SiO_2. According to the study by Grey *et al*. for β- and γ'-$NaFeO_2$ meta-oxide, a coupled substitution of $Si^{4+} \leftrightarrow Fe^{3+} + Na^+$ occurs in the dissolution of SiO_2 in $NaFeO_2$. In particular, vacancy (Va) is coupled with Si^{4+} at adjacent interstitial site when Si^{4+} substitutes Fe^{3+} in the framework of tetrahedra and removes Na^+ from the framework cavities. That is, Va is not formed randomly in the solution but clearly associated to the position of Si^{4+} during the SiO_2 dissolution in $NaFeO_2$. This dissolution mechanism was modeled previously by Moosavi-Khoonsari and Jung [23] using the Compound Energy Formalism (CEF) [24] with ($NaFe^{4+}$, $SiVa^{4+}$)O_2 model structure. The crystal structure of potassium-containing meta-oxides, such as K_2MgSiO_4, $KAlO_2$, $KGeO_2$, and $KFeO_2$, have their low-temperature polymorphs of orthorhombic structure, which is the same crystal structure as β- and γ'-$NaFeO_2$. The solution mechanism of the high-temperature polymorph of K_2MgSiO_4 meta-oxide was assumed to be the same as the low-temperature one because of structural similarity and

lack of experimental data on the solution mechanism. Therefore, both low- and high-temperature polymorphs of K_2MgSiO_4 were described in this study using the CEF with $(K_2Mg^{4+}, VaSi^{4+})SiO_4$. That is, the molar Gibbs energy of K_2MgSiO_4 solution is expressed by:

$$G^{sol} = (y_i G_i^o + y_j G_j^o) + RT(y_i \ln y_i + y_j \ln y_j) + \sum_{n\geq 0}{}^{n}L_{ij} y_i y_j (y_j - y_i)^n \quad (14)$$

where G_i^o is the molar Gibbs energy of the end-member *i* of the solution; y_i is the site fraction of the species *i*; *R* is the gas constant; ${}^{n}L_{ij}$ are the excess interaction parameters. For example, in the K_2MgSiO_4 solution, y_i and y_j are the mole fractions of K_2Mg^{4+} and $VaSi^{4+}$.

3.4.2 β- and β″-Alumina Solid Solutions

There are two solid solution phases in the K_2O-Al_2O_3 and K_2O-MgO-Al_2O_3 systems: β- and β″-alumina. In the binary system, β-alumina has about 2-3 mol % excess K_2O from the stoichiometric $KAl_{11}O_{17}$ and β″-alumina has also about 2-3 mol % excess Al_2O_3 from ideal stoichiometry $KAl_{5.5}O_{8.75}$. In the ternary system, β″-alumina has about 10 mol % of MgO solubility, while only about 5-7 mol % excess MgO can dissolve in the β-alumina at 1400 °C.

The base crystal structures of β- and β″-alumina solutions are essentially the same. The schematics of lattice structure and conduction plane of β- and β″-alumina are presented in Figs. 3.4 and 3.5, respectively. The structural data was taken from Collin *et al*. [25] and Boilot *et al*. [26] for β- and β″-alumina, respectively, and they were re-drawn using VESTA software [27].

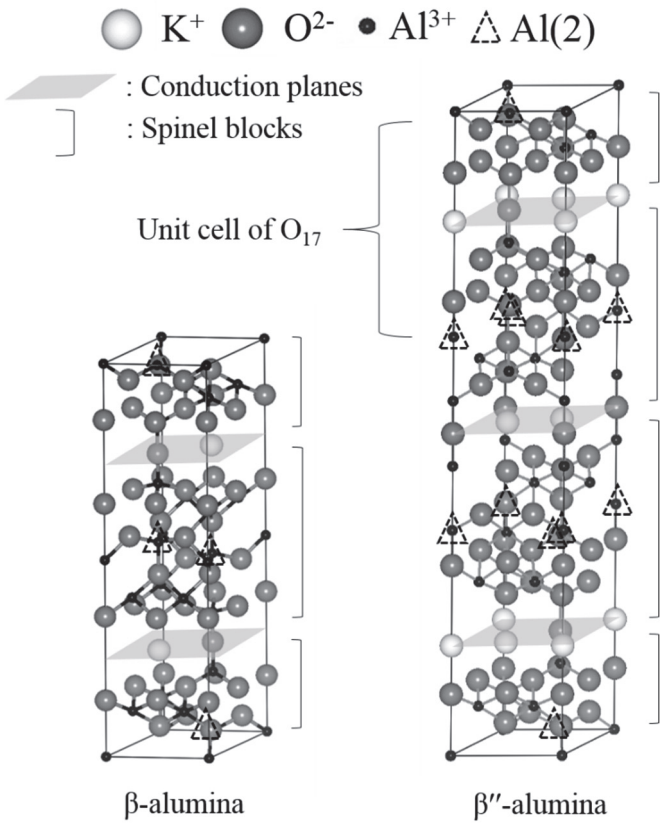

Figure 3.4 Schematic lattice structures of K β- and β″-alumina.

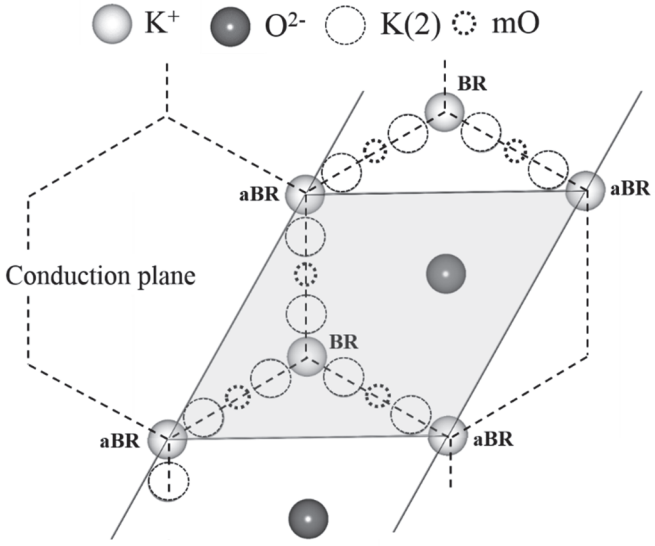

Figure 3.5 Schematics of conduction plane of K β- and β″-alumina.

According to the structural crystallographic studies [28-30], β-alumina is composed of two spinel (spinel-like) blocks with one conduction plane in between for the unit cell structure [28, 30]. β″-alumina is composed of three spinel blocks with two conduction planes [29]. In the spinel blocks, there are two tetrahedral sites and two octahedral sites for Al^{3+} ions. When MgO dissolves in these solutions, one of the two tetrahedral sites is predominantly occupied by Mg^{2+} according to experimental analyses [26, 30]. This site is generally known as the Al(2) site. In the structure of β- and β″-alumina, the conduction plane where ionic conduction happens, consists of Al-O-Al bonds and K^+ ions. The conduction planes can have two sites for K^+ ions and one site for O^{2-} ions. In earlier studies, Beevers-Ross (BR) and anti Beevers-Ross (aBR) were defined for K^+ sites, and mid oxygen (mO) for O^{2-} site [28]. More recent studies reported that K^+ ions are observed in slightly shifted positions from their original BR and aBR sites (which are called K(2) sites) when O^{2-} ions occupy mO sites. [26, 30, 31]. The mO sites are predominantly occupied by additional interstitial O^{2-} ions due to the dissolution of K_2O. When Mg^{2+} ions substitute Al^{3+} in the Al(2) tetrahedral site, additional K^+ can enter the BR and aBR sites of β- and β″-alumina [25, 26]. Although β- and β″-alumina have different sizes of unit cells, the basic building block of both solution consists of one conduction plane with two of half spinel blocks (O_{17}) as shown in Fig. 3.4. Based on the structural information, the lattice structure of β- and β″-alumina can be formulated in the one unit cell (O_{17}) as follows:

$$[K^+, Va]_1^{BR}[K^+, Va]_1^{aBR}[Al^{3+}, Mg^{2+}]_2^{Al(2)}[O^{2-}, Va]_1^{mO}\, Al_9^{Al(other)}O_{17} \quad (15)$$

BR, aBR, Al(2), and mO stand for Beever-Ross, anti Beever-Ross, Al(2), and mid-oxygen site, respectively, followed by the notations reported in many crystallographic studies [25, 28, 31-33]. As K(2) site is essentially same as BR and aBR sites (no configurational entropy can be generated

by K(2) sites), K(2) were not included in the present β- and β″-alumina model. Species in the same bracket can mix in the same sublattice. Proper sublattice structure is important to describe the configurational entropy of the solution.

The Gibbs energies of the β- and β″-alumina solutions were described within the framework of the Compound Energy Formalism (CEF) [24] considering the sublattice structure in Eq. (15):

$$G^{sol\text{n}} = \sum_i \sum_j \sum_k \sum_l Y_i^{BR} Y_j^{aBR} Y_k^{Al(2)} Y_l^{mO} G_{ijkl}^{o} - T\Delta S^{conf} + G^{E} \tag{16}$$

where Y_i^{BR}, Y_j^{aBR}, $Y_k^{Al(2)}$, and Y_l^{mO} represent the site fractions of components *i*, *j*, *k*, and *l* in the respective sublattice; G_{ijkl}^{o} is the Gibbs energy of an end-member $[i]^{BR}[j]^{aBR}[k]^{Al(2)}[l]^{mO}\,Al_9^{Al(other)}O_{17}$; ΔS^{conf} is the configurational entropy of the solution expressed as a function of random distribution of cations in each sublattice:

$$\Delta S^{conf} = -R\left(\sum_i Y_i^{BR} \ln Y_i^{BR} + \sum_j Y_j^{aBR} \ln Y_j^{aBR} + 2\sum_k Y_k^{Al(2)} \ln Y_k^{Al(2)} + \sum_l Y_l^{mO} \ln Y_l^{mO}\right) \tag{17}$$

and G^{E} is the excess Gibbs energy of the solution:

$$G^{sol\text{n}} = \sum_a \sum_b \sum_c \sum_d \sum_e Y_a^m Y_b^m Y_c^n Y_d^p Y_e^q L_{ab;c;d;e}^{m;n;p;q} \tag{18}$$

where $L_{ab;c;d;e}^{m;n;p;q}$ is the interaction energy between cations *a* and *b* in the *m* sublattice when other sublattices of *n*, *p*, and *q* are occupied by cations of *c*, *d*, and *e*, respectively. The interaction parameter $L_{ab;c;d;e}^{m;n;p;q}$ is expressed using the Redlich-Kister polynomials as a function of site fractions.

In the present study, no excess Gibbs energy parameters was used for β- and β″-alumina solutions. The main model parameter in the solution described by the CEF is the Gibbs energy of end-members. The β- and β″-alumina solutions contain 16 end-members, as listed in Eqs. 19 to 35. A schematic presentation of the solution Gibbs energy structure is depicted in Fig. 3.6. All end-members and charge-neutral composition lines are shown in the figure. For convenience, alphabetic abbreviations are used to represent each ionic species: K = K^+, M = Mg^{2+}, A = Al^{3+}, O = O^{2-}, and V stands for Vacancy. For example, G_{KVAO} stands for the Gibbs energy of the end-member containing K^+ in the first BR sublattice, Va in the second aBR sublattice, Al^{3+} in the third Al(2) sublattice, and O^{2-} in the fourth mO sublattice. The symbol Δ represents site exchange reactions which is used to determine the Gibbs energy of hypothetical end-member. These Δ parameters have physical meanings and are more logical approaches to determine hypothetical end-member Gibbs energies than assigning arbitrary Gibbs energy value to the end-member. As β- and β″-alumina have very similar structures, the Gibbs energies of an end-member should be very close to each other. In the present study, the following procedure was used to determine the Gibbs energies of end-members of the solution.

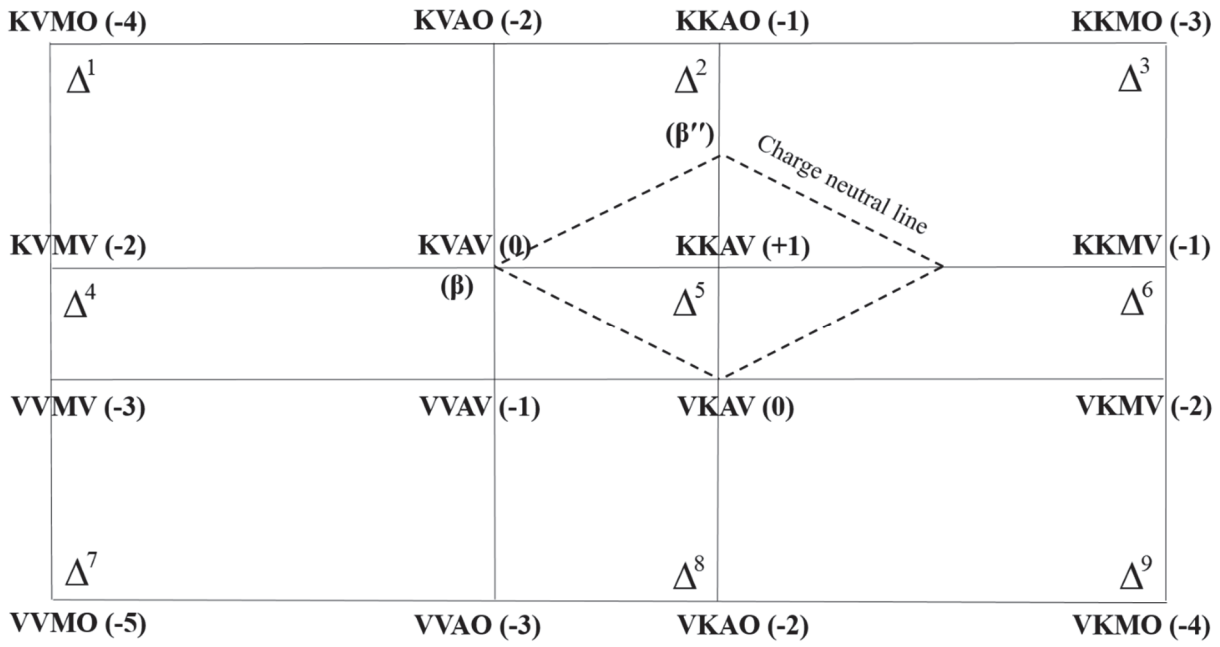

Figure 3.6 Schematic diagram of the end-members in β and β″-alumina solid solutions.

Binary β-alumina

$$G_{KVAV} = G^{o}_{KAl_{11}O_{17}(\beta-alumina)} \tag{19}$$

$$G_{KKAO} = G_{KKAV} = \tfrac{1}{2}(G^{o}_{K_4Al_{22}O_{35}(\beta''-alumina)} + \Delta S^{conf} + G^{add(1)}) \tag{20}$$

Binary β″-alumina

$$G_{KKAO} = G_{KKAV} = \tfrac{1}{2}(G^{o}_{K_4Al_{22}O_{35}(\beta''-alumina)} + \Delta S^{conf}) \tag{21}$$

$$G_{KVAV} = G^{o}_{KAl_{11}O_{17}(\beta-alumina)} + G^{add(2)} \tag{22}$$

Common binary end-members

$$\Delta^2 = G_{KVAO} + G_{KKAV} - G_{KKAO} - G_{KVAV}\,, \qquad G_{KVAO} = G_{KVAV} + \Delta^2 \tag{23}$$

$$I^1 = G_{VKAV} - G_{KVAV}\,, \qquad G_{VKAV} = G_{KVAV} + I^1 \tag{24}$$

$$\Delta^5 = G_{KVAV} + G_{VKAV} - G_{KKAV} - G_{VVAV}, \qquad G_{VVAV} = 2 \cdot G_{KVAV} - G_{KKAV} + I^1 \tag{25}$$

$$I^2 = G_{VKAO} - G_{KVAO}, \qquad G_{VKAO} = G_{KVAV} + \Delta^2 + I^2 \tag{26}$$

$$\Delta^8 = G_{VVAV} + G_{VKAO} - G_{VKAV} - G_{VVAO}, \qquad G_{VVAO} = 2 \cdot G_{KVAV} - G_{KKAV} + \Delta^2 + I^2 \tag{27}$$

Ternary β- and β″-alumina

$$G_{KKMV} = G_{KVAV} + G^{add(K-Mg)} \tag{28}$$

$$G_{KVMV} = G_{KVAV} + G^{add(Va-Mg)} \tag{29}$$

$$\Delta^1 = G_{KVMO} + G_{KVAV} - G_{KVAO} - G_{KVMV}, \qquad G_{KVMO} = G_{KVAV} + G^{add(Va-Mg)} + I^1 \tag{30}$$

$$\Delta^3 = G_{KKAO} + G_{KKMV} - G_{KKMO} - G_{KKAV}, \qquad G_{KKMO} = G_{KVAV} + G^{add(K-Mg)} \tag{31}$$

$$\Delta^4 = G_{KVMV} + G_{VVAV} - G_{KVAV} - G_{VVMV}, \qquad G_{VVMV} = 2 \cdot G_{KVAV} - G_{KKAV} + G^{add(Va-Mg)} + I^1 \tag{32}$$

$$\Delta^6 = G_{KKAV} + G_{VKMV} - G_{KKMV} - G_{VKAV}, \qquad G_{VKMV} = 2 \cdot G_{KVAV} - G_{KKAV} + G^{add(K-Mg)} + I^1 \tag{33}$$

$$\Delta^7 = G_{VVMV} + G_{VVAO} - G_{VVAV} - G_{VVMO}, \qquad G_{VVMO} = 2 \cdot G_{KVAV} - G_{KKAV} + G^{add(Va-Mg)} + \Delta^2 + I^2 \tag{34}$$

$$\Delta^9 = G_{VKAV} + G_{VKMO} - G_{VKMV} - G_{VKAO}, \qquad G_{VKMO} = 2 \cdot G_{KVAV} - G_{KKAV} + G^{add(K-Mg)} + \Delta^2 + I^1 \tag{35}$$

The Gibbs energies of charge-neutral stable end-members of β-alumina (KVAV) and β″-alumina (0.5·KKAO + 0.5·KKAV) were first determined from the thermodynamic data in the binary K_2O-Al_2O_3 system. Then, the limited solubility ranges of both β- and β″-alumina solutions were reproduced using the Gibbs energy parameters, $G^{add(1)}$ for β-alumina and of $G^{add(2)}$ for β″-alumina. Charged end-member of KVAO in Eq. 23 was determined by the site exchange reaction (Δ^2) with the end-members of β-alumina (KVAV) and β″-alumina (KKAO and KKAV). Phase diagram data were mainly considered to evaluate Δ^2. The end-member KVAO represents unstable β- and β″-alumina when excess O^{2-} occupy the mO sites without charge-balanced K^+ in aBR site.

The inverse β-alumina, VKAV is modeled considering the inversion reaction from β-alumina (KVAV). The inversion parameter (I^1) was set to reproduce the K^+ distribution between BR and aBR site (Eq. 24). The end-member of VVAV was set based on the site exchange reaction Δ^5, which was set to be zero (Eq. 25). The Gibbs energy of VKAO (Eq. 26) is the determinant of the K^+ distribution between BR and aBR sites as it is for the VKAV (Eq. 24). Then, the VVAO was derived assuming $\Delta^8 = 0$ in Eq. 27. The solubility of MgO was modeled using an additional Gibbs energy of $G^{add(K-Mg)}$ to the Gibbs energy of β-alumina (KVAV) to determine the Gibbs energy of KKMV end-member (Eq. 28). KKMV represents the charge-balanced substitution of Al^{3+} with Mg^{2+} in the Al(2) site coupled with additional K^+ in aBR site. Mg^{2+} substitution in Al(2) site without charge compensating K^+ in aBR site was represented by KVMV in Eq. 29. Other hypothetical end-members containing Mg^{2+} in the ternary system were modeled with an assumption that the site exchange reaction energy Δ equals to zero (Eqs. 30-35). In fact, the solubility of MgO in β- and β″-alumina is only determined by the Gibbs energies of KKMV and KVMV.

3.4.3 Nepheline and Kalsilite Solid Solutions

$K_2MgSi_3O_8$ solid solutions were described by the MQM. Low-temperature $K_2MgSi_3O_8$ has the structure of nepheline, $NaAlSiO_4$, and forms solid solution with $NaAlSiO_4$ and $KAlSiO_4$. Therefore, the consistent thermodynamic solution model for $NaAlSiO_4$ was adopted. At low temperatures, there is a small but noticeable solubility of SiO_2 in these three types of nepheline structures: $K_2MgSi_3O_8$, $NaAlSiO_4$, and $KAlSiO_4$ [34, 35]. An extensive solubility between $KAlSiO_4$ and $K_2MgSi_3O_8$ was found [34], and $KAlSiO_4$ and $NaAlSiO_4$ form a complete solid solution [36, 37]. Therefore, these compounds with the nepheline structure should be modeled

consistently. Previously, $NaAlSiO_4$ with excess SiO_2 solubility was modeled [35] using the MQM. In this study, this $K_2MgSi_3O_8$ nepheline solution was modeled using the MQM with $K_2MgSi_3O_8$-Si_2O_4 solid solution. The high-temperature polymorph of $K_2MgSi_3O_8$, which has a kalsilite-like structure, was described using the same framework as the nepheline solution. At high temperatures, there is a limited solubility between $K_2MgSi_3O_8$ and $KAlSiO_4$ [34] and between $KAlSiO_4$ and $NaAlSiO_4$ [36, 37], but no mutual solubility between $K_2MgSi_3O_8$ and $NaAlSiO_4$.

3.4.4 α- and α′-Ca_2SiO_4 Solid Solutions

Limited solubility of potassium into α- and α′-Ca_2SiO_4 (C_2S) were found in the literature for the K_2O-CaO-SiO_2 system. Although the exact solution mechanism is not known, a maximum of about 9 mol % of K_2CaSiO_4 (KCS) solubility was measured in α′-C_2S at 1300 °C [38], and 3.5 and 8.3 mol % KCS into the C_2S phase were found for the samples equilibrated at different temperatures (cannot be known precisely) [39, 40]. The solution model was taken from the previous thermodynamic optimization by Jung *et al*. [41]. The α- and α′-C_2S solutions were modeled using the random mixing model with a polynomial expansion of the excess Gibbs energy. The chemical formula of both solutions are $(K_2^{2+}, Ca^{2+})_2 SiO_4$.

The Gibbs energy of the C_2S solutions can be expressed as:

$$G^{so\ln} = (X_i G_i^o + X_j G_j^o) + 2RT(X_i \ln X_i + X_j \ln X_j) + \sum_{m,n\geq 0} q_{ij}^{mn} (X_i)^m (X_j)^n \quad (36)$$

where G_i^o is the molar Gibbs energy of the end-member *i* of the solution; X_i is the mole fraction of the species *i*; *R* is the gas constant; q_{ij}^{mn} are the excess interaction parameters. For both solutions, X_i and X_j are the mole fractions of K_2^{2+} and Ca^{2+}.

3.4.5 Metasilicate and Disilicate Solid Solutions

Limited solubility between K_2SiO_3 and Na_2SiO_3 (metasilicate), between $K_2Si_2O_5$ and $Na_2Si_2O_5$ (high- and intermediate-temperature disilicates), and a complete solid solution for low-temperature disilicates are modeled. The solution mechanisms of metasilicate and disilicate are adopted from the previous optimization by Konar *et al*. [42]. As alkali silicate and aluminosilicate systems often show systematic trend in phase diagram and thermodynamic properties, the solid solutions reported for meta- and disilicates in the Li_2O-Na_2O-SiO_2 system [43, 44] were considered in this study to reproduce the phase diagram data [45] and the thermodynamic property data [46, 47] simultaneously. The formation of these solid solutions in the K_2O-Na_2O-SiO_2 system is also inferred from many stoichiometric ternary compounds reported in the range of 8 to 50 mol % K_2O in the disilicate compositions. A range of solid solution is more reasonable instead of five different stoichiometric compounds with the same crystal structure. The meta- and disilicate solutions are modeled using the CEF [24]. The chemical formula of meta- and disilicate solutions are $(K_2^{2+}, Na_2^{2+})SiO_3$ and $(K_2^{2+}, Na_2^{2+})Si_2O_5$, respectively, with miscibility gaps that produce K_2O- and Na_2O-rich solid solutions.

That is, the Gibbs energy of meta- and disilicate solutions are expressed by:

$$G^{soln} = (y_i G_i^o + y_j G_j^o) + RT(y_i \ln y_i + y_j \ln y_j) + \sum_{n\geq 0}{}^{n}L_{ij} y_i y_j (y_j - y_i)^n \quad (37)$$

where G_i^o is the molar Gibbs energy of the end-member *i* of the solution; y_i is the site fraction of the species *i*; *R* is the gas constant; ${}^{n}L_{ij}$ are the excess interaction parameters. For both solutions, y_i and y_j are the mole fractions of K_2^{2+} and Na_2^{2+}.

References

[1] L. Kaufman, J. Agren, CALPHAD, first and second generation - Birth of the materials genome, Scr. Mater. 70 (2014) 3-6.
[2] C.W. Bale, E. Belisle, P. Chartrand, S.A. Decterov, G. Eriksson, A.E. Gheribi, K. Hack, I.H. Jung, Y.B. Kang, J. Melancon, A.D. Pelton, S. Petersen, C. Robelin, J. Sangster, P. Spencer, M.A. Van Ende, FactSage thermochemical software and databases, 2010-2016, CALPHAD: Comput. Coupling Phase Diagrams Thermochem. 54 (2016) 35-53.
[3] P. Chartrand, A.D. Pelton, Modeling the charge compensation effect in silica-rich Na2O-K2O-Al2O3-SiO2 melts, CALPHAD: Comput. Coupling Phase Diagrams Thermochem. 23 (1999) 219-230.
[4] E. Moosavi-Khoonsari, I.-H. Jung, Critical evaluation and thermodynamic optimization of the Na2O–FeO–Fe2O3–Al2O3–SiO2 system, Journal of the European Ceramic Society 37(2) (2017) 787-800.
[5] A.D. Pelton, S.A. Degterov, G. Eriksson, C. Robelin, Y. Dessureault, The modified quasichemical model I - binary solutions, Metall. Mater. Trans. B 31B (2000) 651-659.
[6] E. Ising, Beitrag zur Theorie des Ferromagnetismus, Zeitschrift für Physik 31(1) (1925) 253-258.
[7] A. Pelton, P. Chartrand, The modified quasi-chemical model: Part II. Multicomponent solutions, Metallurgical and Materials Transactions A 32(6) (2001) 1355-1360.
[8] A.D. Pelton, A general "geometric" thermodynamic model for multicomponent solutions, CALPHAD: Comput. Coupling Phase Diagrams Thermochem. 25(2) (2001) 319-328.
[9] D. De Sousa Meneses, M. Eckes, L. del Campo, C.N. Santos, Y. Vaills, P. Echegut, Investigation of medium range order in silicate glasses by infrared spectroscopy, Vib. Spectrosc. 65 (2013) 50-57.
[10] R. Sawyer, H.W. Nesbitt, R.A. Secco, High resolution X-ray Photoelectron Spectroscopy (XPS) study of K2O-SiO2 glasses: evidence for three types of O and at least two types of Si, J. Non-Cryst. Solids 358(2) (2012) 290-302.
[11] T. Maehara, T. Yano, S. Shibata, M. Yamane, Structure and phase transformation of alkali silicate melts analyzed by Raman spectroscopy, Philos. Mag. 84(29) (2004) 3085-3099.
[12] W.J. Malfait, W.E. Halter, Y. Morizet, B.H. Meier, R. Verel, Structural control on bulk melt properties: Single and double quantum 29Si NMR spectroscopy on alkali-silicate glasses, Geochim. Cosmochim. Acta 71(24) (2007) 6002-6018.
[13] S. Sen, R.E. Youngman, NMR study of Q-speciation and connectivity in K2O-SiO2 glasses with high silica content, J. Non-Cryst. Solids 331(1-3) (2003) 100-107.
[14] H. Maekawa, T. Maekawa, K. Kawamura, T. Yokokawa, The structural groups of alkali silicate glasses determined from silicon-29 MAS-NMR, J. Non-Cryst. Solids 127(1) (1991) 53-64.
[15] M.C. Davis, D.C. Kaseman, S.M. Parvani, K.J. Sanders, P.J. Grandinetti, D. Massiot, P. Florian, Q(n) Species Distribution in K2O·2SiO2 Glass by 29Si Magic Angle Flipping NMR, J. Phys. Chem. A 114(17) (2010) 5503-5508.
[16] C. Huang, A.N. Cormack, Structural differences and phase separation in alkali silicate glasses, J. Chem. Phys. 95(5) (1991) 3634-42.
[17] B.O. Mysen, P. Richet, Silicate glasses and melts properties and structure, Elsevier2005.

[18] S. Sukenaga, K. Kanehashi, H. Shibata, N. Saito, K. Nakashima, Structural Role of Alkali Cations in Calcium Aluminosilicate Glasses as Examined Using Oxygen-17 Solid-State Nuclear Magnetic Resonance Spectroscopy, Metall. Mater. Trans. B 47(4) (2016) 2177-2181.
[19] B.O. Mysen, F. Seifert, D. Virgo, Structure and redox equilibriums of iron-bearing silicate melts, Am. Mineral. 65(9-10) (1980) 867-84.
[20] A. Shukla, Development of a critically evaluated thermodynamic database for the systems containing alkaline-earth oxides, Department of chemical engineering, UNIVERSITÉ DE MONTRÉAL - ÉCOLE POLYTECHNIQUE DE MONTRÉAL, 2012, pp. 1-349.
[21] A.D. Pelton, Thermodynamics and Phase Diagrams of Materials, Phase Transformations in Materials, Wiley-VCH Verlag GmbH & Co. KGaA2005, pp. 1-80.
[22] I.E. Grey, B.F. Hoskins, I.C. Madsen, A structural study of the incorporation of silica into sodium ferrites, Na1-x[Fe1-xSixO2], x = 0 to 0.20, J. Solid State Chem. 85(2) (1990) 202-19.
[23] E. Moosavi-Khoonsari, I.-H. Jung, Critical Evaluation and Thermodynamic Optimization of the Na2O-FeO-Fe2O3-SiO2 System, Metallurgical and Materials Transactions B 47(1) (2016) 291-308.
[24] M. Hillert, The compound energy formalism, J. Alloys Compd. 320(2) (2001) 161-176.
[25] G. Collin, R. Comes, J.P. Boilot, P. Colomban, Crystal structure and ion-ion correlation of ion-rich β alumina type compounds. I. Magnesium doped potassium rich β alumina, Solid State Ionics 1(1-2) (1980) 59-68.
[26] J.P. Boilot, G. Collin, P. Colomban, R. Comes, X-ray-scattering study of the fast-ion conductor β"-alumina, Phys. Rev. B: Condens. Matter 22(12) (1980) 5912-23.
[27] K. Momma, F. Izumi, VESTA 3 for three-dimensional visualization of crystal, volumetric and morphology data, J. Appl. Crystallogr. 44(6) (2011) 1272-1276.
[28] C.A. Beevers, M.A.S. Ross, The crystal structure of "beta alumina," Na2O.11Al2O3, Z. Kristallogr., Kristallgeom., Kristallphys., Kristallchem. 97 (1937) 59-66.
[29] G. Yamaguchi, K. Suzuki, Structures of alkali polyaluminates, Bull. Chem. Soc. Jap. 41 (1968) 93-9.
[30] P.D. Dernier, J.P. Remeika, Structural determinations of single-crystal K β-alumina and cobalt-doped K β-alumina, J. Solid State Chem. 17(3) (1976) 245-53.
[31] N. Iyi, Z. Inoue, S. Kimura, The crystal structure of highly nonstoichiometric potassium β-alumina, K1.50Al11.0O17.25, J. Solid State Chem. 61(1) (1986) 81-9.
[32] W.L. Roth, F. Reidinger, S. LaPlaca, Studies of stabilization and transport mechanisms in beta and beta" alumina by neutron diffraction, Plenum, 1976, pp. 223-41.
[33] D.P. Birnie, III, On the structural integrity of the spinel block in the β"-alumina structure, Acta Crystallogr., Sect. B: Struct. Sci. 68(2) (2012) 118-122.
[34] R.S. Roth, Phase equilibriums research in portions of the potassium oxide-magnesium oxide-iron(III)oxide-aluminum oxide-silicon dioxide system, Adv. Chem. Ser. 186 (1980) 391-408.
[35] E. Jak, P. Hayes, A.D. Pelton, S.A. Decterov, Thermodynamic modeling of the Al2O3-CaO-FeO-Fe2O3-PbO-SiO2-ZnO system with addition of K and Na with metallurgical applications, Proc. VIII Int'l Conf. on Molten Slags, Fluxes and Salts, Santiago, Chile (2009) 473-490.
[36] J.F. Schairer, The alkali-feldspar join in the system NaAlSiO4-KAlSiO4SiO2, J. Geol. 58 (1950) 512-17.
[37] O.F. Tuttle, J.V. Smith, The nepheline-kalsilite system. II. Phase relations, Am. J. Sci. 256 (1958) 571-89.
[38] N.F. Fedorov, E.R. Brodkina, Solid solutions in the system 2CaO·SiO2-K2O·CaO·SiO2, Izv. Akad. Nauk SSSR, Neorg. Mater. 2(4) (1966) 745-8.

[39] H. Suzukawa, The alkali phases in portland cement. II. The potassium phase, Zem.-Kalk-Gips 9 (1956) 390-6.
[40] G. Lai, T. Nojiri, K. Nakano, Studies of the stability of β-calcium silicate (β-Ca2SiO4) doped by minor ions, Cem. Concr. Res. 22(5) (1992) 743-54.
[41] I.-H. Jung, S.A. Decterov, A.D. Pelton, Critical thermodynamic evaluation and optimization of the CaO-MgO-SiO2 system, J. Eur. Ceram. Soc. 25(4) (2005) 313-333.
[42] B. Konar, P. Hudon, I.H. Jung, A coupled experimental phase diagram study and thermodynamic modeling of the Li2O-Na2O-SiO2 system, Unpublished work (2017).
[43] A.R. West, Phase equilibriums in the system sodium metasilicate-lithium metasilicate, J. Am. Ceram. Soc. 59(3-4) (1976) 118-21.
[44] A.R. West, Phase equilibriums in the system sodium metasilicate-lithium metasilicate-silicon dioxide, J. Am. Ceram. Soc. 59(3-4) (1976) 124-7.
[45] F.C. Kracek, The ternary system: K2SiO3-Na2SiO3-SiO2, J. Phys. Chem. 36 (1932) 2529-42.
[46] R. Chastel, C. Bergman, J. Rogez, J.C. Mathieu, Excess thermodynamic functions in ternary sodium oxide-potassium oxide-silica melts by Knudsen cell mass spectrometry, Chem. Geol. 62 (1987) 19-29.
[47] C.T. Moynihan, A.J. Easteal, D.C. Tran, J.A. Wilder, E.P. Donovan, Heat capacity and structural relaxation of mixed-alkali glasses, J. Am. Ceram. Soc. 59(3-4) (1976) 137-40.

Chapter 4 Coupled Experimental Study and Thermodynamic Optimization of the K_2O-SiO_2 System

Dong-Geun Kim, Marie-Aline Van Ende, Pierre Hudon and In-Ho Jung

Submitted to Journal of Non-Crystalline Solids.

In this chapter, results of experimental and thermodynamic optimization studies of the K_2O-SiO_2 system is described. Thermal analyses with sealed Pt capsules were performed to measure the K_2O-rich region of the system. The Modified Quasichemical Model was used to optimize the liquid solution.

Abstract

Key phase diagram experiments and thermodynamic optimization were performed for the binary K_2O-SiO_2 system. For the first time, the temperature of eutectic reaction: Liquid → K_4SiO_4 + K_2SiO_3 was successfully measured at 714 ± 6 °C using thermal analysis technique with sealed Pt capsules. Thermodynamic optimization based on the critical evaluation of all available experimental data was conducted to obtain a set of self-consistent thermodynamic functions for the K_2O-SiO_2 system. This optimization can well reproduce all available and reliable thermodynamic properties and phase diagram data as well as melt structure in the K_2O-SiO_2 system.

Key words: K_2O-SiO_2; thermodynamic optimization; phase diagram; thermal analysis; sealed Pt capsule

4.1 Introduction

Phase diagram and thermodynamic properties of the K_2O-SiO_2 system are important in various applications. K_2O and SiO_2 are traditionally and widely used as glass components [1]. More recently, they became the main components for various types of glass-ceramics and ion-exchanged (strengthened) glass [2-6]. In glass-melting furnaces, the chemical reaction between SiO_2 refractories and K_2O vapor can be understood through studying the K_2O-SiO_2 system [7]. This binary system is also essential to understand alkali silicate glass properties [8-10]. In biofuel industry, K_2O-containing silicate slags in biomass and coal combustion processes can cause refractory corrosion [11, 12]. In steelmaking industry, alkali-oxide containing fluxes are considered as replacements for CaF_2 as refining and casting fluxes due to the environmental concerns. Phase equilibria of the K_2O-SiO_2 system is important in geological mineralogy studies as well. K_2O-containing aluminosilicates are one of the most abundant rock-forming minerals on earth [13]. However, due to the extremely hygroscopic and volatile properties of K_2O, no phase diagram experiments have been successfully conducted in the K_2O-rich region of the K_2O-SiO_2 system. As a result, thermodynamic modeling studies [7, 14-21] of this binary system are limited to the high silica region. The thermodynamic properties and phase diagram cannot be accurately reproduced when K_2O is over 50 mol %.

Thermodynamic optimization of the K_2O-SiO_2 system has been conducted by several researchers using various thermodynamic models for the liquid solution. In 1978, based on the vapor pressure measurements of potassium, Eliezer *et al*. [18] used Redlich-Kister polynomial equation to describe the liquid solution of K_2O-SiO_2. In their work, the obtained phase diagram and thermodynamic properties are only valid in the composition range of SiO_2 from 60 to 100 mol %. In 1991, Kim and Sanders [16] employed the regular, quasi-regular, and sub-regular solution

models to describe the liquid phase. The phase diagram was only roughly reproduced and no thermodynamic property data were compared. In 1993, Wu *et al*. [14] applied the Modified Quasichemical Model (MQM) [22-26] to reproduce the activity data of K_2O [27-29] and the phase diagram data of the K_2O-SiO_2 [30]. The optimized results are only valid in the composition range between K_2SiO_3 and SiO_2 and the predicted phase equilibria in the K_2O-rich region are unreasonable. In 2001, Allendorf and Spear [7] used the Modified Associate Model [31] to describe the liquid phase. K_2O, $2/3 \cdot K_2SiO_3$, $1/2 \cdot K_2Si_2O_5$, $1/3 \cdot K_2Si_4O_9$, and Si_2O_4 associates were used as the liquid species. In this work, the SiO_2 liquidus was not reproduced well. In 2002, the liquid phase was described by Forsberg [17] using the random mixing model. Due to the strong short-range ordering in alkali-silicate slag systems, it was improper to use the random mixing model for the liquid solution and the activity data were not reproduced well. The calculations of Forsberg [17] were also limited up to the composition of K_4SiO_4 because $KSi_{0.25}O$ ($1/4\ K_4SiO_4$) and SiO_2 were considered as liquid end-member components. In 2005, Romero-Serrano *et al*. [15] used the structural liquid model [32, 33] to reproduce the same set of experimental data as considered in Ref. [14]. Although the liquidus of SiO_2 was better reproduced, the experimentally measured metastable liquid immiscibility was not taken into consideration. The optimization did not cover the entire composition range either. In 2006, Yazhenskikh *et al*. [19] used the Modified Associate Model with the same associate species as in Allendorf and Spear's work [7]. The calculated activity curve displayed weird shape with two inflexion points, which is the artifact resulting from strong associate formations in the liquid phase. Therefore, the calculation results were different from the trend of the experimental data. In 2007, Saulov [20] used the MQM for liquid phase and reported the entire composition range of the system. However, the shape of the calculated K_4SiO_4 liquidus was unreasonable because of using the questionable melting point of

K_4SiO_4 reported by Stypula *et al*. [34]. In 2013, Zhang *et al*. [21] conducted thermodynamic optimization using an ionic two sublattice model [35, 36] for the liquid solution. In this work, some critical experimental thermodynamic data of the solid compounds such as the enthalpies of formation ($\Delta H^{o}_{298.15K}$) of K_2SiO_3 and $K_2Si_2O_5$ were not taken into consideration. Besides, the compound K_4SiO_4 was not included as a stable phase, the metastable liquid miscibility gap was not considered, and the SiO_2 liquidus was poorly reproduced. In summary, up to now, there is no complete thermodynamic optimization of the K_2O-SiO_2 system considering all available thermodynamic properties and phase diagram data in the entire composition range. All the previous thermodynamic modeling work is concentrated on the SiO_2-rich region of the system due to the lack of phase diagram data in the K_2O-rich side.

The main goal of this work is to investigate the K_2O-rich region of the K_2O-SiO_2 phase diagram and develop an accurate set of thermodynamic functions for all stable phases in the entire composition range. In the present study, the eutectic temperature between K_4SiO_4 and K_2SiO_3 was investigated using thermal analysis techniques with sealed Pt capsules. Thermodynamic optimization of the K_2O-SiO_2 system was performed using the MQM based on the critical evaluation of all the experimental data from the literature and the present study. This study is part of a large thermodynamic database development project for the K_2O-Na_2O-CaO-MgO-Al_2O_3-SiO_2 system for applications in glassmaking, steelmaking, and combustion industries. All the thermodynamic calculations were performed using the FactSage software [37].

4.2 Experimental Method

4.2.1 Starting Materials

Starting materials were prepared using reagent grade K_2CO_3 (99.997 wt. %, Alfa Aesar) and SiO_2 (99.995 wt. %, Alfa Aesar). Batches of 5 to 10 g of the materials were mixed in an agate mortar for 1 hour. Due to the hygroscopic nature of the starting materials, mixing was performed in isopropyl alcohol (H_2O < 0.02 vol. %) to prevent moisture pickup from air. In order to dry off the alcohol, the mixtures were kept in a drying oven at 120 °C for more than 12 hours and then cooled down to room temperature in a desiccator. To obtain K_2O, which is extremely hygroscopic, the decarbonation of K_2CO_3 ($K_2CO_3 \rightarrow K_2O + CO_2$) was conducted using only the required amount of premixed material just before each experiment. The decarbonation temperature with minimum volatile loss of K_2O was set according to preliminary Thermo-Gravimetric Analysis (TGA) measurements. Several steps of annealing temperatures were set from 600 to 760 °C for 8 to 48 hours. As vapor pressure of CO_2 is much higher than K_2O at the decarbonation temperatures, volatile loss of K_2O was assumed to be minor. The weight of each sample was measured before and after decarbonation to confirm the completion of the decarbonation reaction. A small amount of K_2O loss could be inevitable and some unreacted K_2CO_3 could possibly remain; unfortunately, it was hard to directly determine the loss of K_2O in the decarbonation but the volatile loss of K_2O was estimated based on the thermal analysis results compared to the K_2O-SiO_2 phase diagram data (see more details in Section 4.4.2). After the decarbonation, the mixtures of K_2O and SiO_2 were stored in a drying oven to cool them down to 120 °C and subsequently in a desiccator to reach room temperature. Then, the mixtures were crushed and packed into one-side-sealed platinum (Pt) tubes with dimensions of about 12 mm/17mm in length, 3.2 mm in outer diameter and 0.2 mm in wall thickness. The open end of the Pt tubes was gently crimped to remove the air and welded into

capsules using an electric arc welder to ensure gas-tight condition. The integrity of the welding was checked with an optical microscope before the main experiments. Two starting compositions were prepared for the thermal analysis: 40 mol % K_2O and 67 mol % K_2O.

4.2.2 Thermal Analysis

Differential Scanning Calorimetry (DSC), Differential Thermal Analysis (DTA), and Thermo-Gravimetric Analysis (TGA) measurements were conducted using a Jupiter STA 449 F3 thermal analyzer under an argon flowing atmosphere at a rate of 20 $mL \cdot min^{-1}$. For DSC/TGA, sealed Pt capsules were placed inside a DSC Al_2O_3 crucible with an outer diameter of 6.8 mm and a capacity of 85 μL. For DTA/TGA, a DTA Al_2O_3 crucible with an outer diameter of 8 mm and a height of 23 mm was used. The heating and cooling cycles were performed at a rate of 10 $K \cdot min^{-1}$. TGA was simultaneously performed to confirm that there was no leakage of the sealed capsules during the experiments. Three heating and cooling cycles were run for each sample to obtain reliable and reproducible results. Temperature and sensitivity calibrations were conducted by measuring the melting temperatures and enthalpies of the following eight reference materials: Indium (In), tin (Sn), bismuth (Bi), zinc (Zn), aluminum (Al), silver (Ag), gold (Au), and nickel (Ni).

After experiments, Electron Probe Microanalyzer (EPMA) or X-Ray Diffraction (XRD) phase analysis could not be carried out because the K_2O/SiO_2 mixtures become fully hydrated during polishing and transportation for such analysis.

4.3 Thermodynamic Models

In the K_2O-SiO_2 system, there are six stoichiometric compounds and a liquid solution. These compounds are K_2O, SiO_2, K_4SiO_4, K_2SiO_3, $K_2Si_2O_5$, and $K_2Si_4O_9$. The Gibbs energies of the gas

species were taken from the FactSage pure substance database [37], where most of the data were from the JANAF Tables [38].

4.3.1 Stoichiometric Compounds

The Gibbs energy of a stoichiometric compound is described as:

$$G_T^o = \Delta H_{298.15K}^o + \int_{298.15K}^{T} C_P dT - T(S_{298.15K}^o + \int_{298.15K}^{T} C_P / T dT) \quad (1)$$

where $\Delta H_{298.15K}^o$ and $S_{298.15K}^o$ are the standard enthalpy of formation and standard entropy at 298.15 K, respectively; C_P is the heat capacity as a function of temperature; T is the absolute temperature.

4.3.2 Liquid Solution

The Modified Quasichemical Model (MQM) in the pair approximation [39] was employed to express the Gibbs energy function of the liquid oxide phase. The MQM takes into account the short-range ordering (SRO) of second-nearest-neighbor cations in the oxide melt. The quasichemical reaction considered in the binary oxide melt is:

$$(A-A)+(B-B)=2(A-B);\ \Delta g_{A-B} \quad (2)$$

where A and B are the cationic species K^+ and Si^{4+} in the solution; $(A-B)$ represents a second-nearest-neighbor pair of A and B cations with a common O^{2-} anion; Δg_{A-B} is the Gibbs energy of the reaction, which is a model parameter. Δg_{A-B} can be expanded as a function of pair fractions and temperature:

$$\Delta g_{A-B} = \Delta g^{o}_{AB} + \sum_{i\geq 1} g^{i0}_{AB} X^{i}_{AA} + \sum_{j\geq 1} g^{0j}_{AB} X^{j}_{BB} \tag{3}$$

where Δg^{o}_{AB}, g^{i0}_{AB}, and g^{0j}_{AB} are parameters as a function of temperature; X_{AA} and X_{BB} are the pair fractions of $(A-A)$ and $(B-B)$, respectively.

The Gibbs energy of the liquid solution is expressed as:

$$G^{so\ln} = (n_A g^{o}_{A} + n_B g^{o}_{B}) - T\Delta S^{conf} + (n_{AB}/2)\Delta g_{A-B} \tag{4}$$

where n_i and g^{o}_{i} are the number of moles and the molar Gibbs energy of pure component *i*, respectively; n_{AB} is the number of moles of $(A-B)$ pairs; ΔS^{conf} is the configurational entropy of the solution expressed as a function of random distribution of quasichemical pairs based on one-dimensional Ising model [40]:

$$\Delta S^{conf} = -R(n_A \ln X_A + n_B \ln X_B) - R[n_{AA} \ln(\frac{X_{AA}}{Y_A^2}) + n_{BB} \ln(\frac{X_{BB}}{Y_B^2}) + n_{AB} \ln(\frac{X_{AB}}{2Y_A Y_B})] \tag{5}$$

where Y_i is the coordination-equivalent fraction of *i*, which has the following relationships:

$$X_A = \frac{n_A}{n_A + n_B} = 1 - X_B \tag{6}$$

$$X_{ij} = \frac{n_{ij}}{n_{AA} + n_{BB} + n_{AB}} \tag{7}$$

$$Y_A = \frac{Z_A n_A}{Z_A n_A + Z_B n_B} = \frac{Z_A X_A}{Z_A X_A + Z_B X_B} = 1 - Y_B \tag{8}$$

$$Y_i = X_{ii} + X_{ij}/2 \tag{9}$$

where Z_A and Z_B are the coordination numbers of A and B, respectively. The coordination numbers are allowed to vary with composition as follows:

$$\frac{1}{Z_A} = \frac{1}{Z_{AA}^A}\left(\frac{2n_{AA}}{2n_{AA}+n_{AB}}\right) + \frac{1}{Z_{AB}^A}\left(\frac{n_{AB}}{2n_{AA}+n_{AB}}\right) \tag{10}$$

Z_{AA}^A and Z_{AB}^A are the coordination numbers of A when all nearest neighbors of an A are As and all nearest neighbors of an A are Bs, respectively; Z_{BB}^B and Z_{BA}^B are defined in a similar manner.

The SRO behavior in the liquid solution can be well described by setting the coordination numbers of cations and anions. In this work, the coordination numbers of K^+ (Z_{KK}^K), Si^{4+} (Z_{SiSi}^{Si}), and O^{2-} are set to be 0.6887, 2.7549, and 1.3774, respectively. Therefore, a strong SRO in the K_2O-SiO_2 liquid solution is clearly reproduced near the orthosilicate (K_4SiO_4) composition. All coordination numbers employed in this study are consistent with those used in the molten oxide database (FToxid) of the FactSage software [37]. The details of the model equations can be found in Ref. [39].

4.4 Experimental Results

4.4.1 Sensitivity Tests for Sealed Pt Capsules in Thermal Analysis

The sensitivity of DTA with sealed Pt capsules was confirmed using pure potassium chromate (K_2CrO_4) and diopside ($CaMgSi_2O_6$). The corresponding DTA curves of K_2CrO_4 and $CaMgSi_2O_6$ are depicted in Fig. 4.1 (a) and (b), respectively. A polymorphic transition (α to β) of K_2CrO_4 sample in a sealed Pt capsule was detected at 670 °C, which is in good agreement with the reported

value of 666 °C [41]. The melting temperature of $CaMgSi_2O_6$ sample in a sealed Pt capsule was measured to be at 1397 °C. This value is reasonably close to the reported melting temperature of $CaMgSi_2O_6$ at 1392 °C [41]. This analysis confirms that samples sealed in this type of Pt capsules can be used for DTA experiments without interfering the heat incidents.

4.4.2 Key Samples of the K_2O-SiO_2 System

DSC/TGA experiments were carried out on three 40 mol % K_2O samples. DTA/TGA experiments were performed on one 67 mol % K_2O sample. The results are presented in Fig. 4.2 summarized in Table 4.1. No mass loss was recorded by TGA during DSC and DTA measurements because of using sealed Pt capsules.

For the 40 mol % K_2O samples, two polymorphic transitions (α to β and β to γ transitions for $K_2Si_2O_5$), eutectic reaction, and the liquidus temperature were successfully measured as shown in Fig. 4.2 (a) and (b). The liquidus determined in this study (about 1013 °C on average) is close to that measured for the 37 mol % K_2O (1014.1 °C) reported by Kracek *et al*. [30] This may indicate the actual K_2O content in the present sample would be less than 40 mol %. As explained in the sample preparation, the K_2O-SiO_2 starting materials for DTA and DSC experiments were prepared by the decarbonation of K_2CO_3-SiO_2 mixtures. During the decarbonation process, a small loss of K_2O can be possible which can shift the starting sample composition.

In order to measure the eutectic reaction between K_4SiO_4 (67 mol % K_2O) and K_2SiO_3 (50 mol % K_2O), starting materials of 67 mol % K_2O were prepared assuming a small amount of K_2O loss in the sample preparation. Initially, the DSC was employed on the 67 mol % K_2O samples in Pt capsules of about 1 cm in length. The sealing of the capsules failed several times most probably due to high vapor pressure of K_2O during the heating cycle. However, the DTA crucible can hold

a longer Pt capsule about 1.5 cm in length, which can endure higher K_2O vapor pressure. For this reason, DTA was employed instead of DSC for the thermal analysis of the 67 mol % K_2O samples.

The DTA results are presented in Fig. 4.2 (c) and the corresponding TGA curves are depicted in Fig. 4.2 (d). As can be seen in Fig. 4.2 (c), distinctive and reproducible thermal incidents, which should correspond to the eutectic temperature, were recorded at 714 ± 6 °C. No other transition was recorded up to 1200 °C. The melting temperatures of K_4SiO_4 and K_2SiO_3 are sufficiently lower than 1200 °C. Therefore, it can be assumed that the present experimental sample composition should be very close to eutectic composition between K_4SiO_4 and K_2SiO_3. According to the present thermodynamic optimization results discussed below, the eutectic composition should be about 59 mol % K_2O. This means that the volatile loss of the K_2O in the decarbonation would be about 8 mol %, which change the DSC sample composition from 68 mol % to 59 mol % K_2O. The probable error of ± 6 °C for the eutectic temperature was obtained considering the maximum deviation (± 5 °C) from the preliminary Pt capsule tests for reference materials (see Fig. 4.1), and the standard deviations (2σ) of 67 mol % K_2O samples (± 3 °C), respectively.

It should be noted that this eutectic temperature is the first experimental data measured at the composition of K_2O over 50 mol % in this binary system. This finding is important to constrain the phase equilibria in K_2O-rich region of the system for thermodynamic optimization. Although the complete decarbonation of starting experimental samples was assumed in the present study, a small amount of K_2CO_3 may remain after the carbonation, which can influence to the liquidus temperature and eutectic temperature. Considering this possibility, the eutectic temperature between K_4SiO_4 and K_2SiO_3 could be slightly higher than the present measurement, but most probably the difference would be within the error range of the present DTA results.

4.5 Thermodynamic Evaluation and Optimization

All phase diagram and thermodynamic property data of the K_2O-SiO_2 system in the literature were critically reviewed. New key phase diagram data measured in this study (eutectic temperature between K_4SiO_4 and K_2SiO_3 in Section 4.4.2) and all the reliable experimental data in the literature were simultaneously considered to obtain a set of thermodynamic functions for all the phases in the system. Since the thermodynamic properties of solid compounds, such as K_2SiO_3 and $K_2Si_2O_5$, are relatively well investigated, the Gibbs energies of the solid compounds were first fixed. Afterwards, the phase diagram and the thermodynamic properties of the liquid solution were simultaneously reproduced by optimizing the liquid model parameters and enthalpy of formation of solid compounds. The optimized model parameters are listed in Table 4.2.

4.5.1 Phase Diagram Data

The phase diagram of the K_2O-SiO_2 system from the present optimized parameters is calculated and shown in Fig. 4.3 along with all the experimental data. This binary system consists of 12 stable solid phases and a liquid phase at 1 atm pressure. The stable solid phases are: K_2O, SiO_2 (α- and β-quartz, β-tridymite, and β-cristobalite), orthosilicate (K_4SiO_4), metasilicate (K_2SiO_3), disilicate (α-, β-, and γ-$K_2Si_2O_5$), tetrasilicate (α- and β-$K_2Si_4O_9$). The compounds K_4SiO_4, K_2SiO_3, and $K_2Si_2O_5$ have the monoclinic structure [42-45] and $K_2Si_4O_9$ has the triclinic structure [44].

Due to the highly volatile and hygroscopic characteristics of K_2O, the phase diagram in the K_2O-rich region has not been well studied in the literature. Reliable thermodynamic compilations were performed by Barin [41] and Berman *et al*. [46] regarding the polymorphic transitions and melting points of K_2O and SiO_2. Wollast [47] proposed a solubility of K_2O in SiO_2, nevertheless, no other

supporting evidence was found in the literature. Also, no noticeable solubility of other alkali oxides or alkaline-earth oxides in SiO_2 has ever been reported.

The phase diagram in the composition range between K_2SiO_3 and SiO_2 was studied extensively by Kracek *et al*. [30, 48, 49]. The liquidus and invariant reactions were measured by equilibration/quenching experiments and thermal analysis. The compounds K_2SiO_3, $K_2Si_2O_5$, and $K_2Si_4O_9$ were identified using petrographic microscopy. The phase diagram reported by Kracek *et al*. [48] in 1929 contained some uncertainties on the liquidus of cristobalite (SiO_2). Later, it was improved in the work of 1930 [49]. The authors in 1929 originally proposed that $K_2Si_2O_5$ was formed with excess K_2O and SiO_2, which implied $K_2Si_2O_5$ as a possible solid solution. However, in their later study in 1937 [30], $K_2Si_2O_5$ was revised as a stoichiometric compound. Bockris *et al*. [50] reported the liquidus in the composition range between $K_2Si_2O_5$ and SiO_2 based on viscosity measurements using a rotating crucible viscometer. Steiler [29] reported the liquidus of $K_2Si_4O_9$ using activity data obtained from the thermosgravimetric method. Morey and Fenner [51] measured the melting temperatures of K_2SiO_3 and $K_2Si_2O_5$ using the equilibration/quenching method and petrographic microscopy for phase analysis. The melting temperature of $K_2Si_4O_9$ was measured by Golubkov and Shakhmatkin [52] using small angle X-ray scattering (SAXS) technique. All the experimental data from Kracek *et al*. [30], Bockris *et al.* [50], Steiler [29], Morey and Fenner [51], and Golubkov and Shakhmatkin [52] are in good agreement with each other. In Fig. 4.3, it can be seen that the calculated phase diagram well reproduced all the experimental data.

No eutectic points were reported between K_2O and K_4SiO_4 or between K_4SiO_4 and K_2SiO_3 due to experimental difficulties. The reported melting point of K_4SiO_4 by Stypula *et al*. [34] is ambiguous. In their work, the melting point of K_4SiO_4 is simply listed without providing any source of data. It

seems that the melting point is purely first approximation. In the present experiments (Section 4.4.2), the eutectic reaction temperature for Liquid → K_4SiO_4 + K_2SiO_3 was measured to be 714 ± 6 °C. This eutectic temperature was used in the present optimization to constrain the Gibbs energy of the liquid phase, especially for the composition range with more than 50 mol % K_2O.

Recent phase diagram data from Meshalkin and Kaplun [53] and Akdogan *et al*. [54] were not considered in this study because their experiments were conducted using open crucibles in air. Significant deviations in sample composition were shown in their results because of the highly hygroscopic and volatile nature of K_2O.

Regarding the liquid immiscibility in the high SiO_2 region of the system, Rey [55] first reported SiO_2 activity at 1600 °C from an approximate calculation using phase diagram data. It showed positive deviations from ideal behavior, indicating a possible liquid miscibility gap formation. Later, many researchers reported the possible existence of a sub-solidus (metastable) liquid immiscibility [56-60]. Several attempts were made to find the critical point of the metastable immiscibility gap. From a theoretical model based on the activation energy of ionic conduction, Anderson and Stuart [61] mentioned that K^+ ions migrate very slowly when the SiO_2 content is high, which leads to difficulties in the experimental observation of liquid phase separation. Charles [56] proposed a possible metastable liquid immiscibility in the temperature range of 500 to 600 °C at 85 or 92.5 mol % SiO_2. This proposal was based on replica electron microscopy measurements and the relation between ionic radius and critical temperature in other alkali oxide systems. Charles [56] also found an evidence of phase segregation in the microscopic observation, which implied that the critical point is possibly above the glass transition temperature. Later, Charles [57] estimated the critical point of the miscibility gap at 350 °C and 95.5 mol % SiO_2 based on activity

calculations from the volatilization data reported by Preston and Turner [62, 63]. Moriya *et al*. [58] used mixtures of K_2O-SiO_2 with 10 to 17.5 mol % Li_2O to overcome slow kinetics, and reported the critical point at 750 °C and about 92 mol % SiO_2. However, this result is less reliable due to additional Li_2O contents. Gupta and Mishra [60] observed phase separation in the K_2O-SiO_2 glasses at the composition between 56.7 and 85 mol % SiO_2 using replica Transmission Electron Microscopy (TEM). This observation was also supported by electrical conductivity measurements. More recent work from Kawamoto and Tomozawa [59] suggested that the critical temperature of this immiscibility is 555 °C at 94.5 mol % SiO_2 based on the measured immiscibility in the K_2O-Li_2O-SiO_2 and K_2O-Na_2O-SiO_2 systems. In summary, the metastable liquid immiscibility exists in the high SiO_2 region of the binary K_2O-SiO_2 system. The critical point seems slightly above the glass transition temperature based on the discrepancies of experimental observations. To know the critical temperature of the metastable miscibility gap more accurately, experimentally measured glass transition temperatures were collected. Many researchers reported the glass transition temperature in the composition range between 50 and 100 mol % SiO_2 in the system, as shown in Fig. 4.3. Glass transition temperatures were reported by Kawamoto and Tomozawa [59] using viscosity data, Nemilov [64] with thermal expansion measurements, Dietzel and Sheybany [65] and Shelby [66] using dilatometry, Boesch and Moynihan [67], Bershtein *et al*. [68], Borisova *et al*. [69], and Malfait *et al*. [70] with DSC. In general, the reported data showed reasonable agreements with each other. All the reported temperatures are between 551.4 to 583.2 °C at the composition of over 90 mol % SiO_2. This is close to the critical point of liquid immiscibility reported by Charles [56] and Kawamoto and Tomozawa [59]. According to the present evaluation, the data from Moriya *et al*. [58] at 750 °C and Charles [57] at 350 °C are less likely. The critical point optimized in this study is at 588.9 °C and 94.9 mol % SiO_2, which is slightly higher than the

glass transition temperature. The optimized metastable liquid miscibility gap in the K_2O-SiO_2 system is presented in Fig. 4.3.

4.5.2 Thermodynamic Properties

Thermodynamic properties ($\Delta H^{o}_{298.15K}$, $S^{o}_{298.15K}$, and C_P) of the solid and liquid phases of K_2O and SiO_2 were taken from the FACT-oxide database [37]. Both K_2O and SiO_2 properties were originally evaluated by Wu *et al*. [14] using thermodynamic data compilation from Barin [41], Berman *et al*. [46, 71, 72], and Chase *et al*. [73, 74]. Compiled experimental data of thermodynamic properties and optimized values are listed in Table 4.2. All the thermodynamic property data for solid compounds and the liquid solution are shown in Figs. 4.4 to 4.11 along with the calculated results from the present study.

4.5.2.1 Potassium Metasilicate (K_2SiO_3)

The enthalpy of formation ($\Delta H^{o}_{298.15K}$) of K_2SiO_3 from K_2O and SiO_2 has been reported by several researchers. Their results are listed in Table 4.2 and plotted in Fig. 4.4. Spencer [75] estimated $\Delta H^{o}_{298.15K}$ from the ionic charge/ionic radius of the cation using the method proposed by Slough [76]. The enthalpy of fusion (ΔH^{o}_{fus}) was also proposed based on the same estimation used to obtain $\Delta H^{o}_{298.15K}$. Kroger and Fingas [77] reported $\Delta H^{o}_{298.15K}$ using gas equilibration technique which measured the equilibrium pressure of CO_2 for the reaction $K_2CO_3 + SiO_2 = K_2SiO_3 + CO_2$ from 808 to 898 K. Takahashi and Yoshio [78] determined $\Delta H^{o}_{298.15K}$ using hydrofluoric (HF) acid solution calorimetry. Borisova and Ushakov [69] also determined the value from the solution calorimetry experiments.

The entropy at 298.15 K ($S^o_{298.15K}$) and heat capacity (C_P) of K_2SiO_3 from the literature and the present optimization are listed in Table 4.2 and C_P is depicted in Fig. 4.5. Stull *et al*. [79] used adiabatic calorimetry to measure C_P from 15 to 298.15 K. Based on the C_P measurement, $S^o_{298.15K}$ was calculated to be 146.1 J·mol^{-1}·K^{-1}. Although the starting materials had slightly low purity (97.3 %), this is the only C_P data measured below 298.15 K. The heat content ($H_T - H_{298.15K}$) was measured by Beyer *et al.* [80] using drop calorimetry up to 1249 K as shown in Fig. 4.6. Then, the corresponding high-temperature C_P was derived from the heat content data. The low-temperature C_P measured from Stull *et al.* [79] and the high-temperature C_P derived from Beyer *et al.* [80] are in good agreement as can be seen in Fig. 4.5.

In the present optimization, $S^o_{298.15K}$ and C_P were fixed based on the studies of Stull *et al*. [79] and Beyer *et al*. [80], respectively. $\Delta H^o_{298.15K}$ from the solution calorimetry data of Takahashi and Yoshio [78] (-1535.5 kJ·mol^{-1}) and Borisova and Ushakov [69] (-1543.4 kJ·mol^{-1}) were considered to be more reliable than the indirect [77] and estimated [75, 76] values. In this study, $\Delta H^o_{298.15K}$ was optimized to be -1543.8 kJ·mol^{-1} from elemental reference state, which is within the experimental error range (± 9 kJ·mol^{-1}) of Borisova and Ushakov [69]. Although, no specific error range was reported by Takahashi and Yoshio [78], the optimized $\Delta H^o_{298.15K}$ is also in reasonable agreement with their results when considering the similar error range of ± 9 kJ·mol^{-1}. The calculated ΔH^o_{fus} of K_2SiO_3 from this study is 33.3 kJ·mol^{-1}, which is smaller than the estimated value from Spencer (48.1 kJ·mol^{-1}) [75].

4.5.2.2 Potassium Disilicate ($K_2Si_2O_5$)

All the experimental measurements of $\Delta H^o_{298.15K}$ of $K_2Si_2O_5$ are listed in Table 4.2 and plotted in Fig. 4.4. Kracek *et al*. [81] measured $\Delta H^o_{298.15K}$ using HF acid solution calorimetry. Slough [76], Kroger and Fingas [77], Takahashi and Yoshio [78], and Borisova and Ushakov [69] reported $\Delta H^o_{298.15K}$ using the same experimental methods used for the measurements of $\Delta H^o_{298.15K}$ for K_2SiO_3 (Section 4.5.2.1). Heats of transition (ΔH^o_{tr}) of $K_2Si_2O_5$ from α to β and β to γ were measured by Beyer *et al*. [80] using copper-block drop calorimetry. ΔH^o_{tr} from β to γ was also determined by Kracek *et al*. [30] using DTA. The ΔH^o_{fus} of $K_2Si_2O_5$ were reported by several researchers using various methods. In 1973, Takahashi and Yoshio [82] used drop calorimetry to measure the heat content of both glass and crystal $K_2Si_2O_5$ from 298 K to 1273 K, and obtained C_P of both glass and solid. By combining these C_P data with the melting point (1309 K) reported by Kracek *et al.* [83], together with the ΔH^o_{tr} from crystal to glass at 298.15 K determined using HF acid solution calorimetry (14.2 kJ·mol^{-1}), Takahashi and Yoshio calculated the ΔH^o_{fus} of $K_2Si_2O_5$ to be 31.8 kJ·mol^{-1}. Azandegbe *et al*. [84] estimated ΔH^o_{fus} to be 46.6 kJ·mol^{-1} from the thermodynamic properties determined from their electromotive force (EMF) measurement. Spencer [75] estimated ΔH^o_{fus} to be 41.0 kJ·mol^{-1} based on the systematic trend of other alkali and alkaline-earth silicate systems. Around 1980s, Eliezer *et al*. [18] performed vapor pressure measurement using atomic absorption method, and estimated ΔH^o_{fus} (71.1 kJ·mol^{-1}) through thermodynamic calculations. Beyer *et al*. [80] used the same calculation method as Takahashi and Yoshio [82] to obtain ΔH^o_{fus} to be 35.2 kJ·mol^{-1}. Beyer *et al*. used copper-block drop calorimetry to measure the heat content of crystal and glass of $K_2Si_2O_5$, the melting point of 1318 K was

obtained from Kracek *et al*. [30], ΔH_{tr}^{o} from crystal to glass at 298.15 K (18.7 kJ·mol^{-1}) was taken from Kracek *et al*. [81]. More recently, Boivin *et al*. [85] measured ΔH_{fus}^{o} (31.3 kJ·mol^{-1}) using DTA. Although they mentioned an error range of ± 9.6 %, the actual error considering the calibration and experimental set up can be more than 50 % in DTA. Overall, ΔH_{fus}^{o} of $K_2Si_2O_5$ in the literature are indirectly measured or estimated. The reported values are widely scattered from 28.3 to 77.1 kJ·mol^{-1}.

The $S_{298.15K}^{o}$ of $K_2Si_2O_5$ from the literature are listed in Table 4.2 and the C_P are depicted in Fig. 4.5 with the optimized curve. Beyer *et al*. [80] measured C_P between 5 and 308 K using an adiabatic calorimetry. Based on the C_P, $S_{298.15K}^{o}$ was calculated to be 190.6 J·mol^{-1}·K^{-1}. Spencer [75] reported $S_{298.15K}^{o}$ (182.0 J·mol^{-1}·K^{-1}) based on the systematic analysis from other alkali and alkaline-earth silicate systems. In the case of the high-temperature C_P, Beyer *et al*. [80] used drop calorimetry to measure the heat content of α-$K_2Si_2O_5$ at temperature range from 298 to 510 K, β-$K_2Si_2O_5$ between 510 and 867 K, and γ-$K_2Si_2O_5$ between 867 and 1318 K. Takahashi and Yoshio [82] used drop calorimetry to measure the heat content of $K_2Si_2O_5$ from 298 K to 1273 K, and derived the C_P. Low-temperature C_P and the derived high-temperature C_P from the heat content data by Bayer *et al*. [80] are consistent with each other as can be seen in Fig. 4.5. The heat content data from Takahashi and Yoshio [82] are higher by about 2 % at temperature range from 873 to 1309 K and by about 12 % at 373 K compared to the data from Beyer *et al*. The heat content data of $K_2Si_2O_5$ [80, 82] are also shown in Fig. 4.6 in comparison with the calculated results from this study.

In the present study, $S^{o}_{298.15K}$ was taken from the experimental value by Beyer *et al*. [80] instead of the estimated value by Spencer [75]. The high-temperature C_P of Beyer *et al*. was slightly modified according to Ref. [46], and one integrated C_P function was employed instead of three functions for each phase (α, β, and γ) proposed by Beyer *et al*. In this way, unreasonable decrease of C_P at high temperatures is avoided. The optimized value of $\Delta H^{o}_{298.15K}$ is -2503.7 kJ·mol^{-1}, which is consistent with the value by Kracek *et al*. (-2507.2 kJ·mol^{-1}) [81] within the experimental error range. ΔH^{o}_{tr} was taken from Beyer *et al*. [80] instead of Kracek *et al*. [30], because the enthalpy measurement by Beyer *et al*. using drop calorimeter is more accurate than DTA. The calculated ΔH^{o}_{fus} of $K_2Si_2O_5$ in the present study is 53.0 kJ·mol^{-1}, which is within the reported range of 28.3 to 77.1 kJ·mol^{-1} from the indirect measurements and estimations.

4.5.2.3 Potassium Tetrasilicate ($K_2Si_4O_9$)

Kracek *et al*. [81] and Borisova and Ushakov [69] measured $\Delta H^{o}_{298.15K}$ of $K_2Si_4O_9$ using solution calorimetry. Goranson and Kracek [86] measured ΔH^{o}_{tr} at 865 K (3.2 kJ·mol^{-1}) and ΔH^{o}_{fus} (49.0 kJ·mol^{-1}) using the DTA technique. Geisinger *et al*. [87] calculated ΔH^{o}_{fus} to be 43.2 kJ·mol^{-1} using a vibrational model based on the data from Raman spectroscopy and powder infrared (IR) spectroscopy. In this calculation, an empirical equation from Anderson [88] and a mode-partitioning method from Kieffer [89-92] were applied. Eliezer *et al*. [18] reported ΔH^{o}_{fus} of 87.9 kJ·mol^{-1} based on vapor pressure measurements and thermodynamic evaluation. In summary, the reported ΔH^{o}_{fus} of $K_2Si_4O_9$ values are in a range of 43 to 87.9 kJ·mol^{-1} from the literature.

Geisinger *et al*. [87] derived the low-temperature C_P of $K_2Si_4O_9$ between 20 and 300 K and high-temperature C_P at 298, 700, and 1000 K using a vibrational model based on the results from Raman and IR spectroscopy. $S^o_{298.15K}$ was calculated from low-temperature C_P (233.7 $J \cdot mol^{-1} \cdot K^{-1}$). Spencer [75] reported $S^o_{298.15K}$ (265.7 $J \cdot mol^{-1} \cdot K^{-1}$) in his review.

In the present study, $S^o_{298.15K}$ of 265.7 $J \cdot mol^{-1} \cdot K^{-1}$ from Spencer was taken. Although Spencer's value is an estimation, this value is more reasonable than the one from Geisinger *et al*. using vibrational model with spectroscopic measurements. $S^o_{298.15K}$ reported by Geisinger *et al*. is about 16 % lower than the values from both Spencer and the approximation (267.8 $J \cdot mol^{-1} \cdot K^{-1}$) using the Neumann-Kopp rule (NKR). The predictions of $S^o_{298.15K}$ from NKR for the other two compounds K_2SiO_3 and $K_2Si_2O_5$ are in reasonable agreement with experimental data (see Table 4.2). Spencer also estimated reliable $S^o_{298.15K}$ value for $K_2Si_2O_5$ in this system. The high-temperature C_P of $K_2Si_4O_9$ was obtained from the NKR in the temperature range of 298.15 to 1050 K. The calculated high-temperature C_P based on NKR was found to be within about ± 7 % error in comparison with experimentally measured C_P for K_2SiO_3 and $K_2Si_2O_5$. A comparison between the C_P in this study and the C_P data derived by Geisinger *et al*. [87] are shown in Fig. 4.5. The $\Delta H^o_{298.15K}$ of $K_2Si_4O_9$ in the present study was first taken from Kracek *et al*. (-4313.7 $kJ \cdot mol^{-1}$) [81]. It was then modified to -4342.0 $kJ \cdot mol^{-1}$ to reproduce the reliable phase diagram data as shown in Fig. 4.3. This modification was inevitable in the constraints of the optimized thermodynamic properties of K_2SiO_3 and $K_2Si_2O_5$. The calculated ΔH^o_{fus} of $K_2Si_4O_9$ in the present study is 62.5 $kJ \cdot mol^{-1}$, which is in the range of literature data from 43 to 87.9 $kJ \cdot mol^{-1}$.

4.5.2.4 Potassium Orthosilicate (K_4SiO_4)

Pyatenko [93] mentioned that K_4SiO_4 could be unstable considering the balance of charge and the coordination numbers of atoms. Henry [94], Matveev [95], and Matveev and El'kin [96] estimated the Gibbs energy of formation of K_4SiO_4 from the analysis of other silicate compounds and indicated K_4SiO_4 as an unstable phase. However, several crystallographic studies [42, 97], thermodynamic studies [76, 77], and first principles calculations [98] confirm the stability of K_4SiO_4 at 1 atm pressure. The formation mechanism of K_4SiO_4 was explained by O'Keeffe and Hyde [97] and Bernet and Hoppe [42], who synthesized the compound and measured the detailed crystal structure. Structural descriptions of K_4SiO_4 can also be found in the book "Structure, Dynamics and Properties of Silicate melts" by Stebbins *et al*. [99]. Thus, K_4SiO_4 is considered as a stable compound in this study.

Two reports about the $\Delta H^{o}_{298.15K}$ of K_4SiO_4 were found [76, 77]. The experimental values of $\Delta H^{o}_{298.15K}$ are listed in Table 4.2 and depicted in Fig. 4.4. Kroger and Fingas [77] reported -1958.1 kJ·mol^{-1} using gas equilibration technique which measured the equilibrium pressure of CO_2 from the reaction $K_2CO_3 + K_2SiO_3 = K_4SiO_4 + CO_2$ in the temperature range of 1128 to 1248 K. Slough [76] estimated $\Delta H^{o}_{298.15K}$ to be -2064.6 kJ·mol^{-1} from ionic potential relationships. Even though there is no direct measurement for $\Delta H^{o}_{298.15K}$ of K_4SiO_4, both reported values can be considered reasonable. This is because Kroger and Fingas [77] and Slough [76] reported reasonable $\Delta H^{o}_{298.15K}$ values of K_2SiO_3 and $K_2Si_2O_5$ (within 5 %) using the same techniques compared to the corresponding reliable data from solution calorimetry.

In the present study, $\Delta H^{o}_{298.15K}$ of K_4SiO_4 was estimated based on the systematic analysis of two similar alkali silicate systems, Na_2O-SiO_2 and Li_2O-SiO_2. $\Delta H^{o}_{298.15K}$ of M_4SiO_4, M_2SiO_3, and $M_2Si_2O_5$ (M = Na, Li, and K) from the constituent oxides optimized by Romero-Serrano and Pelton [33] for Na_2O system, and by Konar *et al*. [100] for Li_2O system are presented in Fig. 4.4 along with the present optimization for K_2O system. In addition, the first principles calculation results of M_4SiO_4, M_2SiO_3, and $M_2Si_2O_5$ from Deml *et al*. [98] in the K_2O-SiO_2 and Na_2O-SiO_2 systems, and from Saal *et al*. [101] in the Li_2O-SiO_2 system are compared in Fig. 4.4. A clear systematic trend in $\Delta H^{o}_{298.15K}$ can be observed in these alkali silicate systems. According to the first principles calculations [98, 101], $\Delta H^{o}_{298.15K}$ of each of these silicate compounds becomes more negative in the order of Li, Na, and K. The calculated $\Delta H^{o}_{298.15K}$ from both first principles calculations [98, 101] are still noticeably positive than the previous thermodynamic optimization studies [33, 100] and this study. Considering the systematic deviations, we can reasonably estimate $\Delta H^{o}_{298.15K}$ of K_4SiO_4. Since there is no experimental data for $S^{o}_{298.15K}$ and C_P of K_4SiO_4, these values were estimated using the NKR based on constituent oxides K_2O and SiO_2, and then $S^{o}_{298.15K}$ was modified within ± 5 % range. The optimized value of $\Delta H^{o}_{298.15K}$ from this study is in good agreement with the estimation from Slough [76] and the systematic trend from the first principles calculation results. It also well reproduced the eutectic temperature between K_4SiO_4 and K_2SiO_3 measured from this study as depicted in Fig 4.3. The optimized data of $\Delta H^{o}_{298.15K}$ and $S^{o}_{298.15K}$ of K_4SiO_4 are listed in Table 4.2.

4.5.2.5 Liquid

Activity of the K_2O-SiO_2 melt was investigated by several researchers. Callow [102] employed the rates of volatilization measurements reported by Preston and Turner [103] and calculated the activity of K_2O using a direct relation between rate of volatilization and vapor pressure. Then, the activity of SiO_2 was calculated using the Gibbs-Duhem relationship. Charles [57] employed the similar procedure to obtain the activity of SiO_2 with some modifications in the relation between rate of volatilization data and vapor pressure. Frohberg *et al*. [27] reported the activity of SiO_2 at 1373 K using EMF measurements. Similarly, Ravaine *et al*. [28] reported the activity of K_2O in the temperature range of 1123 to 1373 K using EMF. Steiler [29] obtained the activity of K_2O indirectly using the thermogravimetric method. The weight change of the samples (volatilization rate) were measured with a fixed CO/CO_2 ratio at 1573, 1673, and 1773 K, and the activity of K_2O was derived. Smith [104] reported the activity of K_2O in the temperature range between 1227 and 1427 K using EMF. More recently, Zaitsev *et al*. [105] reported the activities of both K_2O and SiO_2 at 1373, 1573, 1673, and 1773 K using the Knudsen effusion mass spectrometry (KEMS).

The calculated activities of K_2O and SiO_2 at temperature range from 1173 to 1773 K are compared with these experimental data in Fig. 4.7 (a) to (d). The calculations from the present study are in good agreement with the experimental data as can be seen in Fig 4.7. It should be noted that the experimental data from Zaitsev *et al*. [105] in the high SiO_2 region are unreasonable considering the phase diagram.

The partial molar enthalpy of SiO_2 ($\Delta\bar{h}_{SiO_2}$) was investigated by Willding and Navrotsky [106] and Morishita *et al*. [107] using drop solution calorimetry. The values are depicted in Fig. 4.8, together with the calculated results from this study. Willding and Navrotsky's work was conducted in a

composition range from 66 to 75 mol % SiO_2 at 1760 K and Morishita *et al*.'s was at 75 mol % SiO_2 at 1465 K and 85 mol % SiO_2 at 1663 K. The method of drop solution calorimetry permits direct measurement of enthalpy without complications related to the glass transition. The calculated $\Delta\bar{h}_{SiO_2}$ in this study is in fair agreement with both the experimental data [106, 107] considering their experimental error ranges, as shown in Fig. 4.8.

The experimentally measured partial pressures of potassium (P_K) in equilibrium with the K_2O-SiO_2 melts are plotted in Fig. 4.9 along with the present calculation results. Plante *et al*. [108] used the KEMS to measure P_K at 3.3 to 29.8 mol % K_2O in the temperature range from 1273 K to 1866 K. Later, Plante [109] reported comprehensive data set of P_K at 4.4 to 33.3 mol % K_2O in the temperature range from 1300 to 1800 K using the same experimental procedure. Eliezer *et al*. [18] measured P_K at 7.8 mol % K_2O from 1373 to 1873 K using an atomic absorption method. More recently, Piacente and Matousek [110] measured P_K at 20 mol % K_2O in the temperature range of 1260 to 1567 K using KEMS. It can be seen from Fig. 4.9 that the present thermodynamic calculation results are in good agreement with the experimental vapor pressure data.

Beyer *et al*. [80], Takahashi and Yoshio [82], Richet and Bottinga [111], and Richet and Bottinga [112] measured the heat content data of different compositions of the glass in the K_2O-SiO_2 system using drop calorimetry. In the present study, the glass was considered as a supercooled liquid phase. In Fig. 4.10, the heat content data of the glass from 56.5 ($KS_{1.3}$) to 83.3 (KS_5) mol % SiO_2 are all reasonably reproduced. This means that the MQM with optimized model parameters can well describe the enthalpy of the K_2O-SiO_2 melt in the wide temperature and composition ranges. The calculated enthalpy of mixing (ΔH^{Mix}) at 973 K for the K_2O-SiO_2 as well as the Na_2O-SiO_2 [33]

and the Li_2O-SiO_2 [100] liquid solutions are compared in Fig. 4.11. The results show a systematic increase of the exothermicity of mixing in the order of Li_2O, Na_2O, and K_2O. Borisova and Ushakov [69] measured the heat of solution of the K_2O-SiO_2 glass at 973 K using $2PbO \cdot B_2O_3$ solution calorimetry. Takahashi and Yoshio [78] measured the heat of solution at 298 K, and then converted it into 973 K using heat content measurements [82]. The experimental data are well reproduced considering the possible error in the experiments.

4.6 Structure of Melt

The structure of the K_2O-SiO_2 melt can be calculated from the MQM. Three quasichemical pairs of $K-K$, $K-Si$, and $Si-Si$, which correspond to O^{2-} (free oxygen), O^- (broken oxygen), and O^o (bridged oxygen), respectively, are considered in the calculation. The calculated results at 1000 °C are plotted in Fig. 4.12 along with experimental data. The experimental structural data were measured using infrared (IR) spectroscopy [113], X-ray Photoelectron Spectroscopy (XPS) [10], Raman spectroscopy [114] and Nuclear Magnetic Resonance (NMR) [8, 9, 70, 115] techniques. The calculated results from Molecular Dynamics (MD) [116] were also compared in Fig. 4.12. The available literature data are very well reproduced by the present calculations, even though these structural data were not directly considered throughout the process of thermodynamic optimization. Therefore, it can be said that this MQM can accurately describe not only the thermodynamic properties of liquid solution but also the short-range ordering structure of the K_2O-SiO_2 liquid solution.

4.7 Summary

Coupled experimental phase diagram study and thermodynamic optimization using the MQM were performed for the binary K_2O-SiO_2 system. For the first time, the eutectic temperature between K_4SiO_4 and K_2SiO_3 was successfully measured to be at 714 ± 6 °C using DTA with sealed Pt capsules. All the available thermodynamic and phase equilibrium data in the literature have been critically assessed. A set of optimized Gibbs energy functions for all phases in the K_2O-SiO_2 system was obtained from the thermodynamic optimization, which reproduces the eutectic point measured in this study as well as all available and reliable experimental data in the literature. The phase diagram in the K_2O-rich region is well established for the first time. Strong short-range ordering structure in the K_2O-SiO_2 melt is also well calculated by the present modeling. The present optimized model parameters can be used to calculate any thermodynamic properties and phase diagram in the entire composition and temperature ranges of the K_2O-SiO_2 system.

Acknowledgments

Financial supports from Tata Steel Europe, POSCO, Nucor Steel, Rio Tinto Iron and Titanium, Hyundai Steel, Nippon Steel and Sumitomo Metals Corp., JFE Steel, Voestalpine, RHI, and the Natural Sciences and Engineering Research Council of Canada are gratefully acknowledged. One of the authors (D.-G. Kim) also acknowledges the McGill Engineering Doctorate Award (MEDA) from McGill University.

References

[1] B.O. Mysen, P. Richet, Silicate glasses and melts properties and structure, Elsevier, 2005.
[2] V. Saraswati, K.V.S.R. Anjaneyulu, Crystallization of mica in the potassium oxide-silicon dioxide-magnesium oxide-magnesium fluoride glass system, Bull. Mater. Sci., 13 (1990) 283-291.
[3] C.C. Gonzaga, P.F. Cesar, C.Y. Okada, C. Fredericci, F. Beneduce Neto, H.N. Yoshimura, Mechanical properties and porosity of dental glass-ceramics hot-pressed at different temperatures, Mater. Res. (Sao Carlos, Braz.), 11 (2008) 301-306.
[4] L. Song, J. Wu, Z. Li, X. Hao, Y. Yu, Crystallization mechanisms and properties of α-cordierite glass–ceramics from K2O–MgO–Al2O3–SiO2 glasses, Journal of Non-Crystalline Solids, 419 (2015) 16-26.
[5] A. Tandia, K.D. Vargheese, J.C. Mauro, A.K. Varshneya, Atomistic understanding of the network dilation anomaly in ion-exchanged glass, Journal of Non-Crystalline Solids, 358 (2012) 316-320.
[6] Y. Yu, M. Wang, D. Zhang, B. Wang, G. Sant, M. Bauchy, Stretched exponential relaxation of glasses at low temperature, Phys. Rev. Lett., 115 (2015) 165901/165901-165901/165905.
[7] M.D. Allendorf, K.E. Spear, Thermodynamic analysis of silica refractory corrosion in glass-melting furnaces, J. Electrochem. Soc., 148 (2001) B59-B67.
[8] S. Sen, R.E. Youngman, NMR study of Q-speciation and connectivity in K2O-SiO2 glasses with high silica content, J. Non-Cryst. Solids, 331 (2003) 100-107.
[9] M.C. Davis, D.C. Kaseman, S.M. Parvani, K.J. Sanders, P.J. Grandinetti, D. Massiot, P. Florian, Q(n) Species Distribution in K2O·2SiO2 Glass by 29Si Magic Angle Flipping NMR, J. Phys. Chem. A, 114 (2010) 5503-5508.
[10] R. Sawyer, H.W. Nesbitt, R.A. Secco, High resolution X-ray Photoelectron Spectroscopy (XPS) study of K2O-SiO2 glasses: evidence for three types of O and at least two types of Si, J. Non-Cryst. Solids, 358 (2012) 290-302.
[11] M. Zevenhoven-Onderwater, R. Backman, B.J. Skrifvars, M. Hupa, The ash chemistry in fluidised bed gasification of biomass fuels. Part I: predicting the chemistry of melting ashes and ash-bed material interaction, Fuel, 80 (2001) 1489-1502.
[12] I.-L. Naezelius, J. Fagerstroem, C. Boman, D. Bostroem, M. Oehman, Slagging in Fixed-Bed Combustion of Phosphorus-Poor Biomass: Critical Ash-Forming Processes and Compositions, Energy Fuels, 29 (2015) 894-908.
[13] W.A. Deer, R.A. Howie, J. Zussman, An Introduction to the Rock-Forming Minerals, Pearson; 2 edition, 1996.
[14] P. Wu, G. Eriksson, A.D. Pelton, Optimization of the thermodynamic properties and phase diagrams of the sodium oxide-silica and potassium oxide-silica systems, J. Am. Ceram. Soc., 76 (1993) 2059-2064.
[15] A. Romero-Serrano, C. Gomez-Yañez, M. Hallen-Lopez, J. Araujo-Osorio, Thermodynamic Modeling of Alkali Metal Oxide-Silica Binary Melts, Journal of the American Ceramic Society, 88 (2005) 141-145.
[16] S.S. Kim, T.H. Sanders, Jr., Thermodynamic modeling of phase diagrams in binary alkali silicate systems, J. Am. Ceram. Soc., 74 (1991) 1833-1840.
[17] S. Forsberg, Optimization of thermodynamic properties of the K2O-SiO2 system at high temperatures, J. Phase Equilib., 23 (2002) 211-217.

[18] N. Eliezer, R.A. Howald, M. Marinkovic, I. Eliezer, Vapor pressure measurements, thermodynamic parameters, and phase diagram for the system potassium oxide-silicon oxide at high temperatures, J. Phys. Chem., 82 (1978) 1021-1026.
[19] E. Yazhenskikh, K. Hack, M. Mueller, Critical thermodynamic evaluation of oxide systems relevant to fuel ashes and slags. Part 1: Alkali oxide-silica systems, CALPHAD: Comput. Coupling Phase Diagrams Thermochem., 30 (2006) 270-276.
[20] D. Saulov, Application of the modified quasichemical model to solutions with strong short-range ordering, J. Non-Cryst. Solids, 353 (2007) 2845-2851.
[21] L. Zhang, C. Schmetterer, P.J. Masset, Thermodynamic description of the M2O-SiO2 (M = K, Na) systems, Comput. Mater. Sci., 66 (2013) 20-27.
[22] A.D. Pelton, M. Blander, Thermodynamic analysis of ordered liquid solutions by a modified quasichemical approach-application to silicate slags, Metall. Trans. B, 17B (1986) 805-815.
[23] M. Blander, A.D. Pelton, Analyses and predictions of the thermodynamic properties of multicomponent silicates, in, Metall. Soc. AIME, 1984, pp. 295-304.
[24] M. Blander, A.D. Pelton, Thermodynamic analysis of binary liquid silicates and prediction of ternary solution properties by modified quasichemical equations, Geochim. Cosmochim. Acta, 51 (1987) 85-95.
[25] A.D. Pelton, M. Blander, A least squares optimization technique for the analysis of thermodynamic data in ordered liquids, CALPHAD: Comput. Coupling Phase Diagrams Thermochem., 12 (1988) 97-108.
[26] A.D. Pelton, G. Eriksson, M. Blander, A Quasi-chemical Model for the Thermodynamic Properties of Multicomponent Slags, Proceedings of the 3rd International Syposium on Metallurgical Slags and Fluxes, (1989) 66-69.
[27] M.G. Frohberg, E. Caune, M.L. Kapoor, Measurement of the activity of the oxygen ions in the fluid systems sodium oxide-silicon dioxide and potassium oxide-silicon dioxide, Arch. Eisenhuettenw., 44 (1973) 585-588.
[28] D. Ravaine, E. Azandegbe, J.L. Souquet, Potentiometric measurements of electrochemical cells consisting of fused silicates; interpretation of results by a statistical model, Silic. Ind., 40 (1975) 333-340.
[29] J.M. Steiler, Thermodynamic study on liquid slags of potassium oxide-silica system, in, IRSID, 1982, pp. 21-21/21-36.
[30] F.C. Kracek, N.L. Bowen, G.W. Morey, Equilibrium relations and factors influencing their determination in the system K2SiO3-SiO2, J. Phys. Chem., 41 (1937) 1183-1193.
[31] K.E. Spear, T.M. Besmann, E.C. Beahm, Thermochemical modeling of glass: application to high-level nuclear waste glass, MRS Bull., 24 (1999) 37-43.
[32] P.L. Lin, A.D. Pelton, A structural model for binary silicate systems, Metall. Trans., B, 10B (1979) 667-675.
[33] A. Romero-Serrano, A.D. Pelton, Extensions of a structural model for binary silicate systems, Metall. Mater. Trans. B, 26B (1995) 305-315.
[34] A. Stypula, B. Ziemba, D. Szeszo, J. Zawila, Technological problems in the manufacture of potassium water glass, Szklo Ceram., 49 (1998) 2-5.
[35] M. Hillert, B. Jansson, B. Sundman, J. Aagren, A two-sublattice model for molten solutions with different tendency for ionization, Metall. Trans. A, 16A (1985) 261-266.
[36] B. Sundman, Modification of the two-sublattice model for liquids, CALPHAD: Comput. Coupling Phase Diagrams Thermochem., 15 (1991) 109-119.

[37] C.W. Bale, E. Belisle, P. Chartrand, S.A. Decterov, G. Eriksson, A.E. Gheribi, K. Hack, I.H. Jung, Y.B. Kang, J. Melancon, A.D. Pelton, S. Petersen, C. Robelin, J. Sangster, P. Spencer, M.A. Van Ende, FactSage thermochemical software and databases, 2010-2016, CALPHAD: Comput. Coupling Phase Diagrams Thermochem., 54 (2016) 35-53.
[38] M.W. Chase, S. National Institute of, Technology, NIST-JANAF thermochemical tables, American Chemical Society ; American Institute of Physics for the National Institute of Standards and Technology, [Washington, D.C.]; Woodbury, N.Y., 1998.
[39] A.D. Pelton, S.A. Degterov, G. Eriksson, C. Robelin, Y. Dessureault, The modified quasichemical model I - binary solutions, Metall. Mater. Trans. B, 31B (2000) 651-659.
[40] E. Ising, Beitrag zur Theorie des Ferromagnetismus, Zeitschrift für Physik, 31 (1925) 253-258.
[41] I. Barin, Thermochemical Data of Pure Substances, VCH, 1989.
[42] K. Bernet, R. Hoppe, Crystal structure of potassium silicate (K4[SiO4]), Z. Anorg. Allg. Chem., 589 (1990) 129-138.
[43] R. Werthmann, R. Hoppe, On potassium silicate (K2SiO3), the first alkali metal cyclotrisilicate, and rubidium silicate (Rb2SiO3), cesium silicate (Cs2SiO3), rubidium germanate (Rb2GeO3) and cesium germanate (Cs2GeO3), Rev. Chim. Miner., 18 (1981) 593-607.
[44] H. Schweinsberg, F. Liebau, Preparation and crystallographic data of K2Si2O5, KHSi2O5I, and K2Si4O9, Z. Anorg. Allg. Chem., 387 (1972) 241-251.
[45] B.H.W.S. De Jong, H.T.J. Super, A.L. Spek, N. Veldman, G. Nachtegaal, J.C. Fischer, Mixed alkali systems: structure and 29Si MASNMR of Li2Si2O5 and K2Si2O5, Acta Crystallogr., Sect. B: Struct. Sci., B54 (1998) 568-577.
[46] R.G. Berman, T.H. Brown, Heat capacity of minerals in the system sodium monoxide-potassium monoxide-calcium oxide-magnesium oxide-iron(II) oxide-iron(III) oxide-aluminum oxide-silicon dioxide-titanium dioxide-water-carbon dioxide: representation, estimation, and high temperature extrapolation, Contrib. Mineral. Petrol., 89 (1985) 168-183.
[47] R. Wollast, Proposed some modifications of the phase diagram of systems silica - alkali oxides, Silic. Ind., 26 (1961) 89-92.
[48] F.C. Kracek, N.L. Bowen, G.W. Morey, The system: potassium metasilicate-silica, J. Phys. Chem., 33 (1929) 1857-1879.
[49] F.C. Kracek, The cristobalite liquidus in the alkali oxide-silica systems and the heat of fusion of cristobalite, J. Am. Chem. Soc., 52 (1930) 1436-1442.
[50] J.O.M. Bockris, J.D. Mackenzie, J.A. Kitchener, Viscous flow in silica and binary liquid silicates, Trans. Faraday Soc., 51 (1955) 1734-1748.
[51] G.W. Morey, C.N. Fenner, Ternary system: water-potassium silicate-silica, J. Am. Chem. Soc., 39 (1917) 1173-1229.
[52] V.V. Golubkov, B.A. Shakhmatkin, Specific features of temperature dependences of the intensity of small-angle x-ray scattering in oxide systems at liquidus temperatures, Glass Phys. Chem., 25 (1999) 335-341.
[53] A.B. Meshalkin, A.B. Kaplun, The complex investigation of the phase equilibria and melt characteristics in borate and silicate systems, J. Cryst. Growth, 275 (2005) e115-e119.
[54] G. Akdogan, H. Johto, P. Taskinen, Phase equilibria study of K-O-Si system in equilibrium with air, J. Eur. Ceram. Soc., 34 (2014) 4053-4058.
[55] M. Rey, Thermodynamic activity of silica and of oxides in silicate melts, Discuss. Faraday Soc., (1948) 257-265.

[56] R.J. Charles, Metastable liquid immiscibility in alkali metal oxide-silica systems, J. Am. Ceram. Soc., 49 (1966) 55-62.
[57] R.J. Charles, Activities in lithium oxide, sodium oxide, and potassium oxide-silicon dioxide solutions, J. Am. Ceram. Soc., 50 (1967) 631-641.
[58] Y. Moriya, D.H. Warrington, R.W. Douglas, Metastable liquid-liquid immiscibility in some binary and ternary alkali silicate glasses, Phys. Chem. Glasses, 8 (1967) 19-25.
[59] Y. Kawamoto, M. Tomozawa, Prediction of immiscibility boundaries of the systems K2O-SiO2, K2O-Li2O-SiO2, K2O-Na2O-SiO2, and K2O-BaO-SiO2, J. Am. Ceram. Soc., 64 (1981) 289-292.
[60] Y.P. Gupta, U.D. Mishra, Electrical conduction and electron microscopy of vitreous solid in the potassium oxide-silicon dioxide system, J. Phys. Chem. Solids, 30 (1969) 1327-1334.
[61] O.L. Anderson, D.A. Stuart, Calculation of activation energy of ionic conductivity in silica glasses by classical methods, J. Am. Ceram. Soc., 37 (1954) 573-580.
[62] E. Preston, W.E.S. Turner, Study of the volatilization from potassium-oxide-silica glasses, J. Soc. Glass Technol., 27 (1933) 122-144.
[63] E. Preston, W.E.S. Turner, METHODS OF DETERMINING THE CONSTITUTION OF GLASSES*, Journal of the American Ceramic Society, 17 (1934) 26-33.
[64] S.V. Nemilov, Viscosity of glasses of sodium oxide-potassium oxide-silicon dioxide and lithium oxide-potassium oxide-silicon dioxide systems in softening point regions, Zh. Prikl. Khim. (Leningrad), 42 (1969) 55-62.
[65] A. Dietzel, H.A. Sheybany, Problems related to the filling of structural voids in glass-simple alkali silicate glasses, Verres Refract., 2 (1948) 63-80.
[66] J.E. Shelby, Thermal expansion of mixed-alkali silicate glasses, J. Appl. Phys., 47 (1976) 4489-4496.
[67] L.P. Boesch, C.T. Moynihan, Effect of thermal history on conductivity and electrical relaxation in alkali silicate glasses, J. Non-Cryst. Solids, 17 (1975) 44-60.
[68] V.A. Bershtein, V.M. Egorov, Y.A. Emel'yanov, R.P. Kelina, V.A. Stepanov, G.D. Cherkas, Ion interactions between framework sections and relaxation transitions in alkali silicate glasses, Fiz. Khim. Stekla, 6 (1980) 179-189.
[69] N.V. Borisova, V.M. Ushakov, High-temperature calorimetry of glasses and crystals in the K2O-SiO2 system, Glass Phys. Chem., 24 (1998) 318-322.
[70] W.J. Malfait, W.E. Halter, Y. Morizet, B.H. Meier, R. Verel, Structural control on bulk melt properties: Single and double quantum 29Si NMR spectroscopy on alkali-silicate glasses, Geochim. Cosmochim. Acta, 71 (2007) 6002-6018.
[71] R.G. Berman, T.H. Brown, Erratum. Heat capacity of minerals in the system sodium monoxide-potassium monoxide-calcium oxide-magnesium oxide-iron(II) oxide-iron(III) oxide-aluminum oxide-silicon dioxide-titanium dioxide-water-carbon dioxide: representation, estimation, and high temperature extrapolation, Contrib. Mineral. Petrol., 94 (1986) 262.
[72] R.G. Berman, T.H. Brown, H.J. Greenwood, An Internally Consistent Thermodynamic Data Base for Minerals in the System Na2O-K2O-CaO-MgO-FeO-Fe2O3-Al2O3-SiO2-TiO2-H2O-CO2, Atomic Energy of Canada Limited, TR-377 (1985) 62.
[73] M.W. Chase, Jr., C.A. Davies, J.R. Downey, Jr., D.J. Frurip, R.A. McDonald, A.N. Syverud, JANAF Thermochemical Tables. Third Edition. Part I, aluminum-cobalt, J. Phys. Chem. Ref. Data, Suppl., 14 (1985) 1-926.

[74] M.W. Chase, Jr., C.A. Davies, J.R. Downey, Jr., D.J. Frurip, R.A. McDonald, A.N. Syverud, JANAF Thermochemical Tables. Third Edition. Part II, chromium-zirconium, J. Phys. Chem. Ref. Data, Suppl., 14 (1985) 927-1856.
[75] P.J. Spencer, Thermodynamic properties of silicates, in, Natl. Phys. Lab., 1973, pp. 36 pp.
[76] W. Slough, Comparison of methods available for the estimation of enthalpies of formation for double oxide systems, Nat. Phys. Lab. (U. K.), Div. Chem. Stand., Rep., No. 25 (1973) 12 pp.
[77] C. Kroger, E. Fingas, Action of quartz and alkali silicates upon alkali carbonates, Z. Anorg. Allg. Chem., 213 (1933) 12-57.
[78] K. Takahashi, T. Yoshio, Thermochemical investigations of glasses. II. Oxygen-alkali metal bond energy in alkali silicates. (R2O-SiO2, Yogyo Kyokai Shi, 78 (1970) 329-337.
[79] D.R. Stull, D.L. Hildenbrand, F.L. Oetting, G.C. Sinke, Low-temperature heat capacities of 15 inorganic compounds, J. Chem. Eng. Data, 15 (1970) 52-56.
[80] R.P. Beyer, M.J. Ferrante, R.R. Brown, G.E. Daut, Thermodynamic properties of potassium metasilicate and disilicate, in, Bur. Mines, 1980, pp. 24 pp.
[81] F.C. Kracek, K.J. Neuvonen, G. Burley, R.J. Gorden, Contributions of Thermochemical and X-ray Data to the Problem of Mineral Stability, Carnegie Inst. Washington, Ybk., 52 (1953) 69-75.
[82] K. Takahashi, T. Yoshio, Thermodynamic quantities of alkali silicates in the temperature range from 25.deg. to melting point, Yogyo Kyokai Shi, 81 (1973) 524-533.
[83] F.C. Kracek, The ternary system: K2SiO3-Na2SiO3-SiO2, J. Phys. Chem., 36 (1932) 2529-2542.
[84] E. Azandegbe, I. Ansara, J.L. Souquet, Electrochemistry of liquid alkali metal siliconates. Application to the calculation of heats of fusion of definite compounds, C. R. Acad. Sci., Ser. C, 276 (1973) 1247-1250.
[85] P. Boivin, J.C. Berthelay, Y. Blanc, A. Coulet, R. Castanet, Determination of temperature and enthalpy of melting of alkali disilicates by differential calorimetric analysis, J. Mater. Sci., 28 (1993) 1834-1838.
[86] R.W. Goranson, F.C. Kracek, An experimental investigation of the phase relations of K2Si4O9 under pressure, J. Phys. Chem., 36 (1932) 913-926.
[87] K.L. Geisinger, N.L. Ross, P. McMillan, A. Navrotsky, Potassium silicate (K2Si4O9): Energetics and vibrational spectra of glass, sheet silicate, and wadeite-type phases, Am. Mineral., 72 (1987) 984-994.
[88] O.L. Anderson, The use of ultrasonic measurements under modest pressure to estimate compression at high pressure, Phys. Chem. Solids, 27 (1966) 547-565.
[89] S.W. Kieffer, Thermodynamics and lattice vibrations of minerals: 1. Mineral heat capacities and their relationships to simple lattice vibrational models, Rev. Geophys. Space Phys., 17 (1979) 1-19.
[90] S.W. Kieffer, Thermodynamics and lattice vibrations of minerals: 3. Lattice dynamics and an approximation for minerals with application to simple substances and framework silicates, Rev. Geophys. Space Phys., 17 (1979) 35-59.
[91] S.W. Kieffer, Thermodynamics and lattice vibrations of minerals: 2. Vibrational characteristics of silicates, Rev. Geophys. Space Phys., 17 (1979) 20-34.
[92] S.W. Kieffer, Thermodynamics and lattice vibrations of minerals. 4. Application to chain and sheet silicates and orthosilicates, Rev. Geophys. Space Phys., 18 (1980) 862-886.
[93] Y.A. Pyatenko, Mineralogically Probable and Improbable Crystal Structures, International Geology Review, 26 (1984) 40-46.

[94] M. Henry, Application of the partial charge model to the aqueous chemistry of silica and silicates, Top. Mol. Organ. Eng., 15 (1997) 273-334.
[95] G.M. Matveev, Chemical stability of glassy and ceramic materials, Zh. Vses. Khim. Obshchest., 12 (1967) 711-712.
[96] G.M. Matveev, G.B. El'kin, Thermodynamic stability of compounds of main binary silicate systems, Teor. Osn. Khim. Tekhnol., 26 (1992) 759-762.
[97] M. O'Keeffe, B.G. Hyde, Stoichiometry and the structure and stability of inorganic solids, Nature, 309 (1984) 411-414.
[98] A.M. Deml, A.M. Holder, R.P. O'Hayre, C.B. Musgrave, V. Stevanovic, Intrinsic Material Properties Dictating Oxygen Vacancy Formation Energetics in Metal Oxides, J. Phys. Chem. Lett., 6 (2015) 1948-1953.
[99] J.F. Stebbins, P.F. McMillan, D.B. Dingwell, Editors, Structure, Dynamics and Properties of Silicate Melts. [In: Rev. Mineral., 1995; 32], Mineralogical Society of America, 1995.
[100] B. Konar, M.A. Van Ende, I.-H. Jung, Critical evaluation and thermodynamic optimization of the Li-O, and Li2O-SiO2 systems, Journal of European Ceramic Society, (2016) Accepted.
[101] J.E. Saal, S. Kirklin, M. Aykol, B. Meredig, C. Wolverton, Materials Design and Discovery with High-Throughput Density Functional Theory: The Open Quantum Materials Database (OQMD), JOM, 65 (2013) 1501-1509.
[102] R.J. Callow, Activities in alkali oxide-silica melts, Trans. Faraday Soc., 46 (1950) 663-673.
[103] E. Preston, W.E.S. Turner, Volatilization and the constitution of glass. A reply to a criticism of G. W. Morey, J. Am. Ceram. Soc., 18 (1935) 170-173.
[104] D.D.W. Smith, Thermodynamic properties and behavior of potassium oxide in potassium oxide-alumina and potassium oxide-calcium oxide silicates, Master's thesis, MIT, USA, (1984).
[105] A.I. Zaitsev, N.E. Shelkova, N.P. Lyakishev, B.M. Mogutnov, Thermodynamic properties of K2O-SiO2 melts, Zh. Fiz. Khim., 74 (2000) 1021-1028.
[106] M.C. Wilding, A. Navrotsky, The dissolution of silica and alumina in silicate melts. In situ high temperature calorimetric studies, Neues Jahrb. Mineral., Abh., 172 (1998) 177-201.
[107] M. Morishita, Direct measurement of relative partial molar enthalpy of SiO2 in SiO2-M2O (M = Li, Na, K, Cs) binary and SiO2-CaO-Al2O3 ternary melts, J. Am. Ceram. Soc., 87 (2004) 1550-1555.
[108] E.R. Plante, C.D. Olson, T. Negas, Interaction of K2O with slag in open cycle, coal fired MHD, Proc. Sixth Int. Conf. on Magnetohydrodynamic Electrical Power Generation, Washington, DC, June 9-13, CONF750601-P2 (1975) 211-218.
[109] E.R. Plante, Vaper Pressure Measurements of Potassium over K2O-SiO2 Solutions by a Knudsen Effusion Mass Spectrometric Method, NBS Special Publication 561/1: Characterization of High Temperature Vapors and Gases, Washington, 1 (1979) 265-281.
[110] V. Piacente, J. Matousek, Alkali vapor pressures over some simple silicate melts, Collect. Czech. Chem. Commun., 48 (1983) 1528-1531.
[111] P. Richet, Y. Bottinga, Heat capacity of aluminum-free liquid silicates, Geochim. Cosmochim. Acta, 49 (1985) 471-486.
[112] P. Richet, Y. Bottinga, Heat capacity of liquid silicates: new measurements on sodium aluminosilicate and potassium silicate, Geochim. Cosmochim. Acta, 44 (1980) 1535-1541.
[113] D. De Sousa Meneses, M. Eckes, L. del Campo, C.N. Santos, Y. Vaills, P. Echegut, Investigation of medium range order in silicate glasses by infrared spectroscopy, Vib. Spectrosc., 65 (2013) 50-57.

[114] T. Maehara, T. Yano, S. Shibata, M. Yamane, Structure and phase transformation of alkali silicate melts analyzed by Raman spectroscopy, Philos. Mag., 84 (2004) 3085-3099.
[115] H. Maekawa, T. Maekawa, K. Kawamura, T. Yokokawa, The structural groups of alkali silicate glasses determined from silicon-29 MAS-NMR, J. Non-Cryst. Solids, 127 (1991) 53-64.
[116] C. Huang, A.N. Cormack, Structural differences and phase separation in alkali silicate glasses, J. Chem. Phys., 95 (1991) 3634-3642.

Tables

Table 4.1 Results of thermal analysis with sealed Pt capsule.

Sample	Composition (mol %)				Thermal incidences (°C)			
	Nominal		Actual*		$K_2Si_2O_5$	$K_2Si_2O_5$	Eutectic	Liquidus
	K_2O	SiO_2	K_2O	SiO_2	α to β	β to γ		
40%K_2O	40	60	37	63	217.9	570.8	806.4	1027.4
					220.6	551.5	826.9	1005.0
					220.4	592.0	791.1	1005.8
67%K_2O	67	33	59	41			714.1	

*: Actual composition is estimated considering the volatile loss of K_2O during the sample preparation.

Table 4.2 Optimized model parameters for liquid solution and thermodynamic properties of compounds relative to elemental standard state.

Liquid solution

Phase	$\Delta H^{o}_{298.15K}$ (J·mol^{-1})	$S^{o}_{298.15K}$ (J·mol^{-1}·K^{-1})	C_P (J·mol^{-1}·K^{-1})	References	Experimental methods / Remarks
K_2O (*l*)	-334298.010	128.857	75.947+0.0171460002016·T -591639.9844·T^{-2} (298.15-1013 K) 107.000 (>1013 K)	16Bal [37]	
SiO_2 (*l*)	-896795.870	50.829	83.514-2455359.982·T^{-2}-374.693·$T^{-0.5}$+280072194.424·T^{-3} (298.15-1996 K) 85.772 (>1996 K)	16Bal [37]	

$Z^{K}_{KK} = 0.6887$, $Z^{Si}_{SiSi} = 2.7549$

$\Delta g_{KO_{0.5}-SiO_2} = (-329699.2 + 33.472 \cdot T) + (-227400.4) X_{Si-Si} + (-100416) X^{3}_{Si-Si} + (182004 + 7.5312 \cdot T) X^{5}_{Si-Si}$

Solid compounds

Phase	$\Delta H^{o}_{298.15K}$ (kJ·mol^{-1})	$S^{o}_{298.15K}$ (J·mol^{-1}·K^{-1})	C_P (J·mol^{-1}·K^{-1})	Reference	Experimental method / Remarks
K_2O (s)	-361.497997	102.006	75.947+0.0171460002016·T -591639.9844·T^{-2} (298.15-373 K) 107.000 (>1013 K)	16Bal [37]	
SiO_2 (s1) (α-Qz)	-910.699942	41.460	80.012-3546683.999·T^{-2}-240.276·$T^{-0.5}$+491568369.44·T^{-3} (298.15-373 K) 80.012+ 0.00844002·T -3546683.999·T^{-2}-4.521270*10^{-5}·T^{2} + 491568369.44·T^{-3} + 6.055*10^{-8}·T^{3}-240.276·$T^{-0.5}$ (373-848 K) 0.0418 (>848 K)	16Bal [37]	
SiO_2 (s2) (β-Qz)	-908.626770	44.207	80.012-3546683.999·T^{-2}-240.276·$T^{-0.5}$+491568369.44·T^{-3} (298.15-1996 K) 85.772 (>1996 K)	16Bal [37]	

SiO_2 (s4) (β-Trd)	-907.045134	45.524	75.373-5958095.078·T^{-2}+958246122.88·T^{-3} (298.15-1991 K) 85.772 (>1991 K)	16Bal [37]	
SiO_2 (s6) (β-Crs)	-906.377230	46.029	83.514-2455359.982·T^{-2}-374.693·$T^{-0.5}$+280072194.424·T^{-3} (298.15-1996 K) 85.772 (>1996 K)	16Bal [37]	
K_2SiO_3	-1535.832			33Kro [77]	Gas equilibration
	-1535.280			70Tak [78]	Solution calorimetry
	-1546.250 ±12.55			73Spe [75]	Estimation
	-1543.398 ±9			98Bor [69]	Solution calorimetry
		146.147		70Stu [79]	Adiabatic calorimetry
		143.466 ±10.0		NKR	Error ±7%
			118.901 + 0.048810544·T -1415447.2·T^{-2}	80Bey [80]	Drop calorimetry
	-1543.800	146.147	118.901 + 0.048810544·T -1415447.2·T^{-2} (298.15-1260 K)	This study	
α-$K_2Si_2O_5$	-2504.355			33Kro [77]	Gas equilibration
	-2507.242			53Kra [81]	Solution calorimetry
	-2418.352			70Tak [78]	Solution calorimetry
	-2508.152			73Slo [76]	Estimation
	-2470.898 ±3			98Bor [69]	Solution calorimetry
		182.004 ±8.37		73Spe [75]	Estimation
		190.581 ±0.57		80Bey [80]	Adiabatic calorimetry
		184.926 ±12.9		NKR	Error ±7%
			191.857 + 0.0365849·T -1415447.2·T^{-2}	80Bey [80]	Drop calorimetry
α to β	ΔH_{tr}^{o} : 1.213 ±0.004 at 510 K			80Bey [80]	Drop calorimetry
β-$K_2Si_2O_5$			158.005 + 0.0908263·T -998720.8·T^{-2}	80Bey [80]	Drop calorimetry
β to γ	ΔH_{tr}^{o} : 1.590 ±0.005 at 867 K			80Bey [80]	Drop calorimetry
β to γ	ΔH_{tr}^{o} : 1.075 ±0.45 at 867 K			37Kra [30]	DTA
γ-$K_2Si_2O_5$			224.225 + 0.00435136·T	80Bey [80]	Drop calorimetry
α-, β-, γ-$K_2Si_2O_5$			240.72 -14793400·T^{-2} + 2289210000·T^{-3}	85Ber [46]	Data assessment
α-$K_2Si_2O_5$	-2503.700	190.581	240.72 -14793400·T^{-2} + 2289210000·T^{-3} (298.15-1320 K)	This study	
β-$K_2Si_2O_5$	α to β, ΔH_{tr}^{o} : 1.213 at 510 K		240.72 -14793400·T^{-2} + 2289210000·T^{-3} (298.15-1320 K)	This study	

γ-$K_2Si_2O_5$	β to γ, ΔH_{tr}^{o} : 1.590 at 867 K		240.72 -14793400·T^{-2} + 2289210000·T^{-3} (298.15-1320 K)	This study	
α-$K_2Si_4O_9$	-4313.663			53Kra [81]	Solution calorimetry
	-4275.278 ±11			98Bor [69]	Solution calorimetry
		265.684 ±12.5		73Spe [75]	Estimation
		223.72		87Gei [87]	Vibrational modeling
		267.846 ±18.7		NKR	Error ±7%
α to β	ΔH_{tr}^{o} : 3.212 ±0.42	at 865 K		32Gor [86]	DTA
α-$K_2Si_4O_9$	-4342.000	265.684	400.744 + 0.016880·T -21886767.998·T^{-2} - 9.042540296*10^{-5}·T^{2} + 3272346738.88·T^{-3} + 1.211009*10^{-7}·T^{3} -480.552·$T^{-0.5}$ (298.15-1050 K)	This study	
β-$K_2Si_4O_9$	α to β, ΔH_{tr}^{o} : 3.212 at 865 K		400.744 + 0.016880·T -21886767.998·T^{-2} - 9.042540296*10^{-5}·T^{2} + 3272346738.88·T^{-3} + 1.211009*10^{-7}·T^{3} -480.552·$T^{-0.5}$ (298.15-1050 K)	This study	
K_4SiO_4	-1958.112			33Kro [77]	Gas equilibration
	-2064.614			73Slo [76]	Estimation
		245.472 ±17.2		NKR	Error ±7%
	-2065.220	233.198	2·C_P (K_2O, s) + 1·C_P (SiO_2, s2, β-Qz) (298.15-1185 K)	This study	

Qz: Quartz, Trd: Tridymite, Crs: Cristobalite, NKR: Neumann-Kopp rule, $\Delta H_{298.15K}^{o}$ are relative to elements at 298.15 K.

Figures

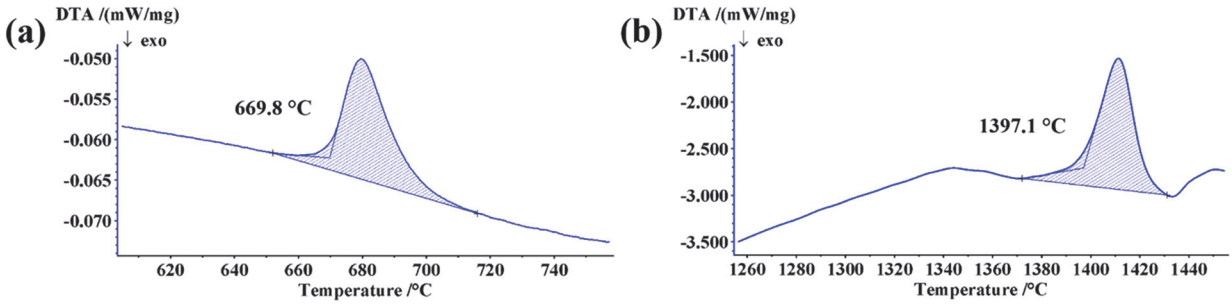

Figure 4.1 DTA results for the samples contained in sealed Pt capsules (a) K_2CrO_4 and (b) $CaMgSi_2O_6$.

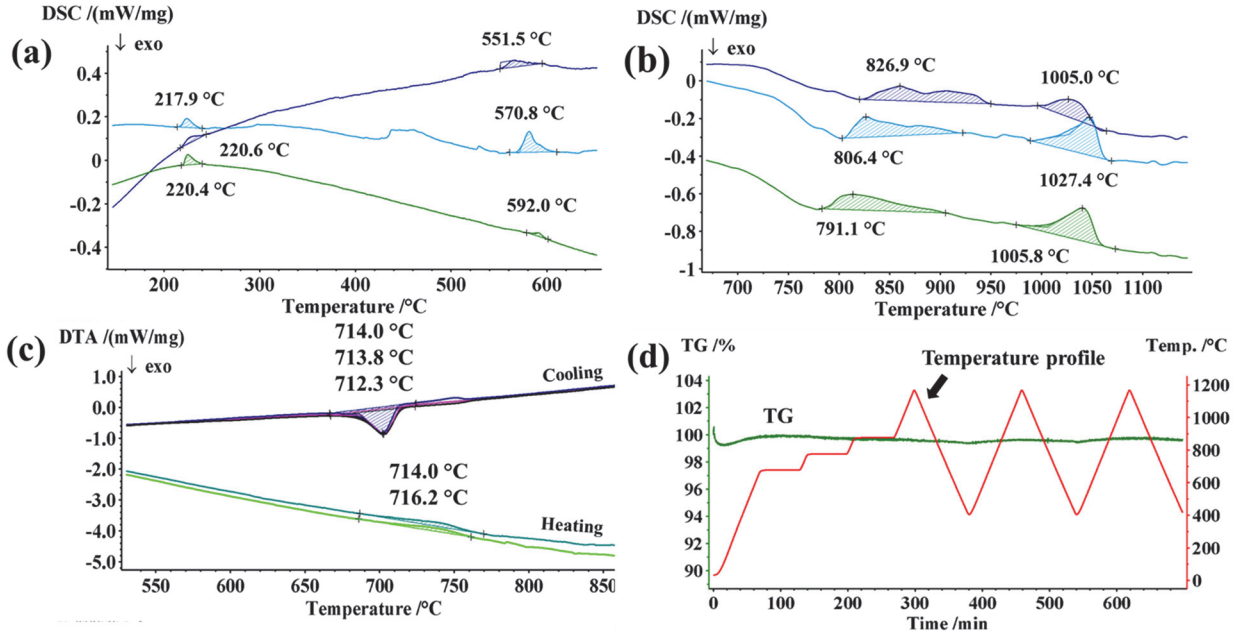

Figure 4.2 Thermal analysis results for the present K_2O-SiO_2 samples using sealed Pt capsule. (a) polymorphic transitions and (b) eutectic and liquidus temperatures for three samples with starting composition of 40 mol % K_2O. (c) Eutectic temperature and (d) corresponding TG analysis for a 67 mol % K_2O sample.

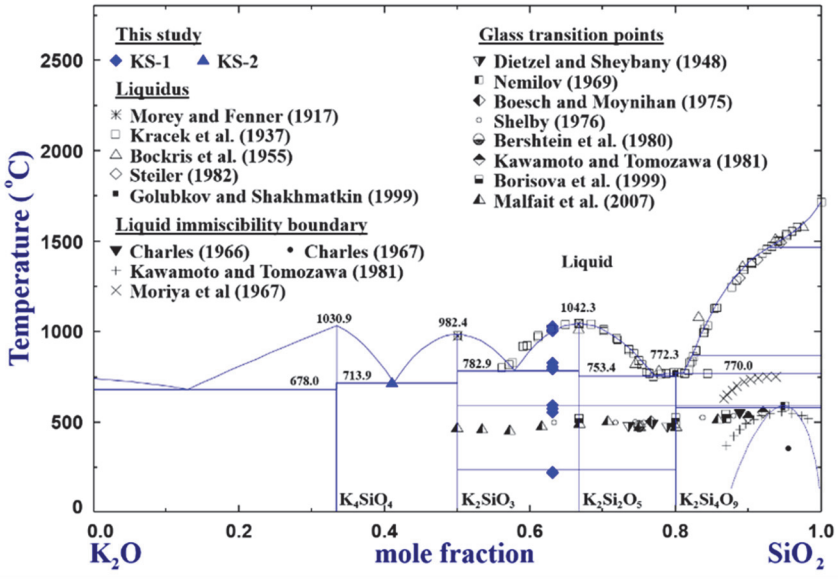

Figure 4.3 Optimized phase diagram of the K_2O-SiO_2 system in comparison with all reliable experimental data. Dotted line indicates the calculated metastable liquid miscibility gap.

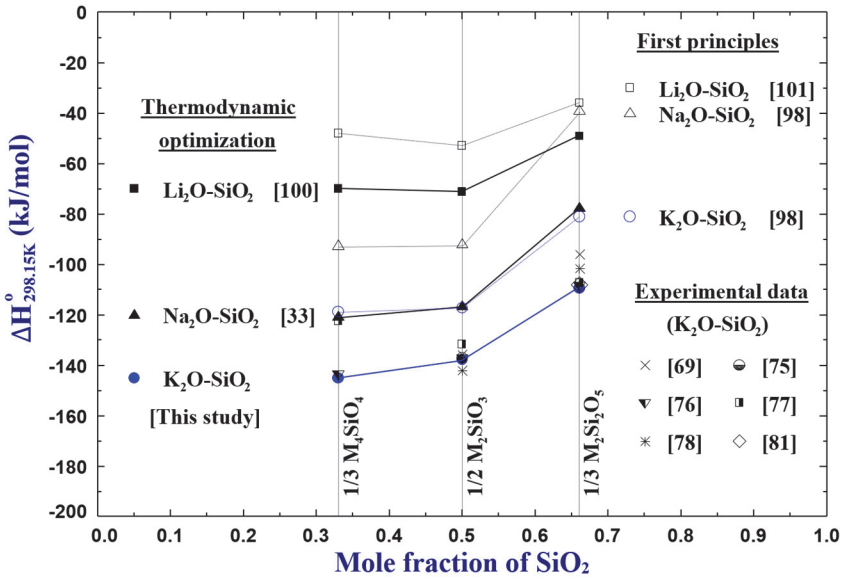

Figure 4.4 The enthalpy of formation of compounds in the Li_2O-SiO_2, Na_2O-SiO_2, and K_2O-SiO_2 systems from the constituent oxides at 298.15 K.

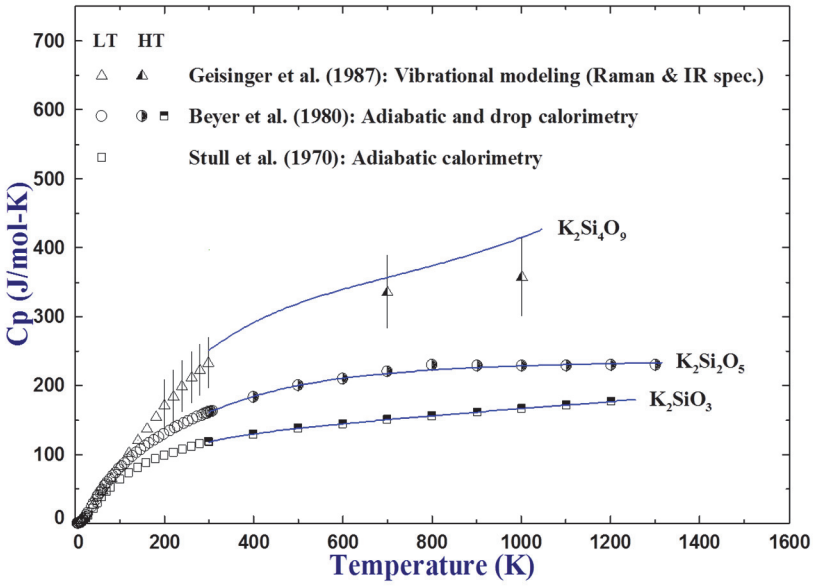

Figure 4.5 Optimized heat capacities of compounds in comparison with experimental data [79, 80, 87].

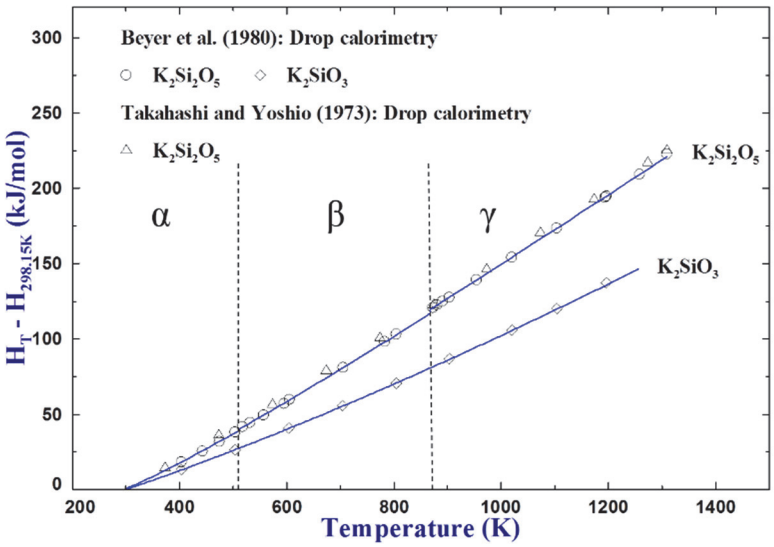

Figure 4.6 Calculated heat contents of compounds in comparison with experimental data [80, 82].

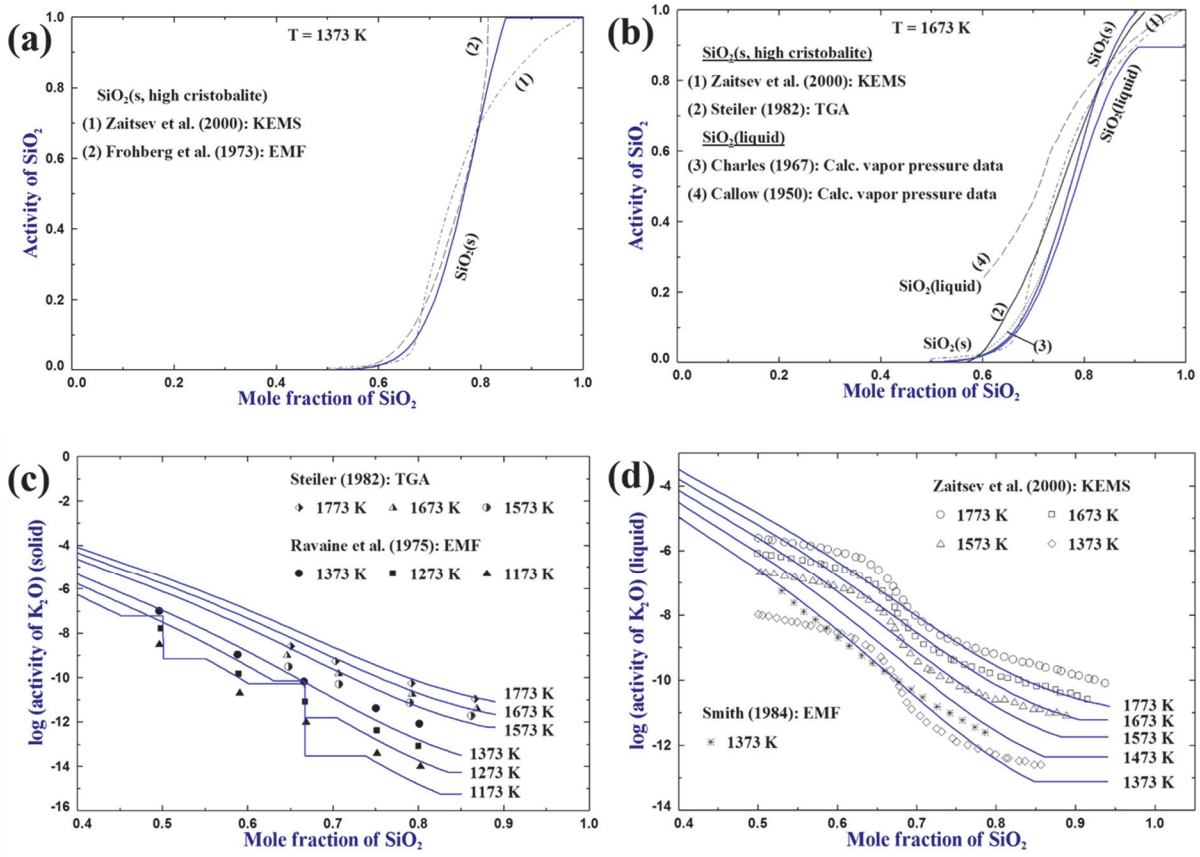

Figure 4.7 Calculated activities of (a) SiO_2 (high cristobalite) at 1373 K, (b) SiO_2 (high cristobalite) and SiO_2 (liquid) at 1673 K, (c) K_2O (solid) at 1173 to 1773 K, (d) K_2O (liquid) at 1373 to 1773 K compared to experimental data, solid lines are from the present optimization.

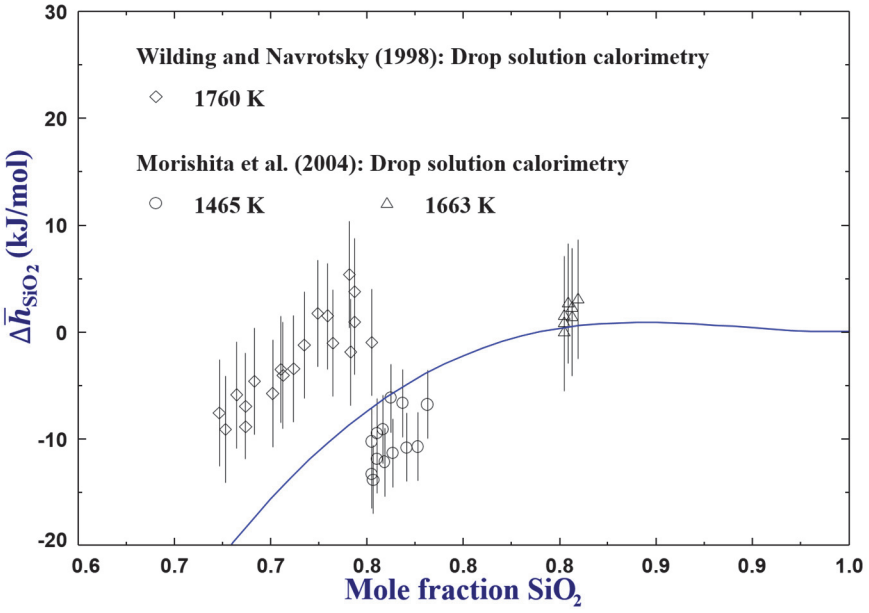

Figure 4.8 Calculated partial molar enthalpy of SiO_2 at 1663 K in comparison with experimental data [106, 107].

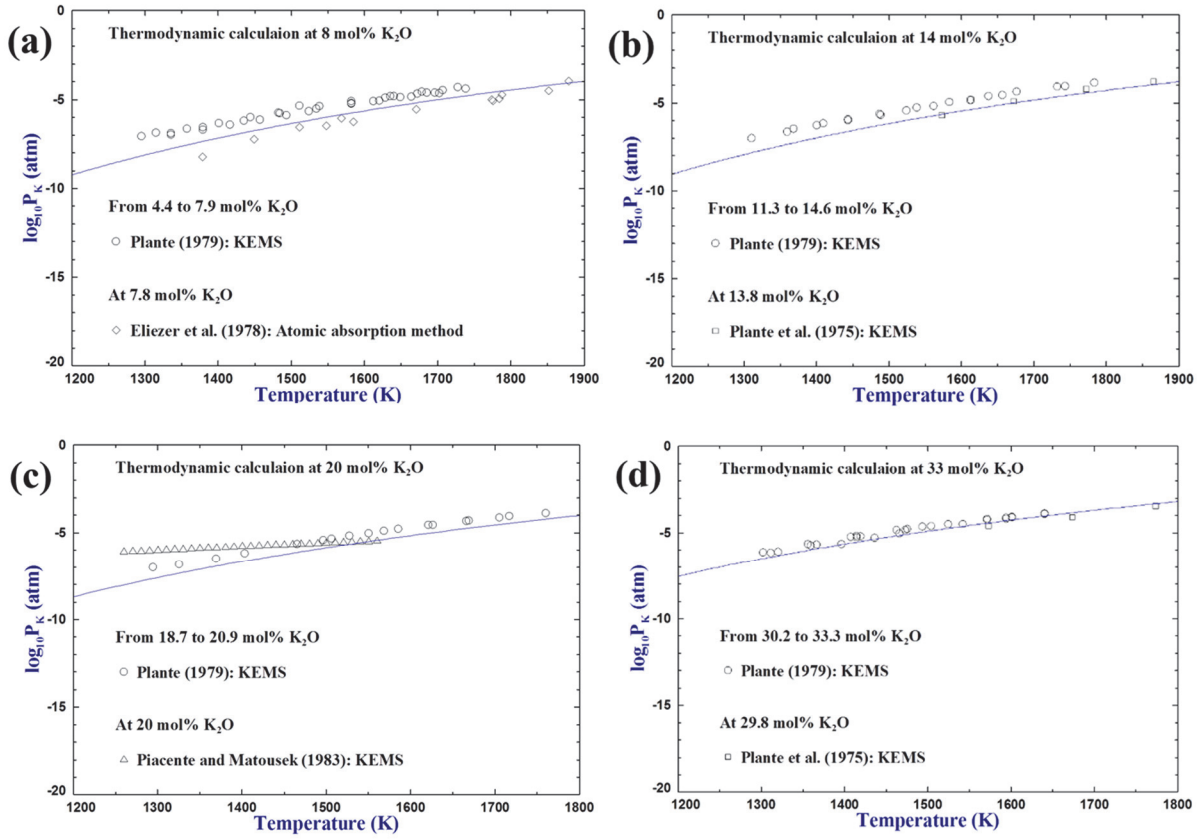

Figure 4.9 Calculated partial pressure of potassium at (a) 8 (b) 14 (c) 20 (d) 33 mol % K_2O in comparison with experimental data [18, 108-110].

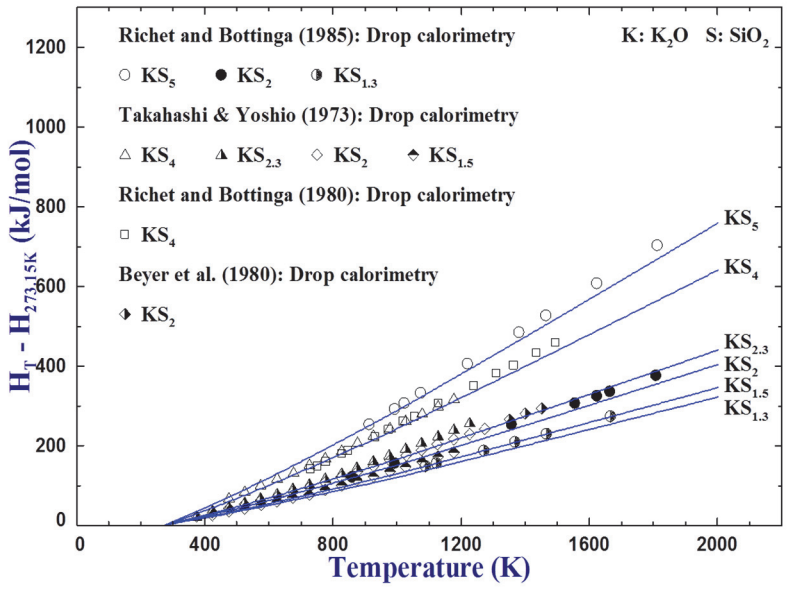

Figure 4.10 Calculated heat contents of liquid K_2O-SiO_2 in comparison with experimental data [80, 82, 111, 112].

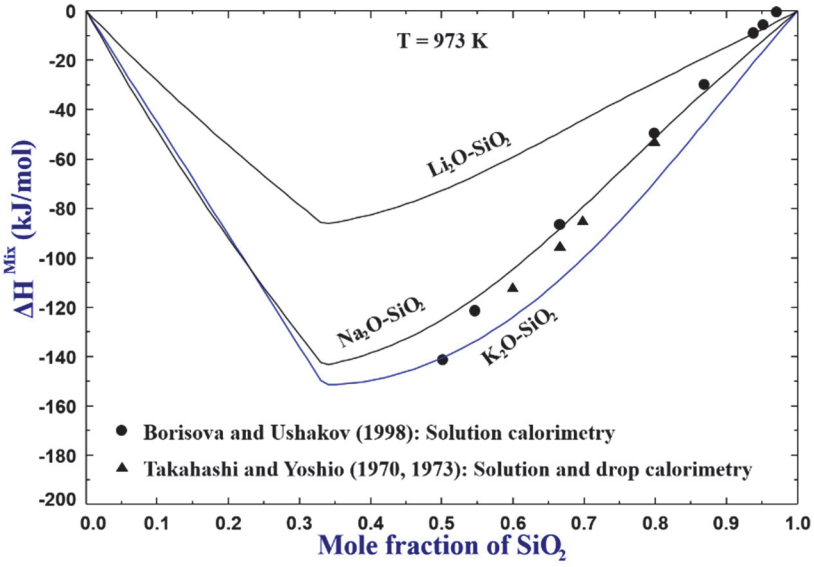

Figure 4.11 Calculated enthalpies of mixing of the liquid Li_2O-, Na_2O-, and K_2O-SiO_2 solutions at 973 K in comparison with experimental data for the K_2O-SiO_2 glass [69, 78, 82].

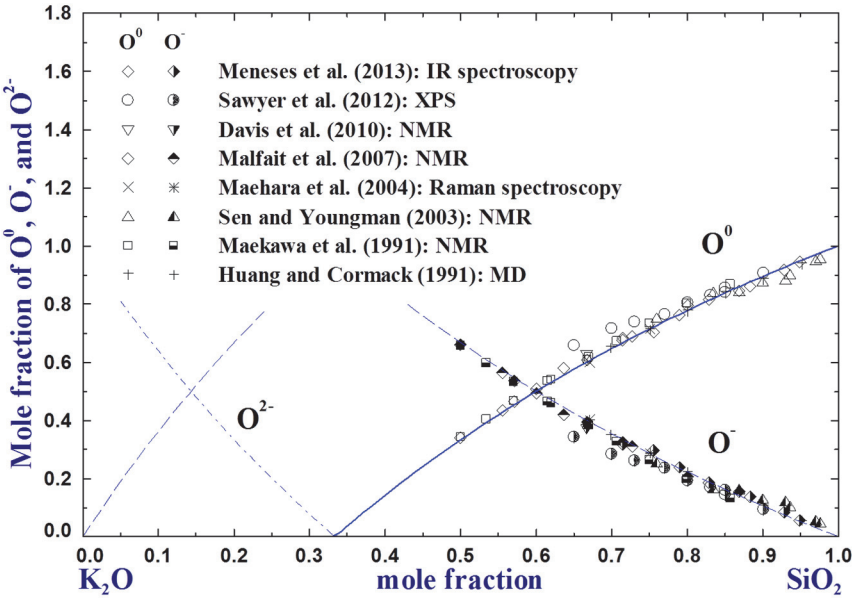

Figure 4.12 Calculated oxygen connectivity in terms of bridged oxygen (O^0), broken oxygen (O^-), and free oxygen (O^{2-}) of the K_2O-SiO_2 melt at 1000 °C in comparison with experimental data [8-10, 70, 113-116].

Chapter 5 Coupled Experimental Study and Thermodynamic Optimization of the K_2O-MgO and K_2O-MgO-SiO_2 Systems

Dong-Geun Kim, Bikram Konar and In-Ho Jung

Submitted to Metallurgical and Materials Transactions B.

In this chapter, experimental results of the K_2O-MgO system and thermodynamic optimization of the K_2O-MgO-SiO_2 system are mainly discussed. Both equilibration/quenching method and thermal analyses using sealed Pt capsules were performed to resolve uncertainties in the K_2O-MgO phase diagram. The optimization of the ternary system was performed based on the K_2O-MgO system as well as the results of K_2O-SiO_2 system described in Chapter 4. The Modified Quasichemical Model was used consistently to extend from the binary systems to the ternary system.

Abstract

Key phase diagram experiments were conducted to reveal the phase diagram of the K_2O-MgO system using thermal analysis and equilibration techniques with sealed Pt crucible. The peritectic reaction of K_6MgO_4 → Liquid + MgO is determined at 858 ± 14 °C for the first time. Based on the critical evaluation of all literature data and the present experimental data, the thermodynamic optimizations of the K_2O-MgO and K_2O-MgO-SiO_2 systems were performed. With the thermodynamically consistent set of Gibbs energy functions of all the phases, all reliable phase diagram and thermodynamic properties of the binary and ternary K_2O-MgO-SiO_2 system were well reproduced. The optimized set of the Gibbs energies of all phases can be used to calculate any unexplored phase diagrams and thermodynamic properties in the system.

Key words: K_2O-MgO, K_2O-MgO-SiO_2, thermodynamic optimization, phase diagram experiments

5.1 Introduction

The K_2O-MgO-SiO_2 system is important in various applications. In pyrometallurgical processes, magnesia (MgO) is the basis of the most commonly used refractories such as magnesia-carbon, dolomite, magnesia-spinel, etc. [1, 2]. SiO_2 is the common component in slag, which is in direct contact with the refractories. In glassmaking, this ternary system is of interest for new silica-based glass optical fibers and mica/cordierite-based glass-ceramics [3-6]. The compounds such as K_2MgSiO_4 and $K_2MgSi_3O_8$ are considered to be good candidates for fertilizer due to slow-releasing potential of K, Mg, and Si for crops [7, 8]. In geological studies, the phase stability and thermodynamic properties of the compounds in this system are essential to understand the complex phase equilibria in multi-component systems such as K_2O-MgO-Al_2O_3-SiO_2, which involve many mineralogically important phases like cordierite, leucite, and potash feldspar, etc. [9] Therefore, accurate phase diagram and thermodynamic information in the K_2O-MgO-SiO_2 system is important.

In the thermodynamic optimization, all the thermodynamic and phase equilibrium data available in the literature are simultaneously evaluated and optimized in thermodynamically consistent manner. As a result, the most reliable thermodynamic description of all phases is obtained. The resultant thermodynamic functions can be used to calculate any phase diagram and thermodynamic properties of the system even which have never been experimentally explored.

There is a lack of thermodynamic property and phase diagram studies in the K_2O-MgO and K_2O-MgO-SiO_2 systems. Up to now, regarding the K_2O-MgO system, only two studies [10, 11] on the

stability of K_6MgO_4 compound are available in the literature. For the K_2O-MgO-SiO_2 system, there have been two phase diagram studies by Roedder [9] and Roth [12] and several studies [9, 12-16] on the structure of the ternary compounds. A thermodynamic optimization on the K_2O-MgO-SiO_2 system was performed by Yazhenskikh *et al*. [17] using the associate model [18] for the description of liquid phase. Even though the liquidus of the ternary system was generally well reproduced, there are some limitations in their optimization. Two stable binary compounds K_6MgO_4 and K_4SiO_4 were neglected in their study. That is, the binary K_2O-MgO and K_2O-SiO_2 systems were less satisfactory. Cristobalite (SiO_2) was formed in the temperature range of 866.9 to 1465.3 °C, where tridymite (SiO_2) should be the stable form of SiO_2 [19]. This leads to a significant alteration of the phase equilibria in the high SiO_2 region of the system. In their optimization, the first order polymorphic transition of K_2MgSiO_4 at 508 °C reported by Dollase [16] was not taken into account, and the solubility of SiO_2 in the $K_2MgSi_3O_8$ [12] was not considered.

The main goal of this study is to discover the phase equilibria of the K_2O-MgO system experimentally and optimize the K_2O-MgO and K_2O-MgO-SiO_2 systems. For the experimental study, equilibration/quenching method and thermal analysis with sealed Pt capsules were employed to accurately determine the phase equilibria of the binary K_2O-MgO system. In the thermodynamic optimization, the Modified Quasichemical Model (MQM) was employed to describe the liquid solution phase. All the thermodynamic calculations in this study were performed using the FactSage software [19]. This study is part of a large thermodynamic database development project for the six-component system K_2O-Na_2O-CaO-MgO-Al_2O_3-SiO_2.

5.2 Experimental Method

5.2.1 Starting Materials

Starting materials were prepared using reagent grade K_2CO_3 (99.997 wt. %, Alfa Aesar) and MgO (99.995 wt. %, Alfa Aesar). Batches of 5 to 10 g of the materials were mixed in an agate mortar for 1 hour. Due to the hygroscopic nature of the starting materials, mixing was performed in isopropyl alcohol (H_2O < 0.02 vol. %) to prevent moisture pickup from air. In order to dry off the alcohol, the mixtures were kept in a drying oven at 120 °C for more than 12 hours and then cooled down to room temperature in a desiccator. To obtain K_2O, which is extremely hygroscopic, the decarbonation of K_2CO_3 ($K_2CO_3 \rightarrow K_2O + CO_2$) was conducted just before each experiment. The decarbonation temperature with minimum volatile loss of K_2O was set to be 725 °C according to the preliminary Differential Scanning Calorimetry (DSC) and Thermo-Gravimetric Analysis (TGA) experiments. The weight of each sample was measured before and after decarbonation to confirm the completion of the decarbonation reaction. A small amount of K_2O loss (about 2 to 5 mol %) was inevitable. After the decarbonation, the mixtures of K_2O and MgO were stored in a drying oven to cool them down to 120 °C and subsequently in a desiccator to reach room temperature. The mixtures were then crushed and packed into one-side-sealed platinum (Pt) tubes with dimensions of about 12 mm in length, 3.2 mm in outer diameter, and 0.2 mm in wall thickness. The open end of the Pt tubes was gently crimped to remove the air and welded into capsules using an electric arc welder to ensure gas-tight condition. The integrity of the welding was checked with an optical microscope before the main experiments. The samples with the starting composition of 20 mol % K_2O and 80 mol % MgO were prepared for thermal analysis and equilibration/quenching experiments.

5.2.2 Thermal Analysis

DSC/TGA measurements were conducted using a Jupiter STA 449 F3 thermal analyzer under an argon flowing atmosphere at a rate of 20 $mL \cdot min^{-1}$. Sealed Pt capsule was placed inside an Al_2O_3 crucible with an outer diameter of 6.8 mm and a capacity of 85 μL for the DSC/TGA measurements. The heating and cooling cycles were performed at a rate of 10 $K \cdot min^{-1}$. TGA was simultaneously performed to confirm no leakage of the sealed capsules during the experiments. Three samples were tested in the thermal analysis. Two heating and cooling cycles were run for each sample to obtain reliable and reproducible results. Temperature and sensitivity calibrations were conducted by measuring the melting temperatures and enthalpies of the following eight reference materials: Indium (In), tin (Sn), bismuth (Bi), zinc (Zn), aluminum (Al), silver (Ag), gold (Au), and nickel (Ni). The reliability of the thermal analysis using sealed Pt capsules was confirmed in the previous study [20].

5.2.3 Equilibration/Quenching Method

For the equilibration experiments, a muffle box furnace (ST-1700C, SentroTech, $MoSi_2$ heating elements) was used. B-type thermocouple ($Pt_{30}Rh$-Pt_6Rh) was located at about 10 mm away from the sample. The temperature of the furnace was controlled within ± 1 °C by a PID controller connected to the thermocouple. The temperature of the furnace was calibrated by melting diopside mineral ($CaMgSi_2O_6$, melting point at 1392 °C [21]). For each equilibration experiment, several Pt capsules containing the K_2O-MgO mixtures were placed in a porous Al_2O_3 holder at the hot zone of the furnace. Equilibration experiments were carried out at 700 °C for 167 hours, 800 and 950 °C for 66 hours. After the equilibration process, the samples contained in Pt capsules were immediately quenched in cold water, mounted in epoxy resin and polished with lapping oil (water-

free lubricant) just before phase characterization to avoid the hydration of K_2O. For the transportation to characterization, the polished samples were put in a glass vial filled with desiccants in a vacuumed desiccator.

Phase characterization was conducted using X-Ray Diffractometer (Bruker D8 Discover, Madison, WI, Cu *K*α-radiation) equipped with VANTEC detector. All XRD profiles were identified with the Powder Diffraction Files (PDF) of the International Centre for Diffraction Data (ICDD) using the DIFFRAC.EVA software package (Bruker AXS, Karlsruhe, Germany, 2000).

5.3 Thermodynamic Models

5.3.1 Stoichiometric Compounds

The Gibbs energy of a stoichiometric compound is described as:

$$G_T^o = \Delta H_{298.15K}^o + \int_{298.15K}^{T} C_P dT - T(S_{298.15K}^o + \int_{298.15K}^{T} C_P/T dT) \quad (1)$$

where $\Delta H_{298.15K}^o$ and $S_{298.15K}^o$ are the standard enthalpy of formation and standard entropy at 298.15 K, respectively; C_P is the heat capacity as a function of temperature; T is the absolute temperature.

If no thermodynamic data of binary and ternary solid compounds were available, the $S_{298.15K}^o$ and C_P of compounds were first approximated using the Neumann-Kopp rule (NKR) using the pure substance data of K_2O, MgO, and SiO_2 from the FToxid database [19]. In the NKR, SiO_2 polymorphs were selected based on the structure of each ternary compound. Then, the $\Delta H_{298.15K}^o$ of the solid compounds were optimized to reproduce the phase diagram data.

5.3.2 Liquid Solution

The Modified Quasichemical Model (MQM) in the pair approximation [22] was employed to express the Gibbs energy function of the liquid oxide phase. The MQM takes into account the short-range ordering (SRO) of second-nearest-neighbor cations in the oxide melt. The quasichemical reaction considered in the binary oxide melt is:

$$(A-A)+(B-B)=2(A-B);\ \ \Delta g_{A-B} \tag{2}$$

where A and B are the cationic species in solution; $(A-B)$ represents a second-nearest-neighbor pair of A and B cations with a common O^{2-} anion; Δg_{A-B} is the Gibbs energy of the reaction, which is a model parameter. Δg_{A-B} can be expanded as functions of pair fractions and temperature:

$$\Delta g_{A-B}=\Delta g^{o}_{AB}+\sum_{i\geq 1} g^{i0}_{AB}X^{i}_{AA}+\sum_{j\geq 1} g^{0j}_{AB}X^{j}_{BB} \tag{3}$$

where Δg^{o}_{AB}, g^{i0}_{AB}, and g^{0j}_{AB} are parameters, which can be a function of temperature; X_{AA} and X_{BB} are the pair fractions of $(A-A)$ and $(B-B)$, respectively.

The Gibbs energy of the liquid solution is expressed as:

$$G^{sol}=(n_A g^{o}_A+n_B g^{o}_B)-T\Delta S^{conf}+(n_{AB}/2)\Delta g_{A-B} \tag{4}$$

where n_i and g^{o}_i are the number of moles and the molar Gibbs energy of pure component *i*, respectively; n_{AB} is the number of moles of $(A-B)$ pairs; ΔS^{conf} is the configurational entropy of the solution expressed as a function of random distribution of quasichemical pairs based on one-

dimensional Ising model [23]. The details of the thermodynamic equations for the MQM can be found in Ref. [22].

The SRO behavior in the liquid solution can be well described by setting the coordination numbers of cations. In this work, the coordination numbers of K^+ (Z_{KK}^{K}), Mg^{2+} (Z_{MgMg}^{Mg}), and Si^{4+} (Z_{SiSi}^{Si}) are set to be 0.6887, 1.3774, 2.7549, respectively. The coordination numbers are consistent with those used in the molten oxide database (FToxid) of the FactSage software [19].

Once each binary solution is optimized, the Gibbs energy of the ternary solution can be calculated using a so-called geometric interpolation technique. Kohler and Toop-type models are commonly used to express symmetric and asymmetric ternary systems, respectively [24]. In the K_2O-MgO-SiO_2 system, Δg_{K-Si} and Δg_{Mg-Si} are very negative (strong SRO behavior) while Δg_{K-Mg} shows an ideal solution behavior. Hence, the ternary Gibbs energy was calculated using the asymmetric Toop interpolation technique with SiO_2 as an asymmetric component. The details of the interpolation method are well described in Ref. [25]. The details of the MQM equations for the ternary system considering the interpolation model can be found in Ref. [24]. In the present study, the model parameters of Δg_{K-Si} and Δg_{Mg-Si} were taken from the previous studies for the K_2O-SiO_2 and MgO-SiO_2 systems [20, 26], respectively. The binary model parameter of Δg_{K-Mg} was set to be zero (ideal solution) based on the present optimization study. Small ternary model parameters were used to reproduce the phase diagram data more accurately.

After a preliminary optimization study, it was found that the phase diagram, especially in the SiO_2-rich region (liquidus of SiO_2 and the primary region of $MgSiO_3$ pyroxene) in the ternary K_2O-MgO-SiO_2 system, cannot be easily reproduced by the liquid solution with three components K_2O,

MgO, and SiO_2. In particular, the liquidus slope of SiO_2 in the K_2MgSiO_4-SiO_2 section clearly shows a similarity to that of the $NAlO_2$-SiO_2 system where N = Na, K, and Li alkali elements. It is well-known that the liquidus of SiO_2 in the $NAlO_2$-SiO_2 system can be reproduced with consideration of the so-called charge compensation phenomenon [27]. That is, the formation of a $NAlO_2$ type associate component replacing SiO_2 is used for the modeling of the liquid phase in alkali aluminosilicate systems [28, 29]. In this study, a similar associate, K_2MgSiO_4, was considered for the charge compensation in the high SiO_2 region. The coordination number of K_2MgSi^{8+} was set to be twice the coordination number of Si^{4+}. In this ternary system, the K_2MgSiO_4 associate was considered instead of K_2MgO_2 because the K_2O-MgO solution is an ideal solution, while solid K_2MgSiO_4 has the same meta-oxide structure as $NAlO_2$ in an alkali aluminate system. Then, the Gibbs energy of liquid K_2MgSiO_4 and the corresponding binary and ternary interaction parameters were optimized as additional model parameters of the liquid solution.

In summary, the liquid solution in the K_2O-MgO-SiO_2 system was modeled using a quaternary K_2O-MgO-SiO_2-K_2MgSiO_4 solution. The Gibbs energies of the quaternary solution were calculated using the interpolation model [25]. Two subgroups were assumed for the liquid components; acid group: SiO_2 and basic group: K_2O, MgO, and K_2MgSiO_4. When two basic group components and one acid group component were mixed in a ternary solution, the Toop interpolation technique was used with the acid component as an asymmetric component, and for a ternary solution composed of all basic group components, the symmetric Kohler interpolation technique was used. The Gibbs energy of a quaternary solution can be calculated from sub-ternary solutions as described in Ref. [25].

5.3.3 Solid Solutions

There are four solid solution phases in the K_2O-MgO-SiO_2 system. High- and low-temperature K_2MgSiO_4 (meta-oxide), high-temperature $K_2MgSi_3O_8$ (kalsilite-like), and low-temperature $K_2MgSi_3O_8$ (nepheline-like). These K_2MgSiO_4 and $K_2MgSi_3O_8$ solid solutions have an excess solubility of SiO_2.

The dissolution mechanism of SiO_2 into low-temperature K_2MgSiO_4 meta-oxide (KMS) is adopted from Grey *et al*.'s study [30]. In fact, this is the only comprehensive crystal structure study for the meta-oxide solid solution which revealed the dissolution mechanism of SiO_2. According to the study by Grey *et al*. for β- and γ'-$NaFeO_2$ meta-oxide, a coupled substitution of $Si^{4+} \leftrightarrow Fe^{3+} + Na^+$ occurs in the dissolution of SiO_2 in $NaFeO_2$. In particular, vacancy (Va) is coupled with Si^{4+} at adjacent interstitial site when Si^{4+} substitutes Fe^{3+} in the framework of tetrahedra and remove Na^+ from the framework cavities. That is, Va is not formed randomly in the solution but clearly associated to the position of Si^{4+} during the SiO_2 dissolution in $NaFeO_2$. This dissolution mechanism was previously modeled by Moosavi-Khoonsari and Jung [31] using the Compound Energy Formalism (CEF) [32] with $(NaFe^{4+}, SiVa^{4+})O_2$ model structure. The crystal structure of potassium-containing meta-oxides, such as K_2MgSiO_4, $KAlO_2$, $KGeO_2$, and $KFeO_2$, have their low-temperature polymorphs of orthorhombic structure, which is the same crystal structure as β- and γ'-$NaFeO_2$. The solution mechanism of the high-temperature polymorph of K_2MgSiO_4 meta-oxide was assumed to be the same as the low-temperature one because of structural similarity and lack of experimental data on the solution mechanism. Therefore, both low- and high-temperature polymorphs of K_2MgSiO_4 were described in this study using the CEF with $(K_2Mg^{4+}, VaSi^{4+})SiO_4$. That is, the molar Gibbs energy of the K_2MgSiO_4 solution is expressed by:

$$G^{sol\ln} = (y_i G_i^o + y_j G_j^o) + RT(y_i \ln y_i + y_j \ln y_j) + \sum_{n\geq 0}{}^{n}L_{ij} y_i y_j (y_j - y_i)^n \quad (5)$$

where G_i^o is the molar Gibbs energy of the end-member *i* of the solution; y_i is the site fraction of the species *i*; *R* is the gas constant; ${}^{n}L_{ij}$ are the excess interaction parameters. For the K_2MgSiO_4 solution, y_i and y_j are the site fractions of K_2Mg^{4+} and $VaSi^{4+}$.

The $K_2MgSi_3O_8$ solid solutions were described by the MQM. Low-temperature $K_2MgSi_3O_8$ has the structure of nepheline ($NaAlSiO_4$), and forms a solid solution with $NaAlSiO_4$ and $KAlSiO_4$. Therefore, the consistent thermodynamic solution model for $NaAlSiO_4$ was adopted. At low temperatures, there is a small but noticeable solubility of SiO_2 in these three types of nepheline structures: $K_2MgSi_3O_8$, $NaAlSiO_4$, and $KAlSiO_4$ [12, 33]. An extensive solubility between $KAlSiO_4$ and $K_2MgSi_3O_8$ was found [12], and $KAlSiO_4$ and $NaAlSiO_4$ form a complete solid solution [34, 35]. Therefore, these compounds with the nepheline structure should be modeled consistently. Previously, $NaAlSiO_4$ with excess SiO_2 solubility was modeled using the MQM [33]. In this study, this $K_2MgSi_3O_8$ nepheline solution was modeled by the MQM with a $K_2MgSi_3O_8$-Si_2O_4 solid solution. The high-temperature polymorph of $K_2MgSi_3O_8$, which has a kalsilite-like structure, was described using the same framework as the nepheline solution. At high temperatures, there is a limited solubility between $K_2MgSi_3O_8$ and $KAlSiO_4$ [12] and between $KAlSiO_4$ and $NaAlSiO_4$ [34, 35], but no mutual solubility between $K_2MgSi_3O_8$ and $NaAlSiO_4$.

5.4 Experimental Results

A possible formation of K_6MgO_4 in the K_2O-MgO system was previously reported in Refs. [10, 11]. But no information about the thermal stability of this compound has been reported. The main focus of the present experimental study on the K_2O-MgO system was the determination of the

peritectic invariant reaction of Liquid + MgO → K_6MgO_4. Starting materials of 20 mol % K_2O and 80 mol % MgO were used to minimize the experimental difficulties due to the extremely hygroscopic and volatile nature of K_2O.

The DSC results are summarized in Table 5.1. The average thermal incident in these measurements is 858 ± 14 °C. The relatively large experimental error range of ± 14.4 °C might result from the existence of some unavoidable hydrate phases (e.g. KOH). During the DSC experiments, no mass loss was recorded by TGA, which confirmed the reliability of this experimental method. To confirm the existence of the K_6MgO_4 compound in the equilibrium phase diagram, the three K_2O-MgO samples were annealed at 700, 800, and 950 °C. The annealing temperatures were set intentionally below and above the DSC transition temperature of 858 °C. The XRD results of these quenched samples are depicted in Fig. 5.1 and the identified equilibrium phases are summarized in Table 5.1. The two samples annealed at lower temperatures (700 °C for 167 hours and 800 °C for 66 hours) show similar XRD patterns, indicating the existence of solid K_6MgO_4 and MgO. The sample equilibrated at 950 °C for 66 hours shows no evidence of K_6MgO_4. The amorphous background in these XRD profiles is due to the epoxy resin and the moisture at the sample surface during the analysis. Since the reaction volume of X-ray beam as well as the exposure time were kept consistent for all three samples, the higher intensity of amorphous background for the 950 °C sample can be concluded as the existence of liquid (glass) phase at this temperature. KOH identified in these samples is the result of hydration of the highly hygroscopic K_2O during sample handling. Thus, according to the XRD results in Fig. 5.1, K_6MgO_4 and MgO are the equilibrium phases at 700 and 800 °C below the DSC transition temperature, and a liquid and MgO are the stable phases at 950 °C above that temperature. It is concluded from the present DSC and

quenching experiments that the peritectic reaction of Liquid + MgO → K_6MgO_4 occurs at 858 ± 14 °C in the K_2O-MgO system.

5.5 Critical Evaluation and Thermodynamic Optimization

All phase diagram and thermodynamic data of the K_2O-MgO and K_2O-MgO-SiO_2 systems available in the literature were critically reviewed. Then, new phase diagram experimental data from this study and all reliable experimental data in the literature were simultaneously considered to obtain a set of thermodynamic functions for all phases in these two systems. The model parameters of the K_2O-SiO_2 [20] and MgO-SiO_2 [26] systems were taken from the previous studies without any modification. The optimized model parameters in this study are listed in Tables 5.2 and 5.3.

5.5.1 The K_2O-MgO System

The optimized phase diagram of the K_2O-MgO system in the present study is plotted in Fig. 5.2 along with all experimental data. There are only two previous studies on the phase diagram experiments of the K_2O-MgO system [10, 11]. Bardin *et al*. [10] annealed K_2O powder in MgO crucibles at 700, 800, and 900 °C for 1 hour. K_2O and MgO mixtures were also annealed in MgO crucibles at 800 °C for 1 to 3 hours. The stable compound K_6MgO_4 was found from XRD analysis, and its crystal structure was analyzed to be hexagonal with possible space group of $P6_3/mmc$, $P6_3mc$, or $P\bar{6}2c$. Later, Darriet *et al*. [11] synthesized the K_6MgO_4 compound through melting K_2O powder in MgO crucibles at 800 °C under dry nitrogen atmosphere. The K_6MgO_4 compound was found to be stable at 800 °C after 3 hours equilibration. With XRD analysis, Darriet *et al*. confirmed the space group of K_6MgO_4 to be $P6_3mc$, as listed in Table 5.4. In these two studies,

the equilibration time was only up to 3 hours below the solidus temperature, and open crucible was employed. The melting/decomposition temperature of the K_6MgO_4 compound was not reported in their studies. The present experimental study confirms the peritectic melting of K_6MgO_4 into MgO and liquid at 858 ± 14 °C using the DSC and quenching experiments. In particular, a sealed Pt capsule was employed to minimize the evaporation and hydration of K_2O during the experiments. Therefore, the present experimental data were considered to be more reliable than the previous study.

No thermodynamic data for the liquid solution are available in the literature. The Gibbs energy of the liquid solution in the K_2O-MgO system is optimized as an ideal solution in this study. The standard enthalpy of formation ($\Delta H^{o}_{298.15K}$) of the K_6MgO_4 compound was reported in the range between -1739.98 and -1617.97 kJ·mol^{-1} [36-39] from first principles calculations. In this study, the $\Delta H^{o}_{298.15K}$ was determined to reproduce the peritectic melting point of K_6MgO_4. The optimized $\Delta H^{o}_{298.15K}$ is -1696.23 kJ·mol^{-1}, which is within the range of results from the first principles calculations. According to the optimized phase diagram in Fig. 5.2, the eutectic reaction of Liquid → K_2O + K_6MgO_4 is calculated at 739.2 °C.

5.5.2 The K_2O-MgO-SiO_2 System

All stable compounds and experimentally investigated isoplethal sections in the K_2O-MgO-SiO_2 system are shown in Fig. 5.3. There are 15 stable phases in the K_2O-MgO-SiO_2 system at 1 atm pressure: liquid, K_2O, MgO, SiO_2 (α- and β-quartz, β-tridymite, β-cristobalite), K_2MgSiO_4 (low- and high-temperature polymorphs), $K_2MgSi_3O_8$ (low- and high-temperature polymorphs), $K_2MgSi_5O_{12}$, $K_2Mg_5Si_{12}O_{30}$, $K_4Mg_2Si_5O_{14}$, and $K_{10}Mg_5Si_{11}O_{32}$. The crystal structures of these solid compounds are summarized in Table 5.4.

The phase diagram of the K_2O-MgO-SiO_2 system was first investigated by Roedder [9] using equilibration/quenching experiments followed by phase analysis using petrographic microscopy and XRD technique. 133 compositions of the starting materials were investigated in the SiO_2-$MgSiO_3$-K_2MgSiO_4-K_2SiO_3 quadrilateral. Four stable ternary solids were found in his study: K_2MgSiO_4 (KMS), $K_2MgSi_3O_8$ (KMS_3), $K_2MgSi_5O_{12}$ (KMS_5), and $K_2Mg_5Si_{12}O_{30}$ (KM_5S_{12}). The melting temperatures of these compounds are listed in Table 5.5. The melting temperature of KMS at 1650 °C had a large error range due to experimental difficulties related to highly volatile K_2O at high temperatures. The error range of KMS melting temperature was not well specified by the author. MgO was detected near the melting point of KMS, which indicates possible incongruent melting behavior of KMS. KMS_3 and KMS_5 were reported to melt congruently at 1134 ± 1 and 1089 ± 1 °C, respectively. KM_5S_{12} melted incongruently at 1174 ± 2 °C (KM_5S_{12} → Liquid + $MgSiO_3$). Besides the four ternary compounds mentioned above, Roedder also proposed the possible formation of KMS_2. Roedder reported 13 invariant reactions in this ternary system with reasonable accuracy based on his phase diagram measurements in a wide range of compositions. The details of these invariant reactions are listed in Table 5.6. In his study, tridymite SiO_2 was identified in the temperature range where quartz SiO_2 should be stable. Roedder explained that K_2O and MgO might dissolve into the tridymite lattice and extend the primary phase field of tridymite metastably, which is similar to the metastable tridymite phase with large solubility of Na_2O and CaO reported by Lukesh [40]. The reported primary phase field of $MgSiO_3$ by Roedder was rather strange, it encroaches upon the area where SiO_2 was expected based on the systematic trend in other alkali alkaline-earth silicate systems.

Roth [12] conducted equilibration/quenching experiments and XRD analysis in the KMS-SiO_2 section. Except the region near KMS_3, Roth reported similar liquidus as Roedder in this system.

Besides KMS, KMS_3, and KMS_5 compounds, which were already reported by Roedder [9], two more ternary compounds $K_4Mg_2Si_5O_{14}$ ($K_2M_2S_5$) and $K_{10}Mg_5Si_{11}O_{32}$ ($K_5M_5S_{11}$) were found by Roth. The melting behaviors of these two compounds are shown in Table 5.5. $K_2M_2S_5$ and $K_5M_5S_{11}$ compounds can be the possible other stoichiometric phases close to KMS_2 composition mentioned by Roedder. Roth reported incongruently melting KMS_3 at 1070 °C: $KMS_3 \rightarrow K_2M_2S_5$ + Liquid. $K_2M_2S_5$ compound was defined as an orthorhombic phase because it showed a similar XRD pattern as $KFeSiO_4$ [41]. $K_5M_5S_{11}$ compound was identified as a tetragonal phase. However, the details of the structural information of $K_2M_2S_5$ and $K_5M_5S_{11}$ compounds were not provided in his study or other literature.

Dollase [16] found a first order transition of KMS at 508 °C using DSC. The low- and high-temperature polymorphs of KMS were determined using XRD to have an orthorhombic structure with space group of $Pca2_1$ and a cubic structure with space group of $F\bar{4}3m$, respectively. More recently, Thompson *et al*. [42] reported the cubic structure ($F\bar{4}3m$) using Roedder's XRD profile. Many stoichiometric compounds related to the cristobalite-type structure were also studied by Thompson *et al*. and the reliability of the structural data of KMS was confirmed. Roedder [9] reported two polymorphs for $K_2MgSi_3O_8$ (KMS_3); pseudohexagonal high-temperature polymorph (α-KMS_3) and orthorhombic or pseudohexagonal low-temperature polymorph (β-KMS_3). There was no noticeable heat incident in his DTA results. Later, Roth [12] reported a monoclinic structure for α-KMS_3 and hexagonal structure for β-KMS_3 using XRD. The transition temperature was determined at 900 °C based on equilibration/quenching experiments. It should be noted that $KAlSiO_4$ and $NaAlSiO_4$, which are structural counterparts of KMS_3, are known to have first-order transitions [33, 43]. Therefore, in the present optimization, the polymorphic transition of KMS_3 is reproduced at 899.9 °C based on the results of Roth.

The structure of $K_2MgSi_5O_{12}$ compound (KMS_5) was first reported as monotropic cubic (BCC) by Roedder [9]. Even though two polymorphs were indicated in the XRD results, the transition was rather gradual in the DTA results and no clear transition temperature was found. Later, Bell *et al*. [14] and Kohn *et al*. [44] studied the order-disorder transition (second order transition) of KMS_5 using Transmission Electron Microscopy (TEM), Magic Angle Spinning Nuclear Magnetic Resonance (MAS NMR), and synchrotron XRD. The low-temperature polymorph was found to have an ordered monoclinic structure ($P2_1/c$), and the high-temperature polymorph have a disordered cubic structure ($Ia\,3d$). Redfern and Henderson [15] reported high-temperature orthorhombic KMS_5 with $Pbca$ structure from XRD analysis and its incongruent melting in between 800 and 900 °C, which is much lower than the congruent melting point of 1089 ± 1 °C reported by Roedder [9]. In this study, the second order transition of KMS_5 was considered and the congruent melting of KMS_5 by Roedder was reproduced at 1070.3 °C.

Roedder [9] proposed that $K_2Mg_5Si_{12}O_{30}$ compound (KM_5S_{12}) has a hexagonal structure, because crystallization occurred as hexagonal tablets and the optical properties of KM_5S_{12} were similar to hexagonal β-quartz (SiO_2). Later, the hexagonal structure of KM_5S_{12} was confirmed by Seifert and Schreyer [13] with a space group of $P6/mcc$ based on XRD analysis. Roedder reported that KM_5S_{12} melted incongruently at 1174 ± 2 °C. Seifert and Schreyer described the incongruent melting of KM_5S_{12} at about 1180 °C. Although the experiments by Seifert and Schreyer were performed at high pressure, the estimated melting temperature is in good agreement with Roedder's results.

Roth [12] found two compounds $K_4Mg_2Si_5O_{14}$ ($K_2M_2S_5$) and $K_{10}Mg_5Si_{11}O_{32}$ ($K_5M_5S_{11}$) between KMS and KMS_3. Roth reported that $K_2M_2S_5$ and $K_5M_5S_{11}$ have orthorhombic and tetragonal

structures, respectively. Small solubility of SiO_2 in $K_2M_2S_5$ (≤ 5 mol %) and in $K_5M_5S_{11}$ (≤ 1.5 mol %) were also determined at temperature ranges between 970 and 1150 °C and 777 to 1160 °C, respectively. However, they are considered as stoichiometric compounds in the present study for the sake of simplicity. Roth reported that $K_5M_5S_{11}$ melted incongruently into KMS and liquid at 1160 °C. $K_2M_2S_5$ melted at 1150 °C, but it was uncertain to determine congruent/incongruent melting. In this study, the stable temperature ranges of $K_2M_2S_5$ and $K_5M_5S_{11}$ are calculated to be from 973.5 to 1145.0 °C and from 782.7 to 1160.7 °C, respectively, which are in good agreements with the results of Roth [12].

The optimized phase diagram of the K_2MgSiO_4-SiO_2 system is calculated in Fig. 5.4 along with experimental data. As this section contains all ternary compounds except KM_5S_{12}, the reproduction of this section is essential for the accurate modeling of this ternary system. A large solubility of SiO_2 into KMS was found up to about 30 mol % at 1160 °C and a small solubility of SiO_2 was found in KMS_3. Thus, the compound $K_2MgSi_2O_6$ (KMS_2) proposed by Roedder [9] can be concluded as a part of this solid solution. Due to $K_2M_2S_5$ and $K_5M_5S_{11}$ compounds, the liquidus between KMS and KMS_3 region reported by Roth [12] was slightly higher than the result of Roedder. In the optimization of this study, the liquidus data reported by Roedder were in general considered to be reliable experimental data for most of the composition range. However, two compounds $K_2M_2S_5$ and $K_5M_5S_{11}$ reported by Roth were included as stable phases, and the solubility of SiO_2 in KMS and KMS_3 were adopted from Roth as well. As shown in Fig. 5.4, the stable phase fields, including the solid solutions of KMS and KMS_3, are reasonably well reproduced based on the experimental data from Roedder [9] and Roth [12]. Even though the small solubility range of KMS_3 has no significant effect in the K_2O-MgO-SiO_2 ternary system, this should be taken into account in the optimization of multi-component solid solutions in the K_2O-

MgO-Al_2O_3-SiO_2 system. The melting/decomposition temperatures of the ternary compounds, KMS, $K_5M_5S_{11}$, $K_2M_2S_5$, KMS_3, and KMS_5, in this system show good agreement with experimental data as shown in Table 5.5. In the optimization of this study, the incongruent melting behavior of KMS (K_2MgSiO_4 → Liquid + MgO) was calculated to occur at 1650.3 °C, which is in good agreement with the reported temperature of 1650 °C. KMS_3 was calculated to melt congruently, which agrees with the experimental observation of Roedder, instead of incongruent melting proposed by Roth. Roth reported about 5 mol % solubility of SiO_2 in $K_2M_2S_5$. This solubility can alter the melting behavior of KMS_3 into incongruent melting. However, due to insufficient structural and solution mechanism information of KMS_3 in Roth's study, the melting behavior of KMS_3 was reproduced based on Roedder's results. Roedder reported the melting point of KMS_3 with 2 days of equilibration and also reported the KMS_3 liquidus in other pseudo-binary sections. The discrepancy remaining in the melting behavior of KMS_3 can be resolved when more experimental data are available in the future.

As discussed in section 5.3.2, without introducing the associate K_2MgSiO_4 it was very difficult to describe the liquidus of SiO_2 at about 0.75 to 0.9 mole fraction of SiO_2 (Fig. 5.4). That is, the liquidus of SiO_2 was less steep without this associate. With consideration of thermodynamic calculations in higher order systems, the Gibbs energy of K_2MgSiO_4 was set very positive compared to the solid K_2MgSiO_4 to maintain liquid K_2MgSiO_4 associate species at its stoichiometric composition to be less than 10^{-6} mole fraction in the liquid solution. That is, nearly no liquid K_2MgSiO_4 associate forms in the calculation unless strong binary parameters with K_2MgSiO_4 were given. To reproduce the liquidus of SiO_2, negative binary interaction parameters between K_2MgSiO_4 and SiO_2 were introduced.

The isoplethal sections, $MgSiO_3$-$K_2Si_7O_{15}$, KM_5S_{12}-KMS_5, M_2S-KMS_5, M_2S-KMS_3, KMS_5-KS_4, KMS_5-KS_2, KMS_3-KS_2, KMS-KS_2, and KMS-KS, reported by Roedder [9] are compared with the present optimization in Fig. 5 (a) to (i), respectively. Overall, all the phase diagrams of these sections were well reproduced in this study within 2 mol % error in terms of K_2O, MgO, and SiO_2 amount. In the $MgSiO_3$-$K_2Si_7O_{15}$ section shown in Fig. 5.5 (a), the incongruent melting behavior of KM_5S_{12} compound at 1174 °C (KM_5S_{12} → MS + Liquid) is well reproduced. In the KM_5S_{12}-KMS_5 section shown in Fig. 5.5 (b), the liquidus between KM_5S_{12} and KMS_5 are well represented as well. The liquidus of M_2S in Fig. 5.5 (c) and (d) also show good agreement with the experimental data. The calculated liquidus of KMS_5 in Fig. 5.5 (e) is in good agreement with the experimental data considering the possible error in the experiment. In Fig. 5.5 (f), the liquidus of KMS_3 by Roedder at 0.5 to 0.6 mole fractions of KS_2 in the section is based on a simple speculation. In his real experimental data for this section, only liquidus of KMS_5 was measured at low KS_2 region and no liquidus of KMS_3 was determined. Therefore, the accuracy of the phase diagram by Roedder in the middle of this section is doubtful. The eutectic points in Fig. 5.5 (g) to (i) are also well reproduced considering the error range in experiments.

Liquidus projection of the K_2O-MgO-SiO_2 system is calculated in Fig. 5.6 (a) and (b). All the invariant reactions involving liquid are listed in Table 5.6 compared with the experimental ones from Roedder [9]. As can be seen in Table 5.6, the invariant reactions are well reproduced within 2 mol % error of the concentrations of K_2O, MgO, and SiO_2 and in a temperature range of ± 35 °C except the reaction P. Roedder reported noticeable metastable solubility of K_2O and MgO in tridymite. The transition temperature of tridymite to quartz could be suppressed in his study than ideal transition temperature. The measured invariant temperature for reaction P involving tridymite was calculated to be 1019.1 °C in this study, which is about 55 °C higher than the reported value

by Roedder. This discrepancy possibly comes from the inequilibrium condition of the experiments in this composition range. The primary crystalline region of proto-enstatite $MgSiO_3$ reaches close to 80 mol % SiO_2 region as can be seen in Fig. 5.6 (a). Such an extension of $MgSiO_3$ primary phase region is very exceptional among all ternary oxide systems containing $MgSiO_3$. In fact, Roedder [9] also pointed out that this was rather strange and unexpected results. In the preliminary modeling in this study, when the liquid solution was described using the MQM with three components: K_2O, MgO, and SiO_2, it was very difficult to reproduce such an extended primary region of $MgSiO_3$. In the final modeling in this study, this primary region was reasonably well reproduced with the help of a ternary parameter related to the K_2MgSiO_4 associate. Thus, the introduction of the K_2MgSiO_4 associate is very necessary to reproduce the phase relationships in the SiO_2-rich region in this ternary system.

Limited thermodynamic data for solid and liquid phases were experimentally determined in this system. No enthalpy of formation of ternary compounds were measured experimentally. Jain *et al*. [38] estimated $\Delta H^o_{298.15K}$ of KMS and KMS_5 using first principles calculations. Dollase [16] measured the enthalpy of transition (ΔH^o_{tr}) of KMS using DSC and reported ΔH^o_{tr} to be 1965.3 $J \cdot mol^{-1}$ at 508 °C. Stebbins *et al*. [45] reported the heat capacity (C_P) of glass at KMS_4 composition (16.88 mol % K_2O, 16.44 mol % MgO, and 66.68 mol % SiO_2) using DSC up to 557 °C.

In the present study, $S^o_{298.15K}$ and C_P of ternary compounds were determined using the Neumann-Kopp rule (NKR), and $\Delta H^o_{298.15K}$ were determined to reproduce the phase diagram. Only $S^o_{298.15K}$ of $K_2M_2S_5$ and $K_5M_5S_{11}$ compounds were slightly changed from the values estimated using NKR to reproduce the thermal stability region in the KMS – SiO_2 section (see Fig. 5.4). The optimized

$\Delta H^o_{298.15K}$ of KMS and KMS_5 in the present study have about 0.6 % and 2.3 % deviations, respectively, from the results of first principle calculations by Jain *et al*. [38]. The transition enthalpy (ΔH^o_{tr}) of KMS from Dollase [16] was employed without any modification. ΔH^o_{tr} of KMS_3 was estimated in the present study. As KMS and KMS_3 compounds are structurally very close to $KAlO_2$ and $KAlSiO_4$, respectively, the difference of ΔH^o_{tr} between KMS_3 and $KAlSiO_4$ [43] was assumed to be the same as the one between KMS [16] and $KAlO_2$ [46]. Fig. 5.7 shows the molar C_P of glass at KMS_4 composition determined by Stebbins *et al*. [45]. The C_P of liquid at KMS_4 composition and C_P of solids KMS_3 and KMS_5 were also calculated from the present thermodynamic modeling. As can be seen in Fig. 5.7, the calculated liquid C_P from the present study is higher than the experimentally measured glass C_P. This makes sense considering that C_P of glass below the glass transition temperature should be similar as C_P of solid and lower than theoretical liquid C_P. In fact, the molar C_P of glass determined by Stebbins *et al*. [45] is very close to the C_P of KMS_3 and KMS_5 compounds from NKR. This confirmed that the estimated C_P of ternary solid compounds are reasonable.

Based on the present optimization, the thermodynamic properties of liquid can be calculated. The iso-activity contours of SiO_2 (cristobalite), MgO (solid), and K_2O (liquid) in the ternary system at 1600 °C are predicted in Fig. 5.8, and the liquid enthalpies of mixing at 1600 °C are calculated and compared with results of the CaO-MgO-SiO_2 system [47] in Fig. 5.9. Iso-activities contours of cristobalite SiO_2 and liquid K_2O show typical trends. However, iso-activity lines of solid MgO show rather unexpected trend. Binary K_2O-MgO liquid is an ideal solution while the MgO-SiO_2 melt has a strong short-range ordering at Mg_2SiO_4 composition. Therefore, if the activity of MgO

in this ternary system varies linearly between both MgO-containing binary systems, the activity of MgO where SiO_2 content is above orthosilicate composition should be very small; for example, the activity of MgO in the CaO-MgO-SiO_2 system decreases drastically at SiO_2 content above orthosilicate composition. But the calculated iso-activity contours of MgO are largely extended toward SiO_2 corner. This means that a strong negative Gibbs energy of mixing exist in this ternary liquid. This is the reason that the primary crystalline region of $MgSiO_3$ is largely extended toward SiO_2 corner.

In fact, the calculated enthalpies of mixing in Fig. 5.9, show strong negative deviations from an ideal solution behavior. The enthalpy of mixing for the K_2MgO_2-SiO_2 melt shows a very negative deviation from an ideal solution. The enthalpies of mixing at orthosilicate and metasilicate sections are also much negative in comparison to nearly ideal behavior in the CaO-MgO-SiO_2 system. This is rather unexpected result. Because both K_2O and MgO are strong basic components, and the K_2O-MgO melt is an ideal solution. One could expect that almost an ideal mixing in the ternary melt along iso-SiO_2 composition; for example, it is the case for the CaO-MgO-SiO_2 melt. A short-range ordering in liquid oxide solution becomes more significant in the ternary K_2O-MgO-SiO_2 melt. The exact reason for this behavior is not known yet. But this phenomenon can explain why we need a ternary associate component in the present liquid modeling, and why many ternary compounds form along the K_2MgO_2-SiO_2 section. More fundamental study on melt structure and chemistry of this ternary system would be expected in the future to answer this short-range ordering behavior.

In the present study, K_2MgSiO_4 associate was introduced in the modeling of liquid phase. As discussed above, this associate was very necessary to reproduce the liquidus of SiO_2 and primary

crystalline area of $MgSiO_3$. No study on the structure of liquid has been performed in this ternary system. It can be an interesting research topic to investigate the charge compensation effect in this ternary K_2O-MgO-SiO_2 melt. Very limited experimental study is available for the thermodynamic properties of liquid and solids in this ternary system. The optimized thermodynamic data in the present study can be helpful to elucidate the thermodynamics of this ternary system.

5.6 Summary

New key experiments and thermodynamic optimization for the K_2O-MgO and K_2O-MgO-SiO_2 systems were performed. The peritectic reaction of Liquid + MgO → K_6MgO_4 in the K_2O-MgO system was successfully determined at 858 ± 14 °C using equilibration/quenching and DSC experiments using sealed Pt capsules. Thermodynamic optimization of the K_2O-MgO and K_2O-MgO-SiO_2 systems was conducted based on the present experimental data as well as all available and reliable experimental data in the literature. In order to reproduce the phase diagram in the ternary system, the MQM with K_2O, MgO, SiO_2, and K_2MgSiO_4 associate component were used for liquid phase modeling. The activities and enthalpies of mixing of ternary liquid phase were predicted from the optimized Gibbs energy function of liquid phase. A strong short-range ordering behavior and possible charge compensation effect in the ternary oxide melt were found from the present study.

Acknowledgments

Financial supports from Tata Steel Europe, POSCO, Nucor Steel, Rio Tinto Iron and Titanium, Hyundai Steel, Nippon Steel and Sumitomo Metals Corp., JFE Steel, Voestalpine, RHI, and the Natural Sciences and Engineering Research Council of Canada are gratefully acknowledged.

Authors (D.-G. Kim and B. Konar) also acknowledge the McGill Engineering Doctorate Award (MEDA) from McGill University.

References

[1] Y.R. Krass, World Production of Steel and Magnesia Refractories: State of the Art and Trends of Development, Refractories and Industrial Ceramics 42(11) (2001) 417-425.
[2] Y.R. Krass, Production technology of wear-resistant magnesian refractories in the context of contemporary trends in developing steel production and other processes, ecology, resource saving, and computerization, Refract. Ind. Ceram. 43(11-12) (2002) 374-382.
[3] K. Tsujikawa, M. Ohashi, Rayleigh Scattering in K2O–MgO–SiO2 and Na2O–B2O3–SiO2 Glasses, Optical Fiber Technology 6(1) (2000) 74-82.
[4] K. Tsujikawa, M. Ohashi, K. Tajima, Optical properties of multicomponent oxide glasses and glass fibers, Electronics and Communications in Japan (Part I: Communications) 86(12) (2003) 21-35.
[5] V. Saraswati, K.V.S.R. Anjaneyulu, Crystallization of mica in the potassium oxide-silicon dioxide-magnesium oxide-magnesium fluoride glass system, Bull. Mater. Sci. 13(4) (1990) 283-91.
[6] L. Song, J. Wu, Z. Li, X. Hao, Y. Yu, Crystallization mechanisms and properties of α-cordierite glass–ceramics from K2O–MgO–Al2O3–SiO2 glasses, Journal of Non-Crystalline Solids 419 (2015) 16-26.
[7] X. Ma, H. Ma, J. Yang, Sintering Preparation and Release Properties of K2MgSi3O8 Slow-Release Fertilizer Using Biotite Acid-Leaching Residues as Silicon Source, Industrial & Engineering Chemistry Research 55(41) (2016) 10926-10931.
[8] A.S. Mangrich, L.C. Tessaro, A.D. Anjos, F. Wypych, J.F. Soares, A slow-release K+ fertilizer from residues of the Brazilian oil-shale industry: synthesis of kalsilite-type structures, Environ. Geol. (Berlin, Ger.) 40(8) (2001) 1030-1036.
[9] E.W. Roedder, The system K2O-MgO-SiO2. I. II, Am. J. Sci. 249 (1951) 81-130,224-48.
[10] J.C. Bardin, M. Avallet, M. Cassou, New oxidized ternary compound of magnesium. Potassium magnesium oxide (K6MgO4), C. R. Acad. Sci., Ser. C 278(10) (1974) 709-12.
[11] B. Darriet, M. Devalette, F. Roulleau, M. Avallet, Crystal structure of hexapotassium magnesium oxide, Acta Crystallogr., Sect. B B30(11) (1974) 2667-9.
[12] R.S. Roth, Phase equilibriums research in portions of the potassium oxide-magnesium oxide-iron(III)oxide-aluminum oxide-silicon dioxide system, Adv. Chem. Ser. 186 (1980) 391-408.
[13] F. Seifert, W. Schreyer, Stability relations of K2Mg5Si12O30, an end member of the merrihueite-roedderite group of meteoritic minerals, Beitr. Mineral. Petrol. 22(3) (1969) 190-207.
[14] A.M.T. Bell, C.M.B. Henderson, S.A.T. Redfern, R.J. Cernik, P.E. Champness, A.N. Fitch, S.C. Kohn, Structures of synthetic K2MgSi5O12 leucites by integrated x-ray powder diffraction, electron diffraction and 29Si MAS NMR methods, Acta Crystallogr., Sect. B: Struct. Sci. B50(1) (1994) 31-41.
[15] S.A.T. Redfern, C.M.B. Henderson, Monoclinic-orthorhombic phase transition in the K2MgSi5O12 leucite analog, Am. Mineral. 81(3-4) (1996) 369-74.
[16] W.A. Dollase, Transformations of the stuffed cristobalites, K2MSiO4, M = Mg, Zn, Co, Cd, with temperature and composition, Phys. Chem. Miner. 25(5) (1998) 389-392.

[17] E. Yazhenskikh, T. Jantzen, K. Hack, M. Mueller, Critical thermodynamic evaluation of oxide systems relevant to fuel ashes and slags: Potassium oxide-magnesium oxide-silica, CALPHAD: Comput. Coupling Phase Diagrams Thermochem. 47 (2014) 35-49.
[18] T.M. Besmann, K.E. Spear, Thermochemical modeling of oxide glasses, J. Am. Ceram. Soc. 85(12) (2002) 2887-2894.
[19] C.W. Bale, E. Belisle, P. Chartrand, S.A. Decterov, G. Eriksson, A.E. Gheribi, K. Hack, I.H. Jung, Y.B. Kang, J. Melancon, A.D. Pelton, S. Petersen, C. Robelin, J. Sangster, P. Spencer, M.A. Van Ende, FactSage thermochemical software and databases, 2010-2016, CALPHAD: Comput. Coupling Phase Diagrams Thermochem. 54 (2016) 35-53.
[20] D.G. Kim, M.A. Van Ende, P. Hudon, I.H. Jung, Coupled experimental study and thermodynamic optimization of the K2O-SiO2 system, Submitted to Journal of Non-Crystalline Solids (2017).
[21] I. Barin, Thermochemical Data of Pure Substances, VCH1989.
[22] A.D. Pelton, S.A. Degterov, G. Eriksson, C. Robelin, Y. Dessureault, The modified quasichemical model I - binary solutions, Metall. Mater. Trans. B 31B (2000) 651-659.
[23] E. Ising, Beitrag zur Theorie des Ferromagnetismus, Zeitschrift für Physik 31(1) (1925) 253-258.
[24] A. Pelton, P. Chartrand, The modified quasi-chemical model: Part II. Multicomponent solutions, Metallurgical and Materials Transactions A 32(6) (2001) 1355-1360.
[25] A.D. Pelton, A general "geometric" thermodynamic model for multicomponent solutions, CALPHAD: Comput. Coupling Phase Diagrams Thermochem. 25(2) (2001) 319-328.
[26] P. Wu, G. Eriksson, A.D. Pelton, M. Blander, Prediction of the thermodynamic properties and phase diagrams of silicate systems - evaluation of the iron(II) oxide-magnesia-silica system, ISIJ Int. 33(1) (1993) 26-35.
[27] B.O. Mysen, F. Seifert, D. Virgo, Structure and redox equilibriums of iron-bearing silicate melts, Am. Mineral. 65(9-10) (1980) 867-84.
[28] P. Chartrand, A.D. Pelton, Modeling the charge compensation effect in silica-rich Na2O-K2O-Al2O3-SiO2 melts, CALPHAD: Comput. Coupling Phase Diagrams Thermochem. 23 (1999) 219-230.
[29] E. Moosavi-Khoonsari, I.-H. Jung, Critical evaluation and thermodynamic optimization of the Na2O–FeO–Fe2O3–Al2O3–SiO2 system, Journal of the European Ceramic Society 37(2) (2017) 787-800.
[30] I.E. Grey, B.F. Hoskins, I.C. Madsen, A structural study of the incorporation of silica into sodium ferrites, Na1-x[Fe1-xSixO2], x = 0 to 0.20, J. Solid State Chem. 85(2) (1990) 202-19.
[31] E. Moosavi-Khoonsari, I.-H. Jung, Critical Evaluation and Thermodynamic Optimization of the Na2O-FeO-Fe2O3-SiO2 System, Metallurgical and Materials Transactions B 47(1) (2016) 291-308.
[32] M. Hillert, The compound energy formalism, J. Alloys Compd. 320(2) (2001) 161-176.
[33] E. Jak, P. Hayes, A.D. Pelton, S.A. Decterov, Thermodynamic modeling of the Al2O3-CaO-FeO-Fe2O3-PbO-SiO2-ZnO system with addition of K and Na with metallurgical applications, Proc. VIII Int'l Conf. on Molten Slags, Fluxes and Salts, Santiago, Chile (2009) 473-490.
[34] J.F. Schairer, The alkali-feldspar join in the system NaAlSiO4-KAlSiO4SiO2, J. Geol. 58 (1950) 512-17.
[35] O.F. Tuttle, J.V. Smith, The nepheline-kalsilite system. II. Phase relations, Am. J. Sci. 256 (1958) 571-89.

[36] A.M. Deml, A.M. Holder, R.P. O'Hayre, C.B. Musgrave, V. Stevanovic, Intrinsic Material Properties Dictating Oxygen Vacancy Formation Energetics in Metal Oxides, J. Phys. Chem. Lett. 6(10) (2015) 1948-1953.
[37] J.E. Saal, S. Kirklin, M. Aykol, B. Meredig, C. Wolverton, Materials Design and Discovery with High-Throughput Density Functional Theory: The Open Quantum Materials Database (OQMD), JOM 65(11) (2013) 1501-1509.
[38] A. Jain, S.P. Ong, G. Hautier, W. Chen, W.D. Richards, S. Dacek, S. Cholia, D. Gunter, D. Skinner, G. Ceder, K.A. Persson, Commentary: The Materials Project: A materials genome approach to accelerating materials innovation, APL Mater. 1(1) (2013) 011002/1-011002/11.
[39] S.P. Ong, W.D. Richards, A. Jain, G. Hautier, M. Kocher, S. Cholia, D. Gunter, V.L. Chevrier, K.A. Persson, G. Ceder, Python Materials Genomics (pymatgen): A robust, open-source python library for materials analysis, Comput. Mater. Sci. 68 (2013) 314-319.
[40] J.S. Lukesh, The tridymite problem, Am. Mineral. 27 (1942) 143-144.
[41] R.S. Roth, C.L. McDaniel, H.S. Parker, L.P. Cook, T. Negas, D.B. Minor, The System K2O-Al2O3-Fe2O3-SiO2 Part II. Crystal Chemistry of Phases on the Joins KFeO2-SO2 and KAISiO4-KFeSiO4., Abstr. Geol. Soc. Am. 9(7) (1977) 1149.
[42] J.G. Thompson, R.L. Withers, S.R. Palethorpe, A. Melnitchenko, Cristobalite-related oxide structures, J. Solid State Chem. 141(1) (1998) 29-49.
[43] L.B. Pankratz, High-temperature heat contents and entropies of dehydrated analcite, kaliophilite, and leucite, U. S. Bur. Mines, Rep. Invest. No. 7073 (1968) 8 pp.
[44] S.C. Kohn, C.M.B. Henderson, R. Dupree, NMR studies of the leucite analogs X2YSi5O12, where X = K, Rb, Cs; Y = Mg, Zn, Cd, Phys. Chem. Miner. 21(3) (1994) 176-90.
[45] J.F. Stebbins, I.S.E. Carmichael, L.K. Moret, Heat capacities and entropies of silicate liquids and glasses, Contrib. Mineral. Petrol. 86(2) (1984) 131-48.
[46] R.P. Beyer, M.J. Ferrante, R.R. Brown, Thermodynamic properties of potassium aluminate, J. Chem. Thermodyn. 12 (1980) 985-91.
[47] I.-H. Jung, S.A. Decterov, A.D. Pelton, Critical thermodynamic evaluation and optimization of the CaO-MgO-SiO2 system, J. Eur. Ceram. Soc. 25(4) (2005) 313-333.

Tables

Table 5.1 DSC and equilibration experimental results for the K_2O-MgO system.

Sample	Composition		Thermal incidences (°C)	Equilibration		Equilibrium phases*
	K_2O (mol %)	MgO (mol %)		Temp. (°C)	Time (hour)	
1	20	80	853.8	950	66	Liquid + MgO (+ KOH)
2	20	80	872.7	800	66	K_6MgO_4 + MgO (+ KOH)
3	20	80	843.9	700	167	K_6MgO_4 + MgO (+ KOH)

* KOH was formed during the preparation of XRD analysis, so it is not equilibrium phase in experimental condition.

Table 5.2 Optimized thermodynamic properties of compounds in the K_2O-MgO and K_2O-MgO-SiO_2 systems in comparison with the literature data.

Compound	$\Delta H^{o}_{298.15K}$ (kJ·mol^{-1})	$S^{o}_{298.15K}$ (J·mol^{-1}·K^{-1})	C_P (J·mol^{-1}·K^{-1})	Reference
K_6MgO_4 (K_3M)	-1696.230	333.000	$3\cdot C_P$ (K_2O) + $1\cdot C_P$ (MgO) (298-1200K)	This study
	-1739.977			15Dem[36]
	-1700.811			13Jai[38], 13Ong[39]
	-1617.966			13Saa[37]
LT-K_2MgSiO_4 (KMS)	-2180.240	173.636	$1\cdot C_P$ (K_2O) + $1\cdot C_P$ (MgO) + $1\cdot C_P$ (SiO_2, Crs) (298-2000K)	This study
	-2167.085			13Jai[38]
	$\Delta H^{o}_{tr(LT\rightarrow HT)}$	1.960 (kJ·mol^{-1}) at 507.85 °C		This study
		1.965 (kJ·mol^{-1}) at 508 °C		98Dol[16]
HT-K_2MgSiO_4 (KMS)	-2178.275	176.152	$1\cdot C_P$ (K_2O) + $1\cdot C_P$ (MgO) + $1\cdot C_P$ (SiO_2,Crs) (298-2000K)	This study
LT-$K_2MgSi_3O_8$ (KMS_3)	-4086.850	265.362	$1\cdot C_P$ (K_2O) + $1\cdot C_P$ (MgO) + $3\cdot C_P$ (SiO_2,Trd) (298-2000K)	This study
	$\Delta H^{o}_{tr(LT\rightarrow HT)}$	0.890 (kJ·mol^{-1}) at 899.85 °C		This study
HT-$K_2MgSi_3O_8$ (KMS_3)	-4085.960	266.121	$1\cdot C_P$ (K_2O) + $1\cdot C_P$ (MgO) + $3\cdot C_P$ (SiO_2,Trd) (298-2000K)	This study
$K_2MgSi_5O_{12}$ (KMS_5)	-5922.850	359.101	$1\cdot C_P$ (K_2O) + $1\cdot C_P$ (MgO) + $5\cdot C_P$ (SiO_2,Crs) (298-2000K)	This study
	-6056.683			13Jai[38]
$K_2Mg_5Si_{12}O_{30}$ (KM_5S_{12})	-14830.800	782.800	$1\cdot C_P$ (K_2O) + $5\cdot C_P$ (MgO) + $12\cdot C_P$ (SiO_2,Trd) (298-2000K)	This study
$K_4Mg_2Si_5O_{14}$ ($K_2M_2S_5$)	-7187.000	521.284	$2\cdot C_P$ (K_2O) + $2\cdot C_P$ (MgO) + $5\cdot C_P$ (SiO_2,Trd) (298-2000K)	This study

$K_{10}Mg_5Si_{11}O_{32}$ ($K_5M_5S_{11}$)	-16578.500	1215.871	$5\cdot C_P$ (K_2O) + $5\cdot C_P$ (MgO) + $11\cdot C_P$ (SiO_2,Trd) (298-2000K)	This study

Crs: Cristobalite, Trd: Tridymite, Qz: Quartz, $\Delta H^{o}_{298.15\,K}$ are relative to elements at 298.15 K, data for all other compounds were taken from Kim *et al*. [20] and Wu *et al*. [26].

Table 5.3 Optimized model parameters of the solutions ($J \cdot mol^{-1}$ and $J \cdot mol^{-1} \cdot K^{-1}$).

Liquid solution (MQM)
$Z_{KK}^{K} = 0.6887$, $Z_{MgMg}^{Mg} = 1.3774$, $Z_{SiSi}^{Si} = 2.7549$, $Z_{K_2MgSi\ K_2MgSi}^{K_2MgSi} = 5.5098$, $Z_{K_2MgSi\ Si}^{K_2MgSi} = 2.7549$, $Z_{Si\ K_2MgSi}^{Si} = 0.9183$
<u>The K_2O-MgO system</u>
$\Delta g_{K-Mg} = 0$
<u>The K_2O-MgO-SiO_2 system</u>
$q_{K,Si(Mg)}^{001} = -60668$, $q_{K,Si(Mg)}^{002} = -33472$, $q_{K,Si(Mg)}^{011} = -150624$, $q_{K,Si(Mg)}^{041} = -79496$
$g_{K_2MgSiO_4(associate)}^{o} = g_{K_2O,liquid}^{o} + g_{MgO,liquid}^{o} + g_{SiO_2,liquid}^{o} - 251040$
$\Delta g_{K_2MgSi-Si} = -85772 - 79496 \cdot X_{Si-Si}$
$q_{K_2MgSi,Si(Mg)}^{001} = -41840$
K_2MgSiO_4 solid solutions (CEF)
$(K_2Mg^{4+}, VaSi^{4+})SiO_4$
<u>High-temperature K_2MgSiO_4</u>
$G_{K_2MgSiO_4}^{o} = G_{K_2MgSiO_4(HT)}^{o}$
$G_{VaSi_2O_4}^{o} = 2*(G_{SiO_2(Crs)}^{o} + 6000)$
${}^{0}L_{K_2Mg,VaSi} = -140582.4 - 12.552 \cdot T$
<u>Low-temperature K_2MgSiO_4</u>
$G_{K_2MgSiO_4}^{o} = G_{K_2MgSiO_4(LT)}^{o}$
$G_{VaSi_2O_4}^{o} = 2*(G_{SiO_2(Crs)}^{o} + 5000)$
${}^{0}L_{K_2Mg,VaSi} = -133888 - 8.368 \cdot T$
$K_2MgSi_3O_8$ solid solutions (MQM)
$Z_{AA}^{A} = 1.3774$, $Z_{BB}^{B} = 0.6887$, $Z_{AB}^{A} = 1.3774$, $Z_{BA}^{B} = 2.0662$, $A = K_2MgSi_3$, $B = VaSi_2$
<u>High-temperature $K_2MgSi_3O_8$ (Kalsilite)</u>
$G_{K_2MgSi_3O_8}^{o} = G_{K_2MgSi_3O_8(HT)}^{o}$
$G_{VaSi_2O_4}^{o} = 2*(G_{SiO_2(Trd)}^{o} + 6276)$

$\Delta g_{K_2MgSi_3,VaSi_2} = 0$

Low-temperature $K_2MgSi_3O_8$ (Nepheline)

$G^o_{K_2MgSi_3O_8} = G^o_{K_2MgSi_3O_8(LT)}$

$G^o_{VaSi_2O_4} = 2*(G^o_{SiO_2(Trd)} + 6276)$

$\Delta g_{K_2MgSi_3,VaSi_2} = 0$

Binary model parameters of the K_2O-SiO_2 and MgO-SiO_2 systems were taken from Kim *et al*. [20] and Wu *et al*. [26], respectively. The description of the ternary parameters of the MQM can be found in Ref. [24].

Table 5.4 Crystal structures of compounds in the K_2O-MgO and K_2O-MgO-SiO_2 systems.

Phase	Crystal system	Space group	Exp. Technique	Reference
K_6MgO_4 (binary compound)	Hexagonal	$P6_3mc$	XRD	74Bar[10] 74Dar[11]
K_2MgSiO_4 (KMS)	Cubic	$F\bar{4}3m$	OM, XRD	51Roe[9]
	Cubic (*h*)	$F\bar{4}3m$	DSC, XRD	98Dol[16]
	Orthorhombic (*l*)	$Pca2_1$		
$K_2MgSi_3O_8$ (KMS_3)	Hexagonal (*h*)		OM, XRD	51Roe[9]
	Orthorhombic (*l*) Hexagonal (*l*)			
	Monoclinic (*h*)		XRD	80Rot[12]
	Hexagonal (*l*)			
$K_2MgSi_5O_{12}$ (KMS_5)	Cubic	(BCC)	OM, XRD	51Roe[9]
	Cubic (*dry*)	$Ia\,3d$	MAS NMR, TEM, S-XRD	94Bel[14]
	Monoclinic (*hyd*)	$P2_1/c$		
	Orthorhombic (*h*) (metrically cubic)	*Pbca*	XRD	96Red[15]
	Monoclinic (*l*)	$P2_1/c$		
$K_2Mg_5Si_{12}O_{30}$ (KM_5S_{12})	Hexagonal		OM, XRD	51Roe[9]
	Hexagonal	$P6/mcc$	XRD	69Sei[13]
$K_4Mg_2Si_5O_{14}$ ($K_2M_2S_5$)	Orthorhombic		XRD	80Rot[12]
$K_{10}Mg_5Si_{11}O_{32}$ ($K_5M_5S_{11}$)	Tetragonal		XRD	80Rot[12]

(*h*): High-temperature phase, (*l*): Low-temperature phase, (*dry*): Dry synthesis, (*hyd*): Hydrothermal synthesis, OM: Optical microscopy, XRD: X-ray Diffraction, MAS NMR: Magic angle spinning nuclear magnetic resonance, TEM: Transmission electron microscopy, S-XRD: Synchrotron X-ray diffraction.

Table 5.5 Comparison of experimental and optimized transition temperatures of ternary compounds in the K_2O-MgO-SiO_2 system.

Phase	Transition	Experiment			This study
		Temp. (°C)	Techniques	Reference	Temp. (°C)
K_2MgSiO_4 (KMS)	KMS(*h*) → L+M (or L)	1650*	OM, XRD	51Roe[9]	1650.4
	KMS(*l*) → KMS(*h*)	508	DSC, XRD	98Dol[16]	507.8
$K_2MgSi_3O_8$ (KMS_3)	KMS_3 → L	1134 ±1	OM, XRD	51Roe[9]	1121.1
	KMS_3 → $K_2M_2S_5$+L	1070	XRD	80Rot[12]	
	KMS_3 (*l*) → KMS_3 (*h*)	900			899.9
$K_2MgSi_5O_{12}$ (KMS_5)	KMS_5 → L	1089 ±1	OM, XRD	51Roe[9]	1070.3
	KMS_5 → L+?	800-900	XRD	96Red[15]	
	KMS_5 (*l*) → KMS_5 (*h*)	349			
$K_2Mg_5Si_{12}O_{30}$ (KM_5S_{12})	KM_5S_{12} → L+$MgSiO_3$	1174 ±2	OM, XRD	51Roe[9]	1165.5
		~1180	XRD (high-P Exp.)	69Sei[13]	
$K_4Mg_2Si_5O_{14}$ ($K_2M_2S_5$)	$K_2M_2S_5$ → L+$K_5M_5S_{11}$	1150	XRD	80Rot[12]	1145.0
$K_{10}Mg_5Si_{11}O_{32}$ ($K_5M_5S_{11}$)	$K_5M_5S_{11}$ → L+KMS	1160	XRD	80Rot[12]	1160.7

K: K_2O, M: MgO, S: SiO_2, (*h*): High-temperature phase, (*l*): Low-temperature phase, OM: Optical microscopy, XRD: X-ray diffraction, DSC: Differential Scanning Calorimetry, high-P Exp.: High-pressure experiment, *: measurements with large error range.

Table 5.6 Experimental and calculated invariant reaction points in the K_2O-MgO-SiO_2 system involving liquid phase (see the liquidus projection in Fig. 5.6).

Invariant reactions **1-22**: this study (alphabets): 51Roe [9]	Type	Temperature (°C)			Liquid composition (mol %)								
					K_2O			MgO			SiO_2		
		51Roe [9]	14Yaz [17]	This study	51Roe [9]	14Yaz [17]	This study	51Roe [9]	14Yaz [17]	This study	51Roe [9]	14Yaz [17]	This study
1 (N) MS+S(Crs)+S(Trd)	P	1470±?		1465.4	0.035		0.049	0.176		0.176	0.789		0.775
2 (O) MS+S(Trd)+KM_5S_{12}	P	1165±2		1165.0	0.074		0.086	0.131		0.140	0.795		0.774
MS+S(Crs)+KM_5S_{12}	R	1165±2	1158		0.074	0.072		0.131	0.141		0.795	0.787	
3 (P) S(Trd)+KM_5S_{12}+KMS_5	E	963±3		1019.1	0.098		0.107	0.109		0.110	0.792		0.783
S(Crs)+KM_5S_{12}+KMS_5	E	963±3	1000		0.098	0.100		0.109	0.110		0.792	0.791	
4 (R) S(Trd)+KMS_5+KS_4	E	715±10			0.170			0.032			0.798		
S(Qz)+KMS_5+KS_4	E			717.1	0.170		0.177	0.032		0.027	0.798		0.796
S(Qz)+KMS_5+KS_4	R	715±10	685		0.170	0.193		0.032	0.034		0.798	0.772	
5 (U) M_2S+MS+KM_5S_{12}	P	1155±2	1162	1154.2	0.105	0.097	0.101	0.172	0.177	0.170	0.723	0.727	0.729
6 (X) M_2S+KM_5S_{12}+KMS_5	P	1042±7	1074	1060.9	0.131	0.123	0.128	0.179	0.171	0.168	0.691	0.706	0.704
7 (Z) M_2S+KMS_3+KMS_5	E	1013±3	1037	1041.5	0.157	0.166	0.158	0.184	0.195	0.179	0.659	0.640	0.663
8 (B′) KMS_3+KMS_5+KS_2	P	795±15	789	801.1	0.222	0.218	0.237	0.079	0.075	0.056	0.700	0.707	0.707
9 (C′) KMS_5+KS_2+KS_4	E	685±20	656	706.2	0.212	0.213	0.214	0.041	0.036	0.028	0.747	0.750	0.758
10 (F′) KMS_3+KMS(?)+KS_2	E	905±5			0.293			0.101			0.606		
KMS_3+($K_5M_5S_{11}$)+KS_2	E	905±5		865.1	0.293		0.310	0.101		0.081	0.606		0.608
($K_5M_5S_{11}$)+KMS+KS_2	P	905±5	911		0.293	0.311		0.101	0.089		0.606	0.600	
11 (G′) KMS_3+KMS(?)+M_2S	E	1105±10			0.221			0.234			0.545		

: KMS_3+($K_2M_2S_5$)+M_2S	E	1105±10		1118.2	0.221		0.200	0.234		0.215	0.545		0.584
: ($K_5M_5S_{11}$)+KMS+M_2S	R	1105±10	1162		0.221	0.210		0.234	0.240		0.545	0.549	
12 (K′) KMS(?)+M_2S+M	P	1350±50	1424	1310.4	0.235	0.231	0.209	0.335	0.347	0.333	0.430	0.422	0.458
13 (M′) KMS(?)+KS_2+KS	E	720±?	755	742.1	0.429	0.417	0.395	0.009	0.013	0.038	0.562	0.571	0.567
14 KMS_5+S(Qz)+S(Trd)	P			866.9			0.148			0.046			0.806
15 Liq#2+MS+S(Crs)	M			1491.7			0.045			0.206			0.749
16 Liq#2+MS+S(Crs)	M			1491.7			0.037			0.295			0.668
17 KMS_5+KMS_3(HT,LT)	P			899.9			0.218			0.077			0.705
18 $K_5M_5S_{11}$+$K_2M_2S_5$+KMS_3	P			973.5			0.282			0.108			0.609
19 KMS+$K_5M_5S_{11}$+M_2S	P			1158.9			0.216			0.240			0.544
20 KMS+K_2S+MgO	P			936.1			0.575			0.123			0.301
21 K_2S+K_3M+MgO	P			748.2			0.782			0.032			0.185
22 K_2O+K_2S+K_3M	E			677.8			0.866			0.003			0.131

K: K_2O, M:MgO, S:SiO_2, E: eutectic, P: peritectic, R: reaction, M: monotectic, (?): unclear phase by Roedder [9], Crs: Cristobalite, Trd: Tridymite, Qz: Quartz.

Figures

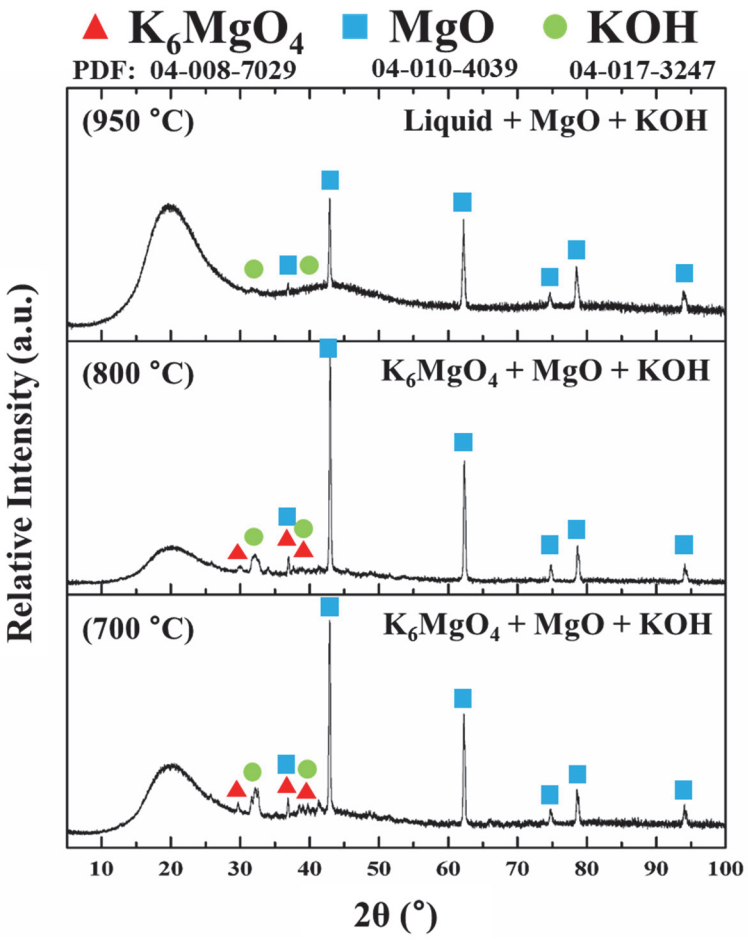

Figure 5.1 XRD patterns of three equilibration/quenched samples.

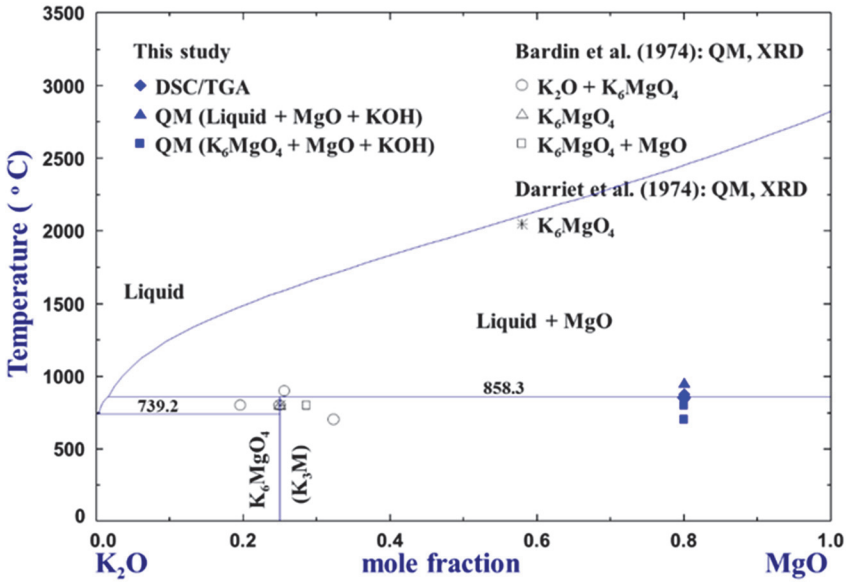

Figure 5.2 Optimized phase diagram of the K_2O-MgO system in comparison with experimental data.

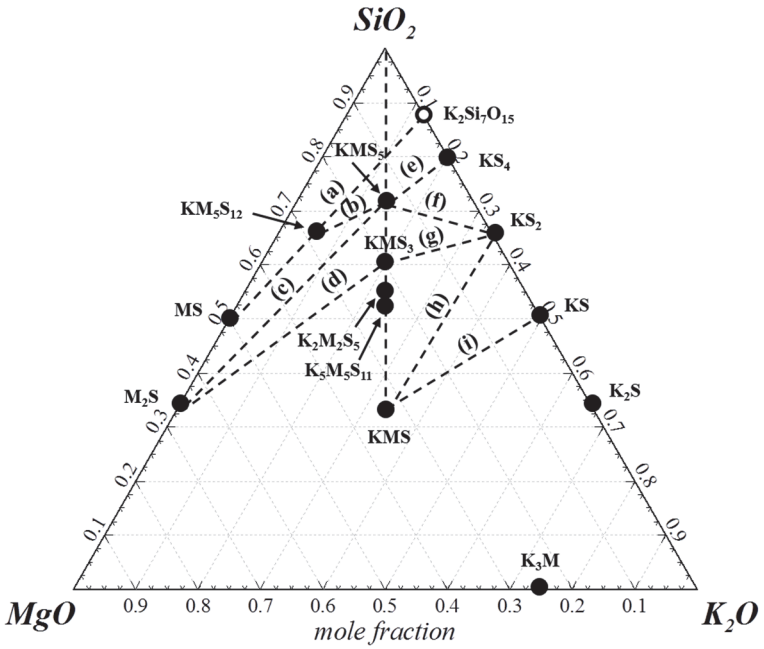

Figure 5.3 Schematic diagram of the K_2O-MgO-SiO_2 system showing all stable compounds and experimentally investigated isoplethal sections (K: K_2O, M: MgO, S: SiO_2).

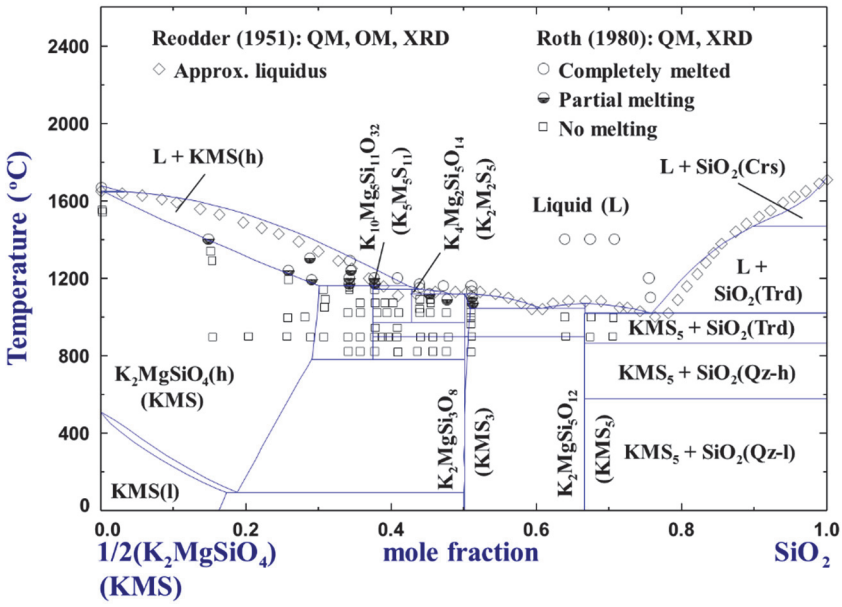

Figure 5.4 Optimized phase diagram of the ½(K_2MgSiO_4)-SiO_2 section (Qz: Quartz, Trd: Tridymite, Crs: Cristobalite, h: high-temperature and l: low-temperature polymorphs).

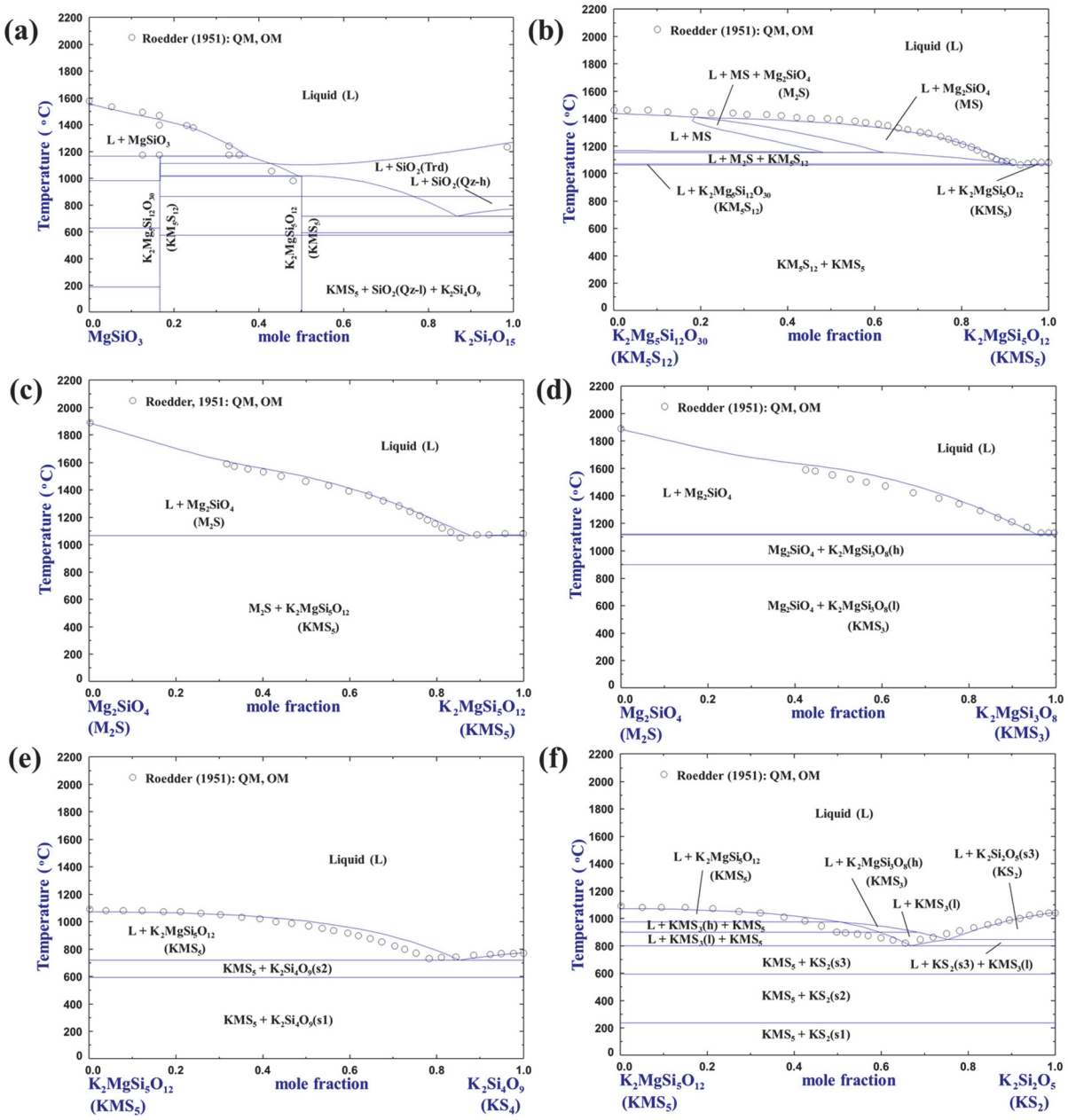
(a)
Roedder (1951): QM, OM
Liquid (L)
L + MgSiO3
L + SiO2(Trd)
L + SiO2(Qz-h)
K2Mg5Si12O30 (KM5S12)
K2MgSi5O12 (KMS5)
KMS5 + SiO2(Qz-l) + K2Si4O9
Temperature (°C)
MgSiO3
mole fraction
K2Si7O15
(b)
Roedder (1951): QM, OM
Liquid (L)
L + MS + Mg2SiO4 (M2S)
L + Mg2SiO4 (MS)
L + MS
L + M2S + KM5S12
L + K2Mg5Si12O30 (KM5S12)
L + K2MgSi5O12 (KMS5)
KM5S12 + KMS5
Temperature (°C)
K2Mg5Si12O30 (KM5S12)
mole fraction
K2MgSi5O12 (KMS5)
(c)
Roedder, 1951: QM, OM
Liquid (L)
L + Mg2SiO4 (M2S)
M2S + K2MgSi5O12 (KMS5)
Temperature (°C)
Mg2SiO4 (M2S)
mole fraction
K2MgSi5O12 (KMS5)
(d)
Roedder (1951): QM, OM
Liquid (L)
L + Mg2SiO4
Mg2SiO4 + K2MgSi3O8(h)
Mg2SiO4 + K2MgSi3O8(l) (KMS3)
Temperature (°C)
Mg2SiO4 (M2S)
mole fraction
K2MgSi3O8 (KMS3)
(e)
Roedder (1951): QM, OM
Liquid (L)
L + K2MgSi5O12 (KMS5)
KMS5 + K2Si4O9(s2)
KMS5 + K2Si4O9(s1)
Temperature (°C)
K2MgSi5O12 (KMS5)
mole fraction
K2Si4O9 (KS4)
(f)
Roedder (1951): QM, OM
Liquid (L)
L + K2MgSi5O12 (KMS5)
L + K2MgSi3O8(h) (KMS3)
L + K2Si2O5(s3) (KS2)
L + KMS3(l)
L + KMS3(h) + KMS5
L + KMS3(l) + KMS5
KMS5 + KS2(s3)
L + KS2(s3) + KMS3(l)
KMS5 + KS2(s2)
KMS5 + KS2(s1)
Temperature (°C)
K2MgSi5O12 (KMS5)
mole fraction
K2Si2O5 (KS2)

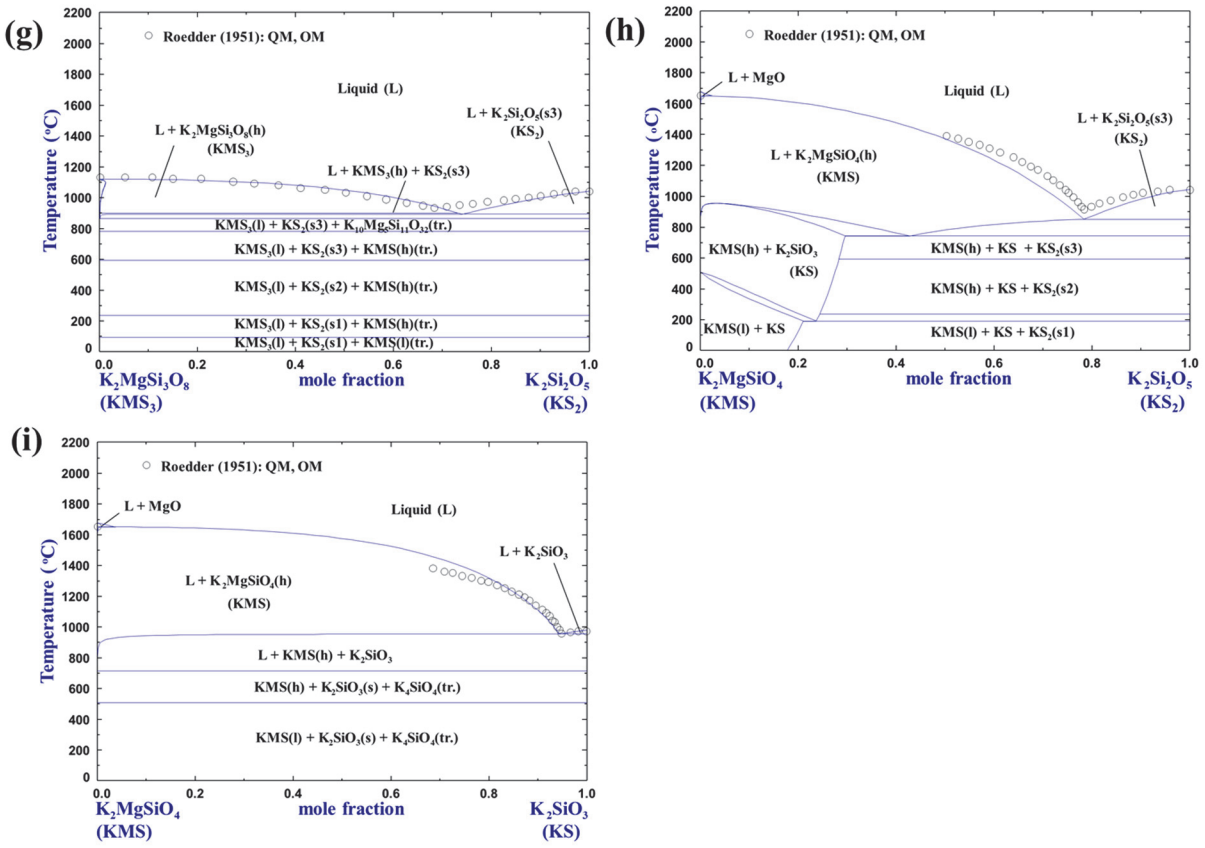

Figure 5.5 Optimized phase diagram sections of (a) $MgSiO_3$-$K_2Si_7O_{15}$ (b) $K_2Mg_5Si_{12}O_{30}$-$K_2MgSi_5O_{12}$ (c) Mg_2SiO_4-$K_2MgSi_5O_{12}$ (d) Mg_2SiO_4-$K_2MgSi_3O_8$ (e) $K_2MgSi_5O_{12}$-$K_2Si_4O_9$ (f) $K_2MgSi_5O_{12}$-$K_2Si_2O_5$ (g) $K_2MgSi_3O_8$-$K_2Si_2O_5$ (h) K_2MgSiO_4-$K_2Si_2O_5$ (i) K_2MgSiO_4-K_2SiO_3 (Qz: Quartz, Trd: Tridymite, Crs: Cristobalite).

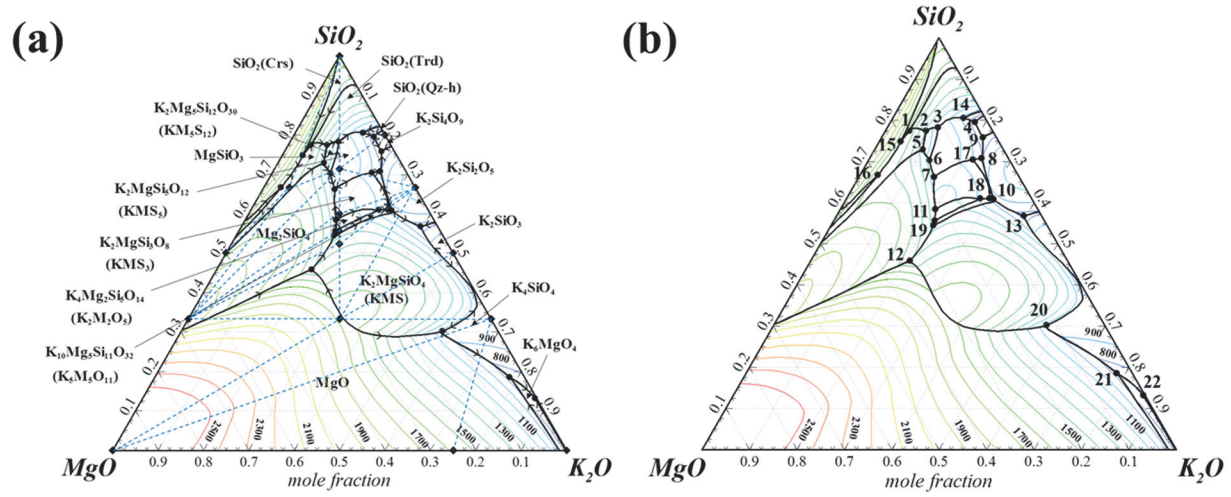

Figure 5.6 Optimized liquidus projection of the K_2O-MgO-SiO_2 system indicating (a) primary phase regions, alkemade lines with solidification paths, (b) invariant reaction points (for the details of invariant reaction, see Table 5.6).

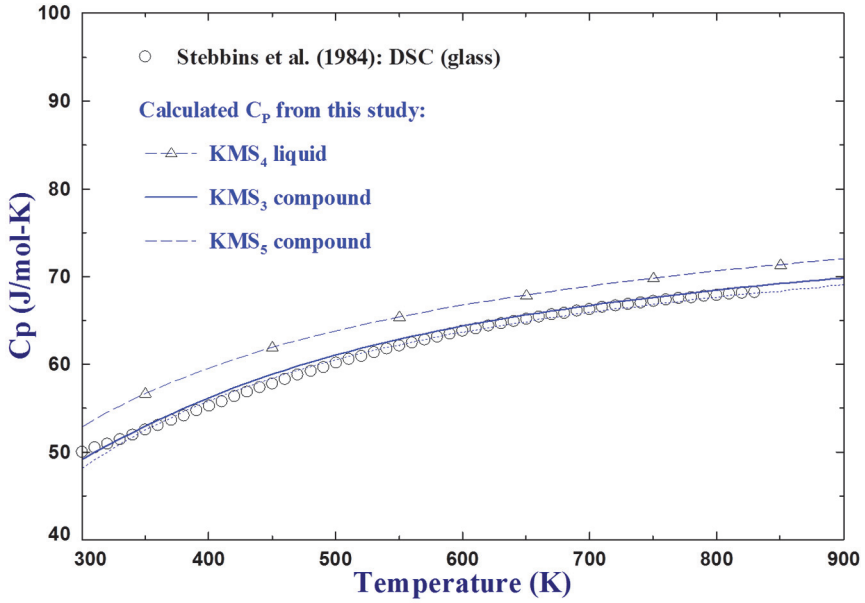

Figure 5.7 Experimentally measured heat capacity of the 16.88 K_2O, 16.44 MgO, and 66.68 SiO_2 (mol %; KMS_4) glass compared with KMS_3 and KMS_5 compounds.

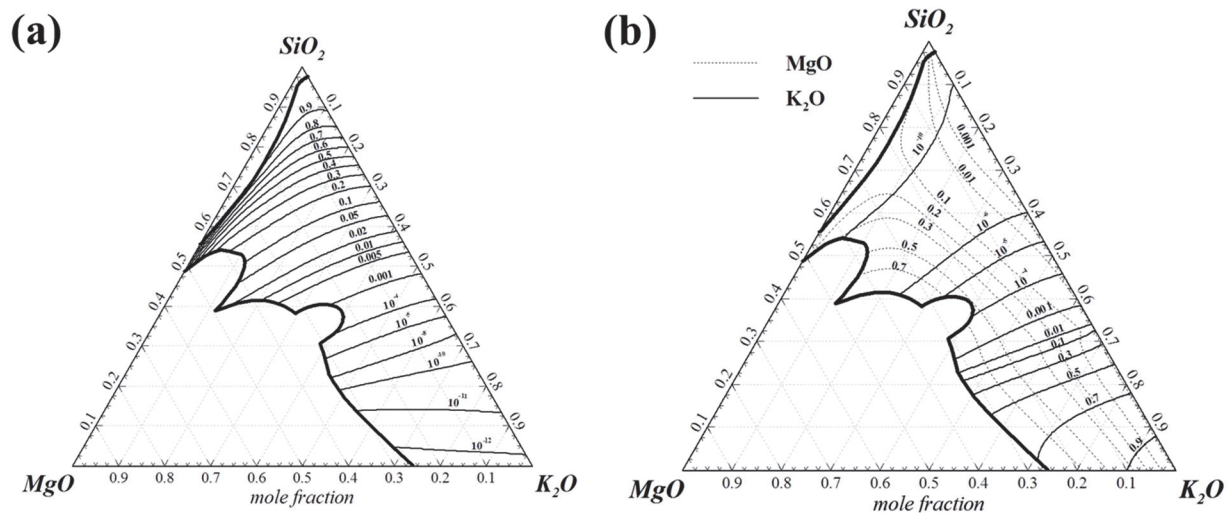

Figure 5.8 Iso-activity contours of (a) SiO_2 (cristobalite), (b) MgO (solid), and K_2O (liquid) at 1600 °C in the K_2O-MgO-SiO_2 system, ( ): reference state.

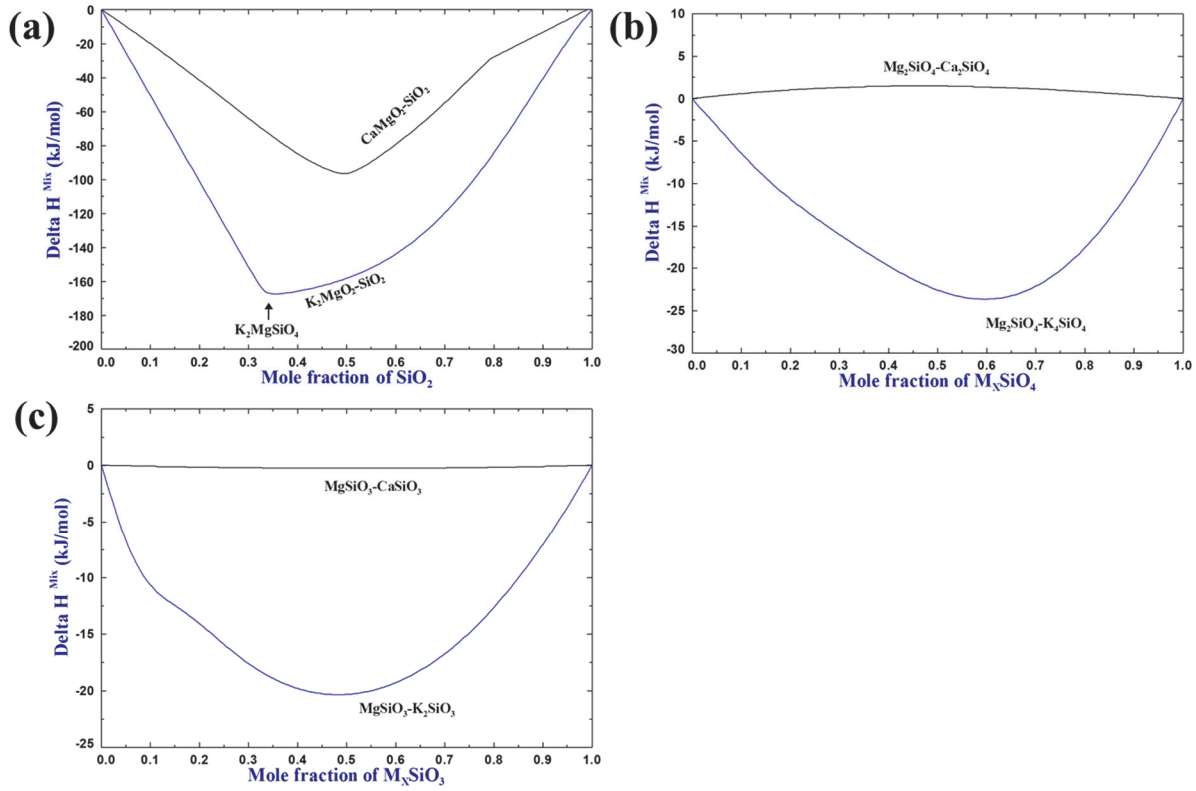

Figure 5.9 The liquid enthalpy of mixing at 1600 °C (a) of the N_XMgO_2-SiO_2 systems (b) orthosilicate section, N_XSiO_4 (c) metasilicate section, N_XSiO_3 (N = K, Ca).

Chapter 6 Thermodynamic Modeling of the K_2O-Al_2O_3 and K_2O-MgO-Al_2O_3 Systems with Emphasis on β- and β″-Alumina

Dong-Geun Kim, Elmira Moosavi-Khoonsari and In-Ho Jung

To be submitted.

In this chapter, we discussed experimental results of the K_2O-Al_2O_3 system and thermodynamic optimizations of the K_2O-Al_2O_3 and K_2O-MgO-Al_2O_3 systems. Equilibration/quenching experiments were performed to resolve large discrepancies in the K_2O-Al_2O_3 phase diagram. The Compound Energy Formalism was used to model the β″- and β-alumina solid solutions. The optimization of the K_2O-MgO-Al_2O_3 system was based on the K_2O-Al_2O_3 system in this chapter and the K_2O-MgO system explored in Chapter 5.

Abstract

A critical evaluation and thermodynamic modeling study was performed with key phase diagram experiments to investigate the K_2O-Al_2O_3 and K_2O-MgO-Al_2O_3 systems. For the first time, potassium β- and β″-alumina solid solutions were described using the Compound Energy Formalism with accurate cation distribution in their sublattices. From the new experimental results, the stability of potassium β″-alumina was assured up to 1600 °C. A large discrepancy reported in the literature, of the eutectic temperature between $KAlO_2$ and β-alumina in the K_2O-Al_2O_3 system, was resolved. A set of self-consistent Gibbs energy functions for all stable phases in the K_2O-MgO-Al_2O_3 system was obtained. As a result, any phase diagram sections and thermodynamic properties of the K_2O-MgO-Al_2O_3 system can be calculated from the optimized Gibbs energy

functions. In particular, the cation distribution in the β- and β″-alumina solid solutions is calculated depending on the non-stoichiometry of solution and temperature.

Key words: K_2O-Al_2O_3, K_2O-MgO-Al_2O_3, potassium beta alumina, thermodynamic optimization, equilibration/quenching experiments

6.1 Introduction

β- and β″-alumina are excellent solid ionic conductors, which make them attractive for energy storage applications. Alkali metal thermal electric converter (AMTEC) is being considered as a new energy storage technology for spacecraft and hybrid electric vehicles [1] because it can be five times more efficient than the traditional radioisotope (plutonium-238) heat sources used in spacecraft. Na β″-alumina has been used as a solid electrolyte in AMTEC. More recently, K β″-alumina was found to have advantages over Na β″-alumina [2]. The higher ionic conductivity and vapor pressure of K at low temperatures make K β″-alumina AMTEC 25% more efficient than Na β″-alumina ones [3]. At the same time, K β″-alumina cells have longer lifetime due to low operation temperature [2]. However, there is a very limited understanding on the thermodynamic properties and stabilities of K β- and β″-alumina. Studying the K_2O-MgO-Al_2O_3 system is essential for the K β- and β″-alumina in battery applications.

In the thermodynamic optimization, all the phase diagram and thermodynamic data are critically evaluated and optimized to obtain a set of self-consistent thermodynamic functions to reproduce all available and reliable experimental data. The thermodynamic models employed to describe the solid and liquid solutions are based on the structure of the respective solution to capture the nature of configurational entropy more accurately. Using the optimized thermodynamic functions,

unexplored phase stability and thermodynamic properties can be accurately predicted in a thermodynamically correct manner.

There is no comprehensive thermodynamic description of the K_2O-MgO-Al_2O_3 system. Up to now, only binary K_2O-Al_2O_3, K_2O-MgO, and MgO-Al_2O_3 systems have been studied [4-11]. There are large uncertainties in the phase diagram data in the literature due to the high hygroscopicity and volatility of K_2O and the high melting point of Al_2O_3. In the K_2O-Al_2O_3 system, there are large discrepancies on the eutectic temperature between $KAlO_2$ and β-alumina in the literature. Moya *et al*. [12] reported this eutectic temperature to be at 1450 °C. Roth [13] measured it at 1910 °C. Schaefer *et al*. [14] proposed it to be at 1780 °C. For the K_2O-MgO-Al_2O_3 system, the isothermal sections at 1100 and 1400 °C were reported by Van Hoek *et al*. [15]. However, only the one at 1400 °C was considered to be under equilibrium condition. Schaefer *et al*. [14] also proposed several isothermal sections based on different alumina starting materials. Overall, accurate phase diagrams of the K_2O-Al_2O_3 and K_2O-MgO-Al_2O_3 systems and thermodynamic properties of β- and β″-alumina solutions are not available.

The aim of this study was to perform the thermodynamic optimization of the K_2O-MgO-Al_2O_3 system. In order to resolve inconsistencies in the available experimental data regarding the thermal stability of β- and β″-alumina and the eutectic temperature in the K_2O-Al_2O_3 system, equilibration/quenching experiments and thermal analyses were also conducted in the present study. In the experiments, sealed Pt capsules were used to avoid hydration and evaporation of K_2O. Accurate thermodynamic models considering the structure of β- and β″-alumina were developed for the first time and applied to the description of the thermodynamic and structural properties of β- and β″-alumina solutions. Phase stability and structural changes related to β- and β″-alumina in

the K_2O-Al_2O_3 and K_2O-MgO-Al_2O_3 systems were well predicted. All the thermodynamic calculations were performed using the FactSage software [16].

6.2 Experiments on the K_2O-Al_2O_3 System

In order to resolve the uncertainties in the eutectic reaction between $KAlO_2$ and β-/β″-alumina in the K_2O-Al_2O_3 system, key phase diagram experiments were performed.

6.2.1 Starting Materials

Starting materials were prepared using reagent grade K_2CO_3 (99.997 wt. %, Alfa Aesar) and Al_2O_3 (99.99 wt. %, Alfa Aesar). Batches of 5 to 10 g of the materials were mixed for 1 hour with isopropyl alcohol (H_2O < 0.02 vol. %) to prevent moisture pickup from air. In order to dry off the alcohol, the mixtures were kept in a drying oven at 120 °C for more than 12 hours and then cooled down to room temperature in a desiccator. To obtain K_2O, which is extremely hygroscopic, the decarbonation of K_2CO_3 ($K_2CO_3 \rightarrow K_2O + CO_2$) was conducted just before each experiment. The decarbonation temperature with minimum volatile loss of K_2O was set to be 830 °C according to the preliminary Thermo-Gravimetric Analysis (TGA). The weight of each sample was measured before and after decarbonation to confirm the completion of the decarbonation reaction. After the decarbonation, the mixtures of K_2O and Al_2O_3 were stored in a drying oven to cool them down to 120 °C and subsequently in a desiccator to reach room temperature. The mixtures were then crushed and packed into one-side-sealed platinum (Pt) tubes with dimensions of about 17 mm in length, 3.2 mm in outer diameter, and 0.2 mm in wall thickness. The open end of the Pt tubes was gently crimped to remove the air and welded into capsules using an electric arc welder to ensure gas-tight condition. The integrity of the welding was checked with an optical microscope before

the main experiments. The starting composition of 35 mol % K_2O and 65 mol % Al_2O_3 was prepared for the samples used in thermal analysis and equilibration/quenching experiments.

6.2.2 Thermal Analysis

Differential Thermal Analysis (DTA) and TGA measurements were conducted using a Jupiter STA 449 F3 thermal analyzer under an argon flowing atmosphere at a rate of 20 $mL \cdot min^{-1}$. The sealed Pt capsules were placed inside an Al_2O_3 crucible with an outer diameter of 8 mm and a height of 23 mm for the DTA/TGA measurements. The heating and cooling cycles were performed at a rate of 10 $K \cdot min^{-1}$. TGA was simultaneously performed to confirm that there was no leakage of the sealed capsules during the experiments. Three heating and cooling cycles were run for each sample to obtain reliable and reproducible results. Temperature and sensitivity calibrations were conducted by measuring the melting temperatures and enthalpies of the eight reference materials. The reliability on the thermal analysis of using sealed Pt capsules was determined in the previous study [17].

6.2.3 Equilibration/Quenching Method

For the equilibration experiments, a muffle box furnace (ST-1700C, SentroTech, $MoSi_2$ heating elements) was used. The temperature of the furnace was controlled using a PID controller within ± 1 °C. For each equilibration experiment, several Pt capsules containing the K_2O-Al_2O_3 mixtures were placed in a porous Al_2O_3 holder, which were then placed in the box furnace. Equilibration was conducted at 1500 °C for 2 hours and 1600 °C for 1 hour. After the equilibration, the samples contained in Pt capsules were immediately quenched in cold water, mounted in epoxy resin and polished with lapping oil (water-free lubricant) just before phase characterization to avoid the

hydration of K_2O. For the transportation to characterization, the polished samples were put in a glass vial filled with desiccants in a vacuumed desiccator.

Phase characterization was conducted using X-Ray Diffractometer (Bruker D8 Discover, Madison, WI, Cu *K*α-radiation) equipped with a VANTEC detector. All XRD profiles were identified with the Powder Diffraction Files (PDF) of the International Centre for Diffraction Data (ICDD) using the DIFFRAC.EVA software package (Bruker AXS, Karlsruhe, Germany, 2000). As K_2O is extremely volatile, it was very difficult to perform quantitative analysis using electron probe micro-analyzer (EPMA). (see Section 6.2.4) Therefore, only micrographs were taken to investigate morphology of the sample.

6.2.4 Experimental Results

The discrepancy regarding the eutectic reaction between $KAlO_2$ and β-/β″-alumina, which was reported at 1450 °C by Moya [12] and at 1910 °C by Roth [13], was successfully resolved in this study. In three different DTA measurements, no heat incident was recorded in the temperature range from 1250 to 1550 °C. The XRD results of the samples equilibrated at 1500 and 1600 °C are shown in Fig. 6.1 (a). For both samples, hydrated $KAlO_2$ phase of $KAlO_2 \cdot 1.5H_2O$ and β″-alumina phase ($K_{1.59}Al_{10.8}O_{17}$) were identified. Thus, the stability of the β″-alumina phase was confirmed up to 1600 °C in the equilibration/quenching experiments with XRD analysis. The $KAlO_2$ phase easily gets hydrated into $KAlO_2 \cdot 1.5H_2O$ phase during transportation of the samples. Unfortunately, quantitative analysis of these two phases was impossible using EPMA due to the volatile loss of K_2O and the hydration of the sample surface. Fig. 6.1 (b) shows images of hydrated surface of the sample inside the microscope. EPMA analysis with an accelerating voltage of 8 kV, a beam current of 4 nA, a beam size of 20 μm, and correction with ZAF method (this was deemed

reasonable for Na oxide samples) was performed on the samples, all quantitative analysis results showed about 64.9 wt. % total counts. In Fig. 6.1 (b), two phases with different morphologies can be seen: needle-shape and more round shape. The round shape phase is considered as $KAlO_2 \cdot 1.5H_2O$, which is readily hydrated as shown in the X700 image. Thus, the needle-like phase should be β″-alumina. Based on these experimental results, β″-alumina is confirmed to be stable up to 1600 °C and the eutectic temperature between $KAlO_2$ and β-alumina should be above 1600 °C.

6.3 Thermodynamic Models

6.3.1 Stoichiometric Compounds

The Gibbs energy of a stoichiometric compound is described as:

$$G_T^o = \Delta H_{298.15K}^o + \int_{298.15K}^{T} C_P dT - T(S_{298.15K}^o + \int_{298.15K}^{T} C_P / T dT) \quad (1)$$

where $\Delta H_{298.15K}^o$ and $S_{298.15K}^o$ are the standard enthalpy of formation and standard entropy at 298.15 K, respectively; C_P is the heat capacity as a function of temperature; T is the absolute temperature.

6.3.2 Liquid Solution

The Modified Quasichemical Model (MQM) in the pair approximation [18, 19] was employed to express the Gibbs energy function of the liquid oxide phase. The MQM takes into account the short-range ordering (SRO) of second-nearest-neighbor cations in the oxide melt. The cationic species in the liquid solution are K^+, Mg^{2+}, and Al^{3+}, while O^{2-} is a common anion. Based on

experimental observations of the so-called charge compensation effect in alkali aluminosilicate systems, an associate species of KAl^{4+} was also considered as an additional species [20, 21].

The quasichemical reaction considered in the binary oxide melt is:

$$(A-A)+(B-B)=2(A-B);\ \ \Delta g_{A-B} \tag{2}$$

where A and B are the cationic species in solution; $(A-B)$ represents a second-nearest-neighbor pair of A and B cations with a common O^{2-} anion; Δg_{A-B} is the Gibbs energy of the reaction, which is a model parameter. Δg_{A-B} can be expanded as a function of pair fractions and temperature:

$$\Delta g_{A-B}=\Delta g^{o}_{AB}+\sum_{i\geq 1} g^{i0}_{AB}X^{i}_{AA}+\sum_{j\geq 1} g^{0j}_{AB}X^{j}_{BB} \tag{3}$$

where Δg^{o}_{AB}, g^{i0}_{AB}, and g^{0j}_{AB} are parameters, which can be a function of temperature; X_{AA} and X_{BB} are the pair fractions of $(A-A)$ and $(B-B)$, respectively.

The Gibbs energy of the liquid solution is expressed as:

$$G^{so\ln}=(n_A g^{o}_{A}+n_B g^{o}_{B})-T\Delta S^{conf}+(n_{AB}/2)\Delta g_{A-B} \tag{4}$$

where n_i and g^{o}_{i} are the number of moles and the molar Gibbs energy of pure component *i*, respectively; n_{AB} is the number of moles of $(A-B)$ pairs; ΔS^{conf} is the configurational entropy of the solution expressed as a function of random distribution of quasichemical pairs based on one-dimensional Ising model [22]. The details of the thermodynamic equations for the MQM can be found in Ref. [18].

The SRO behavior in the liquid solution can be well described by setting the coordination numbers of cations. In this work, the coordination numbers of unary: K^+ (Z^K_{KK}), Mg^{2+} ($Z^{Mg}_{Mg\,Mg}$), Al^{3+} ($Z^{Al}_{Al\,Al}$), and KAl^{4+} (Z^{KAl}_{KAlKAl}) were set to be 0.6887, 1.3774, 2.0662, and 2.7549, respectively. Binary coordination numbers of $Z^K_{K\,Al}$ (=Z^{Al}_{AlK}) and $Z^K_{K\,KAl}$ (=Z^{KAl}_{KAlK}) were set to be 0.6887, and $Z^{Al}_{Al\,KAl}$ (= $Z^{KAl}_{KAl\,Al}$) was set to be 2.0662, and the rest of binary coordination numbers were set to be default values considering the unary coordination numbers. These coordination numbers are consistent with those used in the molten oxide database (FToxid) of the FactSage software [16].

The Gibbs energy of the ternary solution can be calculated using a so-called geometric interpolation model from the binary model parameters. Symmetric Kohler and asymmetric Toop-type interpolation models are commonly used for the ternary system [19]. For the K_2O-MgO-Al_2O_3 system, Δg_{K-Al} and Δg_{Mg-Al} are very negative while Δg_{K-Mg} is almost ideal. Hence, the ternary Gibbs energy was calculated using the asymmetric Toop interpolation technique with Al_2O_3 as an asymmetric component. Other pseudo-ternary systems involving $KAlO_2$: K_2O-$KAlO_2$-Al_2O_3, K_2O-$KAlO_2$-MgO, and Al_2O_3-$KAlO_2$-MgO systems employed the symmetric Kohler interpolation technique. The details of the interpolation method can be found elsewhere [23].

In the present study, the model parameter Δg_{Mg-Al} for the MgO-Al_2O_3 system was taken from the previous study [4]. Model parameters for the K_2O-Al_2O_3 system (in reality, K_2O-Al_2O_3-$KAlO_2$ solution) were optimized in this study to reproduce the phase diagram and thermodynamic property data. In the K_2O-MgO-Al_2O_3 system (in reality, K_2O-MgO-Al_2O_3-$KAlO_2$ solution), the liquid Gibbs energy was predicted using the above-cited interpolation models with no additional

parameters. That is, only binary solution parameters were used with the appropriate interpolation method.

6.3.3 Solid Solutions

There are two solid solution phases in the K_2O-Al_2O_3 and K_2O-MgO-Al_2O_3 systems: β- and β″-alumina. In the binary system, β-alumina has about 2-3 mol % excess K_2O from the stoichiometric $KAl_{11}O_{17}$ and β″-alumina has also about 2-3 mol % excess Al_2O_3 from ideal stoichiometry $KAl_{5.5}O_{8.75}$. In the ternary system, β″-alumina has about 10 mol % of MgO solubility, while only about 5-7 mol % excess MgO can dissolve in the β-alumina at 1400 °C.

The base crystal structures of β- and β″-alumina solutions are essentially the same. The schematics of lattice structure and conduction plane of β- and β″-alumina are presented in Fig. 6.2 (a) and (b), respectively. The structural data was taken from Collin *et al*. [24] and Boilot *et al*. [25] for β- and β″-alumina, respectively, and they were re-drawn using VESTA software [26]. According to the structural crystallographic studies [27-29], β-alumina is composed of two spinel (spinel-like) blocks with one conduction plane in between for the unit cell structure [27, 29]. β″-alumina is composed of three spinel blocks with two conduction planes [28]. In the spinel blocks, there are two tetrahedral sites and two octahedral sites for Al^{3+} ions. When MgO dissolves in these solutions, one of the two tetrahedral sites is predominantly occupied by Mg^{2+} according to experimental analyses [25, 29]. This site is generally known as the Al(2) site. In the structure of β- and β″-alumina, the conduction plane where ionic conduction happens, consists of Al-O-Al bonds and K^+ ions. The conduction planes can have two sites for K^+ ions and one site for O^{2-} ions. In earlier studies, Beevers-Ross (BR) and anti Beevers-Ross (aBR) were defined for K^+ sites, and mid oxygen (mO) for O^{2-} site [27]. More recent studies reported that K^+ ions are observed in slightly

shifted positions from their original BR and aBR sites (which are called as K(2) sites) when O^{2-} ions occupy mO site. [25, 29, 30]. The mO sites are predominantly occupied by additional interstitial O^{2-} ions due to the dissolution of K_2O. When Mg^{2+} ions substitute Al^{3+} in the Al(2) tetrahedral site, additional K^+ can enter the BR and aBR sites of β- and β″-alumina [24, 25]. Although β- and β″-alumina have different sizes of unit cells, the basic building block of both solution consists of one conduction plane with two of half spinel blocks (O_{17}) as shown in Fig. 6.2. Based on the structural information, the lattice structure of β- and β″-alumina can be formulated in the one unit cell (O_{17}) as follows:

$$[K^+, Va]_1^{BR}[K^+, Va]_1^{aBR}[Al^{3+}, Mg^{2+}]_2^{Al(2)}[O^{2-}, Va]_1^{mO}\, Al_9^{Al(other)}O_{17} \quad (5)$$

BR, aBR, Al(2), and mO stand for Beever-Ross, anti Beever-Ross, Al(2), and mid-oxygen site, respectively, followed by the notations reported in many crystallographic studies [24, 27, 30-32]. As K(2) sites are essentially the same as BR and aBR sites (no configurational entropy can be generated by K(2) sites), K(2) sites were not included in the present β- and β″-alumina model. Species in the same bracket can mix in the same sublattice. A proper sublattice structure is important to describe the configurational entropy of the solution.

The Gibbs energies of the β- and β″-alumina solutions were described within the framework of the Compound Energy Formalism (CEF) [33] considering the sublattice structure in Eq. (5):

$$G^{soln} = \sum_i \sum_j \sum_k \sum_l Y_i^{BR} Y_j^{aBR} Y_k^{Al(2)} Y_l^{mO} G_{ijkl}^o - T\Delta S^{conf} + G^E \quad (6)$$

where Y_i^{BR}, Y_j^{aBR}, $Y_k^{Al(2)}$, and Y_l^{mO} represent the site fractions of components *i*, *j*, *k*, and *l* in their respective sublattice; G_{ijkl}^o is the Gibbs energy of an end-member

$[i]^{BR}[j]^{aBR}[k]^{Al(2)}[l]^{mO}\,Al_9^{Al(other)}O_{17}$; ΔS^{conf} is the configurational entropy of the solution expressed as a function of random distribution of cations in each sublattice:

$$\Delta S^{conf} = -R\left(\sum_i Y_i^{BR}\ln Y_i^{BR} + \sum_j Y_j^{aBR}\ln Y_j^{aBR} + 2\sum_k Y_k^{Al(2)}\ln Y_k^{Al(2)} + \sum_l Y_l^{mO}\ln Y_l^{mO}\right) \quad (7)$$

and G^E is the excess Gibbs energy of the solution:

$$G^{soln} = \sum_a\sum_b\sum_c\sum_d\sum_e Y_a^m Y_b^m Y_c^n Y_d^p Y_e^q L_{ab;c;d;e}^{m;n;p;q} \quad (8)$$

where $L_{ab;c;d;e}^{m;n;p;q}$ is the interaction energy between cations *a* and *b* in the *m* sublattice when other sublattices of *n*, *p*, and *q* are occupied by cations of *c*, *d*, and *e*, respectively. The interaction parameter $L_{ab;c;d;e}^{m;n;p;q}$ is expressed using the Redlich-Kister polynomials as a function of site fractions.

In the present study, no excess Gibbs energy parameters were used for the β- and β″-alumina solutions. The main model parameter in the solution described by the CEF is the Gibbs energy of end-members. The β- and β″-alumina solutions contain 16 end-members, as listed in Eqs. 9 to 25. A schematic presentation of the solution Gibbs energy structure is depicted in Fig. 6.3. All end-members and charge-neutral composition lines are shown in the figure. For convenience, alphabetic abbreviations are used to represent each ionic species: K = K^+, M = Mg^{2+}, A = Al^{3+}, O = O^{2-}, and V stands for Vacancy. For example, G_{KVAO} stands for the Gibbs energy of the end-member containing K^+ in the first BR sublattice, Va in the second aBR sublattice, Al^{3+} in the third Al(2) sublattice, and O^{2-} in the fourth mO sublattice. The symbol Δ represents site exchange reactions which is used to determine the Gibbs energy of hypothetical end-member. These Δ parameters have physical meanings and are more logical approaches to determine hypothetical

end-member Gibbs energies than assigning arbitrary Gibbs energy value to the end-member. As β- and β″-alumina have very similar structures, the Gibbs energies of an end-member should be very close to each other. In the present study, the following procedure was used to determine the Gibbs energies of end-members of the solution.

Binary β-alumina

$$G_{KVAV} = G^{o}_{KAl_{11}O_{17}(\beta-alumina)} \tag{9}$$

$$G_{KKAO} = G_{KKAV} = \tfrac{1}{2}(G^{o}_{K_4Al_{22}O_{35}(\beta''-alumina)} + \Delta S^{conf} + G^{add(1)}) \tag{10}$$

Binary β″-alumina

$$G_{KKAO} = G_{KKAV} = \tfrac{1}{2}(G^{o}_{K_4Al_{22}O_{35}(\beta''-alumina)} + \Delta S^{conf}) \tag{11}$$

$$G_{KVAV} = G^{o}_{KAl_{11}O_{17}(\beta-alumina)} + G^{add(2)} \tag{12}$$

Common binary end-members

$$\Delta^2 = G_{KVAO} + G_{KKAV} - G_{KKAO} - G_{KVAV}, \qquad G_{KVAO} = G_{KVAV} + \Delta^2 \tag{13}$$

$$I^1 = G_{VKAV} - G_{KVAV}, \qquad G_{VKAV} = G_{KVAV} + I^1 \tag{14}$$

$$\Delta^5 = G_{KVAV} + G_{VKAV} - G_{KKAV} - G_{VVAV}, \qquad G_{VVAV} = 2 \cdot G_{KVAV} - G_{KKAV} + I^1 \tag{15}$$

$$I^2 = G_{VKAO} - G_{KVAO}, \qquad G_{VKAO} = G_{KVAV} + \Delta^2 + I^2 \tag{16}$$

$$\Delta^8 = G_{VVAV} + G_{VKAO} - G_{VKAV} - G_{VVAO}, \qquad G_{VVAO} = 2 \cdot G_{KVAV} - G_{KKAV} + \Delta^2 + I^2 \tag{17}$$

Ternary β- and β″-alumina

$$G_{KKMV} = G_{KVAV} + G^{add(K-Mg)} \tag{18}$$

$$G_{KVMV} = G_{KVAV} + G^{add(Va-Mg)} \tag{19}$$

$$\Delta^1 = G_{KVMO} + G_{KVAV} - G_{KVAO} - G_{KVMV}, \qquad G_{KVMO} = G_{KVAV} + G^{add(Va-Mg)} + I^1 \tag{20}$$

$$\Delta^3 = G_{KKAO} + G_{KKMV} - G_{KKMO} - G_{KKAV}, \qquad G_{KKMO} = G_{KVAV} + G^{add(K-Mg)} \tag{21}$$

$$\Delta^4 = G_{KVMV} + G_{VVAV} - G_{KVAV} - G_{VVMV}, \quad G_{VVMV} = 2 \cdot G_{KVAV} - G_{KKAV} + G^{add(Va-Mg)} + I^1 \tag{22}$$

$$\Delta^6 = G_{KKAV} + G_{VKMV} - G_{KKMV} - G_{VKAV}, \quad G_{VKMV} = 2 \cdot G_{KVAV} - G_{KKAV} + G^{add(K-Mg)} + I^1 \tag{23}$$

$$\Delta^7 = G_{VVMV} + G_{VVAO} - G_{VVAV} - G_{VVMO}, \quad G_{VVMO} = 2 \cdot G_{KVAV} - G_{KKAV} + G^{add(Va-Mg)} + \Delta^2 + I^2 \tag{24}$$

$$\Delta^9 = G_{VKAV} + G_{VKMO} - G_{VKMV} - G_{VKAO}, \quad G_{VKMO} = 2 \cdot G_{KVAV} - G_{KKAV} + G^{add(K-Mg)} + \Delta^2 + I^1 \tag{25}$$

The Gibbs energies of charge-neutral stable end-members of β-alumina (KVAV) and β″-alumina (0.5·KKAO + 0.5·KKAV) were first determined from the thermodynamic data in the binary K_2O-Al_2O_3 system. Then, the limited solubility ranges of both β- and β″-alumina solutions were reproduced using the Gibbs energy parameters, $G^{add(1)}$ for β-alumina and $G^{add(2)}$ for β″-alumina. Charged end-member of KVAO in Eq. 13 was determined by the site exchange reaction (Δ^2) with the end-members of β-alumina (KVAV) and β″-alumina (KKAO and KKAV). Phase diagram data were mainly considered to evaluate Δ^2. The end-member KVAO represents unstable β- and β″-alumina when excess O^{2-} occupy the mO sites without charge-balanced K^+ in aBR site. The inverse β-alumina, VKAV is modeled considering the inversion reaction from β-alumina (KVAV). The inversion parameter (I^1) was set to reproduce the K^+ distribution between BR and aBR site (Eq. 14). The end-member of VVAV was set based on the site exchange reaction Δ^5, which was set to be zero (Eq. 15). The Gibbs energy of VKAO (Eq. 16) is the determinant of the K^+ distribution between BR and aBR sites as it is for the VKAV (Eq. 14). Then, the VVAO was derived assuming $\Delta^8 = 0$ in Eq. 17. The solubility of MgO was modeled using an additional Gibbs energy of $G^{add(K-Mg)}$ to the Gibbs energy of β-alumina (KVAV) to determine the Gibbs energy of KKMV end-member (Eq. 18). KKMV represents the charge-balanced substitution of Al^{3+} with Mg^{2+} in

the Al(2) site coupled with additional K^+ in aBR site. Mg^{2+} substitution in Al(2) site without charge compensating K^+ in aBR site was represented by KVMV in Eq. 19. Other hypothetical end-members containing Mg^{2+} in the ternary system were modeled with an assumption that the site exchange reaction energy Δ is equal to zero (Eqs. 20-25). In fact, the solubility of MgO in β- and β″-alumina is only determined by the Gibbs energies of KKMV and KVMV.

6.4 Thermodynamic Evaluation and Optimization

All phase diagram and thermodynamic data of the K_2O-Al_2O_3 and K_2O-MgO-Al_2O_3 systems available in the literature were critically reviewed. Then, new experimental key phase diagram data from this study and all reliable experimental data in the literature were simultaneously considered to obtain a set of thermodynamic functions for all stable phases in these two systems. In the present optimization, the thermodynamic data of solid and liquid K_2O, MgO, and Al_2O_3 and all gas species in this ternary system were taken from the FACT Pure substance database [16], where these data were originally from thermodynamic compilations [36-41]. The model parameters of the MgO-Al_2O_3 [4] and K_2O-MgO systems [7] were taken from the previous studies without modification. Optimized thermodynamic properties of compounds and model parameters of the solutions in the present study are listed in Tables 6.1 and 6.2, respectively.

6.4.1 The K_2O-Al_2O_3 System

The optimized phase diagram of the K_2O-Al_2O_3 system is presented in Fig. 6.4 along with all the experimental data. This binary system contains 6 stable solid phases and a liquid phase at 1 atm pressure. The 6 stable solid phases are K_2O, Al_2O_3 (α-corundum), $KAlO_2$ (low- and high-temperature meta-oxide), $KAl_{11}O_{17}$ (β-alumina), and $KAl_{5.5}O_{8.75}$ (β″-alumina). There is no mutual solubility between K_2O and Al_2O_3. β- and β″-alumina have limited solubility ranges as can be seen

in Fig. 6.4. Due to the high hygroscopicity and volatility of K_2O, the phase diagram of the K_2O-rich region has not been well studied in the literature.

The polymorphic transition of $KAlO_2$ from low-temperature orthorhombic *Pbca* to high-temperature cubic $Fd\bar{3}m$ has been studied by many researchers and reported from 500 to 600 °C (773 to 873 K) using various techniques including DTA, high-temperature XRD, X-ray fluorescence (XRF), neutron diffraction, and calorimetry [42-54]. In the present study, the first order transition of $KAlO_2$ at 537 °C (810 K) measured using drop calorimetry [47] was considered to be reliable among others. The phase transition at 1350 °C (1623 K) reported by De Kroon *et al*. [51] was considered inaccurate because there was no clear transition observed on their reported DTA curves. Roth [13] first estimated the melting point of $KAlO_2$ to be at 2150 ± 100 °C (2423 ± 100 K) from the samples in open Ir crucibles. Due to open crucible experiments, there would be significant loss of K at high temperatures, and shift the target composition. In the same study, Roth also used sealed Mo capsules to investigate the melting temperature. He reported the rupture of Mo capsules at about 2260 °C (2533 K), which may imply that the melting point of $KAlO_2$ should be close to 2260 °C (2533 K). In the present study, the melting point of $KAlO_2$ was optimized to 2235.2 °C (2508.2 K) considering all experimental phase diagram data reported for the K_2O-Al_2O_3 and K_2O-Al_2O_3-SiO_2 systems.

Brownmiller [42] first found the formation of K β-alumina, but the exact composition was not determined. Beevers and Ross [27] reported β-alumina at the stoichiometry of $KAl_{11}O_{17}$. Based on crystal structure investigations using XRD, Yamaguchi and Suzuki [28] proposed $KAl_{11}O_{17}$ and $KAl_{5.34}O_{8.5}$ as the ideal formulae for hexagonal $P6_3mmc$ β-alumina and trigonal $R\bar{3}m$ β″-alumina,

respectively. In Yamaguchi and Suzuki's work, another K β′-alumina was reported at $K_{1.5}Al_{10.83}O_{17}$, however this is within the framework of K β-alumina solution.

The homogeneity range of typical K β-alumina was reported to be from $K_{1.25}Al_{11}O_{17.13}$ to $K_{1.3}Al_{11}O_{17.15}$ in Refs. [25, 29, 35]. That is, the solubility range of K β-alumina is about 1.87 to 2.23 mol % excess K_2O from the stoichiometry of $KAl_{11}O_{17}$. In this study, the nominal composition for K β-alumina was set to be $KAl_{11}O_{17}$ and that of K β″-alumina at $KAl_{5.5}O_{8.75}$, which are close to experimental data by Yamaguchi and Suzuki [28]. The solubility range of K β-alumina was reproduced based on the results from Dernier and Remeika [29] and Collin *et al*. [35]. Since there is no clear solubility limit of K β″-alumina reported in the literature, the present solubility range of K β″-alumina was modeled based on that of Na β″-alumina in the Na_2O-Al_2O_3 system [55].

De Kroon *et al*. [51] studied the $KAlO_2$ compound and confirmed its stability up to 1950 °C (2223 K). The authors observed a small endothermic peak between 1700 and 1780 °C (1973 and 2053 K) using DTA. This peak was attributed to the decomposition of β″-alumina into $KAlO_2$ and β-alumina. In the previous thermodynamic assessments of Refs. [9-11], β″-alumina was calculated to decompose at about 1146 °C (1419 K). In this study, the decomposition temperature of β″-alumina was optimized to be at 1653.0 °C (1926.0 K), which is in good agreement with our own experimental results in Section 6.2.4.

Eliezer and Howald [8] performed thermodynamic assessments to study the melting behavior of K β-alumina. They found that K β-alumina melted incongruently at 1877 °C (2150 K) to α-Al_2O_3 and liquid. This thermodynamic assessment was based on the vapor pressure measurements of Plante *et al.* [56], the activity coefficient of K_2O in the liquid phase and thermodynamic properties

of $KAlO_2$ from Spencer *et al*. [57], and thermodynamic properties of K_2O and Al_2O_3 from Refs. [58, 59]. The reported melting point and the enthalpy of formation at 298.15 K of $KAlO_2$ reported by Spencer *et al*. are proved to be inaccurate according to recent experimental measurements [13, 47, 60]. In this study, the melting behavior of K β-alumina was optimized based on more reliable thermodynamic property data: activity, standard enthalpy of formation at 298.15 K, and heat capacity data for $KAlO_2$. As a result, the activity data in the two-phase regions of β″- and β-alumina, and of β″-alumina and $KAlO_2$ can be well reproduced. The results will be discussed below.

The phase diagram of the K_2O-Al_2O_3 system was first investigated by Roth [13] using equilibration/quenching experiments and XRD analysis with samples sealed in Pt tubes. The liquidus of $KAlO_2$ was determined and the eutectic temperature between $KAlO_2$ and β-alumina was measured to be at about 1910 °C (2183 K). Moya *et al*. [12] investigated the phase diagram between 1200 and 1700 °C (1473 and 1973 K) using sealed Pt capsules, DTA, and equilibration/quenching method followed by XRD. The eutectic temperature between $KAlO_2$ and β-alumina was found to be at 1450 °C (1723 K) using DTA, and it was between 1400 and 1500 °C (1673 and 1773 K) based on the results of the equilibration experiments. Roth indicated that the β-alumina phase has about 5 mol % K_2O solubility in the temperature range of 1000 to 1600 °C (1273 to 1873 K). Moya *et al*. reported the maximum solubility range of the β-alumina phase from 83 to 91 mol % Al_2O_3 at about 1450 °C (1723 K). Neither Roth nor Moya *et al.*'s studies found the existence of the β″-alumina phase. Instead, the proposed stability region of K β-alumina in their work seems to be for both K β-alumina and β″-alumina phases. Schaefer *et al*. [14] reported the K_2O-Al_2O_3 phase diagram based on their DTA measurements and the literature data of K β- and β″-alumina [61]. Schaefer *et al*. proposed 1700 °C (1973 K) as the decomposition temperature

of β″-alumina and 1920 °C (2193 K) for β-alumina in their phase diagram, but no details of their DTA experiments were provided.

In the present optimization, the experimental data from Roth [13] was considered to be reliable for the liquidus of the K_2O-Al_2O_3 system. The eutectic temperature reported by Moya *et al*. [12] is not reasonable according to the experimental results of this study (discussed in Section 6.2.4). The experimental data from Schaefer *et al*. [14] is obviously not in equilibrium conditions, so their data should not be used for the thermodynamic optimization. Although the melting point of $KAlO_2$ from Roth has large uncertainties, it is the only experimental data available in the literature. Through systematic studies on multi-component systems containing K_2O-Al_2O_3, the melting point of $KAlO_2$ and the eutectic temperature between $KAlO_2$ and K β-alumina were optimized to be at 2235.2 °C (2508.2 K) and 1918.8 °C (2191.8 K), respectively. The melting point of K β-alumina was predicted based on its thermodynamic properties determined from the activity data between K β-alumina and α-Al_2O_3 [62]. K β-alumina was calculated to melt incongruently at 1982.4 °C (2255.4 K) into α-Al_2O_3 and liquid. The thermodynamic properties of K β″-alumina were optimized using activity and partial pressure data in the two-phase regions of K β″-alumina and β-alumina, and of K β″-alumina and $KAlO_2$, respectively [56, 63, 64]. The decomposition of K β″-alumina into $KAlO_2$ and K β-alumina is calculated to occur at 1653.0 °C (1926.0 K) in the present study.

The enthalpy of formation ($\Delta H^{o}_{298.15K}$) of the $KAlO_2$ compound was determined to be -1140.5 kJ·mol^{-1} by Bennington and Daut [60] using acid solution (HF) calorimetry. $\Delta H^{o}_{298.15K}$ of -1135.8 kJ·mol^{-1} was also reported by Spencer [57] without experimental details. The low-temperature heat capacity (C_P) of $KAlO_2$ was measured from 4.87 to 303.07 K by Beyer *et al*. [47] using

adiabatic calorimetry. From the low-temperature C_P data, the standard entropy at 298.15 K ($S^o_{298.15K}$) was calculated to be 88.6 J·mol^{-1}·K^{-1}. Beyer *et al*. also measured the heat content ($H_T - H_{298.15K}$) from 406.1 to 1197.8 K using drop calorimetry. The enthalpy of transition (ΔH^o_{tr}) of low- to high-temperature $KAlO_2$ was measured to be 1.295 kJ·mol^{-1}. Husheer *et al*. [48] reported ΔH^o_{tr} to be 1.059 kJ·mol^{-1} from their DSC experiments. In the present thermodynamic optimization, $\Delta H^o_{298.15K}$ from Bennington and Daut and $S^o_{298.15K}$ from Beyer *et al*. were employed. The high-temperature C_P was derived using the heat content data from Beyer *et al*. The C_P and heat content of $KAlO_2$ are plotted in Fig. 6.5 (a) and (b), respectively. The transition temperature of $KAlO_2$ was optimized to be at 536.85 °C (810 K) with a transition enthalpy of 1.295 kJ·mol^{-1}, based on the results of Beyer *et al.* [47].

The activity of K_2O (reference to solid state) in the two-phase region of β-alumina and α-Al_2O_3 was investigated by several researchers. Kumar and Kay [65] measured it using an oxygen concentration cell between 697 and 807 °C (970 and 1080 K). Itoh and Kozuka [62], and Kale and Jacob [66] used a solid-state galvanic cell in the temperature ranges of 688 to 1001 °C (961 to 1274 K) and 327 to 727 °C (600 to 1000 K), respectively, to measure the activity of K_2O. Based on their activity data, these studies also reported the standard Gibbs energy of formation (ΔG^o_f) of β-alumina from their corresponding oxide references. The experimental results of Itoh and Kozuka [62] and Kale and Jacob [66] are in reasonable agreement with each other, but they are not consistent with Kumar and Kay's data [65]. A possible source of error in Kumar and Kay's work may come from the design of the concentration cell. The large difference of oxygen potential of the two electrodes in their work could result in significant semipermeability flux of oxygen in the electrolyte. In the present study, the data from Itoh and Kozuka were considered to be reliable.

Itoh and Kozuka also accurately measured the Na_2O activity in the two-phase region of Na β-alumina and α-Al_2O_3 [67], which is in good agreement with phase diagram data based on the thermodynamic optimization study of the Na_2O-Al_2O_3 system [68]. Shqau and Näfe [63] investigated the activity of K_2O in the two-phase region of K β- and β″-alumina using an oxygen concentration cell with yttria-stabilized zirconia electrolyte. These measurements are considered to be accurate, because stable K β- and β″-alumina were identified in their samples by XRD in the temperature range of 375 to 600 °C (648 to 873 K). They also calculated ΔG_f^o of β″-alumina using the ΔG_f^o data of K_2O from NIST-JANAF [69] and that of K β-alumina from Kale and Jacob [66]. All the experimental activity and Gibbs energy data from the literature are depicted in Fig. 6.6 (a) and (b), respectively, in comparison with the present optimization results. The K_2O activity data for the two-phase regions of K β-alumina and α-Al_2O_3, and of K β- and β″-alumina are well reproduced considering the actual experimental error. Plante *et al*. [56] measured the partial pressure of potassium (P_K) in the two-phase regions of $KAlO_2$ and β″-alumina, and of β-alumina and α-Al_2O_3 using the Knudsen effusion mass spectrometry. Parker *et al*. [64] also reported P_K in the two-phase region of $KAlO_2$ and β″-alumina using mass spectrometry. These thermodynamic data were simultaneously considered with the homogeneity range in the phase diagram for the optimization of the model parameters of β- and β″-alumina. As discussed in Section 6.3, the $\Delta G^o_{KAl_{11}O_{17}(\beta-alu\ \min\ a)}$ and $\Delta G^o_{K_4Al_{22}O_{35}(\beta"-alu\ \min\ a)}$ were fixed first and then additional parameters listed in Table 6.2 were optimized to reproduce all thermodynamic and phase diagram data. The calculated thermodynamic data for β- and β″-alumina are compared with experimental data [56, 64] in Fig 6 (c). Small discrepancies of P_K were found in the two-phase region of β-alumina and

α-Al_2O_3, while the calculated activity of K_2O in this region shows a reasonable agreement with the results from Itoh and Kozuka [62] and Kale and Jacob [66].

6.4.2 The K_2O-MgO-Al_2O_3 System

The optimized isothermal sections of the K_2O-MgO-Al_2O_3 system at 1400 and 1300 °C are calculated in Fig. 6.7 (a) and (b), respectively. The predicted liquidus projection of the system is depicted in Fig. 6.7 (c).

The melting behavior of Mg-stabilized K β″-alumina was investigated by Schaefer *et al*. [14, 70, 71] using $K_{1.7}Mg_{0.7}Al_{10.3}O_{17}$, which was found to be stable up to about 1700 °C. A significant evaporation of K_2O was detected at 1700 °C. Thus, the melting point of Mg-stabilized β″-alumina can be close to 1700 °C considering the significant evaporation might result from liquid formation. The formation of β-alumina could not be observed while decomposing β″-alumina, which implies that the solubility of MgO in β-alumina is smaller than that in β″-alumina. This is consistent with the stability regions of β- and β″-alumina in the K_2O-MgO-Al_2O_3 phase diagram reported in Refs. [15, 72].

Other stoichiometric compounds β‴- and β⁗-alumina were reported in the literature. Schaefer *et al*. [14, 70] found β‴-alumina in pseudoboehmite-based samples and β⁗-alumina in boehmite-based samples. Roth [13] mentioned β″-, β‴-, and β⁗-alumina in his study of the K_2O-MgO-Al_2O_3 system. However, no details were given. Blanc *et al*. [73] identified the structure of β‴-alumina to be hexagonal ($P6_3mmc$) using Transmission Electron Microscopy (TEM) and XRD analyzer. This result was also confirmed by other structural studies [74, 75] using the same experimental techniques. In the phase diagram measurements by Van Hoek *et al*. [15], who used sealed Mo capsules, only β‴-alumina was found at 1400 °C. In the present study, β‴-alumina is

included in the thermodynamic optimization based on the phase diagram measurements by Van Hoek *et al*. as well as structural studies [73-75]. β‴-alumina is not considered because there is no clear evidence in the literature regarding the structure and stability in equilibrium condition.

For the overall phase diagram of the K_2O-MgO-Al_2O_3 system, Van Hoek *et al*. [15] performed equilibration/quenching experiments followed by XRD phase analysis. To minimize the hydration of K_2O contained in samples, a glove box was used for sample preparations and XRD phase analysis was performed under vacuum condition. Sealed Mo capsules were used to prevent the volatile loss of K_2O. The authors found a ternary compound β‴-alumina and maximum about 10 mol % solubility of MgO in β″-alumina at 1400 ºC. They also conducted experiments at 1100 ºC. However, the results were not reliable due to slow kinetics at lower temperatures. Ham *et al*. [72] and Kim and Lim [76] studied the reaction kinetics between β-alumina and β″-alumina with open crucibles at different temperatures. The maximum solubility of MgO in β″-alumina was measured to be $K_{1.67}Mg_{0.67}Al_{10.33}O_{17}$ at 1300 °C. In the experiments performed at lower temperatures of about 1000 °C, β″-alumina was not formed due to the slow reaction kinetics. At about 1200 °C, the thermodynamically stable $KAlO_2$ first appeared, and then, β-alumina, which has a similar structure to α-Al_2O_3 (hexagonal), was formed. When temperature was set at 1400 and 1500 °C, the volatile loss of K_2O was significant, and as a result, β″-alumina could readily transform into β-alumina. Considering reaction kinetics and volatile loss of K_2O, the solubility of MgO in β″-alumina can be larger than $K_{1.67}Mg_{0.67}Al_{10.33}O_{17}$ at 1300 °C.

In the present study, the optimized isothermal section at 1400 °C in Fig. 6.7 (a) is in good agreement with van Hoek *et al*. [15]. The solubility of MgO in β″-alumina at 1300 °C reported by Ham *et al*. [72] and Kim and Lim [76] are also in reasonable agreement with the present

optimization as depicted in Fig. 6.7 (b). About 10 mol % of MgO in β″-alumina is calculated in the present modeling study. The calculated liquidus surface of the K_2O-MgO-Al_2O_3 system is shown in Fig. 6.7 (c), which is the first report of eutectic points in this ternary system.

The $S^o_{298.15K}$ and C_P of β-, β″-, and β‴-alumina were first approximated using the Neumann-Kopp rule (NKR) using the pure substance data of K_2O, MgO, and Al_2O_3 from the FToxid database [16]. Afterwards, phase diagrams were simultaneously reproduced by optimizing the model parameters of the liquid and solid solutions and $\Delta H^o_{298.15K}$ of the solid compounds. The optimized thermodynamic properties of the compounds are listed in Table 6.1 and are compared with the experimental and estimated data from the literature. The optimized model parameters for the liquid and solid solutions are listed in Table 6.2.

6.5 Cation Distribution and Ionic Conductivity

To understand the solution mechanism of K β- and β″-alumina, the structural studies of Na β- and β″-alumina were reviewed simultaneously. This is because the structure of K and Na β- and β″-alumina are similar [25, 31], and the solution mechanism of Na β- and β″-alumina could give a clue for K β- and β″-alumina. Na β- and β″-alumina have $P6_3mmc$ and $R\bar{3}m$ structures [77, 78], which are identical to the structures of K β-alumina and K β″-alumina (see Section 6.4.2), respectively.

There are two solution mechanisms known for β- and β″-alumina. Usual non-stoichiometry in the β-alumina solution is found to be at $K_{1.3}Al_{11}O_{17.15}$ in the K_2O-Al_2O_3 binary system [24, 25, 35] and at $K_{1.6}Mg_{0.6}Al_{10.4}O_{17}$ for β″-alumina in the K_2O-MgO-Al_2O_3 ternary system [24, 25]. When additional K^+ ions are introduced in the conduction plane (see Fig. 6.2 (b)), interstitial O^{2-} ions are

coupled with K^+ ions near mO site for the charge balance. This happens associated with so-called Frenkel defects or Roth-Reidinger defects in the spinel block [24, 25, 31, 61]. By substituting the Al^{3+} with mono or divalent cations, more than 30 % additional alkali ions can be obtained in the conduction plane. For example, Mg^{2+} ions substitute Al^{3+} ions in Al(2) tetrahedral sites [24, 25], and provide (-) charges to the excess K^+ ions for the charge balance. The solubility limit of MgO is about 10 mol % in β″-alumina, which can make 1.66 moles of K^+ ions in the conduction plane in the unit cell of O_{17} [15, 24, 25, 72, 76]. The conduction plane is loosely packed with K^+ and O^{2-} ions. It has nearly two-dimensional K^+ diffusion, which can make high ionic conductivities in the β- and β″-alumina structures. The ionic conductivity varies with the cationic distribution in the structure.

Conduction happens with K^+ ions hopping between BR and aBR sites, according to the Na β-alumina studies [31, 79, 80]. In the stoichiometric β-alumina, all K^+ ions are perfectly ordered in BR sites. When more K^+ ions are introduced in the β-alumina, it contributes to the conductivity increase through making the structure more disordered. However, when the charge-balanced O^{2-} ions are introduced together with K^+ ions, it decreases the conductivity as it reduces the mobility of adjacent K^+ ions by blocking the conductive channels. To minimize this adverse effect from additional O^{2-} ions, substitution of Al^{3+} ions by Mg^{2+} ions can essentially avoid pairing O^{2-} with K^+ in the conduction plane [81]. In β″-alumina, BR and aBR sites are crystallographically and energetically equivalent [25, 78]. The activation energy for ionic diffusion is smaller and more available sites are given to K^+ ions compared to β-alumina. This will increase the ionic conductivity in β″-alumina as well as decrease interstitial O^{2-} ions.

Quantitative calculation of ionic site occupations can give a good insight on the ionic conductivity in β- and β″-alumina. This can be calculated from the present β- and β″-alumina solution model. Several studies were performed to measure site occupations in K β- and β″-alumina as shown in Fig. 6.8. Dernier and Remeika [29] measured site occupations of K^+ ions in the β-alumina (nominal composition of $K_{2.5}Al_{21.83}O_{34}$) using XRD. Site occupation was found to be 53.8 % in BR sites and 46.2 % in K(2) sites. No significant amount of K^+ ions were found in aBR sites. Collin *et al*. [35] reported site occupations in BR, K(2), and aBR sites for the $K_{2.59}Al_{21.86}O_{34}$ sample using XRD. They found 10.8 % of K^+ ions in aBR sites, 60.2 % and 30.0 % in BR and K(2) sites, respectively. The authors mentioned that the discrepancies from Dernier and Remeika are probably due to different sample preparation conditions. Collin *et al*. produced the β-alumina at high temperatures, while Dernier and Remeika obtained the samples from flux method at low temperatures. Later, Collin *et al*. [24] reported site occupations of binary β-alumina and Mg-doped β-alumina (ternary) using XRD and diffuse scattering method. Almost no O^{2-} ions were found at the interstitial mO sites for the Mg-doped β-alumina. Site occupations of K^+ were found to be 61.5 % in BR, 34.6 % in K(2), and 3.9 % in aBR sites for binary β-alumina. Those for the Mg-doped β-alumina are 42.2 % in BR + aBR, and 57.8 % in K(2) sites. Boiloet *et al*. [25] reported the K^+ occupations at BR + aBR and K(2) sites for the Mg-doped β″-alumina using XRD and X-ray diffuse scattering method. About 9.1 mol % MgO was added into β″-alumina, 61.6 % were found in K(2) sites and 38.4 % in BR + aBR sites.

These experimental data are compared with the present calculations in Fig. 6.8 (a) and (b). In the present β- and β″-alumina model, K(2) sites are not included as they are essentially the same sites as BR or aBR, slightly shifted due to the presence of O^{2-} in mO sites. Therefore, site occupation

(%) of K^+ between BR, aBR. and K(2) were recalculated using the site fractions obtained for the K^+, O^{2-}, and Mg^{2+} from the present study, according to the following relationships.

$$\%BR = \left[Y_{BR} - Y_{BR}(2Y_{Mg-Al(2)}) - \left(\frac{2Y_{mO}}{(Y_{BR} + Y_{aBR})} \right) \right] \cdot \frac{100}{(Y_{BR} + Y_{aBR})} \tag{26}$$

$$\%aBR = \left[Y_{aBR} - Y_{aBR}(2Y_{Mg-Al(2)}) - \left(\frac{2Y_{mO}}{(Y_{BR} + Y_{aBR})} \right) \right] \cdot \frac{100}{(Y_{BR} + Y_{aBR})} \tag{27}$$

$$\%K(2) = \left[Y_{BR}(2Y_{Mg-Al(2)}) + Y_{aBR}(2Y_{Mg-Al(2)}) + \left(\frac{4Y_{mO}}{(Y_{BR} + Y_{aBR})} \right) \right] \cdot \frac{100}{(Y_{BR} + Y_{aBR})} \tag{28}$$

where Y_{BR} and Y_{aBR} are the calculated site fractions of K^+ ions in BR and aBR sites, respectively; Y_{mO} and $Y_{Mg-Al(2)}$ are the calculated site fractions of O^{2-} in mO site and Mg^{2+} in Al(2) site, respectively. The equations were derived based on the neutron diffraction study from Roth *et al*. [31]. The authors investigated the $Na_{1.18}Al_{11}O_{17.09}$ sample at 80 K and found that one additional interstitial oxygen in the conduction plane re-located two adjacent Na^+ ions from BR site and two Na^+ ions from aBR to near mO positions. In the Mg-doped β″-alumina sample at 298.15 K, half of the K^+ ion density from BR (or aBR) was shifted to mO site. The Mg content was mentioned to be somewhat greater than 2/3 per spinel block with their best refinement of site occupation parameters. Although the quantitative effect of Mg^{2+} is difficult to be known from Roth *et al*.'s study, 1:1 ratio of charge-balanced effect can reasonably be assumed for the Mg^{2+} addition. Therefore, the effects of interstitial O^{2-} and additional Mg^{2+} are employed as shown in Eqs. 26 to 28: two times of O^{2-} (Y_{mO}) per total K^+ ions ($Y_{BR} + Y_{aBR}$) can shift K^+ in BR and aBR sites to K(2) site; the total Mg^{2+} addition ($2Y_{Mg-Al(2)}$) shift K^+ in BR and aBR sites to K(2) site.

The cation distribution calculations of this study were performed at 500 °C to compare with the experimental data from Refs. [24, 25, 29, 35]. Unfortunately, it is difficult to know the exact temperature corresponding to the quenched structure. Discrepancies between aBR and K(2) can be due to different sample preparation conditions. K β- and β″-alumina were made from ionic exchange from Na β- and β″-alumina samples. In Dernier and Remeik's study [29], the Na β- and β″-alumina were made by the flux method at 1300 °C. In Collin *et al*.'s work [24], Na β- and β″-alumina were synthesized using the self-crucible heating method with starting materials melted at 2000 °C and cooled down. The self-crucible heating method was used in Boilot *et al*.'s study [25] to melt the samples at 1800 °C and slowly cooled down. These different synthesizing methods can lead to slightly different base structures of K β- and β″-alumina, there should be more K^+ ions in aBR sites in the structure made at high temperatures based on the experimental results for Na β″-alumina [31]. No experimental study clearly indicates what would be the equilibrium temperature of β- and β″-alumina samples and whether the samples were quenched or not. As cation distribution is depending on the temperature, the quenching temperature is very important to analyze the structural information. Due to the lack of this information, we assumed 500 °C for the experimental structure data.

Fig. 6.8 (a) shows the variation of K^+ site distribution with K_2O non-stoichiometry in the K_2O-Al_2O_3 binary system. The stoichiometric K β-alumina is located at 8.5 mol % K_2O. The calculated BR, aBR, and K(2) occupations are in good agreement with the experimental data considering the discrepancies within the corresponding data set. These discrepancies between experimental data set possibly come from different sample preparations. Fig. 6.8 (b) shows the calculated K^+ site distribution in ternary solution. In the calculation, MgO is added gradually to the binary β″-

alumina with 90 mol % Al_2O_3. The results of Collin *et al*. [35] and Boilot *et al*. [25] were well reproduced in the present study.

Because no experimental data were found regarding the temperature effect, Molecular Dynamics (MD) simulations for Na β-alumina were compared in Fig. 6.9 with the K β-alumina results from the present study. Beckers *et al*. [34] performed MD calculations using a hybrid of the two-body and three-body interatomic potentials for stoichiometric β-alumina (91.7 mol % Al_2O_3 in the binary system), non-stoichiometric β-alumina (90.1 mol % Al_2O_3 in the binary system), Mg-doped (1) β-alumina with 1.7 mol % excess MgO and Na_2O/Al_2O_3=0.1, and Mg-doped (2) β-alumina with 3.5 mol % excess MgO and Na_2O/Al_2O_3=0.11. As can be seen from Fig. 6.9, the random distribution increases with temperature. Calculations from the present study are in reasonable agreement with the MD simulation results. The effect of temperature, which generates inverse β-alumina with BR site vacancies, is well reproduced. The predicted BR site vacancies in β-alumina in the binary system are presented in Fig. 6.10. Addition of K_2O in the stoichiometric β-alumina creates permanent BR vacancies as inferred from the experimental observations by Roth *et al*. [31]. At 500 °C, more BR vacancies are created with addition of K_2O compared to the one at 1000 °C. This is because vacancies in BR at 1000 °C are already more than double the quantity at stoichiometric β-alumina compared to 500 °C. The random distribution due to increasing temperature is the dominant factor at 1000 °C. Maximum BR site vacancy can be seen for both temperatures in a composition range between 12 and 13.3 mol % K_2O. When actual K^+ ions in the conduction plane exceed 1.5 to 1.68 mole fractions (unit cell of O_{17}), BR and aBR sites need to accommodate K^+ ions simultaneously.

Boilot *et al*. [25] studied the effect of lattice structure in β- and β″-alumina on ionic conductivity. The authors found that K^+ ions in the conduction plane of β-alumina make the conduction plane more compact, while K^+ in β″-alumina have an opposite effect. Thus, the intersite distances between K^+ and O^{2-} are much smaller in β-alumina. In other words, more pairing occurs in β-alumina, and the conductivity is lower in β-alumina than β″-alumina. In Mg-dopped β- or β″-alumina, the ionic conductivity increases significantly compared to binary β- or β″-alumina. This is because the amount of interstitial oxygens in the conduction plane (i.e. mO in the model) decreases significantly with the Mg^{2+} addition. In the case of binary solid solutions, additional K^+ ions are always paired with interstitial oxygens in mO sites for the charge balance. Therefore, the mobility of K^+ ions is low due to strong interactions with paired oxygens. These paired oxygens simultaneously deactivate the conduction channels as well. However, when Mg^{2+} is added in the solution, K^+ occupation increases in aBR sites and O^{2-} occupation decreases in mO sites. Although direct ionic conductivity calculations are not possible from the present study, the amount of effective K^+ ions for conduction can be predicted from the present model. The predicted results of O^{2-} site occupations with total K^+ ions in the conduction plane are plotted together for the binary β-alumina and ternary Mg-doped β″-alumina solid solutions in Fig. 6.11. In the case of binary β-alumina shown in Fig. 6.11 (a), the amount of total K^+ ions increases with the addition of K_2O. The same trend can be seen for the interstitial O^{2-} ions in mO sites. However, in the case of Mg-doped β″-alumina shown in Fig. 6.11 (b), O^{2-} ions in mO sites decrease while total K^+ ions in the conduction plane increase rapidly. Site occupations of K^+, O^{2-}, Mg^{2+}, as well as Vacancy generations in the lattice structure can be calculated from the present model at any compositions and temperatures within the experimental error range. Quantitative conductivity calculations

would also be possible if accurate diffusion properties of the K^+ ions in the conduction plane were available.

6.6 Summary

The present thermodynamic modeling for the K_2O-Al_2O_3 and K_2O-MgO-Al_2O_3 systems successfully reproduced all reliable experimental phase diagram and thermodynamic property data in the literature. The present experimental results confirmed the thermal stability of β″-alumina up to 1600 °C. In particular, the K β- and β″-alumina solid solutions were described by the CEF considering the accurate sublattice structures. For the first time, thermodynamic and structural properties of K β and β″-alumina can be successfully described using classical thermodynamic calculations. Many site occupation calculations were performed to predict the ionic distributions of K^+, Mg^{2+}, and O^{2-} depending on the composition and temperature. The present model for β and β″-alumina can be used for the prediction of electronic properties if it is in conjunction with ionic diffusivity.

Acknowledgments

Financial supports from Tata Steel Europe, POSCO, Nucor Steel, Rio Tinto Iron and Titanium, Hyundai Steel, Nippon Steel and Sumitomo Metals Corp., JFE Steel, Voestalpine, RHI, and the Natural Sciences and Engineering Research Council of Canada are gratefully acknowledged. Authors (D.-G. Kim and E. Moosavi-Khoonsari) also acknowledge the McGill Engineering Doctorate Award (MEDA) from McGill University.

References

[1] M.A.K. Lodhi, P. Vijayaraghavan, A. Daloglu, An overview of advanced space/terrestrial power generation device: AMTEC, J. Power Sources 103(1) (2001) 25-33.
[2] A. Barkan, T.K. Hunt, B. Thomas, Potassium AMTEC Cell Performance, SAE International, 1999.
[3] M.S. El-Genk, J.-M.P. Tournier, AMTEC/TE static converters for high energy utilization, small nuclear power plants, Energy Convers. Manage. 45(4) (2004) 511-535.
[4] I.-H. Jung, S.A. Decterov, A.D. Pelton, Critical thermodynamic evaluation and optimization of the MgO-Al2O3, CaO-MgO-Al2O3, and MgO-Al2O3-SiO2 systems, J. Phase Equilib. Diffus. 25(4) (2004) 329-345.
[5] H. Mao, M. Selleby, B. Sundman, A re-evaluation of the liquid phases in the CaO–Al2O3 and MgO–Al2O3 systems, Calphad 28(3) (2004) 307-312.
[6] T. Zienert, O. Fabrichnaya, Thermodynamic assessment and experiments in the system MgO–Al2O3, Calphad 40 (2013) 1-9.
[7] D.G. Kim, B. Konar, I.H. Jung, Coupled Experimental Study and Thermodynamic Optimization of the K2O-MgO and K2O-MgO-SiO2 Systems, To be submitted (2017).
[8] I. Eliezer, R.A. Howald, High-temperature thermodynamics and phase equilibria in the potassium oxide-aluminum oxide system, High Temp. Sci. 10 (1978) 1-16.
[9] G. Eriksson, P. Wu, A.D. Pelton, Critical evaluation and optimization of the thermodynamic properties and phase diagrams of the magnesia-alumina, manganese(II) oxide-Al2O3, ferrous oxide-Al2O3, sodium oxide-Al2O3, and potassium oxide-Al2O3 systems, CALPHAD: Comput. Coupling Phase Diagrams Thermochem. 17 (1993) 189-205.
[10] K.E. Spear, M.D. Allendorf, Thermodynamic analysis of alumina refractory corrosion by sodium or potassium hydroxide in glass melting furnaces, J. Electrochem. Soc. 149(12) (2002) B551-B559.
[11] E. Yazhenskikh, K. Hack, M. Mueller, Critical thermodynamic evaluation of oxide systems relevant to fuel ashes and slags Part 2: Alkali oxide-alumina systems, CALPHAD: Comput. Coupling Phase Diagrams Thermochem. 30 (2006) 397-404.
[12] J.S. Moya, E. Criado, A.S. De, The potassium oxide.aluminum oxide-aluminum oxide system, J. Mater. Sci. 17 (1982) 2213-17.
[13] R.S. Roth, Phase equilibriums research in portions of the potassium oxide-magnesium oxide-iron(III)oxide-aluminum oxide-silicon dioxide system, Adv. Chem. Ser. 186 (1980) 391-408.
[14] G.W. Schaefer, A.P. de Kroon, F. Aldinger, Influence of precursor chemistry on phase evolution and stability range in the potassium-beta alumina system, Mater. Res. Soc. Symp. Proc. 393(Materials for Electrochemical Energy Storage and Conversion-Batteries, Capacitors and Fuel Cells) (1995) 61-6.
[15] J.A.M. Van Hoek, F.J.J. Van Loo, R. Metselaar, Phase diagrams of alumina-alkali oxide-alkaline earth oxide systems in relation to alkali corrosion, Key Eng. Mater. 53-55(Austceram '90) (1991) 111-19.
[16] C.W. Bale, E. Belisle, P. Chartrand, S.A. Decterov, G. Eriksson, A.E. Gheribi, K. Hack, I.H. Jung, Y.B. Kang, J. Melancon, A.D. Pelton, S. Petersen, C. Robelin, J. Sangster, P. Spencer, M.A. Van Ende, FactSage thermochemical software and databases, 2010-2016, CALPHAD: Comput. Coupling Phase Diagrams Thermochem. 54 (2016) 35-53.

[17] D.G. Kim, M.A. Van Ende, P. Hudon, I.H. Jung, Coupled experimental study and thermodynamic optimization of the K2O-SiO2 system, Submitted to Journal of Non-Crystalline Solids (2017).
[18] A.D. Pelton, S.A. Degterov, G. Eriksson, C. Robelin, Y. Dessureault, The modified quasichemical model I - binary solutions, Metall. Mater. Trans. B 31B (2000) 651-659.
[19] A. Pelton, P. Chartrand, The modified quasi-chemical model: Part II. Multicomponent solutions, Metallurgical and Materials Transactions A 32(6) (2001) 1355-1360.
[20] C. Mundus, W. Mueller-Warmuth, 27Al magic-angle spinning nuclear magnetic resonance satellite transition spectroscopy of glasses in the system K2O-Al2O3-SiO2, Solid State Nucl. Magn. Reson. 5(1) (1995) 79-88.
[21] S. Sukenaga, K. Kanehashi, H. Shibata, N. Saito, K. Nakashima, Structural Role of Alkali Cations in Calcium Aluminosilicate Glasses as Examined Using Oxygen-17 Solid-State Nuclear Magnetic Resonance Spectroscopy, Metall. Mater. Trans. B 47(4) (2016) 2177-2181.
[22] E. Ising, Beitrag zur Theorie des Ferromagnetismus, Zeitschrift für Physik 31(1) (1925) 253-258.
[23] A.D. Pelton, A general "geometric" thermodynamic model for multicomponent solutions, CALPHAD: Comput. Coupling Phase Diagrams Thermochem. 25(2) (2001) 319-328.
[24] G. Collin, R. Comes, J.P. Boilot, P. Colomban, Crystal structure and ion-ion correlation of ion-rich β alumina type compounds. I. Magnesium doped potassium rich β alumina, Solid State Ionics 1(1-2) (1980) 59-68.
[25] J.P. Boilot, G. Collin, P. Colomban, R. Comes, X-ray-scattering study of the fast-ion conductor β″-alumina, Phys. Rev. B: Condens. Matter 22(12) (1980) 5912-23.
[26] K. Momma, F. Izumi, VESTA 3 for three-dimensional visualization of crystal, volumetric and morphology data, J. Appl. Crystallogr. 44(6) (2011) 1272-1276.
[27] C.A. Beevers, M.A.S. Ross, The crystal structure of "beta alumina," Na2O.11Al2O3, Z. Kristallogr., Kristallgeom., Kristallphys., Kristallchem. 97 (1937) 59-66.
[28] G. Yamaguchi, K. Suzuki, Structures of alkali polyaluminates, Bull. Chem. Soc. Jap. 41 (1968) 93-9.
[29] P.D. Dernier, J.P. Remeika, Structural determinations of single-crystal K β-alumina and cobalt-doped K β-alumina, J. Solid State Chem. 17(3) (1976) 245-53.
[30] N. Iyi, Z. Inoue, S. Kimura, The crystal structure of highly nonstoichiometric potassium β-alumina, K1.50Al11.0O17.25, J. Solid State Chem. 61(1) (1986) 81-9.
[31] W.L. Roth, F. Reidinger, S. LaPlaca, Studies of stabilization and transport mechanisms in beta and beta" alumina by neutron diffraction, Plenum, 1976, pp. 223-41.
[32] D.P. Birnie, III, On the structural integrity of the spinel block in the β″-alumina structure, Acta Crystallogr., Sect. B: Struct. Sci. 68(2) (2012) 118-122.
[33] M. Hillert, The compound energy formalism, J. Alloys Compd. 320(2) (2001) 161-176.
[34] J.V.L. Beckers, K.J. Van der Bent, S.W. De Leeuw, Ionic conduction in Na+-β-alumina studied by molecular dynamics simulation, Solid State Ionics 133(3,4) (2000) 217-231.
[35] G. Collin, J.P. Boilot, A. Kahn, J. Thery, R. Comes, Structural investigation of potassium(+) and thallium(+) β-aluminas, J. Solid State Chem. 21(4) (1977) 283-92.
[36] I. Barin, Thermochemical Data of Pure Substances, VCH1989.
[37] R.G. Berman, T.H. Brown, H.J. Greenwood, An Internally Consistent Thermodynamic Data Base for Minerals in the System Na2O-K2O-CaO-MgO-FeO-Fe2O3-Al2O3-SiO2-TiO2-H2O-CO2, Atomic Energy of Canada Limited TR-377 (1985) 62.

[38] R.G. Berman, T.H. Brown, Heat capacity of minerals in the system sodium monoxide-potassium monoxide-calcium oxide-magnesium oxide-iron(II) oxide-iron(III) oxide-aluminum oxide-silicon dioxide-titanium dioxide-water-carbon dioxide: representation, estimation, and high temperature extrapolation, Contrib. Mineral. Petrol. 89 (1985) 168-83.
[39] R.G. Berman, T.H. Brown, Erratum. Heat capacity of minerals in the system sodium monoxide-potassium monoxide-calcium oxide-magnesium oxide-iron(II) oxide-iron(III) oxide-aluminum oxide-silicon dioxide-titanium dioxide-water-carbon dioxide: representation, estimation, and high temperature extrapolation, Contrib. Mineral. Petrol. 94 (1986) 262.
[40] M.W. Chase, Jr., C.A. Davies, J.R. Downey, Jr., D.J. Frurip, R.A. McDonald, A.N. Syverud, JANAF Thermochemical Tables. Third Edition. Part I, aluminum-cobalt, J. Phys. Chem. Ref. Data, Suppl. 14(1) (1985) 1-926.
[41] M.W. Chase, Jr., C.A. Davies, J.R. Downey, Jr., D.J. Frurip, R.A. McDonald, A.N. Syverud, JANAF Thermochemical Tables. Third Edition. Part II, chromium-zirconium, J. Phys. Chem. Ref. Data, Suppl. 14 (1985) 927-1856.
[42] L.T. Brownmiller, System lime-potash-alumina, Am. J. Sci. 29 (1935) 260-77.
[43] T.F.W. Barth, Non-silicates with cristobalite-like structure, J. Chem. Phys. 3 (1935) 323-5.
[44] O.I. Arakelyan, Polymorphism and isomorphism of some phases of the system Na2O(or K2O)-Al2O3-Fe2O3, Khim. i Prakt. Primenenie Silikatov, Inst. Khim. Silikatov, Akad. Nauk S.S.S.R. (1960) 63-71.
[45] Y. Otsubo, K. Yamaguchi, Y. Kawamura, Thermal behavior of alkali metal aluminates, Nippon Kagaku Zasshi 83 (1962) 352-3.
[46] E.I. Burmakin, G.V. Burov, I.G. Rozanov, G.S. Shekhtman, Structure of potassium monoaluminate, Zh. Neorg. Khim. 23(12) (1978) 3366-8.
[47] R.P. Beyer, M.J. Ferrante, R.R. Brown, Thermodynamic properties of potassium aluminate, J. Chem. Thermodyn. 12 (1980) 985-91.
[48] S.L.G. Husheer, J.G. Thompson, A. Melnitchenko, Cristobalite-Related Phases in the KAlO2-KAlSiO4 System, J. Solid State Chem. 147(2) (1999) 624-630.
[49] J. Sokolowski, A. Kotarba, The structure of potassium aluminium oxide KAlO2, Mater. Sci. Forum 321-324 (2000) 954-959.
[50] J.G. Thompson, R.L. Withers, S.R. Palethorpe, A. Melnitchenko, Cristobalite-related oxide structures, J. Solid State Chem. 141(1) (1998) 29-49.
[51] A.P. de Kroon, G.W. Schäfer, F. Aldinger, Crystallography of potassium aluminate K2O·Al2O3, Journal of Alloys and Compounds 314(1–2) (2001) 147-153.
[52] E.I. Burmakin, V.I. Voronin, L.Z. Akhtyamova, I.F. Berger, G.S. Shekhtman, Potassium aluminate crystalline structure and electroconduction, Russ. J. Electrochem. 40(6) (2004) 619-626.
[53] V.I. Voronin, M.G. Surkova, G.S. Shekhtman, N.A. Anurova, V.A. Blatov, Conduction mechanism in the low-temperature phase of KAlO2, Inorg. Mater. 46(11) (2010) 1234-1241.
[54] V.I. Voronin, G.S. Shekhtman, V.A. Blatov, The natural tiling approach to cation conductivity in KAlO2 polymorphs, Acta Crystallogr., Sect. B: Struct. Sci. 68(4) (2012) 356-363.
[55] R.C. De Vries, W.L. Roth, Critical evaluation of the literature data on beta alumina and related phases. I. Phase equilibriums and characterization of beta alumina phases, J. Amer. Ceram. Soc. 52(7) (1969) 364-9.
[56] E.R. Plante, C.D. Olson, T. Negas, Interaction of K2O with slag in open cycle, coal fired MHD, Proc. Sixth Int. Conf. on Magnetohydrodynamic Electrical Power Generation, Washington, DC, June 9-13 CONF750601-P2(2) (1975) 211-218.

[57] F.E. Spencer, J.C. Hendrie, D. Bienstock, A ternary margules-type model for plasma/slag equilibrium in potassium-seeded coal combustion for magnetohydrodynamic power generation: calculation and comparisons with experiments, Proceedings of the 6th international conference on MHD electric power generation 2 (1975) 181-210.
[58] D.R. Stull, H. Prophet, J. Chao, A.T. Hu, E.W. Phillips, G.C. Karris, S.K. Wollert, S. Levine, J.L. Curnutt, a. et, JANAF Thermochemical Tables (NSRDS-NBS 37). 2nd ed, GPO1971.
[59] R. Hultgren, a. et, Selected Values of the Thermodynamic Properties of the Elements, Amer. Soc. Metals1973.
[60] K.O. Bennington, G.E. Daut, The standard formation data for potassium aluminate (KAlO2), Thermochim. Acta 124 (1988) 241-5.
[61] G. Collin, R. Comes, J.P. Boilot, P. Colomban, Structure, ion-ion correlation and compensation mechanisms in β- and β"-alumina, Solid State Ionics 28-30(Pt. 1) (1988) 324-32.
[62] M. Itoh, Z. Kozuka, Thermodynamic stability of potassium (K+)-β-alumina, J. Am. Ceram. Soc. 71 (1988) C36-C39.
[63] K. Shqau, H. Naefe, Thermodynamic stability of potassium-beta-alumina, J. Am. Ceram. Soc. 88(10) (2005) 2894-2896.
[64] H.S. Parker, R.S. Roth, C.D. Olson, E.R. Plante, A Thermochemical Study of Corrosive Reactions in Oxide Materials, NBS: Properties of Electronic Materials NBSIR 78-1483 (1978) 84-100.
[65] R.V. Kumar, D.A.R. Kay, Thermodynamic stabilities of some β and β″ aluminas, Metall. Trans. B 16B (1985) 295-301.
[66] G.M. Kale, K.T. Jacob, Thermodynamic stability of potassium β-alumina, Metall. Trans. B 20B (1989) 687-91.
[67] M. Itoh, K. Kimura, Z. Kozuka, Measurement of sodium oxide activity in beta-alumina by EMF method, Trans. Jpn. Inst. Met. 26(5) (1985) 353-61.
[68] G. Lambotte, P. Chartrand, Thermodynamic modeling of the (Al2O3 + Na2O), (Al2O3 + Na2O + SiO2), and (Al2O3 + Na2O + AlF3 + NaF) systems, J. Chem. Thermodyn. 57 (2013) 306-334.
[69] M.W. Chase, S. National Institute of, Technology, NIST-JANAF thermochemical tables, American Chemical Society ; American Institute of Physics for the National Institute of Standards and Technology, [Washington, D.C.]; Woodbury, N.Y., 1998.
[70] G.W. Schaefer, A.P. De Kroon, F. Aldinger, Effect of aluminum raw materials on the formation of potassium-beta-aluminas, Solid State Ionics 81(1,2) (1995) 43-51.
[71] G. Schaefer, F. Aldinger, Preparation and phase relations of β- and β″-alumina materials in the ternary system K2O-MgO-Al2O3, CFI, Ceram. Forum Int. 73(2) (1996) 109-13.
[72] C.-H. Ham, S.-K. Lim, C.-K. Lee, S.-E. Yoo, Synthesis and phase relations of potassium-beta-aluminas in the ternary system K2O-MgO-Al2O3, Kongop Hwahak 10(7) (1999) 1086-1091.
[73] M. Blanc, A. Mocellin, J.L. Strudel, Observation of potassium β'"-alumina in sintered alumina, J. Am. Ceram. Soc. 60(9-10) (1977) 403-9.
[74] K.J. Morrissey, C.B. Carter, Analysis of second-phase particles in alumina, Mater. Sci. Res. 15(Adv. Mater. Charact.) (1983) 297-307.
[75] T. Epicier, A. Mamoun, HREM refinement of the distribution of potassium atoms in K-based β'" alumina, Editions de Physique, 1994, pp. 815-816.
[76] W.-S. Kim, S.-K. Lim, Effect of stabilizers (MgO/Li2O) on phase relations of the ternary K+-β/β″-Al2O3 system, Kongop Hwahak 12(3) (2001) 312-317.

[77] X. Lu, G. Xia, J.P. Lemmon, Z. Yang, Advanced materials for sodium-beta alumina batteries: Status, challenges and perspectives, J. Power Sources 195(9) (2010) 2431-2442.
[78] G. Collin, J.P. Boilot, P. Colomban, R. Comes, Host lattices and superionic properties in β- and β″-alumina. I. Structures and local correlations, Phys. Rev. B: Condens. Matter 34(8, Pt. 2) (1986) 5838-49.
[79] K. Edstroem, J.O. Thomas, G.C. Farrington, Sodium-ion distribution in Na+ β-alumina: a crystallographic challenge, Acta Crystallogr., Sect. B: Struct. Sci. B47(2) (1991) 210-16.
[80] M.A. Zendejas, J.O. Thomas, Conduction mechanisms in solid electrolytes: magnesium(2+)-stabilized sodium(1+) beta-alumina, Phys. Scr. 47(3) (1993) 440-50.
[81] W. Hayes, G.F. Hopper, F.L. Pratt, Ionic conductivity of potassium β" alumina in the very-far infrared, J. Phys. C 15(21) (1982) L675-L680.

Tables

Table 6.1 Optimized thermodynamic properties of compounds relative to elemental standard state.

Phase	$\Delta H^{o}_{298.15K}$ (kJ·mol^{-1})	$S^{o}_{298.15K}$ (J·mol^{-1}·K^{-1})	C_P (J·mol^{-1}·K^{-1})	Reference	Experimental method / Remarks
K_2O	-361497.997	102.006	75.947+0.017146·T -591639.9844·T^{-2} (298.15-373 K) 107.000 (>1013 K)	16Bal[16]	
Al_2O_3	-1675699.996	50.820	155.0189 -3861363.0154·T^{-2}-828.387·$T^{-0.5}$+409083646.192·T^{-3} (298.15 – 2327.01 K) 192.464 (>2327.01 K)	16Bal[16]	Corundum
LT-$KAlO_2$	-1135.788			75Spe[57]	Not available
	-1140.546			88Ben[60]	Solution calorimetry
		85.55		80Bey[47]	Adiabatic calorimetry
			68.6115 + 0.069701·T -972131.9821·T^{-2} -0.000026276·T^2 (298.15 – 810.0 K)	80Bey[47]	Drop calorimetry
LT → HT	ΔH^{o}_{tr}: at 795 K			60Ara[44]	DTA
LT → HT	ΔH^{o}_{tr}: at 808 K			62Ots[45]	DTA, HT-XRD
LT → HT	ΔH^{o}_{tr}: at 813 K			78Bur[46]	DTA, HT-XRD
LT → HT	ΔH^{o}_{tr}: 1.295 at 810 K			80Bey[47]	Drop calorimetry
LT → HT	ΔH^{o}_{tr}: 1.059 at 804 K			99Hus[48]	DSC
LT → HT	ΔH^{o}_{tr}: at 773 K			00Sok[49]	HT-XRD

LT → HT	ΔH_{tr}^{o}: at 873 K			01Kro[51]	DTA, XRF, XRD
HT- $KAlO_2$			91.970 + 0.0119999998592·T (>810.0 K)	80Bey[47]	Drop calorimetry
LT-$KAlO_2$	-1140.546	85.55	68.6115 + 0.069701·T -972131.9821·T^{-2} -0.000026276·T^{2} (298.15 – 810.0 K)	This study	
HT- $KAlO_2$	ΔH_{tr}^{o}: 1.295 at 810 K		91.970 + 0.0119999998592·T (>810.0 K)	This study	
$KAl_{11}O_{17}$	-9585.544	309.845	890.577 + 0.008573·T -21533316.577·T^{-2} -4556.12839·$T^{-0.5}$+2249960054.056·T^{-3} (298.15 – 3000.0 K)	This study	
$KAl_{5.5}O_{8.75}$ ($\frac{1}{4}K_4Al_{22}O_{35}$)	-4968.971	171.679	464.275 + 0.008573·T -10914568.28·T^{-2}-2278.06·$T^{-0.5}$+1124980027.03·T^{-3} (298.15 – 2200.0 K)	This study	
$KMg_2Al_{15}O_{25}$	-14210.956	486.055	1322.834 + 0.008573·T -30498350.616·T^{-2}-6805.30035·$T^{-0.5}$+ 3079816570.494·T^{-3} (298.15 – 1800.0 K)	This study	

Table 6.2 Optimized model parameters of the solutions ($J \cdot mol^{-1}$ and $J \cdot mol^{-1} \cdot K^{-1}$).

Liquid solution (MQM)

$Z_{KK}^{K} = 0.6887$, $Z_{MgMg}^{Mg} = 1.3774$ $Z_{Al\,Al}^{Al} = 2.0662$, $Z_{KAl\,KAl}^{KAl} = 2.7549$, $Z_{K\,Al}^{K} = 0.6887$, $Z_{K\,KAl}^{K} = 0.6887$, $Z_{Al\,KAl}^{Al} = 2.0662$

The K_2O-Al_2O_3 system

$g_{K_2O,liquid}^{o}$: $\Delta H_{298.15K}^{o}$ = -334298.010, $S_{298.15K}^{o}$ = 128.857, C_P = 75.947+0.0171460002016$\cdot T$ - 591639.9844$\cdot T^{-2}$ (298.15-1013 K), 107.000 (>1013 K)

$g_{Al_2O_3,liquid}^{o}$: $\Delta H_{298.15K}^{o}$ = -1596353.151, $S_{298.15K}^{o}$ = 43.569, C_P = 179.365-0.009192248$\cdot T$ +975340.98456$\cdot T^{-2}$-828.38698016$\cdot T^{-0.5}$+409083646.192$\cdot T^{-3}$ (298.15-2327.01 K), 192.464 (>2327.01 K)

$g_{KAlO_2,associate}^{o} = \frac{1}{2} \cdot (g_{K_2O,liquid}^{o} + g_{Al_2O_3,liquid}^{o}) - 101252.80$

$\Delta g_{KO_{0.5}-AlO_{1.5}} = -279491.20 - 15.48 \cdot T$

$\Delta g_{KAlO_2-AlO_{1.5}} = 26986.80 \cdot X_{Al-Al} + 13807.20 \cdot X_{Al-Al}^{2}$

The K_2O-MgO-Al_2O_3 system

$\Delta g_{KO_{0.5}-AlO_{1.5}-MgO} = \Delta g_{KO_{0.5}-KAlO_2-AlO_{1.5}} = \Delta g_{KO_{0.5}-KAlO_2-MgO} = \Delta g_{AlO_{1.5}-KAlO_2-MgO} = 0\,(ideal\ solution)$

Ternary interpolations:

$KO_{0.5}$-$AlO_{1.5}$-MgO: Toop-type approximation at constant Al_2O_3

$KO_{0.5}$-$KAlO_2$-$AlO_{1.5}$, $KO_{0.5}$-$KAlO_2$-MgO, $AlO_{1.5}$-$KAlO_2$-MgO: Kohler-type approximations

β- and β″-alumina solid solutions (five-sublattice CEF)

$[K^+, Va]_1^{BR}[K^+, Va]_1^{aBR}[Al^{3+}, Mg^{2+}]_2^{Al(2)}[O^{2-}, Va]_1^{mO}\ Al_9^{Al(other)}O_{17}$

($Al_9^{Al(other)}O_{17}$ in one sublattice)

The notation 'K', 'A', 'M', and 'O' are used for ions of 'K^+', 'Al^{3+}', 'Mg^{2+}', and 'O^{2-}', respectively, 'V' is used for 'Va; Vacancy'.

Binary β-alumina

$$G_{KVAV} = G^o_{KAl_{11}O_{17}(\beta-alumina)}$$

$$G_{KKAO} = G_{KKAV} = \tfrac{1}{2}(G^o_{K_4Al_{22}O_{35}(\beta''-alumina)} + \Delta S^{conf} + G^{add(1)}),$$

$$\Delta S^{conf} = 11.526,\ G^{add(1)} = 16736$$

Binary β″-alumina

$$G_{KKAO} = G_{KKAV} = \tfrac{1}{2}(G^o_{K_4Al_{22}O_{35}(\beta''-alumina)} + \Delta S^{conf}),\ \Delta S^{conf} = 11.526$$

$$G_{KVAV} = G^o_{KAl_{11}O_{17}(\beta-Al_2O_3)} + G^{add(2)},\ G^{add(2)} = 6694.4$$

Common binary end-members

$$\Delta^2 = G_{KVAO} + G_{KKAV} - G_{KKAO} - G_{KVAV},\ \Delta^2 = 4184 + 23.012 \cdot T$$

$$I^1 = G_{VKAV} - G_{KVAV},\ I^1 = 35564 + 4.184$$

$$I^2 = G_{VKAO} - G_{KVAO},\ I^2 = -29288 - 23.012 \cdot T$$

Ternary β-alumina

$$G_{KVMV} = G_{KVAV} + G^{add(Va-Mg)},\ G^{add(Va-Mg)} = 401664$$

Ternary β″-alumina

$$G_{KVMV} = G_{KVAV} + G^{add(Va-Mg)},\ G^{add(Va-Mg)} = 405848$$

Common ternary end-member

$$G_{KKMV} = G_{KVAV} + G^{add(K-Mg)},\ G^{add(K-Mg)} = -41840$$

Binary model parameters of K_2O-MgO and MgO-Al_2O_3 were taken from Kim *et al*. [7] and Jung *et al*. [4], respectively.

Figures

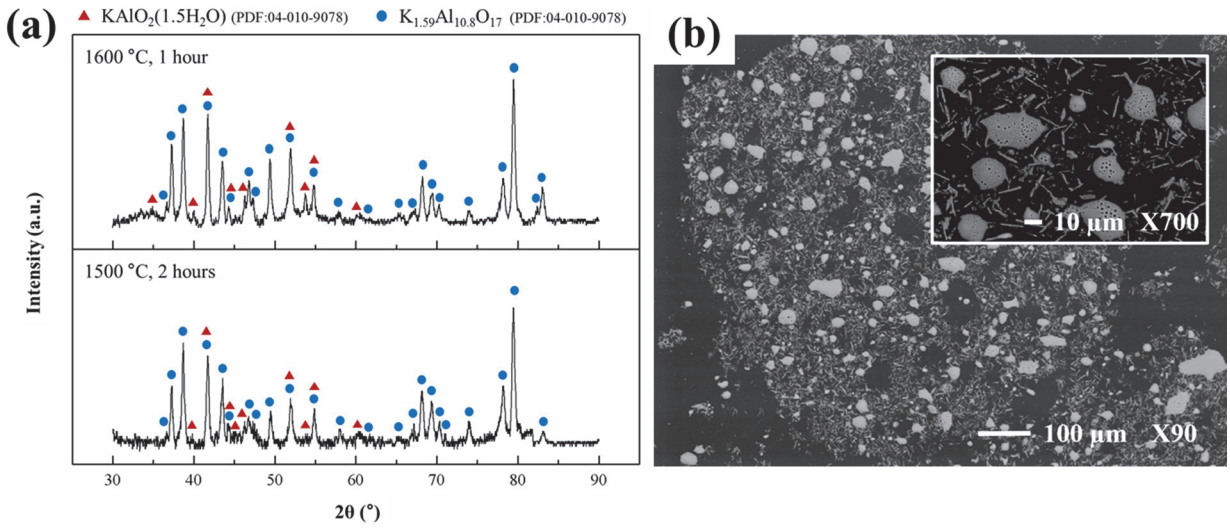

Figure 6.1 (a) The XRD results for two equilibration experiments at 1500 and 1600 °C. (b) BSE images from the sample equilibrated at 1500 °C.

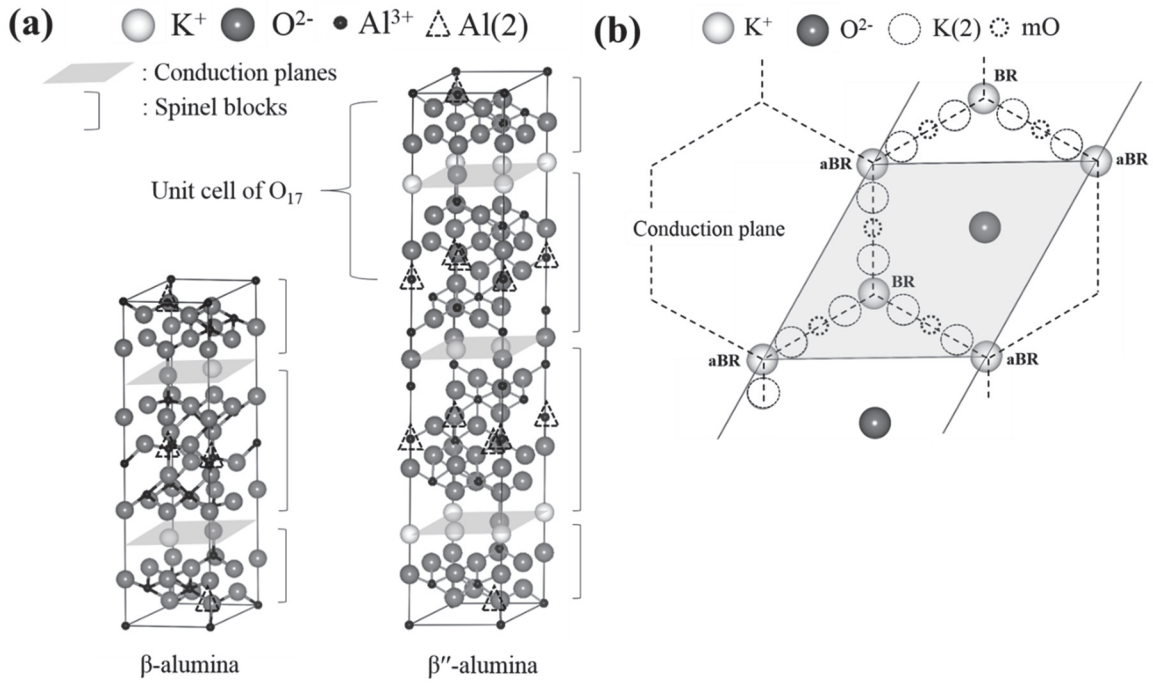

Figure 6.2 Schematic (a) lattice structures of K β- and β″-alumina and (b) conduction plane.

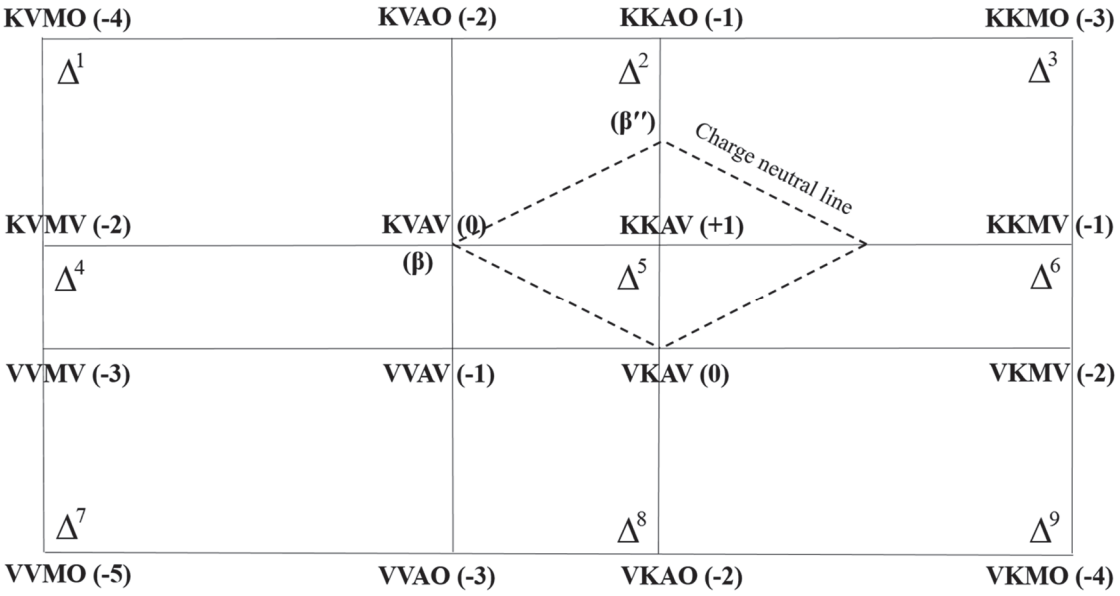

Figure 6.3 Schematic diagram of the end-members in K β- and β″-alumina solid solutions.

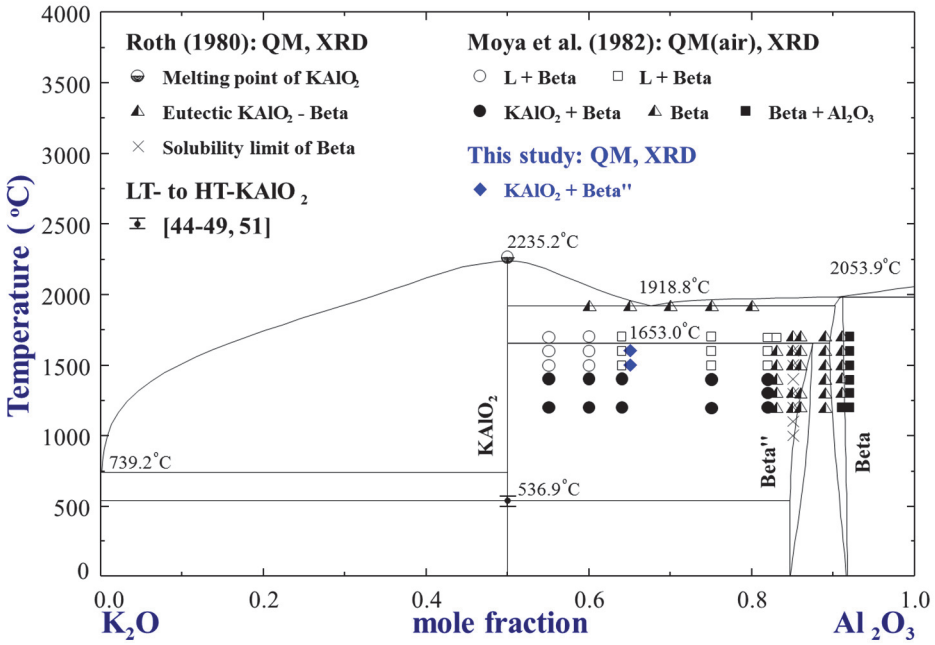

Figure 6.4 Optimized phase diagram of the K_2O-Al_2O_3 system in comparison with experimental data.

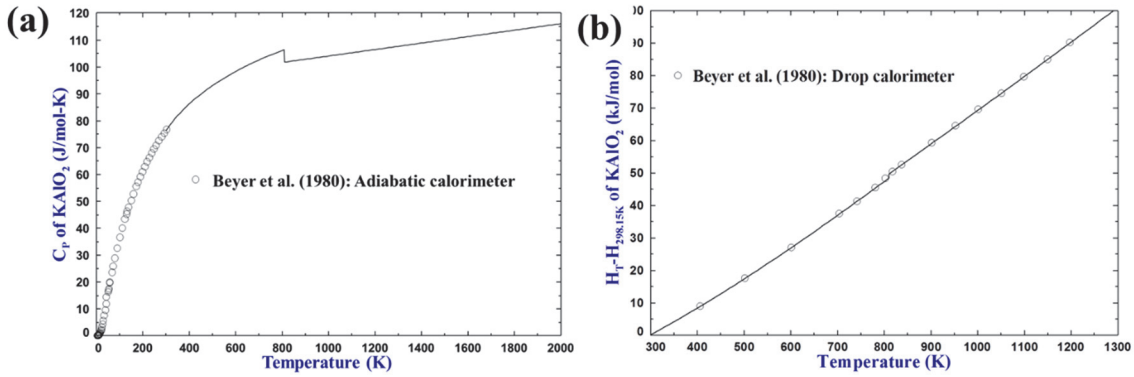

Figure 6.5 Optimized thermodynamic properties of $KAlO_2$, (a) heat capacity, and (b) heat content.

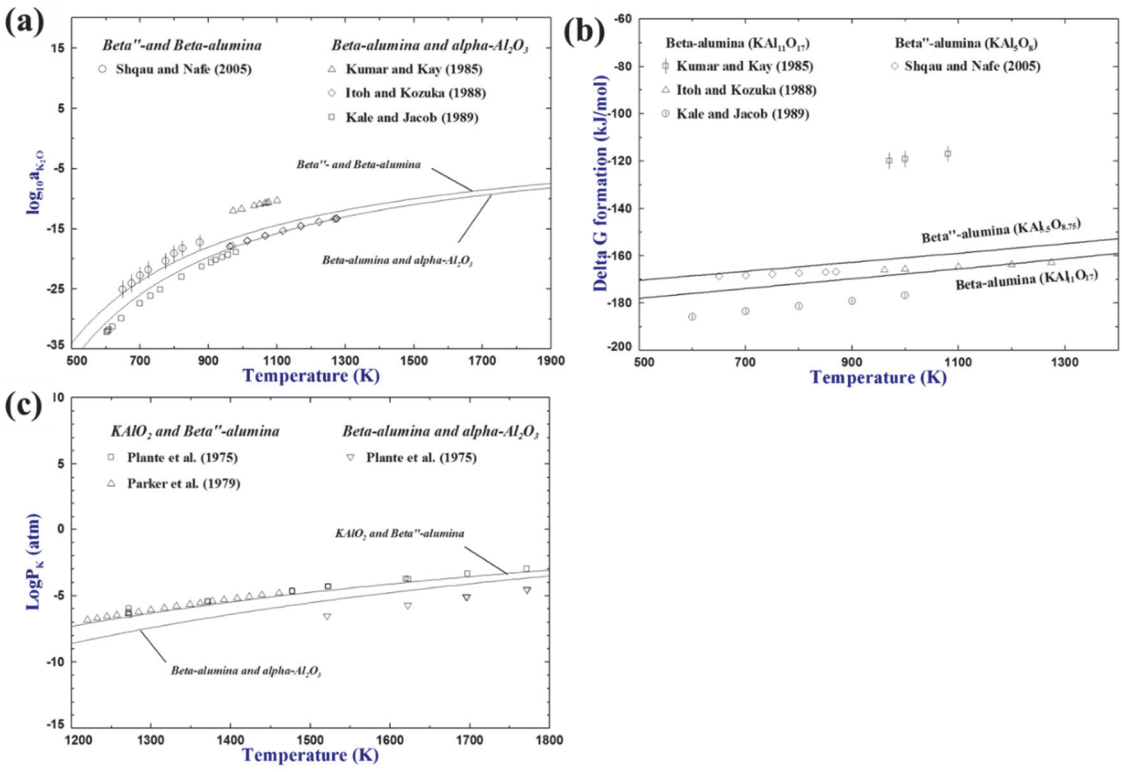

Figure 6.6 Calculated (a) activity of K_2O (reference to solid state) in two-phase regions between β″-alumina and β-alumina and between β-alumina and α-Al_2O_3, (b) standard Gibbs energy of formations of β- and β″-alumina, and (c) partial pressure of potassium (K) in the regions of $KAlO_2$ and β″-alumina and between β-alumina and α-Al_2O_3 compared with experimental data.

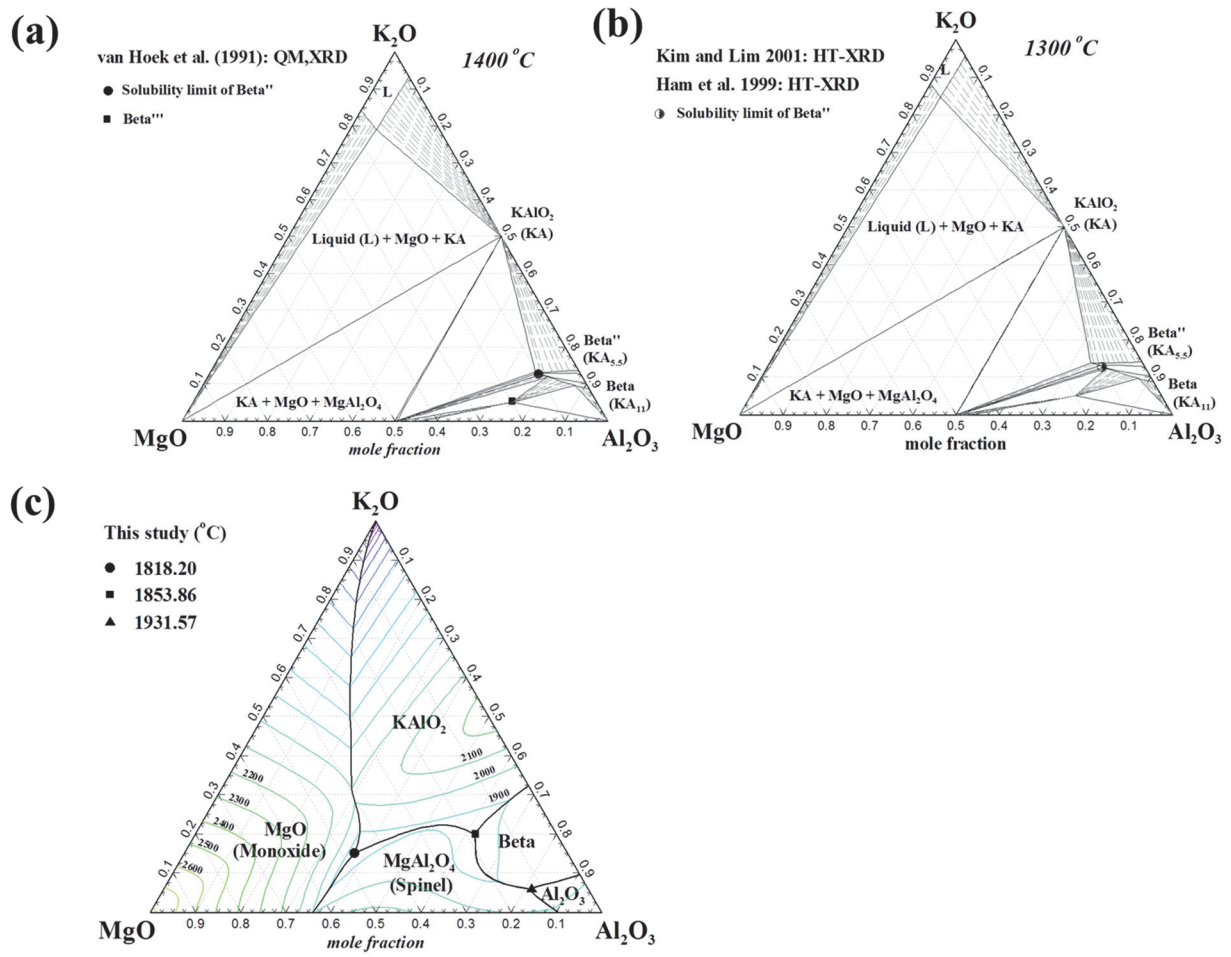

Figure 6.7 Isothermal sections (a) at 1400 ºC, (b) at 1300 ºC, and (c) the liquidus projection of the K_2O-MgO-Al_2O_3 system.

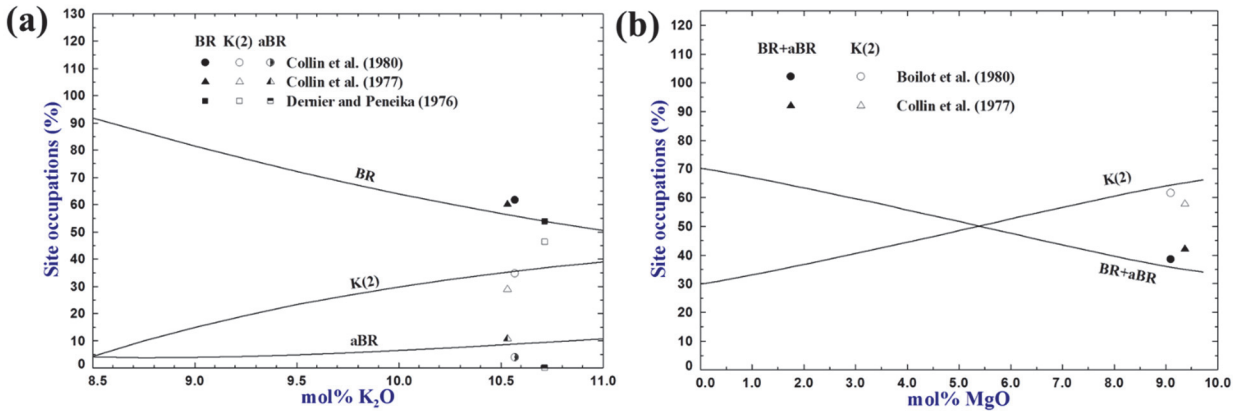

Figure 6.8 Ionic site occupations in (a) binary β-alumina with excess K_2O and (b) ternary β″-alumina with MgO addition (from binary β″-alumina with 90 mol % Al_2O_3) at 500 °C.

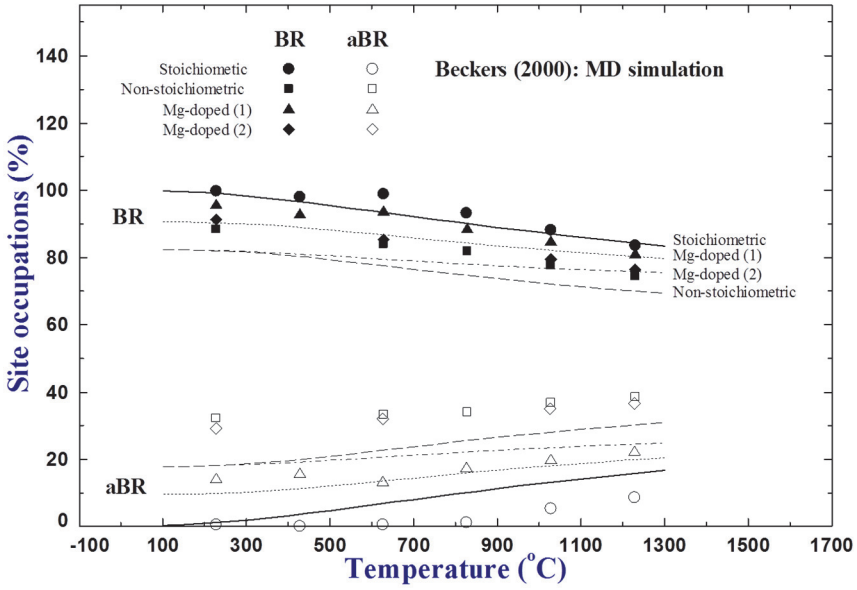

Figure 6.9 Ionic site occupations of stoichiometric (91.7 mol % Al_2O_3 in the binary system), non stoichiometric (90.1 mol % Al_2O_3 in the binary system), and two Mg-doped β-alumina compositions (1: 1.7 mol % excess MgO and Na_2O/Al_2O_3=0.1, and 2: 3.5 mol % excess MgO and Na_2O/Al_2O_3=0.11) from 100 to 1300 °C with MD simulation data.

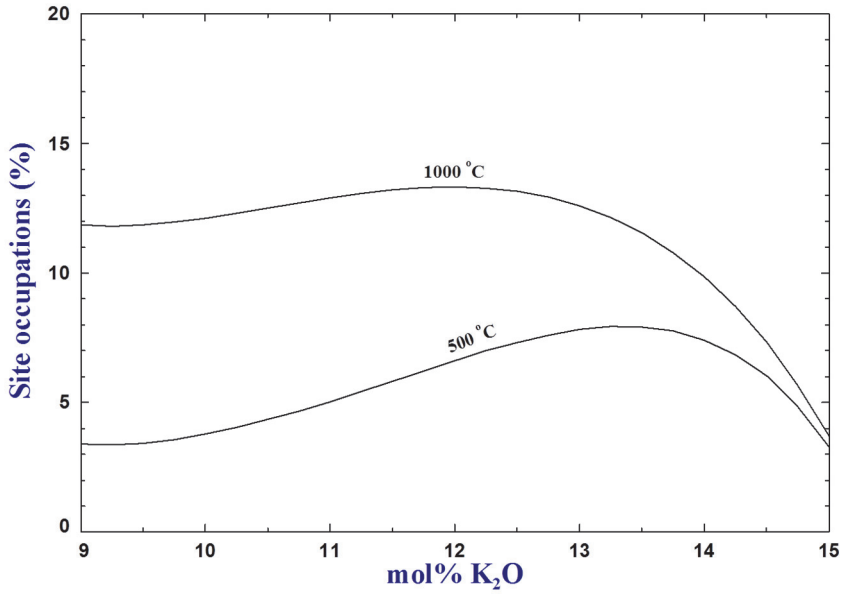

Figure 6.10 Permanent BR site vacancies in β-alumina with excess K_2O at 500 and 1000 °C, predicted from the present model.

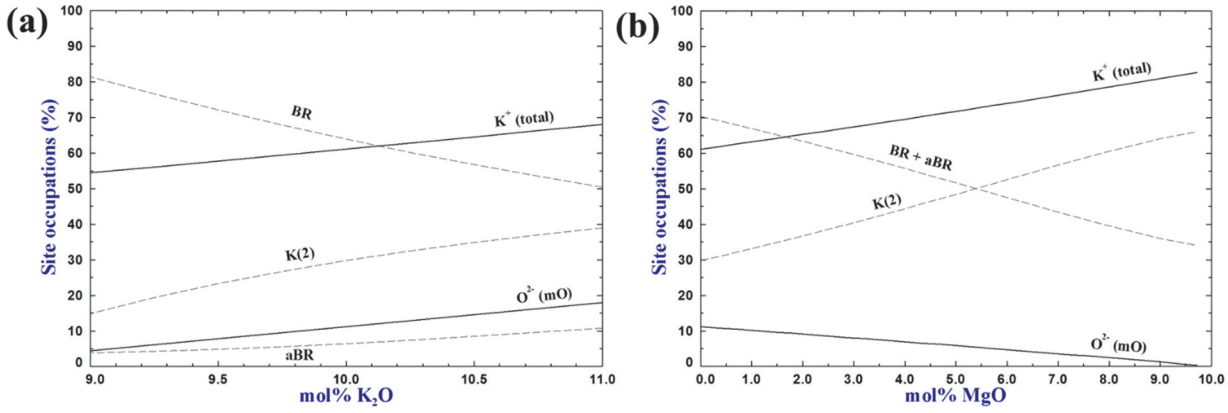

Figure 6.11 Site occupation of interstitial oxygen and total K^+ ions in unit cell (O_{17}) in (a) β-alumina and (b) β″-alumina at 500 °C, predicted from the present model.

Chapter 7 Thermodynamic Optimization of the K_2O-Al_2O_3-SiO_2 System

Dong-Geun Kim, Bikram Konar and In-Ho Jung

To be submitted.

In this chapter, thermodynamic optimization of the K_2O-Al_2O_3-SiO_2 system is discussed. The Modified Quasichemical Model with an associate component $KAlO_2$ was used to optimize the liquid solution. This ternary optimization was followed by of the optimizations of the K_2O-SiO_2 system in Chapter 4 and the K_2O-Al_2O_3 system in Chapter 6.

Abstract

A critical evaluation and thermodynamic optimization of experimental phase diagrams and thermodynamic properties of the K_2O-Al_2O_3-SiO_2 system was performed at 1 bar total pressure. A set of self-consistent thermodynamic functions of all phases in the K_2O-Al_2O_3-SiO_2 system was obtained. The liquid phase was described using the Modified Quasichemical Model with the $KAlO_2$ associate component. The set of optimized model parameters obtained for all phases reproduces available and reliable thermodynamic properties and phase diagram data as well as the melt structure of the K_2O-Al_2O_3-SiO_2 system within the experimental error limit.

Key words: K_2O-Al_2O_3-SiO_2; thermodynamic optimization; phase diagram; glass melt

7.1 Introduction

The K_2O-Al_2O_3-SiO_2 system is important in many industrial and academic applications. There are many researches on the heat treatment of leucite ($KAlSi_2O_6$)-reinforced glass-ceramics, which are the first generation dentistry restoration material, aiming to improve the mechanical properties [1-4]. Lithium disilicate glass-ceramics are the second generation dentistry restoration material. Research reveals that adding K_2O and Al_2O_3 to this type of glass-ceramics can improve the mechanical strength and the densification process during sintering [5, 6]. In glassmaking and ironmaking processes, K_2O vapor from the raw materials circulates in the furnace and has reactions with the alumina, silica, and mullite type refractories. This ternary system is a fundamental system to understand the corrosion mechanism of the refractories in such processes [7-11]. Accurate phase diagram and thermodynamic information of the K_2O-Al_2O_3-SiO_2 system is also important for geology and mineralogy studies. K_2O-containing aluminosilicates are one of the most abundant rock-forming minerals on earth [12]. Kalsilite ($KAlSiO_4$), leucite ($KAlSi_2O_6$), and feldspar ($KAlSi_3O_8$) can form solid solutions with Na_2O, CaO, Fe_tO, MgO, etc. in natural environment. Therefore, studying the phase stability and thermodynamic properties of these compounds is essential to understand the complex phase equilibria in multi-component mineralogical systems [13].

Up to now, the experimental study on the K_2O-Al_2O_3-SiO_2 system has been limited in certain temperature and composition ranges due to the experimental difficulties coming from the high melting point of Al_2O_3, highly hygroscopic and volatile nature of K_2O, and high viscosity of SiO_2-containing melt. Two thermodynamic optimizations have been performed on this system with certain limitations. Chartrand and Pelton [14] used the Modified Quasichemical Model (MQM) [15, 16] to describe the liquid solution. A charge compensation effect, which represents KAl^{4+}

associates substituting Si^{4+} in the aluminosilicate melt, was considered. Their optimization was focused on the SiO_2-rich corner of the ternary system in the composition range of 66 to 100 mol % SiO_2 and the kalsilite compound ($KAlSiO_4$) was not considered. Yazhenskikh *et al*. [17] employed the associate model [18] to describe the liquid phase of this ternary system. In their optimization, binary associate components and two ternary associate species, $KAlSiO_4$ and $KAlSi_2O_6$, were employed. A $KAlO_2$ solid solution with excess SiO_2 was modeled using the Compound Energy Formalism (CEF) [19]. The $KAlO_2$ solid solution, which has two polymorphs, was assumed to be a monotropic phase. $KAlSiO_4$ was treated as a stoichiometric compound although there is a noticeable solubility of SiO_2. The calculated liquidus of $KAlSi_2O_6$ showed rather strange curvatures most probably due to the strong associate model parameters applied in their optimization. The standard entropy at 298.15 K of $KAlSi_3O_8$ was modified to be 6.8 % higher than the experimental data, which is certainly beyond the limit of the experimental error range.

In this study, a comprehensive literature review was performed on all available experimental data of the K_2O-Al_2O_3-SiO_2 system. Based on the most recent optimization studies of the K_2O-SiO_2 [20] and the K_2O-Al_2O_3 [21] systems, a thermodynamic optimization was performed to obtain an accurate set of thermodynamic functions for all stable phases for describing the phase diagram and thermodynamic properties in the entire composition and temperature range. The liquid solution phase was described using the MQM. The charge compensation effect was considered by introducing $KAlO_2$ associate in the liquid solution. The $KAlO_2$ and $KAlSiO_4$ solid solutions were optimized using the CEF and MQM, respectively. This study is part of a large thermodynamic database development project for the K_2O-Na_2O-CaO-MgO-Al_2O_3-SiO_2 system. All thermodynamic calculations in this study were performed using the FactSage software [22].

7.2 Thermodynamic Models

7.2.1 Stoichiometric Compounds

The Gibbs energy of a stoichiometric compound is described as:

$$G_T^o = \Delta H_{298.15K}^o + \int_{298.15K}^{T} C_P dT - T(S_{298.15K}^o + \int_{298.15K}^{T} C_P/T dT) \quad (1)$$

where $\Delta H_{298.15K}^o$ and $S_{298.15K}^o$ are the standard enthalpy of formation and standard entropy at 298.15 K, respectively; C_P is the heat capacity as a function of temperature; T is the absolute temperature.

7.2.2 Liquid Solution

The Modified Quasichemical Model (MQM) in the pair approximation [15, 16] was employed to express the Gibbs energy function of the liquid oxide phase. The MQM takes into account the short-range ordering (SRO) of second-nearest-neighbor cations in the oxide melt. The quasichemical reaction considered in the binary oxide melt is:

$$(A-A)+(B-B)=2(A-B);\ \ \Delta g_{A-B} \quad (2)$$

where A and B are the cationic species in solution; $(A-B)$ represents a second-nearest-neighbor pair of A and B cations with a common O^{2-} anion; Δg_{A-B} is the Gibbs energy of the reaction, which is a model parameter. Δg_{A-B} can be expanded as functions of pair fractions and temperature:

$$\Delta g_{A-B} = \Delta g^{o}_{AB} + \sum_{i\geq 1} g^{i0}_{AB} X^{i}_{AA} + \sum_{j\geq 1} g^{0j}_{AB} X^{j}_{BB} \quad (3)$$

where Δg^{o}_{AB}, g^{i0}_{AB}, and g^{0j}_{AB} are parameters, which can be a function of temperature; X_{AA} and X_{BB} are the pair fractions of $(A-A)$ and $(B-B)$, respectively.

The Gibbs energy of the liquid solution is expressed as:

$$G^{sol} = (n_A g^{o}_{A} + n_B g^{o}_{B}) - T\Delta S^{conf} + (n_{AB}/2)\Delta g_{A-B} \quad (4)$$

where n_i and g^{o}_{i} are the number of moles and the molar Gibbs energy of pure component *i*, respectively; n_{AB} is the number of moles of $(A-B)$ pairs; ΔS^{conf} is the configurational entropy of the solution expressed as a function of random distribution of quasichemical pairs based on one-dimensional Ising model [23]. The details of the thermodynamic equations for the MQM can be found in Ref. [15].

In the optimization of this study, an associate component of $KAlO_2$ is employed in this ternary liquid solution. In molten aluminosilicate systems, K^+ and Al^{3+} strongly associate with each other to replace Si^{4+} in SiO_2 network structure. This is generally known as the charge compensation effect [24]. Sukenaga *et al*. [25] reported that K^+ ions have stronger tendency of associate formation than Na^+ using ^{17}O-solid-state Nuclear Magnetic Resonance (NMR). Many viscosity measurements indirectly show the formation of KAl^{4+}: the addition of K_2O in aluminosilicate melts increases the viscosity [26, 27]. Phase diagram of the K_2O-Al_2O_3-SiO_2 system also implies the formation of $KAlO_2$ associate in the SiO_2-rich region, which can be analyzed using the so-called limiting slope rule [28]. In the pseudo-binary section of $KAlO_2$-SiO_2, for example, the slope of the SiO_2 liquidus close to pure SiO_2 ($X_{SiO_2} \rightarrow 1$) shows that K^+ and Al^{3+} enter into the liquid solution

as KAl^{4+} associate. Therefore, the liquid solution in the K_2O-Al_2O_3-SiO_2 system was treated as a quaternary liquid K_2O-MgO-SiO_2-$KAlO_2$ solution in this study.

The SRO behavior in the liquid solution can be well described by setting the coordination numbers of cations. In this work, the coordination numbers of unary: K^+ (Z^K_{KK}), Al^{3+} (Z^{Al}_{AlAl}), Si^{4+} (Z^{Si}_{SiSi}), and KAl^{4+} (Z^{KAl}_{KAlKAl}) were set to be 0.6887, 2.0662, 2.7549, and 2.7549, respectively. Binary coordination numbers of Z^K_{KAl} ($=Z^{Al}_{AlK}$) and Z^K_{KKAl} ($=Z^{KAl}_{KAlK}$) were set to be 0.6887, Z^{Al}_{AlKAl} ($=Z^{KAl}_{KAlAl}$) was to be 2.0662, and the rest of binary coordination numbers were set to be default values considering the unary coordination numbers. These coordination numbers are consistent with those used in the molten oxide database (FToxid) of the FactSage software [22].

The Gibbs energy of the ternary solution can be calculated using a geometric interpolation technique. Kohler- and Toop-type models are commonly used to express symmetric and asymmetric ternary system, respectively [16]. In the K_2O-Al_2O_3-SiO_2 system, the K_2O-Al_2O_3-$KAlO_2$ ternary was calculated based on the Kohler interpolation technique and the other three SiO_2-containing ternary systems were calculated based on Toop interpolation with SiO_2 as an asymmetric component. The details of the interpolation method are well described in Ref. [29]. In the present study, the model parameter Δg_{K-Si} in the K_2O-SiO_2 system was taken from Ref. [20], Δg_{K-Al} and Δg_{KAl-Al} in the K_2O-Al_2O_3 system from Ref. [21], Δg_{Al-Si} in the Al_2O_3-SiO_2 system from Ref. [30]. Δg_{KAl-Si} was a new binary model parameter optimized in the present study. In addition, ternary model parameters were introduced to reproduce the phase diagram data more accurately. The details of the MQM equations for the ternary system can be found in Ref. [16].

7.2.3 Solid Solutions

There are four solid solution phases in the K_2O-Al_2O_3-SiO_2 system. High- and low-temperature $KAlO_2$ (meta-oxide), high-temperature $KAlSiO_4$ (kalsilite), and low-temperature $KAlSiO_4$ (nepheline). All the $KAlO_2$ and $KAlSiO_4$ solid solutions have an excess solubility of SiO_2.

The dissolution mechanism of SiO_2 into $KAlO_2$ was adopted from the study by Grey *et al*. [31]. In fact, this is the only comprehensive crystal structure study for the meta-oxide solid solution which revealed the dissolution mechanism of SiO_2. According to the study by Grey *et al*. for meta-oxide β- and γ'-$NaFeO_2$, a coupled substitution of $Si^{4+} \leftrightarrow Fe^{3+} + Na^+$ occurs in the dissolution of SiO_2 in $NaFeO_2$. In particular, vacancy (Va) is coupled with Si^{4+} at adjacent interstitial site when Si^{4+} substitutes Fe^{3+} in the framework of tetrahedra and remove Na^+ from the framework cavities. That is, Va is not formed randomly in the solution but clearly associated to the Si^{4+} during the SiO_2 dissolution in $NaFeO_2$. This dissolution mechanism was modeled previously by Moosavi-Khoonsari and Jung [32] using the Compound Energy Formalism (CEF) [19] with ($NaFe^{4+}$, $SiVa^{4+}$)O_2 formula. The crystal structure of potassium-containing meta-oxides, such as $KAlO_2$, K_2MgSiO_4, $KGeO_2$, and $KFeO_2$, have their low-temperature polymorphs in orthorhombic structure, which is the same crystal structure as β- and γ'-$NaFeO_2$. The solution mechanism of the high-temperature polymorph of $KAlO_2$ meta-oxide was assumed to be the same as the low-temperature one because of structural similarity and lack of experimental data of the solution mechanism. Therefore, both low- and high-temperature polymorphs of $KAlO_2$ were described in this study using the CEF with (KAl^{4+}, $VaSi^{4+}$)O_2. That is, the molar Gibbs energy of the $KAlO_2$ solution is expressed by:

$$G^{sol} = (y_i G_i^o + y_j G_j^o) + RT(y_i \ln y_i + y_j \ln y_j) + \sum_{n\geq 0}^{n} L_{ij} y_i y_j (y_j - y_i)^n \quad (5)$$

where G_i^o is the molar Gibbs energy of the end-member *i* of the solution; y_i is the site fraction of the species *i*; *R* is the gas constant; ${}^nL_{ij}$ are the excess interaction parameters. For the $KAlO_2$ solution, y_i and y_j are the mole fractions of KAl and VaSi.

The $KAlSiO_4$ solid solutions were described by the MQM. Low-temperature $KAlSiO_4$ has the structure of nepheline, $NaAlSiO_4$, and they form a complete solid solution between each other [33, 34]. Therefore, the consistent thermodynamic solution model for $NaAlSiO_4$ was adopted. At low temperatures, there is a small but noticeable solubility of SiO_2 in these nepheline structures [35, 36]. Previously, $NaAlSiO_4$ with excess SiO_2 solubility was modeled using the MQM [36]. In this study, this $KAlSiO_4$ nepheline solution was modeled by the MQM with a $KAlSiO_4$-Si_2O_4 solid solution. The high-temperature polymorph of $KAlSiO_4$, which has a kalsilite-like structure, was also described using the same framework as the nepheline solution.

7.3 Thermodynamic Evaluation and Optimization

All phase diagram, structural, and thermodynamic property data of the K_2O-Al_2O_3-SiO_2 system available in the literature were critically reviewed. Afterwards, all reliable experimental data from the literature were considered to obtain a set of thermodynamic functions for all stable phases in this system. Optimized thermodynamic properties of the ternary compounds are listed in Table 7.1 together with experimental data from the literature. The optimized model parameters of the solutions are listed in Table 7.2. Crystal structure and polymorphic transitions of $KAlSiO_4$ and $KAlSi_2O_6$ compounds are summarized in Tables 7.3 and 7.4, respectively.

7.3.1 Phase Diagrams

All stable compounds and experimentally investigated isoplethal sections of the K_2O-Al_2O_3-SiO_2 system are schematically shown in Fig. 7.1. There are 13 stable phases in this system at 1 atm pressure: liquid, K_2O, Al_2O_3, SiO_2 (α- and β-quartz, β-tridymite, β-cristobalite), $KAlO_2$ (low- and high-temperature polymorphs), $KAlSiO_4$ (low- and high-temperature polymorphs), $KAlSi_2O_6$, and $KAlSi_3O_8$. The details of experimental phase diagram data are presented in Figs. 7.2 to 7.4 along with the calculated phase boundaries.

Morey and Bowen [37] studied the melting behavior of $KAlSi_3O_8$ in the $KAlO_2$-SiO_2 section using equilibration/quenching techniques followed by optical microscopic observations (Fig. 7.2). $KAlSi_3O_8$ was found to melt incongruently at 1170 °C to $KAlSi_2O_6$ and SiO_2. One liquidus point at the $KAlSi_3O_8$ composition was detected at 1530 °C. The proposed phase diagram between $KAlSi_2O_6$ and SiO_2 was approximated based on these two measurements. Schairer and Bowen [38] performed experiments and constructed the phase diagram of the K_2O-Al_2O_3-SiO_2 system. A comprehensive phase diagram experimental study was conducted using equilibration technique followed by petrographic microscopy and XRD. The isothermal liquidus boundaries and ternary invariant reaction points were well presented with detailed experimental observations in the temperature range of 700 to 1700 °C. However, the investigated compositions were limited to the SiO_2-rich region of the ternary system and the melting behavior of $KAlSiO_4$ was only approximated due to its high melting point. The melting point of $KAlSiO_4$ was assumed to be about 1755 °C based on adjacent liquidus measurements.

Later, small modifications were made on Schairer and Bowen's work by Osborn and Muan [39]. The authors made a little change mainly on $KAlSiO_4$ and $KAlSi_2O_6$ with Al_2O_3 equilibria. In their

work, detailed descriptions of the changes were not provided, besides a few degrees of temperature differences compared to Schairer and Bowen's data were noticed on the modified re-drawn phase diagram. Cook *et al*. [40] investigated the pseudo-binary section between $KAlO_2$ and $KAlSi_2O_6$. The authors used equilibration/quenching technique with sealed Pt capsules followed by SEM and XRD analysis. Although it was not directly proven by experiments, $KAlSiO_4$ was expected to melt congruently based on the three experiments at the $KAlO_2$:SiO_2 ratio of 50:50. The melting temperature of $KAlSiO_4$ was found to be in between 1834 and 1856 °C. Cook *et al*. also reported a tetragonal phase between $KAlO_2$ and $KAlSiO_4$. However, the stability of the phase is controversial in the literature. Li *et al*. [41] could not find this tetragonal phase using equilibration technique followed by XRD analysis. According to Li *et al*, the $KAlO_2$ solid solution can contain up to 20 mol % SiO_2. Roth [35] reported the phase diagram join of $KAlO_2$-$KAlSi_2O_6$ extended from Cook *et al*.'s work without providing experimental details. In Roth's study, the $KAlO_2$ solid solution has a maximum solubility of SiO_2 about 28 mol % at 1816 °C. $KAlSiO_4$ incongruently melted at 1787 °C. The eutectic between $KAlSiO_4$ and $KAlSi_2O_6$ was at about 61 mol % SiO_2 at 1612 °C. Husheer *et al*. [42] studied the $KAlO_2$ solid solution using DSC followed by SEM and XRD. Husheer *et al*. found a progressive substitution of SiO_2 into the $KAlO_2$ cristobalite-based phase, with the phase transition temperature decreasing gradually as shown in Fig. 7.2. Also, the $KAlO_2$ solid solution reached up to about 23.5 mol % of SiO_2 at 1500 °C. A newly observed phase, α′-$KAlO_2$, was reported at low temperatures (up to about 225 °C). The authors mentioned that the newly observed phase exhibited only a subtle structural difference from the β-$KAlO_2$ phase (high-temperature polymorph). Recently, Lecomte *et al*. [43] investigated two vertical sections of the ternary system using equilibration/quenching technique with sealed Pt capsules followed by XRD analysis.

The optimization of the pseudo-binary section between $KAlO_2$ and SiO_2 in Fig. 7.2 is very important in the modeling of this ternary system. Three ternary compounds exist in this section implying that the liquid solution properties of this system are mostly determined by the properties of this section. Also, most of the experimental studies on this system were performed on this pseudo binary section due to its importance in many geological studies and industrial requirements. In this study, this pseudo binary section is successfully optimized based on all available experimental data. The phase boundaries are well reproduced, including high- and low-temperature polymorphs of the $KAlO_2$ and $KAlSiO_4$ solid solutions. The SiO_2 liquidus slope, which clearly shows the evidence of KAl^{4+} associates in the liquid solution, was properly reproduced. However, some discrepancies remain at high temperatures near $KAlO_2$-rich compositions. In fact, the reported $KAlSiO_4$ melting points from the literature are not consistent with each other. Cook *et al*. [40] reported it to be more than 1834 °C, Roth [35] reported 1787 °C, and Schairer and Bowen [38] reported about 1755 °C. Even though the latter was an estimated value based on adjacent liquidus measurements, it is considered as the most reliable data. In the present thermodynamic modeling, it was also found that reproducing the experimental liquidus with melting points of $KAlSiO_4$ such as 1787 °C [35] or higher (> 1834 °C) [40] was very difficult simultaneously considering the thermodynamic property data. In the present study, the melting point of $KAlSiO_4$ was optimized to be 1753 °C and some discrepancies on the experimental $KAlO_2$ liquidus reported by Roth were ignored. The melting points for the two other ternary compounds $KAlSi_2O_6$ and $KAlSi_3O_8$ were optimized based on the experimental data from Schairer and Bowen [38] and Morey and Bowen [37]. The liquidus between $KAlSiO_4$ and SiO_2 are well reproduced. The $KAlO_2$ solid solution was optimized based on the reported phase boundary between the high- and low-temperature phases by Husheer *et al*. [42] and an approximate maximum solubility by

Roth [35]. The newly found low-temperature phase (α′-$KAlO_2$) from Husheer *et al*. was not considered in the optimization due to the small stability region between the low- and high-temperature polymorphs, which appears below 225 °C (maximum range is from about 10 to 13.5 mol % SiO_2 at 25 °C). The reliability of experimental data can be questionable due to very slow kinetics in this temperature range. The calculated $KAlSiO_4$ solid solution is in good agreement with Cook *et al*.'s experimental data. The $KAlSiO_4$ solid solution and eutectic between $KAlSiO_4$ and $KAlSi_2O_6$ are in good agreement with the experimental data as well [35, 38, 40].

Experimental data are available on several isoplethal sections from Schairer and Bowen [38] and Lecomte *et al*. [43]. Comparisons between the calculations and the experimental data are shown in Fig. 7.3 (a) to (g). Most sections are in very good agreement with the experimental data. However, the calculated section between $KAlSi_2O_6$ and Al_2O_3 (Fig. 7.3 (d)) and the one between $KAlSiO_4$ and Al_2O_3 (Fig. 7.3 (e)) exhibit some deviations from the reported experimental data. In order to reproduce the experimental data for these two sections, additional ternary parameters were introduced considering the amount of KAl^{4+} associate formations in these two sections of the system. However, no ternary parameters could reproduce simultaneously the experimentally measured activity data [44] (see Section 7.3.3.4) and the phase diagram data at SiO_2-rich compositions. In these two pseudo binary sections, the formation of metastable anhydrous muscovite ($KAl_3Si_3O_{11}$) or β-alumina ($KAl_{11}O_{17}$) may affect the phase equilibria. Especially, β-alumina, which decomposes at about 1950 °C in equilibrium condition [21], is known to form easily as a metastable phase when synthesizing with α-Al_2O_3 (corundum) since they are isostructural with hexagonal structure [45, 46]. This may affect the experimental measurements in these sections of the system.

The optimized isothermal liquidus from 800 to 1700 °C and the univariant lines with invariant reaction points of the K_2O-Al_2O_3-SiO_2 system are shown in Fig. 7.4 (a) and (b), respectively, along with the experimental data reported by Schairer and Bowen [38]. The calculated isothermal liquidus are in good agreement with the experiments. Regarding the invariant reaction points, except for peritectics 8 and 10 in Fig. 7.4 (b), all calculated temperatures are within ± 30 °C from the experimental data. Peritectic 8 is 88.7 °C higher than the experiment value and peritectic 10 is 48.7 °C lower. Details of the invariant points are listed in Table 7.5. In the present optimization, one ternary model parameter was used for the liquid phase to reproduce experimental data of ternary eutectic and peritectic points (eutectic 2 and peritectic 8 in Table 7.5 and Fig. 7.4 (b)), pseudo-binary sections of $KAlSi_2O_6$ to Al_2O_3 and $KAlSiO_4$ to Al_2O_3 (Fig. 7.3 (d) and (e), respectively), and the activity data from Oeltjen [44] (see section 7.3.3.4).

7.3.2 Crystal Structure and Polymorphic Transitions of the Compounds

The crystal structure and polymorphic transitions of the $KAlSiO_4$ compound were studied using various experimental techniques. The details of the literature data are summarized in Table 7.3. There are three types of stable crystal structure of $KAlSiO_4$. Lange *et al*. [47] found two phase transitions at 817 and 695 K using DSC and XRD. The phase transition at 817 K was detected as from orthorhombic or hexagonal structure (low-temperature polymorph) to another hexagonal structure (high-temperature polymorph). This transition was also found by Pankratz [48] using drop calorimetry and by Capobianco and Carpenter [49] using TEM and high-temperature XRD. The transition at 695 K can be a symmetry change between two orthorhombic structures or orthorhombic to lower hexagonal symmetry. However, this transition was only reported by Lange *et al*. Later, Capobianco and Carpenter tried to find this transition but could not find any evidence. Therefore, only the transition at about 810 K was adopted in the optimization of the $KAlSiO_4$ phase

of the present study. Some structural studies propose a transition at about 1130 K [49-54]. However, this is known to be a second order transition, which is not included in the present optimization. Other reported transitions show large discrepancies between the studies. Only certain data can be considered having similar trend, however, they are controversial between each other. For example, the phase transition at about 1373 K reported by Minor *et al*. [55] can be considered as the displacive transition measured by Dimitrijevic and Dondur [56] at about the same temperature (from 1273 to 1373 K). These two works both defined structure of $KAlSiO_4$ below 1373 K as orthorhombic (which also corresponds to Cook *et al*.'s result [40], orthorhombic $P2_12_12$). Nevertheless, the proposed structures above 1373 K are different between these two groups of authors. Generally, the phase transitions reported in the literature vary depending on the synthesis techniques, composition of solid solutions and impurities in the sample materials (such as Na, Ca, Mg, etc.).

The crystal structure and polymorphic transitions of the $KAlSi_2O_6$ compounds are summarized in Table 7.4. Many structural studies were performed on this ternary compound and show consistent results with each other. Second order transition occurs at about 920 K from tetragonal, $I4_1/a$ (low-temperature polymorph) to cubic, $Ia3d$ (high-temperature polymorph) [47, 48, 57]. In this study, this second order transition was reproduced at about 918 K by employing the heat capacity data from Lange *et al*. [47]. Another transition can possibly occur at about 940 K involving intermediate Al/Si ordered phase, $I4_1/acd$ [47, 58-60]. However, the existence of this phase transition is still debatable.

The polymorphic transition of $KAlSi_3O_8$ is found to be a second order transition at low temperatures (between about 473 and 773 K). According to Deer *et al*. [12], $KAlSi_3O_8$ has three

polymorphs: high-temperature polymorph (sanidine) has monoclinic ($C2/m$) structure (an Al/Si disordered structure); intermediate-temperature polymorph (orthoclase) has pseudo monoclinic (more Al/Si ordered); low-temperature polymorph (microcline) has fully ordered structure of $C\bar{1}$. Depending on the Al/Si ordering in the tetrahedral site, $KAlSi_3O_8$ can transform into other polymorphs [61]. However, the transition temperature is not clear. The monoclinic-triclinic inversion temperature of $KAlSi_3O_8$ can be presumed to be very low or metastable based on Smith and MacKenzie's study [62]. Another possibility is that there is a triclinic to monoclinic symmetry change at about 473 to 773 K in the orthoclase phase investigations. In this study, the polymorphic transition of $KAlSi_3O_8$ is not considered. This is because the transition temperature is not clear, and it is an order-disorder transition at low temperatures.

Besides $KAlSiO_4$, $KAlSi_2O_6$, and $KAlSi_3O_8$, there are three more ternary compounds reported in this system. Weyberg [63] found the existence of a stoichiometric compound $K_2Al_2SiO_6$ using the fusion of $Al_2Si_2O_5(OH)_4$ with K_2CrO_4. Some CaO (about 2 mol %) and MgO (trace) were also found in this compound. Later, Schairer and Bowen [38] tried to synthesize $K_2Al_2SiO_6$ using high-temperature sintering process (1712 °C). However, it was not successful. According to the more recent study by Cook *et al*. [40], no evidence was found for the existence of $K_2Al_2SiO_6$ in the temperature range of 1400 to 1600 °C (1673 to 1873 K). Cook *et al*. mentioned that the $K_2Al_2SiO_6$ composition may come from about 25 mol % SiO_2 solubility in $KAlO_2$ at 1600 °C (1873 K). A tetragonal phase, possibly at the composition of $K_{1+X}Al_{1+X}Si_{1-X}O_4$ with X about 0.1, was reported by Cook *et al*. Later, Roth [35] mentioned that the stability of this tetragonal phase is doubtful considering the Al/Si ordering in the framework of the unit cell. No distinctive evidence for the existence of this tetragonal phase was found in the literature. Pankratz [64] synthesized a dehydrated muscovite ($KAl_3Si_3O_{11}$) by taking out 4.52 wt. % H_2O from a natural muscovite

($KAl_3Si_3O_{10}(OH)_2$). The natural muscovite used in Pankratz's study contained 3.69 Fe_tO, 0.79 MgO, 0.99 Na_2O, and 0.08 TiO_2 (wt. %) based on chemical analysis. An attempt to synthesize anhydrous muscovite ($KAl_3Si_3O_{11}$) using only the ternary components (K_2O-Al_2O_3-SiO_2) was not successful in the work of Schairer and Bowen [38]. In their work, the theoretical composition at $KAl_3Si_3O_{11}$ was prepared and melted above 1730 °C. Upon cooling, only the phases of Al_2O_3, $KAlSi_2O_6$, mullite, and $KAlSi_3O_8$ were found. In summary, the three phases: $K_2Al_2SiO_6$, the tetragonal phase reported by Cook *et al.*, and $KAl_3Si_3O_{11}$ are not considered in the thermodynamic optimization in this study due to the lack of experimental proof of their stability in equilibrium condition.

7.3.3 Thermodynamic Properties

The thermodynamic properties of the pure compounds, K_2O, Al_2O_3, and SiO_2, were taken from the FToxid database [22]. Those of the binary compounds of the K_2O-SiO_2, K_2O-Al_2O_3, and Al_2O_3-SiO_2 systems were taken from the previous thermodynamic optimizations [20, 21, 30]. The optimized values for these components were employed in the present optimization without any changes. There are sufficient thermodynamic data for ternary solid and liquid in this system. Therefore, the Gibbs energy of all phases can be well constructed in the present thermodynamic optimization.

7.3.3.1 $KAlSiO_4$

The enthalpy of formation ($\Delta H^{o}_{298.15K}$) of $KAlSiO_4$ was first reported by Barany and Adami [65] using solution calorimetry. The sample used in their study had orthorhombic symmetry based on the XRD patterns, which is known to be the high-temperature polymorph of the compound. This result was criticized by Hemingway and Robie [66], because the crystal structure of the stable

$KAlSiO_4$ phase at low temperature should be hexagonal rather than orthorhombic. The experimental data from Hemingway and Robie using solution calorimetry were considered in the present study to be more accurate than Barany and Adami's data. Also, Hemingway and Robie mentioned that the enthalpy of solution of α-quartz used in Barany and Adami's study was found to be incorrect. The low-temperature polymorph with hexagonal structure is supported by many studies [49, 51, 67-69]. The optimized $\Delta H^o_{298.15K}$ in this study is -2123.32 kJ·mol^{-1}, which is within the experimental error range of the reported value by Hemingway and Robie (-2121.92 ± 1.4 kJ·mol^{-1}).

The low-temperature heat capacity (C_P) of $KAlSiO_4$ was measured by Kelley *et al*. [70] from 52.73 to 296.41 K using adiabatic calorimetry. They also reported the standard entropy at 298.15 K ($S^o_{298.15K}$) to be 133.05 J·mol^{-1}·K^{-1} based on the C_P measurements. Later, this $S^o_{298.15K}$ value was corrected to 133.3 J·mol^{-1}·K^{-1} by Hemingway and Robie [66]. Because S^o_{0K} used in Kelley *et al*.'s study was simply assumed to be zero, which is incorrect. Hemingway and Robie corrected the S^o_{0K} considering Al/Si disorder. In this study, the $S^o_{298.15K}$ was optimized to be 134.51 J·mol^{-1}·K^{-1}, which is within the experimental error range from Hemingway and Robie [66] (133.3 ± 1.3 J·mol^{-1}·K^{-1}).

The heat content ($H_T - H_{298.15K}$) was measured by Pankratz [48] in the temperature range between 409.7 and 1799.4 K using drop calorimetry. High-temperature C_P was measured by Lange *et al*. [47] using differential scanning calorimetry (DSC). The heat content data from Pankratz were compared with the calculated heat content based on the high-temperature C_P reported by Lange *et al*. They are in good agreement with each other as shown in Fig. 7.5 (a). In this study, both

derived C_P from Pankratz's data and the C_P from Lange *et al*. were considered to optimize the C_P of the $KAlSiO_4$ compound. The C_P function used in the present study is shown in Table 7.1 and Fig. 7.5 (b). The optimized C_P is also in good agreement with the low-temperature C_P from Kelley *et al*. [70] and the high-temperature C_P from Lange *et al*. [47].

Lange *et al*. [47] reported two thermal incidents at about 695 and 817 K from the DSC record of the $KAlSiO_4$ sample. The peak at 695 K corresponded to the phase change from orthorhombic-O1 to hexagonal structure with a transition heat of 597 J·mol^{-1}. The peak at 817 K was the phase transition between two hexagonal symmetries with a transition heat of 427 J·mol^{-1}. In the temperature range from 409.7 to 1799.4 K, Pankratz [48] observed a discontinuity on the heat content values occurring at 810 K. The enthalpy of transition (ΔH_{tr}^{o}) for this phase change was measured to be 669.44 J·mol^{-1}. Thus, the thermal incident at 695 K reported by Lange *et al*. was controversial to Pankratz's results. Later, Capobianco and Carpenter [49] tried to investigate the transition of $KAlSiO_4$ at 695 K using high-temperature XRD. However, the authors could not find any transition other than the one at 813 K. In the optimization of this study, this first order transition reported by Pankratz is reproduced at 775.2 K with ΔH_{tr}^{o} of 666.4 J·mol^{-1}. This is because the transition reported in Pankratz's study started from 775.4 K based on the actual data points. The onset temperature of the transition from Lange *et al*. was at 781.3 K, which is close to the one from Pankratz. Other phase transitions reported at higher temperature ranges were not considered because of inconsistencies between these data (see Table 7.3) as well as Pankratz's data, which shows no indication of phase change up to 1799.4 K other than the one at 755.4 K.

7.3.3.2 $KAlSi_2O_6$

The $\Delta H^o_{298.15K}$ of $KAlSi_2O_6$ was first reported to be -3019.2 kJ·mol^{-1} by Barany and Adami [65] using solution calorimetry. The $\Delta H^o_{298.15K}$ was re-reassessed by Hemingway and Robie [66] due to the incorrect heat of solution value of α-quartz used in Barany and Adami's study. The $\Delta H^o_{298.15K}$ value was modified to be -3038.7 kJ·mol^{-1}. In this study, $\Delta H^o_{298.15K}$ was calculated to be -3040.1 kJ·mol^{-1}, which is within the experimental error range of -3038.7 ± 2.76 kJ·mol^{-1} in Hemingway and Robie's study.

The C_P was measured at low temperatures (53.07 - 296.26 K) by Kelley *et al*. [70] using adiabatic calorimetry. The $S^o_{298.15K}$ was calculated to be 219.66 J·mol^{-1}·K^{-1} based on the C_P measurements. Later, $S^o_{298.15K}$ was corrected to be 200.2 ± 1.7 J·mol^{-1}·K^{-1} by Hemingway and Robie [66] considering the effect of Al/Si disorder. In this study, $S^o_{298.15K}$ was adopted from Hemingway and Robie's study and modified to the value of 198.5 J·mol^{-1}·K^{-1} within the experimental error limit.

The heat content ($H_T - H_{298.15K}$) was measured by Pankratz [48] using drop calorimetry. High-temperature C_P was directly measured by Lange *et al*. [47] using DSC in the temperature range of 420 to 990 K. The heat content calculated based on Lange *et al*.'s [47] C_P value shows a good agreement with Pankratz's [48] as shown in Fig. 7.6 (a). The high- and low-temperature C_P of $KAlSi_2O_6$ were adopted from Lange *et al*. and Kelley *et al*. [70] to perform the optimization. The calculated C_P from this study and experimental data are depicted in Fig. 7.6 (b).

A phase transformation was observed in $KAlSi_2O_6$ in the temperature range of 848 to 955 K by Pankratz [48], Lange *et al*. [47], and several structural studies [71-73]. Pankratz found the

transition enthalpy was zero using drop calorimetry. The structural studies reported that the transition occurs gradually and continuously. Based on these evidences, the authors of the present paper consider this transition as a second order transition from tetragonal symmetry (low-temperature phase) to cubic symmetry (high-temperature phase) from about 830 to 930 K with the peak temperature at 918 K. The effect of this phase change on C_P was reproduced using Lange *et al*.'s data. This second order phase transition was well reproduced in the present optimization as shown in Fig. 7.6 (b).

7.3.3.3 $KAlSi_3O_8$

The thermodynamic properties of $KAlSi_3O_8$ are taken from the values for the sanidine (high-temperature polymorph). No phase transition from microcline (low-temperature polymorph) and orthoclase (intermediate-temperature polymorph) were considered in this study. This is because the exact temperature of the phase transition is unknown and it seems to occur as a second order transition at low temperatures. In preliminary calculations in this study based on the reported thermodynamic properties for microcline (low-temperature polymorph) and sanidine, one phase transition between the two phases was calculated to be at 281.82 K (8.67 °C). Therefore, the thermodynamic properties of sanidine can possibly represent most of the temperature range of $KAlSi_3O_8$.

The $\Delta H^o_{298.15K}$ of sanidine was measured to be -3951.28 kJ·mol^{-1} by Waldbaum [74] using solution calorimetry. Later, Hemingway and Robie [66] corrected the values due to incorrect heat of solution of α-quartz data used in the work of Waldbaum. The $\Delta H^o_{298.15K}$ in this study was calculated to be -3962.9 kJ·mol^{-1}, which is within the experimental error range of -3959.53 ± 3.37 kJ·mol^{-1} by Hemingway and Robie.

The C_P was measured at low temperatures (54.07 – 296.53 K) by Kelley *et al*. [70] using adiabatic calorimetry. Adularia, one of the polymorphs of feldspar close to orthoclase structure, was used as a sample material. The $S^o_{298.15K}$ based on the C_P measurements was reported to be 219.66 J·mol^{-1}·K^{-1}. This $S^o_{298.15K}$ value was corrected by Hemingway and Robie [66] considering the Al/Si disorder. Openshaw *et al*. [75] studied low-temperature C_P (5 - 300 K) using an adiabatic calorimeter for sanidine. The authors reported the $S^o_{298.15K}$ of 232.9 J·mol^{-1}·K^{-1} based on the C_P measurements. The S^o_{0K} of sanidine in Openshaw *et al*.'s study was determined considering the Al/Si distribution in a disordered phase. More recently, Haselton *et al*. [76] measured the C_P (5 - 300 K) using adiabatic calorimetry for sanidine. In the calculation of $S^o_{298.15K}$ from Haselton *et al*, the value of S^o_{0K} was considered as 18.7 J·mol^{-1}·K^{-1}. The calculated $S^o_{298.15K}$ values are in good agreement with each other except the one from Kelley *et al*. In this study, the $S^o_{298.15K}$ value was modified to be 2.7 % higher than the reported value by Openshaw *et al*. This change was inevitable to reproduce the high temperature stability of $KAlSi_3O_8$ due to the less negative value of $\Delta H^o_{298.15K}$ of the sanidine than the one for the microcline at low temperatures.

The high-temperature C_P (298 to 1000 K) was measured by Hemingway *et al*. [77] using DSC for the microcline and sanidine phases. The calculated C_P from this study and the data from Hemingway *et al*. [77] are depicted in Fig. 7.7 (a) together with the low-temperature C_P data. The heat content ($H_T - H_{298.15K}$) was measured by Kelley *et al*. [70] using drop calorimetry in the temperature range of 400 to 1400 K. However, the samples were microcline and orthoclase rather than sanidine. The heat content for the sanidine can be calculated using the C_P data from

Openshaw *et al*. [75] up to 370 K and from Haselton *et al*. [76] up to 380 K. Both the microcline and sanidine phases have almost identical C_P values based on Openshaw *et al*. and Haselton *et al*. as shown in Fig. 7.7 (b). The C_P measured by Hemingway *et al*. [77] using DSC shows that microcline and sanidine have similar C_P in Fig. 7.7 (a). Therefore, in this study, the data from Hemingway *et al*. and Kelley *et al*. were considered to be reliable for the high-temperature C_P up to 1400 K for the sanidine.

7.3.3.4 Liquid

The activity of K_2O (referenced to liquid state) was measured by Oeltjen [44] using Knudsen effusion mass spectrometry. The composition of the sample was 0.097 K_2O, 0.174 Al_2O_3, and 0.729 SiO_2 in mole fraction in the temperature range of 1789.2 to 1889.8 K. The partial pressure of potassium (P_K) was investigated by Hastie *et al*. [78] using Knudsen effusion mass spectrometry. Samples of five different compositions were measured in the temperature range of 1400 to 2150 K. Roy and Navrotsky [79] investigated the enthalpy of solution (ΔH^{sol}) of several melt compositions between $KAlO_2$ and SiO_2 using solution ($2PbO{\cdot}B_2O_3$) calorimetry at 973 K. Unfortunately, the enthalpy of mixing (ΔH^{Mix}) between $KAlO_2$ and SiO_2 could not be compared in this study because ΔH^{sol} of $KAlO_2$ is not available in the literature.

The calculated activity from this study and experimental values from Oeltjen [44] show good agreement with each other as shown in Fig. 7.8. Both activities increase following the same trend as a function of temperature and it shows a reasonable agreement considering the experimental error. The P_K measured by Hastie *et al*. [78] shows some discrepancies compared to the present calculations as shown in Fig. 7.9. The discrepancies come from insufficient equilibrium time and

composition changes due to the volatile loss of K_2O in the P_K measurements. According to Hastie *et al*., the data at the composition of K_2O = 0.25 (Al_2O_3 = 0.25 and SiO_2 = 0.5) was not fully equilibrated. The calculations from this study show that $KAlSiO_4$ is stable below 2023.9 K. Therefore, only the metastable calculations without the solid phases show good agreement with the reported experimental data. The experimental data at the compositions of 0.093 and 0.087 could not be reproduced in the present calculations. Instead, the calculations at the composition of 0.04 show a reasonable agreement with these experimental data. As K_2O loss in the experimental data was reported in a range of 0.2 to 5.5 wt. % K_2O in Hastie et al.'s work, some composition change may explain these discrepancies.

The structure of the K_2O-Al_2O_3-SiO_2 melt can be calculated from the MQM. The calculated amount of $KAlO_2$ associates in this study is compared with the $NaAlO_2$ associates using the previous optimization of the Na_2O-Al_2O_3-SiO_2 system [14] in the temperature range of 1300 to 2500 K as depicted in Fig. 7.10 (a). The systematic trends between $KAlO_2$ and $NaAlO_2$ associates are well represented in the optimization of this study. Quasichemical pairs in the MQM can be used to calculate the fractions of non-bridged oxygen (NBO) and bridged oxygen (BO) of the melt. The quasichemical pairs of $K-K$, $Al-Al$, $K-Al$, $K-Si$, $K-KAl$, $Al-Si$, and $Al-KAl$ represent the NBO, while the pairs of $Si-Si$, $KAl-KAl$, $Si-KAl$ represent the BO in the present model. Thompson and Stebbins [80] measured NBO pairs along the compositions of $KAlO_2$ – SiO_2 using ^{17}O and ^{27}Al Magic Angle Spinning Nuclear Magnetic Resonance (MAS NMR) technique. The calculations in this study were performed at 1221 K (948 °C) based on the reported glass transition temperature of the $KAlSi_3O_8$ composition [81]. The calculated results are plotted in Fig. 7.10 (b) along with experimental data. The experimental data are well reproduced by the present calculations, even though these structural data were not directly considered

throughout the process of thermodynamic optimization. Therefore, it can be said that proper $KAlO_2$ associate species are considered in the present optimization and they accurately describe not only the thermodynamic properties but also the short-range ordering structure of the K_2O-Al_2O_3-SiO_2 liquid solution.

7.4 Summary

Thermodynamic optimization using the MQM was performed for the K_2O-Al_2O_3-SiO_2 system. All available thermodynamic and phase equilibrium data in the literature have been critically assessed. A set of optimized Gibbs energy functions for all phases in the K_2O-Al_2O_3-SiO_2 system was obtained, which reproduces the reliable experimental data in the literature. Strong short-range ordering structure in the K_2O-Al_2O_3-SiO_2 melt is also well calculated by introducing the $KAlO_2$ associates in the liquid solution. The present optimized model parameters can be used to calculate any thermodynamic properties and phase diagram in the entire composition and temperature ranges of the K_2O-Al_2O_3-SiO_2 system.

Acknowledgments

Financial supports from Tata Steel Europe, POSCO, Nucor Steel, Rio Tinto Iron and Titanium, Hyundai Steel, Nippon Steel and Sumitomo Metals Corp., JFE Steel, Voestalpine, RHI, and the Natural Sciences and Engineering Research Council of Canada are gratefully acknowledged. Authors (D.-G. Kim and B. Konar) also acknowledge the McGill Engineering Doctorate Award (MEDA) from McGill University.

References

[1] M.J. Cattell, T.C. Chadwick, J.C. Knowles, R.L. Clarke, D.Y.D. Samarawickrama, The nucleation and crystallization of fine grained leucite glass-ceramics for dental applications, Dent. Mater., 22 (2006) 925-933.
[2] C.C. Gonzaga, P.F. Cesar, C.Y. Okada, C. Fredericci, F. Beneduce Neto, H.N. Yoshimura, Mechanical properties and porosity of dental glass-ceramics hot-pressed at different temperatures, Mater. Res. (Sao Carlos, Braz.), 11 (2008) 301-306.
[3] M. Mrazova, A. Klouzkova, Leucite porcelain fused to metals for dental restoration, Ceram.-Silik., 53 (2009) 225-230.
[4] X. Chen, T.C. Chadwick, R.M. Wilson, R.G. Hill, M.J. Cattell, Crystallization and flexural strength optimization of fine-grained leucite glass-ceramics for dentistry, Dent. Mater., 27 (2011) 1153-1161.
[5] H.R. Fernandes, D.U. Tulyaganov, M.J. Pascual, V.V. Kharton, A.A. Yaremchenko, J.M.F. Ferreira, The role of K2O on sintering and crystallization of glass powder compacts in the Li2O-K2O-Al2O3-SiO2 system, J. Eur. Ceram. Soc., 32 (2012) 2283-2292.
[6] H.R. Fernandes, D.U. Tulyaganov, A. Goel, J.M.F. Ferreira, Effect of K2O on structure-property relationships and phase transformations in Li2O-SiO2 glasses, J. Eur. Ceram. Soc., 32 (2012) 291-298.
[7] M.D. Allendorf, K.E. Spear, Thermodynamic analysis of silica refractory corrosion in glass-melting furnaces, J. Electrochem. Soc., 148 (2001) B59-B67.
[8] K.E. Spear, M.D. Allendorf, Thermodynamic analysis of alumina refractory corrosion by sodium or potassium hydroxide in glass melting furnaces, J. Electrochem. Soc., 149 (2002) B551-B559.
[9] J. Stjernberg, B. Lindblom, J. Wikstroem, M.L. Antti, M. Oden, Microstructural characterization of alkali metal mediated high temperature reactions in mullite based refractories, Ceram. Int., 36 (2010) 733-740.
[10] L.A.M. Scudeller, E. Longo, J.A. Varela, Potassium vapor attack in refractories of the alumina-silica system, J. Am. Ceram. Soc., 73 (1990) 1413-1416.
[11] S.E. McCune, T.P. Greaney, W.C. Allen, R.B. Snow, Reaction between K2O and Al2O3-SiO2 refractories as related to blast-furnace linings, J. Am. Ceram. Soc., 40 (1957) 187-195.
[12] W.A. Deer, R.A. Howie, J. Zussman, An Introduction to the Rock-Forming Minerals, Pearson; 2 edition, 1996.
[13] G.W. Morey, Data of Geochemistry. 6th ed. Chapter L. Phase Equilibrium Relations of the Common Rock-Forming Oxides Except Water, U.S. Govt. Printing Office, 1964.
[14] P. Chartrand, A.D. Pelton, Modeling the charge compensation effect in silica-rich Na2O-K2O-Al2O3-SiO2 melts, CALPHAD: Comput. Coupling Phase Diagrams Thermochem., 23 (1999) 219-230.
[15] A.D. Pelton, S.A. Degterov, G. Eriksson, C. Robelin, Y. Dessureault, The modified quasichemical model I - binary solutions, Metall. Mater. Trans. B, 31B (2000) 651-659.
[16] A. Pelton, P. Chartrand, The modified quasi-chemical model: Part II. Multicomponent solutions, Metallurgical and Materials Transactions A, 32 (2001) 1355-1360.
[17] E. Yazhenskikh, K. Hack, M. Mueller, Critical thermodynamic evaluation of oxide systems relevant to fuel ashes and slags, Part 5: Potassium oxide-alumina-silica, CALPHAD: Comput. Coupling Phase Diagrams Thermochem., 35 (2011) 6-19.

[18] T.M. Besmann, K.E. Spear, Thermochemical modeling of oxide glasses, J. Am. Ceram. Soc., 85 (2002) 2887-2894.
[19] M. Hillert, The compound energy formalism, J. Alloys Compd., 320 (2001) 161-176.
[20] D.G. Kim, M.A. Van Ende, P. Hudon, I.H. Jung, Coupled experimental study and thermodynamic optimization of the K2O-SiO2 system, Submitted to Journal of Non-Crystalline Solids, (2017).
[21] D.G. Kim, E. Moosavi-Khoonsari, I.H. Jung, Thermodynamic Modeling of the K2O-Al2O3 and K2O-MgO-Al2O3 Systems with Emphasis to β- and β″-Alumina, To be submitted, (2017).
[22] C.W. Bale, E. Belisle, P. Chartrand, S.A. Decterov, G. Eriksson, A.E. Gheribi, K. Hack, I.H. Jung, Y.B. Kang, J. Melancon, A.D. Pelton, S. Petersen, C. Robelin, J. Sangster, P. Spencer, M.A. Van Ende, FactSage thermochemical software and databases, 2010-2016, CALPHAD: Comput. Coupling Phase Diagrams Thermochem., 54 (2016) 35-53.
[23] E. Ising, Beitrag zur Theorie des Ferromagnetismus, Zeitschrift für Physik, 31 (1925) 253-258.
[24] B.O. Mysen, P. Richet, Silicate glasses and melts properties and structure, Elsevier, 2005.
[25] S. Sukenaga, K. Kanehashi, H. Shibata, N. Saito, K. Nakashima, Structural Role of Alkali Cations in Calcium Aluminosilicate Glasses as Examined Using Oxygen-17 Solid-State Nuclear Magnetic Resonance Spectroscopy, Metall. Mater. Trans. B, 47 (2016) 2177-2181.
[26] T. Higo, S. Sukenaga, K. Kanehashi, H. Shibata, T. Osugi, N. Saito, K. Nakashima, Effect of potassium oxide addition on viscosity of calcium aluminosilicate melts at 1673-1873 K, ISIJ Int., 54 (2014) 2039-2044.
[27] G.-H. Zhang, K.-C. Chou, Measuring and modeling viscosity of CaO-Al2O3-SiO2(-K2O) Melt, Metall. Mater. Trans. B, 43 (2012) 841-848.
[28] A.D. Pelton, Thermodynamics and Phase Diagrams of Materials, in: Phase Transformations in Materials, Wiley-VCH Verlag GmbH & Co. KGaA, 2005, pp. 1-80.
[29] A.D. Pelton, A general "geometric" thermodynamic model for multicomponent solutions, CALPHAD: Comput. Coupling Phase Diagrams Thermochem., 25 (2001) 319-328.
[30] G. Eriksson, A.D. Pelton, Critical evaluation and optimization of the thermodynamic properties and phase diagrams of the calcia-alumina, alumina-silica, and calcia-alumina-silica systems, Metall. Trans. B, 24B (1993) 807-816.
[31] I.E. Grey, B.F. Hoskins, I.C. Madsen, A structural study of the incorporation of silica into sodium ferrites, Na1-x[Fe1-xSixO2], x = 0 to 0.20, J. Solid State Chem., 85 (1990) 202-219.
[32] E. Moosavi-Khoonsari, I.-H. Jung, Critical Evaluation and Thermodynamic Optimization of the Na2O-FeO-Fe2O3-SiO2 System, Metallurgical and Materials Transactions B, 47 (2016) 291-308.
[33] J.F. Schairer, The alkali-feldspar join in the system NaAlSiO4-KAlSiO4SiO2, J. Geol., 58 (1950) 512-517.
[34] O.F. Tuttle, J.V. Smith, The nepheline-kalsilite system. II. Phase relations, Am. J. Sci., 256 (1958) 571-589.
[35] R.S. Roth, Phase equilibriums research in portions of the potassium oxide-magnesium oxide-iron(III)oxide-aluminum oxide-silicon dioxide system, Adv. Chem. Ser., 186 (1980) 391-408.
[36] E. Jak, P. Hayes, A.D. Pelton, S.A. Decterov, Thermodynamic modeling of the Al2O3-CaO-FeO-Fe2O3-PbO-SiO2-ZnO system with addition of K and Na with metallurgical applications, Proc. VIII Int'l Conf. on Molten Slags, Fluxes and Salts, Santiago, Chile, (2009) 473-490.
[37] G.W. Morey, N.L. Bowen, The melting of potash feldspar, Am. J. Sci., 4 (1922) 1-21.

[38] J.F. Schairer, N.L. Bowen, The system potassium oxide-alumina-silica, Am. J. Sci., 253 (1955) 681-746.
[39] E.F. Osborn, A. Muan, S. American Ceramic, J.C.F. Edward Orton, F. Edward Orton Junior Ceramic, Phase equilibrium diagrams of oxide systems, American Ceramic Society : Edward Orton, Jr., Ceramic Foundation, Columbus, Ohio, 1960.
[40] L.P. Cook, R.S. Roth, H.S. Parker, T. Negas, The system potassium oxide-aluminum oxide-silicon dioxide. Part 1. Phases on the KAlSiO4-KAlO2 join, Am. Mineral., 62 (1977) 1180-1190.
[41] C. Li, A.F. Reid, S. Saunders, Nonstoichiometric alkali ferrites and aluminates in the systems NaFeO2-TiO2, KFeO2-TiO2, KAlO2-TiO2, and KAlO2-SiO2, J. Solid State Chem., 3 (1971) 614-620.
[42] S.L.G. Husheer, J.G. Thompson, A. Melnitchenko, Cristobalite-Related Phases in the KAlO2-KAlSiO4 System, J. Solid State Chem., 147 (1999) 624-630.
[43] G. Lecomte, B. Pateyron, P. Blanchart, Experimental study and simulation of a vertical section mullite-ternary eutectic (985°C) in the SiO2-Al2O3-K2O system, Mater. Res. Bull., 39 (2004) 1469-1478.
[44] L. Oeltjen, Prediction of thermodynamic properties of coal slags by modelling, in, Inst. fur Werkstoffe und Verfahren der Energietechnik, 1999, pp. i-vi, 1-125.
[45] C.-H. Ham, S.-K. Lim, C.-K. Lee, S.-E. Yoo, Synthesis and phase relations of potassium-beta-aluminas in the ternary system K2O-MgO-Al2O3, Kongop Hwahak, 10 (1999) 1086-1091.
[46] W.-S. Kim, S.-K. Lim, Effect of stabilizers (MgO/Li2O) on phase relations of the ternary K+-β/β″-Al2O3 system, Kongop Hwahak, 12 (2001) 312-317.
[47] R.A. Lange, I.S.E. Carmichael, J.F. Stebbins, Phase transitions in leucite (KAlSi2O6), orthorhombic KAlSiO4, and their iron analogs (KFeSi2O6, KFeSiO4), Am. Mineral., 71 (1986) 937-945.
[48] L.B. Pankratz, High-temperature heat contents and entropies of dehydrated analcite, kaliophilite, and leucite, U. S. Bur. Mines, Rep. Invest., No. 7073 (1968) 8 pp.
[49] C. Capobianco, M. Carpenter, Thermally induced changes in kalsilite (KAlSiO4), Am. Mineral., 74 (1989) 797-811.
[50] Y. Andou, A. Kawahara, The existence of high-low inversion point of kalsilite, Mineral. J., 11 (1982) 72-77.
[51] R.N. Abbott, Jr., KAlSiO4 stuffed derivatives of tridymite: phase relationships, Am. Mineral., 69 (1984) 449-457.
[52] A. Kawahara, Y. Ando, F. Marumo, M. Okuno, The crystal structure of high-temperature form of kalsilite (KAlSiO4) at 950°C, Mineral. J., 13 (1987) 260-270.
[53] C.M.B. Henderson, D. Taylor, The structural behavior of the nepheline family: 3. Thermal expansion of kalsilite, Mineral. Mag., 52 (1988) 708-711.
[54] Y. Okamoto, Structural modification of KAlSiO4 minerals, Okayama University Earth Science Report, 4 (1997) 41-71.
[55] D.B. Minor, R.S. Roth, W.S. Brower, C.L. McDaniel, Alkali ion exchange reactions with rubidium aluminum silicate (RbAlSiO4): a new metastable polymorph of potassium aluminum silicate (KAlSiO4), Mater. Res. Bull., 13 (1978) 575-581.
[56] R. Dimitrijevic, V. Dondur, Synthesis and characterization of KAlSiO4 polymorphs on the SiO2-KAlO2 join. II. The end member of ANA type of zeolite framework, J. Solid State Chem., 115 (1995) 214-224.
[57] D.R. Peacor, High-temperature single-crystal diffractometer study of leucite, (K,Na)AlSi2O6, Z. Kristallogr., 127 (1968) 213-224.

[58] P.J. Heaney, D.R. Veblen, A high-temperature study of the low-high leucite phase transition using the transmission electron microscope, Am. Mineral., 75 (1990) 464-476.
[59] D.M. Hatch, S. Ghose, H.T. Stokes, Phase transitions in leucite, KAlSi2O6. I. Symmetry analysis with order parameter treatment and the resulting microscopic distortions, Phys. Chem. Miner., 17 (1990) 220-227.
[60] J.N. Walsh, R.J. Harrison, S.A.T. Redfern, Anelastic behaviour of leucite KAlSi2O6, Mater. Sci. Eng., A, A442 (2006) 208-211.
[61] J.V. Smith, G. Artioli, A. Kvick, Low albite, NaAlSi3O8: neutron diffraction study of crystal structure at 13 K, Am. Mineral., 71 (1986) 727-733.
[62] J.V. Smith, W.S. MacKenzie, The alkali feldspars. IV. The cooling history of high-temperature sodium-rich feldspars, Am. Mineral., 43 (1958) 872-889.
[63] Z. Weyberg, On the Aluminosilicate K2Al2SiO6, Centr. Min. Geol., (1908) 326-330.
[64] L.B. Pankratz, High-temperature heat contents and entropies of muscovite and dehydrated muscovite, Bur. Mines Rep. Invest., No. 6371 (1964) 6 pp.
[65] R. Barany, L.H. Adami, Heats of formation of lithium sulfate and five potassium- and lithium-aluminum silicates, U. S., Bur. Mines, Rep. Invest., No. 6873 (1966) 18 pp.
[66] B.S. Hemingway, R.A. Robie, Enthalpies of formation of low albite (NaAlSi3O8), gibbsite (Al(OH)3), and NaAlO2; revised values for $\Delta H°f,298$ and $\Delta G°f,298$ of some aluminosilicate minerals, J. Res. U. S. Geol. Surv., 5 (1977) 413-429.
[67] J.V. Smith, T.G. Sahama, Order-disorder in kalsilite, Am. Mineral., 42 (1957) 287-288.
[68] A.J. Perrotta, J.V. Smith, Crystal structure of kalsilite, KAlSiO4, Mineral. Mag., 35 (1965) 588-595.
[69] A.I. Becerro, M. Mantovani, A. Escudero, Hydrothermal synthesis of kalsilite: a simple and economical method, J. Am. Ceram. Soc., 92 (2009) 2204-2206.
[70] K.K. Kelley, S.S. Todd, R.L. Orr, E.G. King, K.R. Bonnickson, Thermodynamic properties of sodium aluminum and potassium aluminum silicates, Bur. Mines Rep. Invest., No. 4955 (1953) 21 pp.
[71] J. Wyart, A study of leucite, Bull. Soc. Fr. Mineral., 61 (1938) 228-238.
[72] R. Sadanaga, T. Ozawa, Thermal transition of leucite, Mineral. J. (Tokyo), 5 (1968) 321-333.
[73] G.T. Faust, Phase transition in synthetic and natural leucite, Schweiz. Mineral. Petrogr. Mitt., 43 (1963) 165 195.
[74] D.R. Waldbaum, High-temperature thermodynamic properties of alkali feldspars, Contrib. Mineral Petrology (Berlin), 17 (1968) 71-77.
[75] R.E. Openshaw, B.S. Hemingway, R.A. Robie, D.R. Waldbaum, K.M. Krupka, The heat capacities at low temperatures and entropies at 298.15°K of low albite, analbite, microcline, and high sanidine, J. Res. U. S. Geol. Surv., 4 (1976) 195-204.
[76] H.T. Haselton, Jr., G.L. Hovis, B.S. Hemingway, R.A. Robie, Calorimetric investigation of the excess entropy of mixing in analbite-sanidine solid solutions: lack of evidence for sodium, potassium short-range order and implications for two-feldspar thermometry, Am. Mineral., 68 (1983) 398-413.
[77] B.S. Hemingway, K.M. Krupka, R.A. Robie, Heat capacities of the alkali feldspars between 350 and 1000 K from differential scanning calorimetry, the thermodynamic functions of the alkali feldspars from 298.15 to 1400 K, and the reaction quartz + jadeite = analbite, Am. Mineral., 66 (1981) 1202-1215.
[78] J.W. Hastie, E.R. Plante, D.W. Bonnell, Alkali vapor transport in coal conversion and combustion systems, ACS Symp. Ser., 179 (1982) 543-600.

[79] B.N. Roy, A. Navrotsky, Thermochemistry of charge-coupled substitutions in silicate glasses: the systems M1/nn+AlO2-SiO2 (M = Li, Na, K, Rb, Cs, Mg, Ca, Sr, Ba, Pb), J. Am. Ceram. Soc., 67 (1984) 606-610.
[80] L.M. Thompson, J.F. Stebbins, Non-bridging oxygen and high-coordinated aluminum in metaluminous and peraluminous calcium and potassium aluminosilicate glasses: high-resolution 17O and 27Al MAS NMR results, Am. Mineral., 96 (2011) 841-853.
[81] P. Richet, Y. Bottinga, Thermochemical properties of silicate glasses and liquids: A review, Rev. Geophys., 24 (1986) 1-25.
[82] D. Cellai, M.A. Carpenter, P.J. Heaney, Phase transitions and microstructures in natural kaliophilite, Eur. J. Mineral., 4 (1992) 1209-1220.
[83] J. Wyart, Crystal structure and twinning of leucite, Compt. rend., 203 (1936) 938-939.
[84] J. Wyart, Crystallographic study of synthetic leucite. Atomic structure and mineral symmetry, Bull. Soc. Fr. Mineral., 63 (1940) 5-17.
[85] D. Taylor, C.M.B. Henderson, Thermal expansion of the leucite group of minerals, Amer. Mineral., 53 (1968) 1476-1489.
[86] K. Hirao, N. Soga, M. Kunugi, Thermal expansion and structure of leucite-type compounds, J. Phys. Chem., 80 (1976) 1612-1616.
[87] F. Mazzi, E. Galli, G. Gottardi, The crystal structure of tetragonal leucite, Am. Mineral., 61 (1976) 108-115.
[88] D.C. Palmer, E.K.H. Salje, W.W. Schmahl, Phase transitions in leucite: X-ray diffraction studies, Phys. Chem. Miner., 16 (1989) 714-719.

Tables

Table 7.1 Thermodynamic properties of ternary compounds.

Phase	$\Delta H^o_{298.15K}$ (kJ·mol^{-1})	$S^o_{298.15K}$ (J·mol^{-1}·K^{-1})	C_P (J·mol^{-1}·K^{-1})	Reference	Experimental method / Remarks
$KAlSiO_4$	-2107.899 ±1.757			66Bar[65]	Solution calorimetry
(LT)	-2121.920 ±1.435			77Hem[66]	Solution calorimetry
		133.051 ±1.255		53Kel[70]	Adiabatic calorimetry
		133.260 ±1.250		77Hem[66]	Data assessment
	$\Delta H^o_{tr(LT-HT)}$: 0.669, temperature : 775.4 to 851.3 K			68Pan[48]	Drop Calorimetry
	$\Delta H^o_{tr(LT-HT)}$: 0.427, temperature : 781.3 to 839.1 K			86Lan[47]	DSC
$KAlSiO_4$	-2123.324	134.510	184.290 + 0.00985 T -1.311*10^{+7} T $^{-2}$ -	This study	C_P based on 53Kel[70],
(LT)			4.654*10^{-6} T ^{2} + 5.407*10^{-10} T ^{3} +		86Lan[47], and 68Pan[48]
			2.139*10^{+9} T $^{-3}$ (298.15 - 2100 K)		
	$\Delta H^o_{tr(LT-HT)}$: 0.666, temperature : 775.2 K			This study	
$KAlSiO_4$	-2122.250	136.376	178.030 + 0.0268 T -1.311*10^{+7} T $^{-2}$ -	This study	
(HT)			1.908*10^{-5} T ^{2} + 4.506*10^{-9} T ^{3} +		
			2.139*10^{+9} T $^{-3}$ (298.15 - 2100 K)		
$KAlSi_2O_6$	-3010.174 ±3.138			66Bar[65]	Solution calorimetry
	-3038.650 ±2.755			77Hem[66]	Solution calorimetry
		184.096 ±1.674		53Kel[70]	Adiabatic calorimetry

		200.200 ±1.700		77Hem[66]	Data assessment
	-3040.080	198.500	160.617 + 275.315 T - 7.857*10^{+6} T $^{-2}$ – 4.296*10^{-4} T ^{2} + 2.725*10^{-7} T ^{3} + 9.592*10^{+8} T $^{-3}$ (298.15-850 K) - 7.888*10^{+4} + 0.292 T - 7.857*10^{+6} T $^{-2}$ – 0.3196 T ^{2} + 1.238*10^{-4} T ^{3} + 9.592*10^{+8} T $^{-3}$ (850-918 K) 240.868 + 0.00146 T – 6.382*10^{+6} T $^{-2}$ (918-2000 K)	This study	C_P based on 53Kel[70], 86Lan[47], and 68Pan[48]
$KAlSi_3O_8$	-3951.278 ±3.891			68Wal[75]	Solution calorimetry
	-3959.530 ±3.370			77Hem[66]	Solution calorimetry
		219.660 ±2.092		53Kel[70]	Adiabatic calorimetry
		232.900 ±0.400		76Ope[76]	Adiabatic calorimetry
		232.900 ±0.400		77Hem[66]	Data assessment
		232.800 ±0.400		83Has[77]	Adiabatic calorimetry
	-3962.900	239.680	397.586 - 2415.9 T $^{-0.5}$ – 8.545*10^{+6} T $^{-2}$ + 1.215*10^{+9} T $^{-3}$ (298.15-1473 K)	This study	C_P based on 53Kel[70] and 81Hem[66]

$\Delta H^{o}_{298.15K}$ are relative to elements at 298.15 K.

Table 7.2 Optimized model parameters of the solutions ($J \cdot mol^{-1}$ and $J \cdot mol^{-1} \cdot K^{-1}$).

Liquid solution (MQM)
$Z^{K}_{K\,K} = 0.6887$, $Z^{Al}_{Al\,Al} = 2.0662$, $Z^{Si}_{Si\,Si} = 2.7549$, $Z^{KAl}_{KAl\,KAl} = 2.7549$, $Z^{K}_{K\,Al} = 0.6887$, $Z^{K}_{K\,KAl} = 0.6887$, $Z^{KAl}_{KAl\,Al} = 2.0662$
$\Delta g_{KAl-Si} = (-101252.8 + 11.67336 \cdot T) + (-53764.4) \cdot X_{Si-Si} + (37656 - 20.92 \cdot T) \cdot X^{3}_{Si-Si}$
$q^{001}_{Si,K(KAl)} = -50208 + 14.644 \cdot T$
$q^{002}_{Si,K(KAl)} = -14644$
$q^{302}_{Si,K(KAl)} = 209200 - 87.864 \cdot T$
$q^{401}_{Si,K(KAl)} = 125520 - 84.9352 \cdot T$
$q^{011}_{Si,K(KAl)} = 71546.4$
$q^{001}_{Si,KAl(Al)} = -27196$
$KAlO_2$ solid solutions (CEF)
(KAl4+, VaSi4+)O_4
<u>High-temperature $KAlO_2$</u>
$G^{o}_{KAlO_2} = G^{o}_{KAlO_2(HT)}$
$G^{o}_{KAlO_2(HT)}$ $\Delta H^{o}_{298.15K}$: -1139250.848, $S^{o}_{298.15K}$: 87.149, C_P : 68.6115 + 0.069701·T - 972131.9821·T^{-2} -0.000026276·T^2 (298.15 – 810.0 K), 91.970 + 0.0119999998592·T (>810.0 K)
$G^{o}_{Va_2Si_2O_4} = 2 * (G^{o}_{SiO_2(s6)} + 6000)$
${}^{0}L_{KAl,Si} = -69036 - 29.288 \cdot T$

Low-temperature $KAlO_2$

$G^o_{KAlO_2} = G^o_{KAlO_2(LT)}$

$G^o_{KAlO_2(LT)}$ $\Delta H^o_{298.15K}$: -1140545.848, $S^o_{298.15K}$: 85.550, C_P : 68.6115 + 0.069701·T - 972131.9821·T^{-2} -0.000026276·T^2 (298.15 – 810.0 K), 91.970 + 0.0119999998592·T (>810.0 K)

$G^o_{Va_2Si_2O_4} = 2*(G^o_{SiO_2(s6)} + 5000)$

${}^0L_{KAl,Si} = -71128 - 14.644 \cdot T$

$KAlSiO_4$ solid solutions (MQM)

$Z^A_{AA} = 0.6887$, $Z^B_{BB} = 0.6887$, $Z^A_{AB} = 0.6887$, $Z^B_{BA} = 2.0662$, $A = KAlSi$, $B = VaSi_2$

High-temperature $KAlSiO_4$ (Kalsilite)

$G^o_{KAlSiO_4} = G^o_{KAlSiO_4(HT)}$

$G^o_{Va_2Si_2O_4} = 2*(G^o_{SiO_2(Trd)} + 6276)$

$\Delta g_{KAlSi-VaSi_2} = -17514.4 + 13.3888 \cdot T$

Low-temperature $KAlSiO_4$ (Nepheline)

$G^o_{KAlSiO_4} = G^o_{KAlSiO_4(LT)}$

$G^o_{Va_2Si_2O_4} = 2*(G^o_{SiO_2(Trd)} + 6276)$

$\Delta g_{KAlSi-VaSi_2} = -17514.4 + 13.3888 \cdot T$

Binary model parameters of the K_2O-SiO_2 and Al_2O_3-SiO_2 systems were taken from Kim *et al*. [21] and Eriksson and Pelton [31], respectively.

Table 7.3 Crystal structures and polymorphic transitions of $KAlSiO_4$ reported in the literature.

Temperature (K) Range	Transitions	Phases/Remarks	References	Exp. technique
695	695	orthorhombic → hexagonal	86Lan[47]	DSC, XRD
810 - 817	810	1st order tran., minor structural chage	68Pan[48]	Drop calorimetry, XRD
	813	hexagonal → hexagonal, 2nd order tran.	89Cap[53]	TEM, HT-XRD
	817	hexagonal → hexagonal (higher symmetry)	86Lan[47]	DSC, XRD
923 - 1023	923	No specific info. (some doubt on tran.)	87Kaw[51]	XRD
	998	$P6_322$ → $P6_3$, 2nd order tran.	92Cel	TEM, HT-XRD
	1023	$P6_3$ → different hexagonal, 1st order tran.	92Cel[83]	TEM, HT-XRD
1123 - 1163	1138	$P6_3$ → $P6_3mc$ & $P6_3/mmc$, 2nd order tran.	82And[49]	HT-XRD
	1123	$P6_3$ → $P6_3mc$ → $P6_3/m$ 2/m 2/c	84Abb[50]	TEM, HT-XRD
	1123	hexagonal → orthorhombic	57Smi[67]	XRD
	1138	$P6_3$ → $P6_3mc$ & $P6_3/mmc$, 2nd order tran.	87Kaw[51]	HT-XRD
	1123	Pseudo hexagonal → $3\sqrt{3}$ kalsilite, 1st order tran.	89Cap[53]	TEM, HT-XRD
	1138	$P6_3$ → $P6_3mc$ or $P6_3/mmc$, 2nd order tran.	97Oka[54]	XRD
	1163	$P6_3$ → $P6_3mc$ & $P6_3/mmc$, 2nd order tran.	88Hen[52]	XRD

	~1273	orthorhombic → hexagonal	57Smi[67]	XRD
1193 - 1293	1373	pseudo orthorhombic (or monoclinic) (metastable, in $KAlSiO_4$-$KFeSiO_4$) → normal low orthorhombic	78Min[55]	XRD
	1193	$3\sqrt{3}$ kalsilite → pseudo hexagonal	89Cap[53]	TEM, HT-XRD
	1273-1373	orthorhombic → hexagonal (Al-Si ordered), 2^{nd} order tran.	95Dim[56]	XRD, NMR, DSC, DTA, IR-spectrometry
1473 - 1758	1723-1758	orthorhombic → orthorhombic (with large unit cell)	77Coo[41]	SEM, XRD
	1473	hexagonal → orthorhombic or monoclinic	95Dim[56]	XRD, NMR, DSC,
	1573	orthorhombic or monoclinic → tetragonal (I41/a)		DTA, IR-spectrometry
	1703	tetragonal (I41/a) → orthorhombic		

Table 7.4 Crystal structures and polymorphic transitions of $KAlSi_2O_6$ reported in the literature.

Temperature (K)	**Phases/Remarks**	**References**	**Exp. technique**
873	tetragonal → cubic	36Wya[84]	XRD
848 - 898	tetragonal → cubic, small swelling in DTA curve	38Wya[71]	DTA, XRD
898	tetragonal ($I4_1/a$) → cubic (Ia3d), (or I4/acd)	40Wya[85]	XRD
891 - 905	tetragonal → cubic, two peaks in DTA curve	63Fau[73]	DTA, XRD
955	tetragonal → cubic, 2nd order transition	68Pan[48]	Drop calorimetry, XRD
878	tetragonal ($I4_1/a$) → cubic (Ia3d)	68Pea[57]	HT-XRD
878	tetragonal → cubic, continuous change up to trans. point	68Tay[86]	XRD
933 - 938	tetragonal → cubic, 2nd order transition	68Sad[72]	XRD
893	tetragonal → cubic, continuous change up to trans. point	76Hir[87]	HT-XRD
903	tetragonal ($I4_1/a$) → cubic, no Al/Si ordered phase	76Maz[74]	XRD
918, 946	tetragonal ($I4_1/a$) → tetragonal ($I4_1/acd$) → cubic (Ia3d)	86Lan[47]	DSC, XRD
918	tetragonal ($I4_1/a$) → tetragonal ($I4_1/acd$)	89Pal[88]	XRD
1123	tetragonal ($I4_1/acd$) → cubic, intermediate phase exist	90Hea[58]	TEM
920, 950	tetragonal ($I4_1/a$) → tetragonal ($I4_1/acd$) → cubic ($Ia\bar{3}d$)	90Hat[59]	Landau and induced representation theory
918, 938	tetragonal ($I4_1/a$) → tetragonal ($I4_1/acd$) → cubic (Ia3d)	06Wal[60]	DSC, XRD, OM

Table 7.5 Experimental and calculated invariant points in the K_2O-Al_2O_3-SiO_2 system involving liquid phase (see the liquidus projection in Fig. 7.4).

Invariant reactions **1-14**: this study	Type	Temperature (°C)			Liquid composition (mol %)								
					K_2O			Al_2O_3			SiO_2		
		55Sch [39]	11Yaz [18]	This study	55Sch [39]	11Yaz [18]	This study	55Sch [39]	11Yaz [18]	This study	55Sch [39]	11Yaz [18]	This study
1 L → Mul + Trd + Fsp	E	985 ±20	985	972.9	6.6	6.4	6.4	7.0	6.8	7.5	86.4	86.8	86.1
2 L → Coru + Lct + Kls	E	1553 ±5	1620	1526.4	17.8	17.4	17.4	23.3	23.3	26.1	58.9	59.3	56.5
3 L → Qz + Fsp + KS_4	E	710 ±20	724	702.4	16.1	18.0	17.5	2.4	1.6	2.1	81.5	80.3	80.4
4 L → KS_4 + Fsp + KS_2	E	695 ±5	707	692.0	22.1	22.0	21.2	2.2	1.2	2.1	75.7	76.8	76.7
5 L → KS_2 + Lct + Kls	E	905 ±10	891	911.0	30.4	30.0	29.6	5.6	5.5	5.7	64.1	64.5	64.8
11 L → Kls + β-A + KA	E			1655.7			24.3			35.6			40.1
12 L → KS + KS_2 + Kls	E			752.4			40.6			2.0			57.4
6 L + Lct → Fsp + Mul	P	1140 ±20	1140	1144.3	8.7	8.8	9.0	9.0	9.6	11.0	82.4	81.6	80.1
7 L + Crn → Lct + Mul	P	1315 ±10	1247	1403.7	10.2	9.4	11.1	12.5	10.8	16.4	77.4	79.8	72.5
8 L + Lct → Fsp + KS_2	P	810 ±5	786	761.3	23.8	23.0	22.4	3.6	3.3	3.2	72.6	73.7	74.4
13 L + Crn → Kls + β-A	P			1660.1			23.5			35.6			41.0
14 L + KA → KS + Kls	P			893.3			44.1			4.9			51.0
9 Crs → Trd	I	1470 ±10	1470	1465.4	1.6	1.5	1.7	4.5	6.3	4.5	93.9	92.2	93.8
10 Trd → Qz	I	867 ±3	870	867.0	11.9	11.4	11.9	4.4	4.8	5.2	83.7	83.8	82.9

E: eutectic, P: peritectic, I: inversion, K: K_2O, A:Al_2O_3, S:SiO_2, Mul: mullite, Trd: tridymite, Fsp: feldspar ($KAlSi_3O_8$), Crn: corundum (Al_2O_3), Lct: leucite ($KAlSi_2O_6$), Kls: kalsilite ($KAlSiO_4$), Qz: quartz, β-A: β-alumina ($KAl_{11}O_{17}$), Crs: cristobalite.

Figures

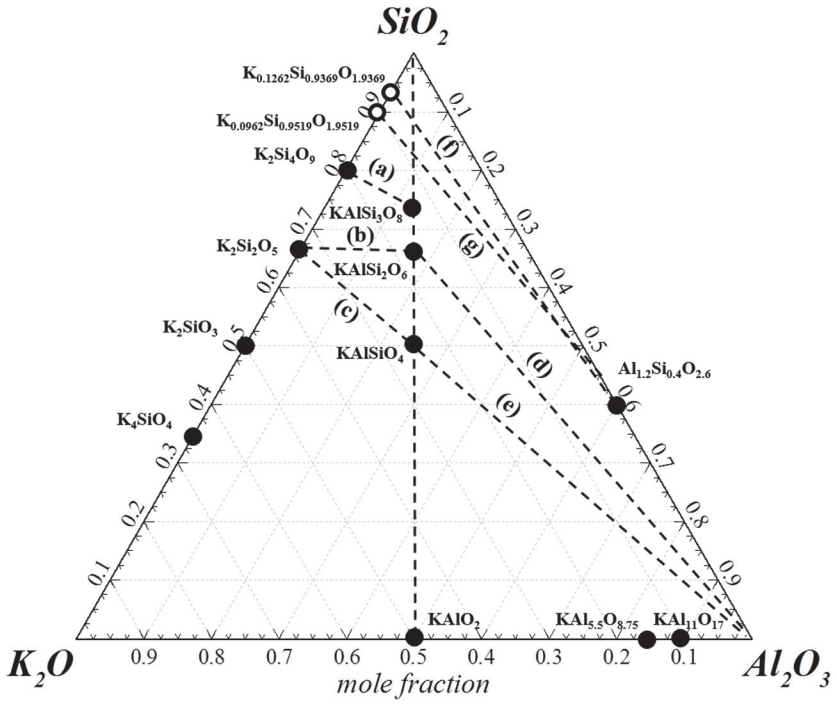

Figure 7.1 Schematic diagram of the K_2O-Al_2O_3-SiO_2 system showing all stable compounds and experimentally investigated isoplethal sections (K: K_2O, A: Al_2O_3, S: SiO_2).

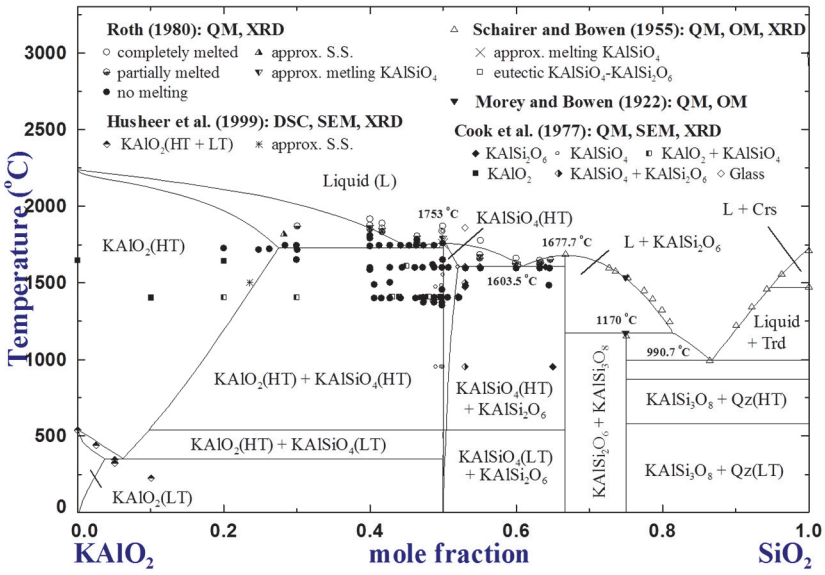

Figure 7.2 Calculated phase diagram of the $KAlO_2$-SiO_2 section with experimental data.

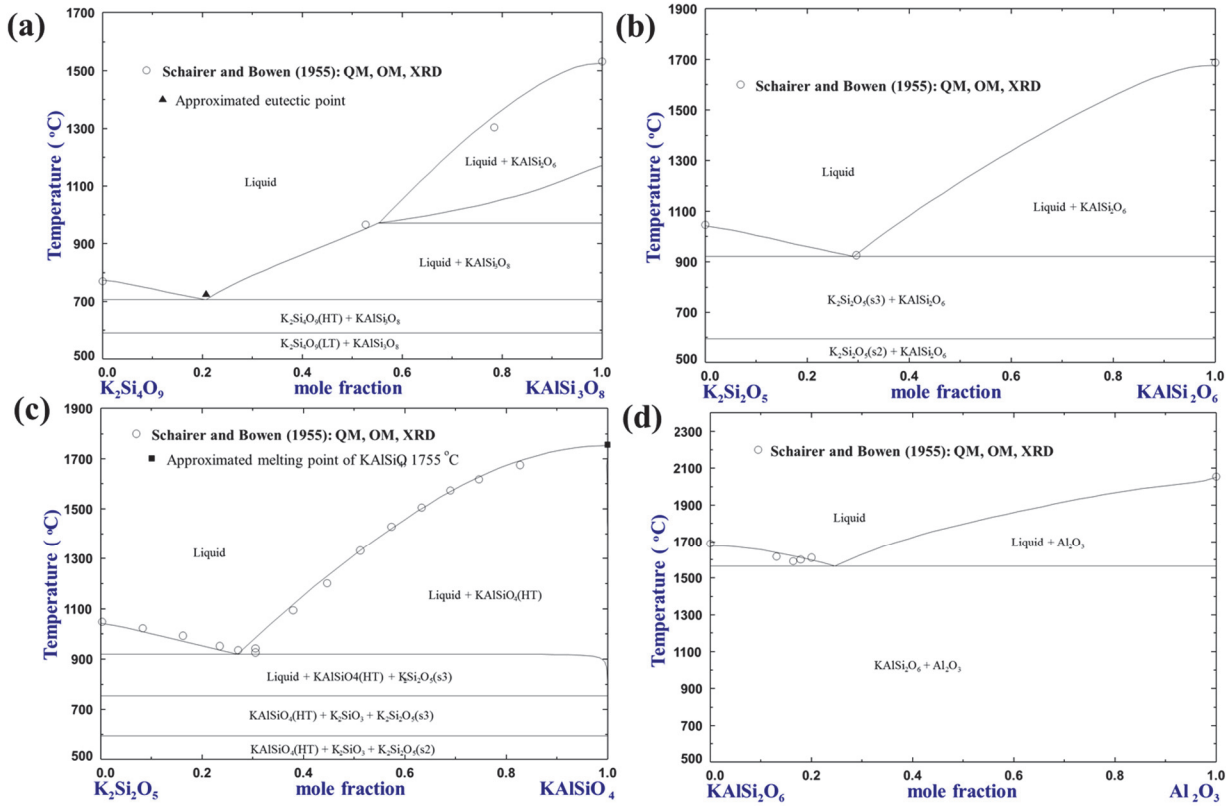

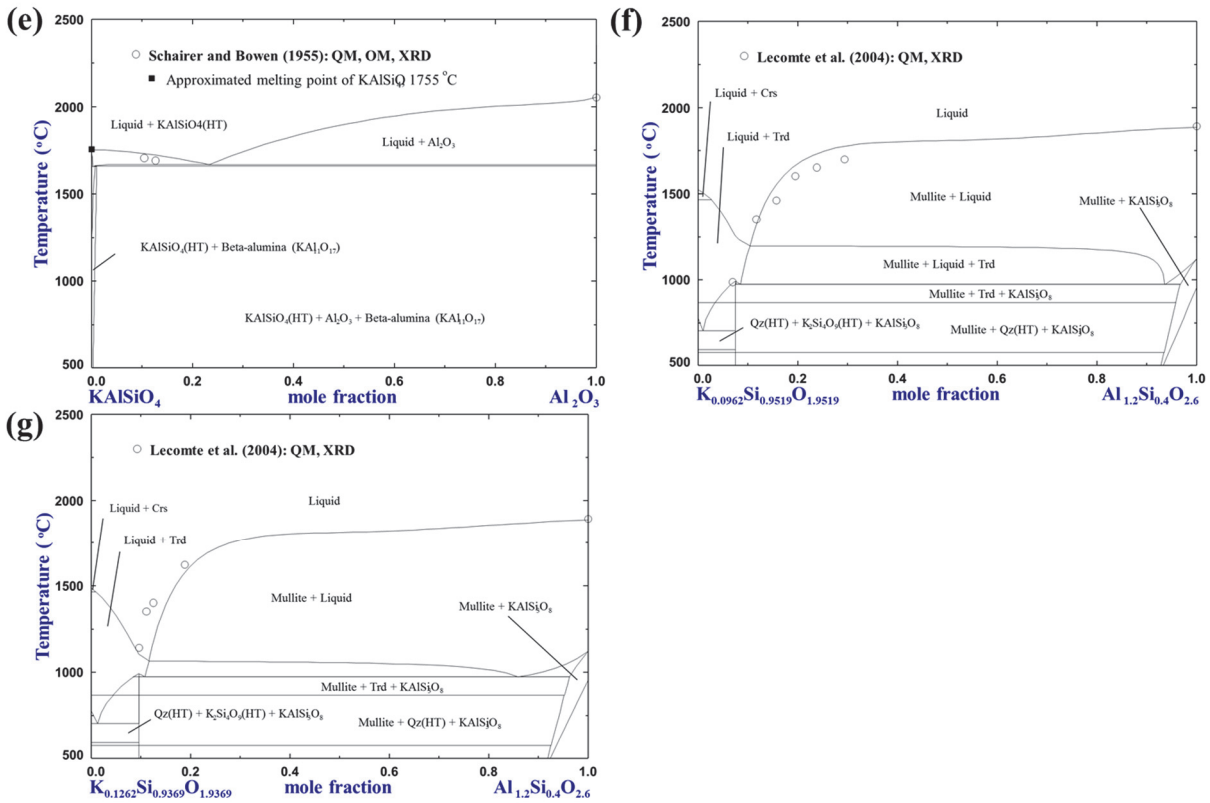

Figure 7.3 Calculated phase diagram of the (a) $K_2Si_4O_9$-$KAlSi_3O_8$ (b) $K_2Si_2O_5$-$KAlSi_2O_6$ (c) $K_2Si_2O_5$-$KAlSiO_4$ (d) $KAlSi_2O_6$-Al_2O_3 (e) $KAlSiO_4$-Al_2O_3 (f) $K_{0.0962}Si_{0.9519}O_{1.9519}$-$Al_{1.2}Si_{0.4}O_{2.6}$ (g) $K_{0.1262}Si_{0.9369}O_{1.9369}$-$Al_{1.2}Si_{0.4}O_{2.6}$ sections with experimental data.

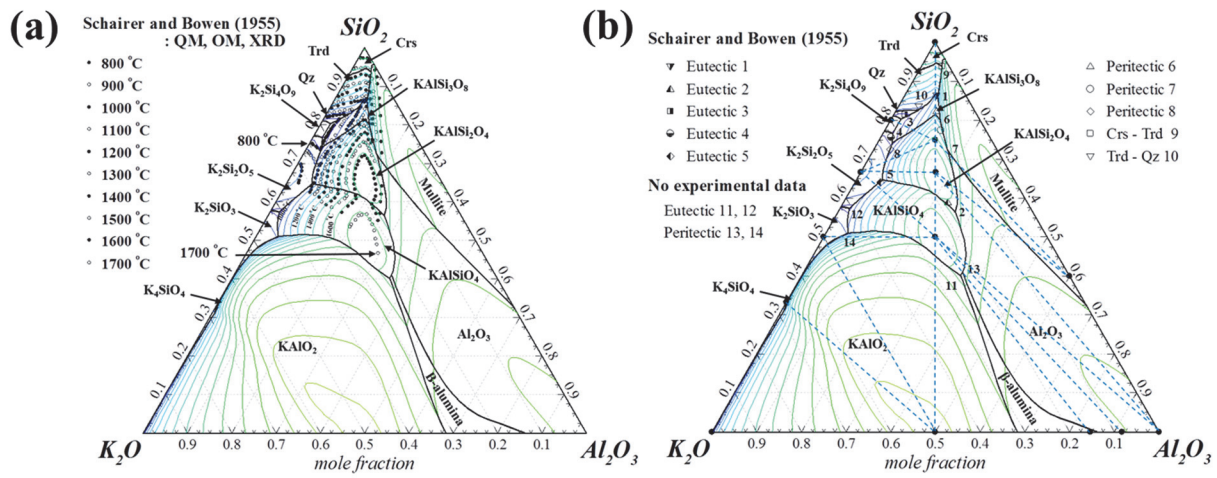

Figure 7.4 Optimized (a) liquidus projection of the K_2O-Al_2O_3-SiO_2 system and (b) invariant reaction points (for the details of invariant reactions, see Table 7.5).

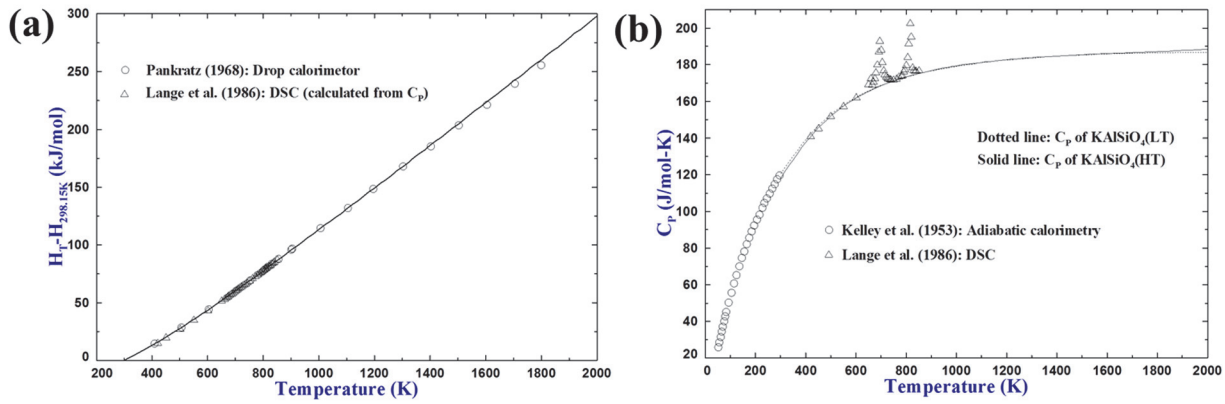

Figure 7.5 (a) Calculated heat content and (b) heat capacity of $KAlSiO_4$ along with experimental data.

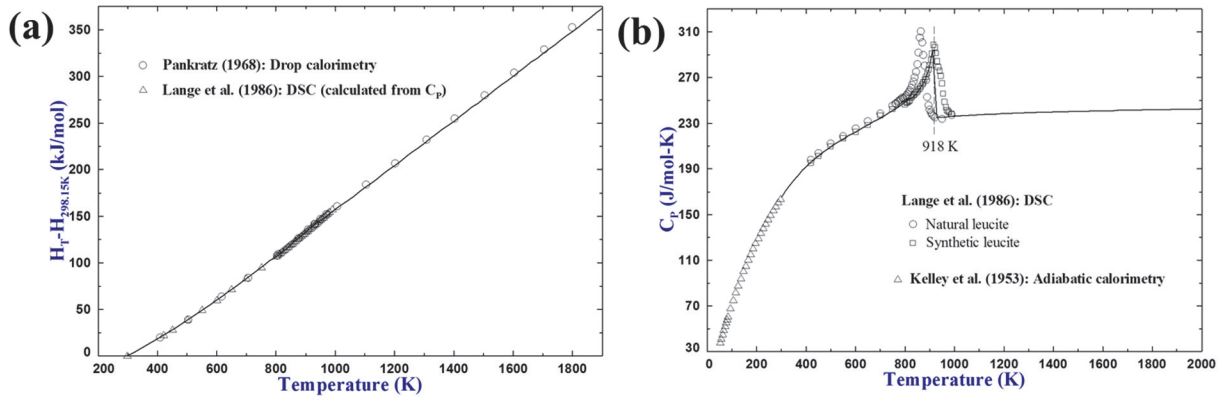

Figure 7.6 (a) Calculated heat content and (b) heat capacity of $KAlSi_2O_6$ along with experimental data.

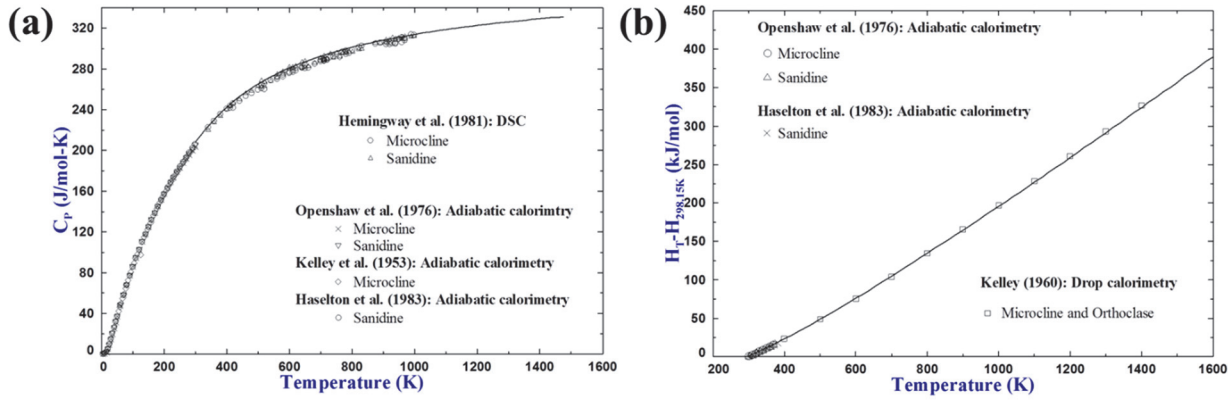

Figure 7.7 (a) Calculated heat capacity and (b) heat content of $KAlSi_3O_8$ along with experimental data.

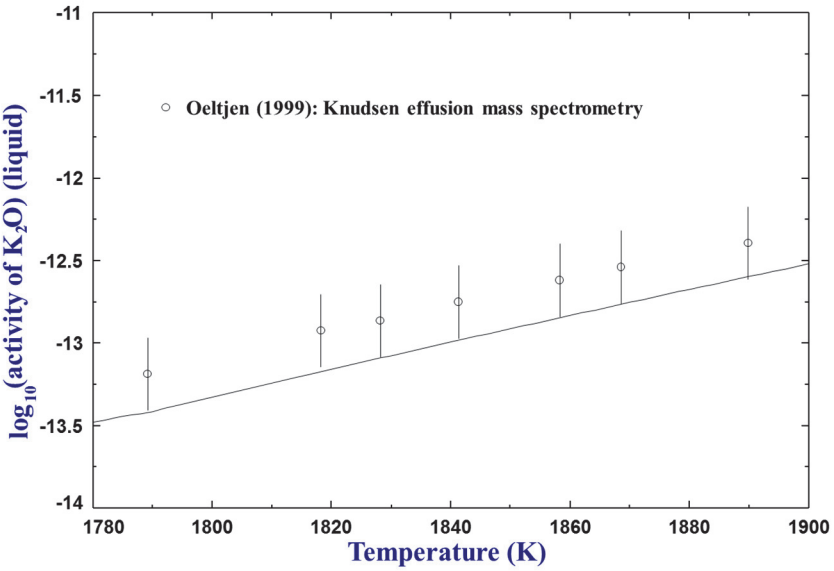

Figure 7.8 Calculated activity of K_2O (referenced to liquid state) at $0.097K_2O$-$0.174Al_2O_3$-$0.729SiO_2$ in mole fraction.

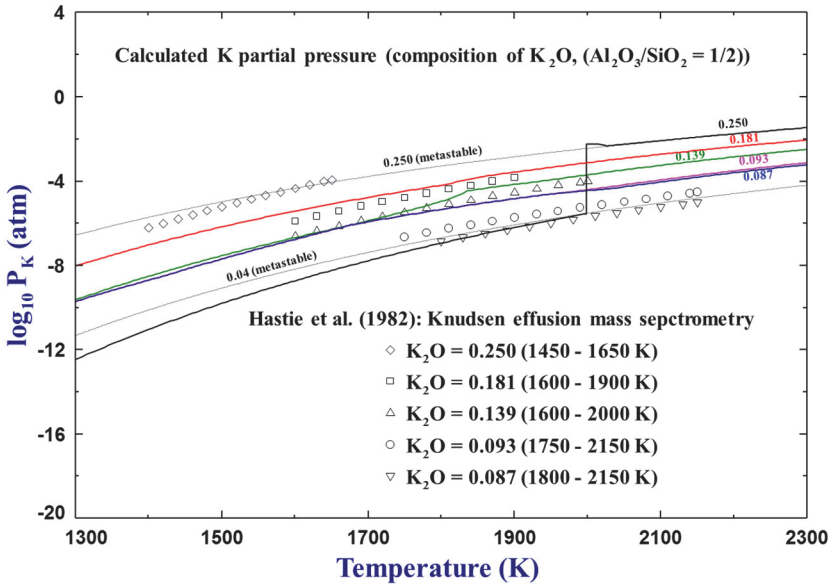

Figure 7.9 Calculated partial pressure of potassium (P_K) with experimental data.

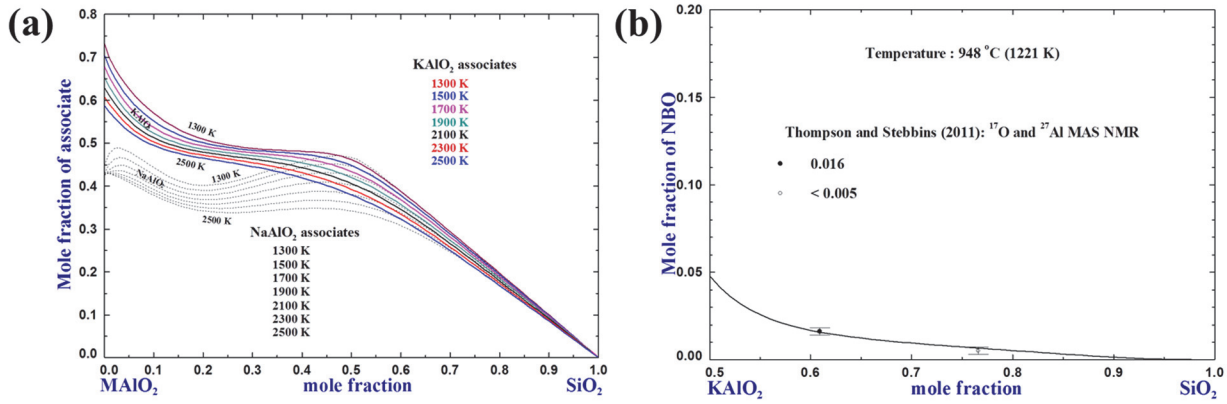

Figure 7.10 Calculated (a) $KAlO_2$ associates along with $NaAlO_2$ associates and (b) non-bridged oxygen (NBO) fractions along the $MAlO_2$-SiO_2 section (M = K, Na).

Chapter 8 Thermodynamic Optimization of the K_2O-CaO-SiO_2 and K_2O-Na_2O-SiO_2 Systems

Dong-Geun Kim and In-Ho Jung

To be submitted.

In this chapter, an expansion of thermodynamic optimizations for the K_2O-CaO-SiO_2 and K_2O-Na_2O-SiO_2 ternary systems is described. The optimizations were performed based on the K_2O-SiO_2 system discussed in Chapter 4. The liquid solution was consistently optimized using the Modified Quasichemical Model.

Abstract

Thermodynamic optimizations of the K_2O-CaO-SiO_2 and K_2O-Na_2O-SiO_2 systems were performed based on the critical evaluation of phase diagram and thermodynamic property data at 1 atm. Stabilities of all ternary compounds reported in the literature for the K_2O-CaO-SiO_2 and K_2O-Na_2O-SiO_2 systems were also critically evaluated. Liquid phase was modeled using the Modified Quasichemical Model. Through thermodynamic optimizations, self-consistent thermodynamic functions were obtained for all stable phases in these two systems. The optimized model parameters well reproduce all available and reliable thermodynamic properties and phase diagram data. The melt structure of the K_2O-Na_2O-SiO_2 system was well predicted in the present study.

Key words: K_2O-CaO-SiO_2, K_2O-Na_2O-SiO_2, thermodynamic optimization, phase diagram, glass melt

8.1 Introduction

The K_2O-CaO-SiO_2 and K_2O-Na_2O-SiO_2 systems are important in many industrial applications. K_2O, CaO, Na_2O, and SiO_2 are the main components of glass, and K_2O/Na_2O mixed alkali effect for glassmaking is an important issue [1-5]. Ashes of common biomass are mainly composed of these components as well; understanding chemistry for these ternary systems is important in biomass combustion to prevent deposit formation and bed agglomeration [6-8]. However, because of the experimental difficulties from the hygroscopic components of K_2O, CaO, and Na_2O, and volatile nature of K_2O and Na_2O, the phase diagram and thermodynamic property data in the literature are limited in certain composition and temperature ranges, and often inconsistent with each other.

Only one thermodynamic optimization work was found in the literature for the K_2O-CaO-SiO_2 system. Zhang *et al*. [9] performed calorimetric experiments and thermodynamic optimization on this system. In their study, the reciprocal ionic liquid model [10] was used to describe the liquid solution. Seven ternary compounds were considered as stable phases: K_2CaSiO_4, $K_4CaSi_3O_9$, $K_2Ca_2Si_9O_{21}$, $K_8CaSi_{10}O_{25}$, $K_4CaSi_6O_{15}$, $K_2Ca_3Si_6O_{16}$, and $K_2Ca_2Si_2O_7$. The calculated univariant lines and phase diagram of the pseudo-binary section between K_2SiO_3 and $CaSiO_3$ show large deviations from the experimental data of Morey *et al*. [11].

Regarding the K_2O-Na_2O-SiO_2 system, Bennour *et al*. [12] employed an interacting pair model to describe the liquid solution, focusing on the entropy expression of the mixed alkali effect. In their optimization, additional Gibbs energy terms for the mixed alkali effect was introduced to reproduce the Knudsen Effusion Mass Spectrometry (KEMS) data reported by Chastel *et al*. [13]. No phase diagram data were considered in their study. Yazhenskikh *et al*. [14] studied the K_2O-Na_2O-SiO_2 system using the associate model [15]. Two methods were proposed to reproduce the

liquidus in the $Na_2Si_2O_5$-$K_2Si_2O_5$ section reported by Kracek *et al*. [16]: i) introducing a ternary compound of $Na_{1.55}K_{0.45}Si_2O_5$; ii) considering possible solubility of potassium into the intermediate-temperature polymorph of $Na_2Si_2O_5$. The calculated Gibbs energy of mixing is in reasonable agreement with that reported by Belton *et al*. [17], who used KEMS.

In this study, a comprehensive literature review was performed on all available experimental data of the K_2O-CaO-SiO_2 and K_2O-Na_2O-SiO_2 systems. The liquid solution phases were described using the Modified Quasichemical Model (MQM). The α- and α′-Ca_2SiO_4 in the K_2O-CaO-SiO_2 system were optimized using the random mixing model. The meta- and disilicate solid solutions were modeled using the Compound Energy Formalism (CEF). This study is part of a large thermodynamic database development project for the K_2O-Na_2O-CaO-MgO-Al_2O_3-SiO_2 system. All the thermodynamic calculations of this study were performed using the FactSage software [18].

8.2 Thermodynamic Models

8.2.1 Stoichiometric Compounds

The Gibbs energy of a stoichiometric compound is described as:

$$G_T^o = \Delta H_{298.15K}^o + \int_{298.15K}^{T} C_P dT - T(S_{298.15K}^o + \int_{298.15K}^{T} C_P/T dT) \quad (1)$$

where $\Delta H_{298.15K}^o$ and $S_{298.15K}^o$ are the standard enthalpy of formation and standard entropy at 298.15 K, respectively; C_P is the heat capacity as a function of temperature; T is the absolute temperature.

In the K_2O-CaO-SiO_2 system, the thermodynamic data of ternary compounds were not available. Therefore, the $S_{298.15K}^o$ and C_P of compounds were first approximated using the Neumann-Kopp

rule (NKR) based on the pure substance data of K_2O, CaO, and SiO_2 from the FToxid database [18]. In the NKR, SiO_2 polymorphs were selected based on the respective structure of each ternary compound. Then, the $\Delta H^o_{298.15K}$ of the solid compounds were optimized to reproduce the phase diagram data. In the K_2O-Na_2O-SiO_2 system, no stoichiometric ternary compound was included in the optimization.

8.2.2 Liquid Solution

The Modified Quasichemical Model (MQM) in the pair approximation [19, 20] was employed to express the Gibbs energy function of the liquid oxide phase. The MQM takes into account the short-range ordering (SRO) of second-nearest-neighbor cations in the oxide melt. The quasichemical reaction considered in the binary oxide melt is:

$$(A-A)+(B-B)=2(A-B);\ \ \Delta g_{A-B} \tag{2}$$

where A and B are the cationic species in solution; $(A-B)$ represents a second-nearest-neighbor pair of A and B cations with a common O^{2-} anion; Δg_{A-B} is the Gibbs energy of the reaction, which is a model parameter. Δg_{A-B} can be expanded as functions of pair fractions and temperature:

$$\Delta g_{A-B} = \Delta g^o_{AB} + \sum_{i\geq 1} g^{i0}_{AB} X^i_{AA} + \sum_{j\geq 1} g^{0j}_{AB} X^j_{BB} \tag{3}$$

where Δg^o_{AB}, g^{i0}_{AB}, and g^{0j}_{AB} are parameters, which can be a function of temperature; X_{AA} and X_{BB} are the pair fractions of $(A-A)$ and $(B-B)$, respectively.

The Gibbs energy of the liquid solution is expressed as:

$$G^{sol} = (n_A g^o_A + n_B g^o_B) - T\Delta S^{conf} + (n_{AB}/2)\Delta g_{A-B} \tag{4}$$

where n_i and g_i^o are the number of moles and the molar Gibbs energy of pure component *i*, respectively; n_{AB} is the number of moles of $(A-B)$ pairs; ΔS^{conf} is the configurational entropy of the solution expressed as a function of random distribution of quasichemical pairs based on one-dimensional Ising model [21]. The details of the thermodynamic equations for the MQM can be found in Ref. [19].

The SRO behavior in the liquid solution can be well described by setting the coordination numbers of cations. In this work, the coordination numbers of unary: K^+ (Z_{KK}^K), Ca^{2+} (Z_{CaCa}^{Ca}), Na^+ (Z_{NaNa}^{Na}), and Si^{4+} (Z_{SiSi}^{Si}) are set to be 0.6887, 1.3774, 0.6887, and 2.7549, respectively. Binary coordination numbers were set to be the default values considering unary coordination numbers. These coordination numbers are consistent with those used in the molten oxide database (FToxid) of the FactSage software [18].

Once each binary solution is optimized, the Gibbs energy of the ternary solution can be calculated using a so-called geometric interpolation technique. Kohler and Toop-type models are commonly used to express symmetric and asymmetric ternary system, respectively [20]. Two binary interactions of Δg_{K-Ca} and Δg_{K-Na} in this study were assumed to be ideal solution due to the lack of experimental data, while Δg_{K-Si} and Δg_{Ca-Si} are very negative (strong SRO behavior) in the K_2O-CaO-SiO_2 system, and Δg_{K-Si} and Δg_{Na-Si} are very negative in the K_2O-Na_2O-SiO_2 system. Hence, the ternary Gibbs energy was calculated using an asymmetric Toop interpolation technique with SiO_2 as an asymmetric component for both ternary systems. The details of the interpolation method are well described in Ref. [22]. The MQM equations for the ternary system considering the interpolation model can be found in Ref. [20]. In the present study, the model

parameters of Δg_{K-Si}, Δg_{Ca-Si}, and Δg_{Na-Si} were taken from the previous studies [23-25]. Small ternary model parameters were introduced to reproduce the phase diagram data more accurately.

8.2.3 Solid Solutions

Limited solubility of potassium into α- and α′-Ca_2SiO_4 (C_2S) were found in the literature for the K_2O-CaO-SiO_2 system. Although the exact solution mechanism is not known, maximum about 9 mol % of K_2CaSiO_4 (KCS) solubility was measured in α′-C_2S at 1300 °C [26], and 3.5 and 8.3 mol % KCS into C_2S phase were found for the samples equilibrated at different temperatures (cannot be known precisely) [27, 28]. The solution model was taken from the previous thermodynamic optimization by Jung *et al*. [29]. The α- and α′-C_2S solutions were modeled using the random mixing model with a polynomial expansion of the excess Gibbs energy. The chemical formula of both solutions are $(K_2^{2+}, Ca^{2+})_2 SiO_4$.

The Gibbs energy of the C_2S solutions can be expressed as:

$$G^{sol} = (X_i G_i^o + X_j G_j^o) + 2RT(X_i \ln X_i + X_j \ln X_j) + \sum_{m,n\geq 0} q_{ij}^{mn} (X_i)^m (X_j)^n \quad (5)$$

where G_i^o is the molar Gibbs energy of the end-member *i* of the solution; X_i is the mole fraction of the species *i*; *R* is the gas constant; q_{ij}^{mn} are the excess interaction parameters. For both solution, X_i and X_j are the mole fractions of K_2^{2+} and Ca^{2+}.

There are four solid solution phases in the K_2O-Na_2O-SiO_2 system. Limited solubility between K_2SiO_3 and Na_2SiO_3 (metasilicate), between $K_2Si_2O_5$ and $Na_2Si_2O_5$ (high- and intermediate-temperature disilicates), and a complete solid solution for low-temperature disilicates are the four solid solution phases. The solution mechanisms of metasilicate and disilicate are adopted from the

previous optimization by Konar *et al*. [30]. As alkali silicate and aluminosilicate systems often show a systematic trend in phase diagram and thermodynamic propetites, the solid solutions reported for meta- and disilicates in the Li_2O-Na_2O-SiO_2 system [31, 32] were considered in this study to reproduce the phase diagram data [16] and the thermodynamic property data [2, 13] simultaneously. The formation of these solid solutions in the K_2O-Na_2O-SiO_2 system is also inferred from many stoichiometric ternary compounds reported in the range of 8 to 50 mol % K_2O in the disilicate compositions. A range of solid solution is more reasonable than five different stoichiometric compounds with the same crystal structure. The meta- and disilicate solutions are modeled using one sublattice mixing formula in the framework of the Compound Energy Formalism (CEF) [33]. The chemical formula of meta- and disilicate solutions are $(K_2^{2+}, Na_2^{2+})SiO_3$ and $(K_2^{2+}, Na_2^{2+})Si_2O_5$, respectively, with miscibility gaps that produce K_2O and Na_2O-rich solid solutions.

That is, the molar Gibbs energy of the meta- and disilicate solutions are expressed by:

$$G^{so\ln} = (y_i G_i^o + y_j G_j^o) + RT(y_i \ln y_i + y_j \ln y_j) + \sum_{n\geq 0}^{n} L_{ij} y_i y_j (y_j - y_i)^n \quad (6)$$

where G_i^o is the molar Gibbs energy of the end-member *i* of the solution; y_i is the site fraction of the species *i*; *R* is the gas constant; ${}^n L_{ij}$ are the excess interaction parameters. For both solutions, y_i and y_j are the mole fractions of K_2^{2+} and Na_2^{2+}.

8.3 Thermodynamic Evaluation and Optimization

All available phase diagram, structural, and thermodynamic property data of the K_2O-CaO-SiO_2 and K_2O-Na_2O-SiO_2 systems in the literature were critically reviewed. Afterwards, all reliable

experimental data from the literature were considered to obtain thermodynamic functions for all stable phases in these two ternary systems.

8.3.1 The K_2O-CaO-SiO_2 System

Crystal structures of all ternary compounds in this system reported in the literature are shown in Table 8.1. The optimized thermodynamic properties of ternary compounds and model parameters of the solutions are listed in Tables 8.2 and 8.3, respectively. The calculated invariant reactions in this study are shown in Table 8.4. The stable compounds and experimentally investigated isoplethal sections of the K_2O-CaO-SiO_2 system are schematically shown in Fig. 8.1. There are 17 stable phases in this system at 1 atm pressure: K_2O, CaO, SiO_2 (α- and β-quartz, β-tridymite, β-cristobalite), K_2CaSiO_4 (KCS), $K_2Ca_2Si_2O_7$ (KC_2S_2), $K_4CaSi_3O_9$ (K_2CS_3), $K_8CaSi_{10}O_{25}$ (K_4CS_{10}), $K_4CaSi_6O_{15}$ (K_2CS_6), $K_2Ca_3Si_6O_{16}$ (KC_3S_6), $K_2Ca_2Si_9O_{21}$ (KC_2S_9), $K_2Ca_6Si_4O_{15}$ (KC_6S_4), and liquid solution, α′- and α- Ca_2SiO_4 (C_2S) solid solutions with excess K_2O. The optimized phase diagrams of the K_2O-CaO-SiO_2 system in the present study are presented in Figs. 8.2 to 8.8 along with all available experimental data.

Morey *et al*. [11, 34] performed phase diagram experiments on the K_2O-CaO-SiO_2 system using the equilibration/quenching method followed by petrographic microscopy and XRD analysis. Liquidus and invariant reactions were measured in the composition range between metasilicates and pure SiO_2. It is because of the experimental difficulties working with K_2O, which is highly volatile and hygroscopic. Platinum (Pt) or gold (Au) foils were used to wrap the sample materials. The weight loss during sample preparations and experiments was assumed to be only the loss of K_2O, then the final compositions were recalculated. Quenching was performed by taking out the crucible from the furnace. When rapid cooling rate was required, the crucibles were quenched into mercury. The liquidus projection was constructed based on the measurements of 160 compositions.

Seven ternary compounds were considered to be stable in this ternary system according to Morey *et al*. [11]: K_2CaSiO_4 (KCS), $K_4CaSi_3O_9$ (K_2CS_3), $K_8CaSi_{10}O_{25}$ (K_4CS_{10}), $K_4CaSi_6O_{15}$ (K_2CS_6), $K_2Ca_3Si_6O_{16}$ (KC_3S_6), $K_2Ca_2Si_9O_{21}$ (KC_2S_9), and $K_2Ca_2Si_6O_{15}$ (KC_2S_6). In their later work [34], the compound KC_2S_6 was proven not to exist in this ternary system. It was a misinterpretation of the KC_3S_6 compound. However, the phase diagram data were not updated. More recently, Chen *et al*. [35] investigated isothermal sections from 1000 to 1200 °C using the equilibration/quenching method followed by electron probe micro-analysis (EPMA). Samples were wrapped in a Pt foil to prevent volatile loss of K_2O. Equilibration time was set between 4 and 72 hours depending on the target composition and temperature. Stable ternary compounds of $K_2Ca_2Si_2O_7$ (KC_2S_2) and $K_2Ca_6Si_4O_{15}$ (KC_6S_4) were found in their experiments. The phase diagram section between Ca_2SiO_4 and K_2CaSiO_4 was investigated by Taylor [36] using the equilibration/quenching method followed by optical microscopy and XRD analysis. Taylor measured the liquidus in the K_2CaSiO_4-rich region of the phase diagram. The reported liquidus showed an evidence of either limited Ca_2SiO_4 solid solution or stoichiometric compound $K_2Ca_{23}Si_{12}O_{48}$ ($KC_{23}S_{12}$). Taylor concluded that $KC_{23}S_{12}$ is a stable compound. However, later studies showed that the $KC_{23}S_{12}$ composition can come from a C_2S solid solution with K_2O. Morey *et al*. [11] first mentioned the possible solubility of K_2O in C_2S. Suzukawa [27] tried to synthesize the ternary compound $KC_{23}S_{12}$. However, it was concluded to be in the range of α-C_2S solid solution through their optical microscopic observations. Fedorov and Brodkina [26] drew a similar conclusion that the $KC_{23}S_{12}$ composition is a part of α′-C_2S solid solution based on XRD results. In the C_2S-KCS pseudo-binary section, the solubility of KCS into α′-C_2S at 1300 °C was reported to be in between 4.3 and 8.9 mol %. Lai *et al*. [28] also found that C_2S was stabilized by the addition of K^+ ions using XRD analysis. The C_2S sample was sintered with excess K^+ ions at 1500 °C and then slowly cooled.

Although the exact temperature of the equilibrium C_2S phase was not known due to the slow cooling, about 3.4 mol % KCS solubility in the C_2S phase was determined in the XRD analysis.

Regarding the compounds in the K_2O-CaO-SiO_2 system, 12 stoichiometric compounds were reported as stable ternary phases in the literature: K_2CaSiO_4 (KCS), $K_2Ca_2Si_2O_7$ (KC_2S_2), $K_4CaSi_3O_9$ (K_2CS_3), $K_8CaSi_{10}O_{25}$ (K_4CS_{10}), $K_4CaSi_6O_{15}$ (K_2CS_6), $K_{9.6}Ca_{1.2}Si_{12}O_{30}$, $K_2Ca_3Si_6O_{16}$ (KC_3S_6), $K_2Ca_2Si_6O_{15}$ (KC_2S_6), $K_2Ca_2Si_9O_{21}$ (KC_2S_9), $K_2Ca_4Si_8O_{21}$ (KC_4S_8), $K_2Ca_6Si_4O_{15}$ (KC_6S_4), $K_2Ca_{23}Si_{12}O_{48}$ ($KC_{23}S_{12}$), and one Ca_2SiO_4 (C_2S) solid solution. A summary of the structural data is given in Table 8.1.

The compound K_2CaSiO_4 (KCS) was first reported by Morey *et al*. [11]. It was determined with a hexagonal bipyramid structure based on refractive index. Later, this compound was also found by some other researchers: Taylor [36], Ohsato *et al*. [37], and Risnes [38] observed KCS as a stable compound using optical microscopy, XRD analysis, and scanning electron microscopy (SEM). Two other studies suggest different crystal systems for KCS: Hughes [39] found KCS with a cubic structure using XRD, and Berezhnoi *et al*. [40] reported KCS in a orthorhombic system using XRD. Later, the stability of the KCS compound was questioned by Arroyabe *et al*. [41]. They insisted that KCS was a misinterpretation of KC_2S_2 ($K_2Ca_2Si_2O_7$). In Arroyabe *et al*.'s study, 1:1:1 ratio of K_2O:CaO:SiO_2 mixture (expected to form a stoichiometry of K_2CaSiO_4) formed $K_2Ca_2Si_2O_7$ and pure K_2O. In a recent investigation of the electric arc furnace (EAF) slag crystallization behavior by Bankole *et al*. [42], the expected KCS phase was not detected using XRD. Therefore, the stability of the KCS compound cannot be fully confirmed based on the literature.

An evidence of crystalline phase at the $K_2Ca_2Si_2O_7$ (KC_2S_2) composition was first reported by Morey *et al*. [11]. Later, Akiyama *et al*. [43] successfully synthesized the stoichiometric compound

of KC_2S_2 and analyzed it as tetragonal system using XRD. The crystal structure was revised in a recent study from Arroyabe and Kahlenberg [44] as a hexagonal system with space group of $P6_3/m$.

The structure of $K_4CaSi_3O_9$ (K_2CS_3) was first investigated by Morey *et al*. [11]. It was analyzed to be in the cubic system with 5 % deviations based on XRD analysis. One of the later studies by Gunawardane and Glasser [45] using XRD also suggested K_2CS_3 as cubic system with some uncertainties. The K_2CS_3 compound was successfully synthesized and analyzed by Berezhnoi *et al*. [40], Risnes [38], and Bankole *et al*. [42] using XRD, IR spectroscopy, and SEM. A most recent study from Arroyabe *et al*. [46] confirmed its crystal structure as cubic system and space group of $Pa\bar{3}$ using XRD.

The crystal structure of $K_8CaSi_{10}O_{25}$ (K_4CS_{10}) was analyzed by Gunawardane and Glasser [45] using XRD. The analysis results showed that K_4CS_{10} belongs to the rhombohedral lattice system, which is in the hexagonal crystal family. This compound was synthesized in two other studies: Morey *et al*. [11] found K_4CS_{10} using optical microscopy and Zhang *et al*. [9] synthesized it and measured its heat capacity using drop calorimetry.

The $K_4CaSi_6O_{15}$ (K_2CS_6) compound is only reported by Morey *et al*. [11] using optical microscopy. They mentioned that the compound was first discovered using hydrothermal crystallization. Later, it was confirmed to exist in dry condition. There is no crystal structure information for this compound in the literature.

Kahlenberg *et al*. [47] reported the $K_{9.6}Ca_{1.2}Si_{12}O_{30}$ compound using XRD. This composition is very close to K_4CS_{10} ($K_8CaSi_{10}O_{25}$) and K_2CS_6 ($K_4CaSi_6O_{15}$), which are disilicate compositions. The crystal system of $K_{9.6}Ca_{1.2}Si_{12}O_{30}$ is found to be trigonal with R3c space group. Trigonal

$K_{9.6}Ca_{1.2}Si_{12}O_{30}$ and rhombohedral $K_8CaSi_{10}O_{25}$ are in the same hexagonal crystal family. This gives an idea of unknown crystal structure of K_2CS_6 as well.

The stability of the $K_2Ca_3Si_6O_{16}$ (KC_3S_6) compound was reported by Morey *et al*. [11] using optical microscopy, but no structural data were given. Morey *et al*. also reported the $K_2Ca_2Si_6O_{15}$ (KC_2S_6) compound. However, the authors corrected later [34] that KC_2S_6 is a misinterpretation of $K_2Ca_3Si_6O_{16}$ (KC_3S_6).

The $K_2Ca_2Si_9O_{21}$ (KC_2S_9) compound was reported by Morey *et al*. [11]. They used the hydrothermal technique to crystallize this compound. The stability region of KC_2S_9 was reported using optical microscopy, while no structural information was given.

Arroyabe *et al*. [48] reported the stoichiometric compound $K_2Ca_4Si_8O_{21}$ (KC_4S_8) using XRD and Raman spectroscopy. The structure was found to be in the triclinic system with $P\bar{1}$ space group.

The possibility of a stable compound $K_2Ca_6Si_4O_{15}$ (KC_6S_4) was first pointed out by Ohsato *et al*. [37]. Later, the structure of the compound was reported to be in the monoclinic system with space group of $P12/c1$ by Arroyabe *et al*. [49] using XRD. In the recent phase diagram experiments from Chen *et al*. [35], the stability region of this compound was reported.

The $K_2Ca_{23}Si_{12}O_{48}$ ($KC_{23}S_{12}$) compound was first found by Taylor [36]. Taylor studied the Ca_2SiO_4-K_2CaSiO_4 section using the equilibration/quenching method followed by optical microscopy and XRD analysis. Even though the possibility of a Ca_2SiO_4 solid solution with excess K_2O was mentioned, the formation of the stoichiometric compound $KC_{23}S_{12}$ was still concluded in his study. Later, Yung *et al*. [50] also successfully synthesized $KC_{23}S_{12}$ with some possible impurities of H_2O / CaF_2 due to the use of gypsum and CaF_2 as starting materials. No structural data were found in these studies.

Zhang *et al*. [9] measured the heat content of two ternary compounds, $K_2Ca_2Si_2O_7$ (KC_2S_2) and $K_8CaSi_{10}O_{25}$ (K_4CS_{10}), using drop calorimetry. However, experimental details were not provided. Only the standard Gibbs energies of the two compounds were given as a function of temperature. In the preliminary calculations in this study using the reported Gibbs energy function of K_4CS_{10} by Zhang *et al*., the thermal stability of this compound is unrealistic; the stability region of K_4CS_{10} cannot correspond with the phase diagram data.

In the present optimization, eight stoichiometric compounds: KCS, KC_2S_2, K_2CS_3, K_4CS_{10}, K_2CS_6, KC_3S_6, KC_2S_9, and KC_6S_4 were considered as stable phases in the K_2O-CaO-SiO_2 system. Melting behaviors of the compounds were reproduced mainly based on Morey *et al*.'s data [11, 34]. Ternary compounds of $K_{9.6}Ca_{1.2}Si_{12}O_{30}$, KC_4S_8, and $KC_{23}S_{12}$ were not included in the present optimization. The stoichiometry of $K_{9.6}Ca_{1.2}Si_{12}O_{30}$ and KC_4S_8 can be misinterpretations from K_4CS_{10} and KC_4S_8 due to the high volatility of K_2O. No experimental data were found regarding the phase stability of the two compounds. The $KC_{23}S_{12}$ compound is considered as a part of C_2S solid solutions. To estimate the heat capacity and entropy at 298.15 K of the KCS, KC_2S_2, and K_4CS_{10} phases, the hexagonal structure of β-tridymite SiO_2 was considered in the Neumann-Kopp approximations because they have similar hexagonal structures. The structure of the disilicate compound K_2CS_6, which was not experimentally measured, was considered as hexagonal considering the similarity with the other disilicate compound K_4CS_{10}. The thermodynamic properties of β-cristobalite SiO_2 were taken to estimate the K_2CS_3 compound, which belongs to the cubic system. Regarding the compounds of KC_3S_6 and KC_2S_9, coesite SiO_2 was used for the estimation because of the compositional similarity with KC_4S_8, which was reported as triclinic. Triclinic system and monoclinic (coesite SiO_2) are structurally closest to each other. The monoclinic compound KC_6S_4 was also estimated using coesite SiO_2. In the thermodynamic

optimization of the present study, the enthalpy of formation at 298.15 K was changed simultaneously with the ternary liquid parameters to reproduce the phase diagram data reported in the literature. A summary of the thermodynamic properties of the ternary compounds is listed in Table 8.2.

The pseudo-binary sections of this system were reported by Morey *et al*. [11, 34] and compared with the present calculations in Figs. 8.2 to 8.5. It can be seen that the liquidus are well reproduced in all sections. In Fig. 8.2, there are some deviations in terms of equilibrium phases for the liquidus, because the KC_2S_2 compound was included in the present optimization, and was absent in Morey *et al*.'s study. Part of the KCS liquidus in Morey *et al*.'s study was reproduced as the liquidus of KC_2S_2 in the present calculation. Morey *et al*. also mentioned a possibility of KC_2S_2 formation. It was difficult to separate between the KCS and KC_2S_2 compounds in phase characterizations. The calculated melting point of KCS shows a good agreement with the experimental data as shown in Fig. 8.3. The decomposition temperature of the K_2CS_3 compound as well as the liquidus temperatures are in good agreement with the experimental data. The melting temperatures of the two compounds K_4CS_{10} and K_2CS_6 are well reproduced in the present optimization as depicted in Fig. 8.4. Some deviations remain for the liquidus of the $CaSi_2O_5$-rich region. This is possibly due to experimental difficulties in the two-phase regions between β-cristobalite SiO_2 (Crs) and liquid, and between β-tridymite SiO_2 (Trd) and liquid. Only partial crystallization of the sample may take place due to slow kinetics. Liquidus in the middle composition ranges in this section was supposed to be in equilibrium with the compound KC_2S_6, which turned out to be a misinterpretation of the compound KC_3S_6. This could be an error source in the phase analysis of this liquidus measurements. In Fig. 8.5, the KC_2S_6 liquidus was originally reported in Morey *et al*.'s work and now reproduced as the KC_3S_6 liquidus in the present optimization. The KC_2S_9 liquidus shows

about 2 mol % deviations near the $K_2Si_4O_9$-rich region. This may come from the experimental difficulties in determining a small amount of crystalline phase precisely in the SiO_2-rich region. The calculated pseudo-binary section between C_2S and KCS is presented in Fig. 8.6. The solubility of K_2O in C_2S measured by Fedorov and Brodkina [26] is well reproduced in the present optimization. The calculated KCS liquidus shows slight deviations from Taylor's data. This may come from the inaccurate analysis of the $KC_{23}S_{12}$ compound by Taylor. In Fig. 8.7, isothermal sections at 1000, 1100, and 1200 °C reported by Chen *et al*. [35] and data from Morey *et al*. [11] are compared with the present optimizations. The liquidus temperatures from both studies are in good agreement with the present calculations. Invariant reaction points are compared with Morey *et al*.'s data [11] in Table 8.4. The present optimization contains a large primary phase field of KC_2S_2 as depicted in Fig. 8.8, whereas the β-C_2S and K_2CS_3 phase fields cover most of those areas in Morey *et al*'s study. Direct comparison of invariant reactions between the experimental data and the present optimization is difficult due to the compounds KC_2S_2 and KC_6S_4, which were not identified as stable phases in Morey *et al*.'s work. The phase equilibria calculated in this study can be considered reliable because the present thermodynamic optimization considers all available and reliable experimental data and reproduces the most recent phase diagram measured by Chen *et al*. [35].

8.3.2 The K_2O-Na_2O-SiO_2 System

The optimized model parameters of the solutions and the calculated invariant reactions in the K_2O-Na_2O-SiO_2 system are listed in Tables 8.5 and 8.6, respectively. All experimentally investigated isoplethal sections of this system are schematically shown in Fig. 8.9. There are 13 stable phases in this system at 1 atm pressure: K_2O, Na_2O (low-, intermediate-, and high-temperature polymorphs), SiO_2 (α- and β-quartz, β-tridymite, β-cristobalite), liquid solution, metasilicate solid

solution and disilicate (low-, intermediate-, and high-temperature) solid solution. It is worth mentioning that there are no stoichiometric ternary compounds in this system. The optimized phase diagrams of this study are presented in Figs. 8.10 to 8.13 along with experimental data. In Figs. 8.14 to 8.16, the calculated thermodynamic properties are compared with experimental data. The calculated oxygen connectivity is compared with experimental data in Fig. 8.17.

The ternary phase diagram of K_2O-Na_2O-SiO_2 was investigated by Kracek *et al*. [16] using the equilibration/quenching method followed by optical microscopy. In the metasilicate section between K_2SiO_3 and Na_2SiO_3 shown in Fig. 8.10, an abnormal liquidus curvature in the K_2SiO_3-rich region was noticed. Kracek *et al*. did not provide explanation for this abnormal shape. In the disilicate section $K_2Si_2O_5$-$Na_2Si_2O_5$ shown in Fig. 8.11, there are some kinks on the liquidus. According to Kracek *et al*., these kinks can be due to the formation of a solid solution between $K_2Si_2O_5$ and $Na_2Si_2O_5$ or the possible existence of ternary compounds. However, no definite solid solution range was found using optical analysis due to rapid unmixing (ex-solution) and complex polymorphic inversions. Kracek *et al*. concluded that $K_2Si_2O_5$ and $Na_2Si_2O_5$ take up excess SiO_2, Na_2O, and K_2O depending on the conditions. A similar type of kinks appears on the phase diagram of the binary K_2O-SiO_2 system reported by Kracek *et al*. [51]. However, the kinks in this binary system were found to be inaccurate in the later work of the same author [52]. Thus, the kinks that Kracek *et al.* reported for the K_2O-Na_2O-SiO_2 system may come from similar experimental errors during the same period of time.

Although Kracek *et al*. [16] reported no formation of stable ternary compounds in their phase diagram measurements, several possible stoichiometric compounds were reported by other researchers. Sakaguchi *et al*. [53] reported a crystalline phase of $Na_{1.3}K_{0.7}Si_2O_5$, which is monoclinic with space group of $P2_1/c$ based on XRD analysis. This compound was synthesized

using NaOH, KOH, and sodium silicate (SiO_2/Na_2O=3.4, moisture content 60 %) at 600 °C for 2 hours. Rakic and Kahlenberg [54] reported a crystalline phase of $NaKSi_2O_5$ using XRD. The starting materials were prepared using NaOH, KOH, and SiO_2 (quartz powder). The mixture was annealed for 2 hours at 1100 °C, then quenched and annealed at 550 °C for 8 days. The $NaKSi_2O_5$ compound was formed with a monoclinic structure and space group $P2_1/n$. Na and K atoms are orderly distributed in this structure. In the same year, Rakic and Kahlenberg [55] reported another crystalline phase of $Na_{1.55}K_{0.45}Si_2O_5$ using XRD. This compound is monoclinic with the space group $P2_1/c$. In the compound, Na and K atoms show definite preference of distribution. More recently, Rakic *et al*. [56] reported a crystalline phase of $Na_{1.84}K_{0.16}Si_2O_5$ synthesized at 1 kbar. The compound is orthorhombic with space group $Pn2_1a$. This is an almost identical structure as β- and C-$Na_2Si_2O_5$. The authors mentioned that small amount of K addition would not change the structure type, which indicates a possible solid solution of disilicate. Spek *et al*. [57] reported a compound at the composition of $K_{1.33}Na_{0.67}Si_2O_5$, which is similar to the one previously reported by Sakaguchi *et al*. at the $Na_{1.3}K_{0.7}Si_2O_5$ composition. The Na and K distribution also show definite preference. Spek *et al*. found that the compound forms a sheet-type silicate structure with 4-, 6-, and 8-membered rings of SiO_4 tetrahedra, which is different from $K_2Si_2O_5$ and $Na_2Si_2O_5$.

In order to better interpret these two pseudo-binary sections in the K_2O-Na_2O-SiO_2 system, another alkali silicate ternary system, Li_2O-Na_2O-SiO_2, was reviewed. According to West [31, 32], there are large solid solutions in the phase diagrams of the Li_2SiO_3-Na_2SiO_3 and $Li_2Si_2O_5$-$Na_2Si_2O_5$ sections. As alkali silicate systems often show systematic trends in terms of phase diagram and thermodynamic properties, it is reasonable to deduce a solid solution in the K_2O-Na_2O-SiO_2 system instead of many ternary compounds with the identical structure.

The optimizations of the pseudo-binary sections: K_2SiO_3-Na_2SiO_3, $K_2Si_2O_5$-$Na_2Si_2O_5$, and Na_2SiO_3-$K_2Si_2O_5$ are shown in Figs. 8.10 to 8.12, respectively. These sections are important for the optimization of this ternary system. Most of the experimental studies reported for this ternary system were performed on these pseudo-binary sections. In the optimization of this study, these pseudo-binary sections are well reproduced based on the phase diagram measurements from Kracek *et al*. [16]. The liquidus in these sections are well reproduced by introducing meta- and disilicate solid solutions. Isothermal liquidus projections based on the optimized model parameters and the calculated ternary invariant points are shown in Fig. 8.13 (a) and (b) along with the experimental data reported by Kracek *et al*. [16]. The calculated isothermal liquidus from 700 to 1000 °C are in good agreement with the reported data. All the calculated invariant points are reproduced within ± 35 °C from the reported experimental error limits. Details of the calculated and measured invariant reactions are shown in Table 8.6.

Several thermodynamic property measurements of the liquid solution of the K_2O-Na_2O-SiO_2 system were found in the literature. Belton *et al*. [17] investigated the standard Gibbs free energy of mixing along the metasilicate (M_2SiO_3) and disilicate ($M_2Si_2O_5$) compositions. Ion-current ratios between K and Na were measured using the Knudsen Effusion Mass Spectrometry (KEMS) at 1100 °C. The calculated Gibbs energies of mixing are shown in Fig. 8.14 (a) and (b). Choudary *et al*. [58] investigated the Gibbs energies of mixing at the meta-, di-, and tetrasilicate compositions at 1100 °C using the KEMS. The reported Gibbs energies show small positive deviations from the ideal solution behavior. More recently, Chastel *et al*. [13] measured the ionic intensity ratio of K and Na at 1100 °C using KEMS. The Gibbs energy of mixing was calculated at 0.5, 0.667, and 0.85 mole fraction of SiO_2 compositions. The author calculated the enthalpy of mixing, which shows slight negative deviations from the ideal solution behavior. Data measured by Belton *et al*.

and Choudary *et al*. (the same research group) show positive deviations while Chastel *et al*.'s data show negative deviations from the ideal behavior based on the KEMS data. Rogez and Mathieu [59] measured the enthalpy of mixing using solution ($2PbO \cdot B_2O_3$) calorimetry at 876 K in the composition range from 50 to 100 mol % SiO_2 of this ternary system (shown in Fig. 8.15). They reported a negative enthalpy of mixing for the disilicate composition and a positive enthalpy of mixing for the metasilicate composition. These calorimetric data show better agreement with Chastel *et al*. at the disilicate compositions, while they show a better agreement with Belton *et al*. and Choudary *et al*. at the metasilicate compositions. Kaibicheva *et al*. [60] and Rudnyi et al. [61] measured the partial pressure of K, Na, and O_2 using the ion-molecule equilibrium method (shown in Fig. 8.16). Disilicate compositions were investigated in the temperature range from 1200 to 1500 K. Almost ideal solution behavior can be expected from the data.

The calculated Gibbs energy and enthalpy of mixing, and partial pressure of potassium are compared with experimental data in Figs. 8.14 to 8.16. The calculated Gibbs energies exhibit some deviations from the experimental data. This is possibly due to the large error range of the experimental technique and the small absolute values reported from these studies. In Figs. 8.14 and 8.15, the measured Gibbs energy and enthalpy data have an error range less than 1 $kJ \cdot mol^{-1}$. However, we think that their experimental technique could easily yield more than 2 $kJ \cdot mol^{-1}$. The calculated Gibbs energy and enthalpy of mixing in the present study show more negative deviations from ideal solution at the disilicate compositions as reported by Chastel *et al*. [13] and Rogez and Mathieu [59]. The results of molecular dynamics (MD) simulations using two-body interatomic potential of the Born-Mayer-Huggins type from Kawamura [62] are also in agreement with the experimental data from Chastel *et al*. for the disilicate section. The calculated Gibbs energy and enthalpy of mixing at the metasilicate compositions are close to ideal solution behavior

in the present optimization, which is in between the data reported by Belton *et al*./Choudary *et al*. and Chastel *et al*. In Fig. 8.16, the calculated partial pressure of potassium shows a reasonable agreement with the experimental data from Kaibicheva *et al*. [60] / Rudnyi *et al*. [61]. It reproduces the trend of data as a function of temperature considering the experimental error range.

In general, the liquid solution properties show almost ideal solution behavior over the entire composition ranges. As the reported thermodynamic property data are not consistent with each other (Figs. 8.14 to 8.16), the optimization of this study was focused more on reproducing the phase diagram data [16]. Reliable phase diagram data, systematic trend of the Gibbs energy, enthalpy of mixing as well as partial pressure data are well reproduced simultaneously considering the meta- and disilicate solid solutions.

Regarding the melt structure, Florian *et al*. [4] investigated the disilicate compositions using 2D ^{17}O Dynamic Angle Spinning (DAS) Nuclear Magnetic Resonance (NMR). Florian *et al*. reported the ratio between non-bridged oxygen (NBO) and bridged oxygen (BO). Huang and Cormack [3] also reported BO/NBO for this ternary system using MD simulations. Compositions at the SiO_2 mole fractions of 0.75 and 0.85 were investigated. The calculated BO/NBO at 500 °C (approximate glass transition temperature) are compared with these data in Fig. 8.17. The experimental data are well reproduced in the present calculations, even though these structural data were not considered in the process of thermodynamic optimization. Therefore, the MQM can accurately describe not only the thermodynamic properties of the liquid solution but also the structure of the K_2O-Na_2O-SiO_2 liquid solution.

8.4 Summary

Thermodynamic optimizations were performed for the K_2O-CaO-SiO_2 and K_2O-Na_2O-SiO_2 systems. All available thermodynamic and phase equilibrium data in the literature have been critically assessed. Sets of optimized Gibbs energy functions for all phases in the K_2O-CaO-SiO_2 and K_2O-Na_2O-SiO_2 systems were obtained, which reproduce the reliable experimental data from the literature. The melt structure in the K_2O-Na_2O-SiO_2 system was also well predicted. The present optimized model parameters can be used to calculate any thermodynamic properties and phase diagram in the entire composition and temperature ranges of the K_2O-CaO-SiO_2 and K_2O-Na_2O-SiO_2 systems.

Acknowledgments

Financial supports from Tata Steel Europe, POSCO, Nucor Steel, Rio Tinto Iron and Titanium, Hyundai Steel, Nippon Steel and Sumitomo Metals Corp., JFE Steel, Voestalpine, RHI, and the Natural Sciences and Engineering Research Council of Canada are gratefully acknowledged. One of the authors (D.-G. Kim) also acknowledges the McGill Engineering Doctorate Award (MEDA) from McGill University.

References

[1] B.O. Mysen, P. Richet, Silicate glasses and melts properties and structure, Elsevier2005.
[2] C.T. Moynihan, A.J. Easteal, D.C. Tran, J.A. Wilder, E.P. Donovan, Heat capacity and structural relaxation of mixed-alkali glasses, J. Am. Ceram. Soc. 59(3-4) (1976) 137-40.
[3] C. Huang, A.N. Cormack, Structure and energetics in mixed-alkali-metal silicate glasses from molecular dynamics, J. Mater. Chem. 2(3) (1992) 281-7.
[4] P. Florian, K.E. Vermillion, P.J. Grandinetti, I. Farnan, J.F. Stebbins, Cation Distribution in Mixed Alkali Disilicate Glasses, J. Am. Chem. Soc. 118(14) (1996) 3493-7.
[5] G.N. Greaves, Structural studies of the mixed alkali effect in disilicate glasses, Solid State Ionics 105(1-4) (1998) 243-248.

[6] M. Zevenhoven-Onderwater, R. Backman, B.J. Skrifvars, M. Hupa, The ash chemistry in fluidised bed gasification of biomass fuels. Part I: predicting the chemistry of melting ashes and ash-bed material interaction, Fuel 80(10) (2001) 1489-1502.
[7] J. Berjonneau, L. Colombel, J. Poirier, M. Pichavant, F. Defoort, J.-M. Seiler, Determination of the Liquidus Temperatures of Ashes from the Biomass Gasification for Fuel Production by Thermodynamical and Experimental Approaches, Energy Fuels 23(12) (2009) 6231-6241.
[8] D. Lindberg, R. Backman, P. Chartrand, M. Hupa, Towards a comprehensive thermodynamic database for ash-forming elements in biomass and waste combustion - Current situation and future developments, Fuel Process. Technol. 105 (2013) 129-141.
[9] L. Zhang, C. Schmetterer, J. Masset Patrick, Thermodynamic Modeling of the CaO-SiO2-M2O (M=K,Na) Systems, HIGH. TEMP. MATER. PROC. 32(3) (2013) 1-6.
[10] M. Hillert, B. Jansson, B. Sundman, J. Aagren, A two-sublattice model for molten solutions with different tendency for ionization, Metall. Trans. A 16A(2) (1985) 261-6.
[11] G.W. Morey, F.C. Kracek, N.L. Bowen, The ternary system K2O-CaO-SiO2, J. Soc. Glass Technol. 14 (1930) 149-187.
[12] F. Bennour, M. Gilbert, J. Rogez, J.C. Mathieu, An interacting pair model for alkaline binary and ternary liquid silicates: application to the systems Na2O-K2O-SiO2 and Na2O-Cs2O-SiO2, Metall. Mater. Trans. B 30B(1) (1999) 67-74.
[13] R. Chastel, C. Bergman, J. Rogez, J.C. Mathieu, Excess thermodynamic functions in ternary sodium oxide-potassium oxide-silica melts by Knudsen cell mass spectrometry, Chem. Geol. 62 (1987) 19-29.
[14] E. Yazhenskikh, K. Hack, M. Mueller, Critical thermodynamic evaluation of oxide systems relevant to fuel ashes and slags, Part 4: Sodium oxide-potassium oxide-silica, CALPHAD: Comput. Coupling Phase Diagrams Thermochem. 32 (2008) 506-513.
[15] E. Yazhenskikh, K. Hack, M. Muller, Thermodynamic assessment of the system Al2O3-K2O-Na2O-SiO2-CaO-MgO, GTT-Technologies, 13th Annual Workshop (2011).
[16] F.C. Kracek, The ternary system: K2SiO3-Na2SiO3-SiO2, J. Phys. Chem. 36 (1932) 2529-42.
[17] G.R. Belton, U.V. Choudary, D.R. Gaskell, Thermodynamics of mixing in molten sodium-potassium silicates, Inst. Min. Metall., 1974, pp. 247-53.
[18] C.W. Bale, E. Belisle, P. Chartrand, S.A. Decterov, G. Eriksson, A.E. Gheribi, K. Hack, I.H. Jung, Y.B. Kang, J. Melancon, A.D. Pelton, S. Petersen, C. Robelin, J. Sangster, P. Spencer, M.A. Van Ende, FactSage thermochemical software and databases, 2010-2016, CALPHAD: Comput. Coupling Phase Diagrams Thermochem. 54 (2016) 35-53.
[19] A.D. Pelton, S.A. Degterov, G. Eriksson, C. Robelin, Y. Dessureault, The modified quasichemical model I - binary solutions, Metall. Mater. Trans. B 31B (2000) 651-659.
[20] A. Pelton, P. Chartrand, The modified quasi-chemical model: Part II. Multicomponent solutions, Metallurgical and Materials Transactions A 32(6) (2001) 1355-1360.
[21] E. Ising, Beitrag zur Theorie des Ferromagnetismus, Zeitschrift für Physik 31(1) (1925) 253-258.
[22] A.D. Pelton, A general "geometric" thermodynamic model for multicomponent solutions, CALPHAD: Comput. Coupling Phase Diagrams Thermochem. 25(2) (2001) 319-328.
[23] D.G. Kim, M.A. Van Ende, P. Hudon, I.H. Jung, Coupled experimental study and thermodynamic optimization of the K2O-SiO2 system, Submitted to Journal of Non-Crystalline Solids (2017).

[24] G. Eriksson, P. Wu, M. Blander, A.D. Pelton, Critical evaluation and optimization of the thermodynamic properties and phase diagrams of the MnO-SiO2 and CaO-SiO2 systems, Can. Metall. Q. 33(1) (1994) 13-21.
[25] P. Wu, G. Eriksson, A.D. Pelton, Optimization of the thermodynamic properties and phase diagrams of the sodium oxide-silica and potassium oxide-silica systems, J. Am. Ceram. Soc. 76 (1993) 2059-64.
[26] N.F. Fedorov, E.R. Brodkina, Solid solutions in the system 2CaO·SiO2-K2O·CaO·SiO2, Izv. Akad. Nauk SSSR, Neorg. Mater. 2(4) (1966) 745-8.
[27] H. Suzukawa, The alkali phases in portland cement. II. The potassium phase, Zem.-Kalk-Gips 9 (1956) 390-6.
[28] G. Lai, T. Nojiri, K. Nakano, Studies of the stability of β-calcium silicate (β-Ca2SiO4) doped by minor ions, Cem. Concr. Res. 22(5) (1992) 743-54.
[29] I.-H. Jung, S.A. Decterov, A.D. Pelton, Critical thermodynamic evaluation and optimization of the CaO-MgO-SiO2 system, J. Eur. Ceram. Soc. 25(4) (2005) 313-333.
[30] B. Konar, P. Hudon, I.H. Jung, A coupled experimental phase diagram study and thermodynamic modeling of the Li2O-Na2O-SiO2 system, Unpublished work (2017).
[31] A.R. West, Phase equilibriums in the system sodium metasilicate-lithium metasilicate, J. Am. Ceram. Soc. 59(3-4) (1976) 118-21.
[32] A.R. West, Phase equilibriums in the system sodium metasilicate-lithium metasilicate-silicon dioxide, J. Am. Ceram. Soc. 59(3-4) (1976) 124-7.
[33] M. Hillert, The compound energy formalism, J. Alloys Compd. 320(2) (2001) 161-176.
[34] G.W. Morey, F.C. Kracek, N.L. Bowen, The ternary system: K2O-CaO-SiO2, J. Soc. Glass Technol. 15 (1931) 57-8.
[35] M. Chen, X. Hou, J. Chen, B. Zhao, Phase Equilibria Studies in the SiO2-K2O-CaO System, Metall. Mater. Trans. B 47(3) (2016) 1690-1696.
[36] W.C. Taylor, System 2CaO.SiO2-K2O.CaO.SiO2, and other phase-equilibrium studies involving potash, J. Res. Natl. Bur. Stand. (U. S.) 27 (1941) 311-23.
[37] H. Ohsato, T. Sugimura, S. Hayashi, T. Ogihara, β-Wollastonite and para-wollastonite precipitated from the join potassium oxide-calcium silicate, Nagoya Kogyo Daigaku Gakuho 32 (1981) 123-30.
[38] H. Risnes, High temperature filtration in biomass combustion and gasification processes, Ph.D. thesis, NUST (2002) 1-238.
[39] H. Hughes, Formation of alkali silicates and aluminosilicates and their occurrence in blast furnaces, Trans. Br. Ceram. Soc. 65(12) (1966) 661-79.
[40] A.S. Berezhnoi, N.V. Lapina, E.V. Lifshits, E.P. Shevyakova, Characteristics of polycomponent high-basicity silicates of the sodium oxide-potassium oxide-calcium oxide-magnesium oxide-silicon dioxide system, Izv. Akad. Nauk SSSR, Neorg. Mater. 12(9) (1976) 1653-8.
[41] E. Arroyabe, R. Tessadri, D.M. Toebbens, V. Kahlenberg, Does K2CaSiO4 exist? A phase-analytical study in the system K2O-CaO-SiO2 with implications for the characterization of residual materials, J. Am. Ceram. Soc. 94(8) (2011) 2652-2655.
[42] L.K. Bankole, R.S. Abdul, N.M. Sharif, Crystallization of potassium calcium silicate from modified industrial EAF slag, Adv. Mater. Res. (Durnten-Zurich, Switz.) 620 (2013) 66-71, 7 pp.
[43] T. Akiyama, Y. Yao, S. Matsuno, A major compound in fused potassium silicate fertilizer, Nippon Dojo Hiryogaku Zasshi 72(4) (2001) 484-488.

[44] E. Arroyabe, V. Kahlenberg, Structural investigations on the fertilizer component K2Ca2Si2O7, Eur. J. Mineral. 23(1) (2011) 101-110.
[45] R.P. Gunawardane, F.P. Glasser, Crystal chemistry and synthesis of ternary silicates and germanates containing alkali (sodium ion, potassium ion) and alkaline earth (calcium ion, strontium ion, barium ion) cations, Z. Anorg. Allg. Chem. 411(2) (1975) 163-72.
[46] E. Arroyabe, R. Kaindl, V. Kahlenberg, Structural and Raman spectroscopic investigations of K4BaSi3O9 and K4CaSi3O9, Z. Anorg. Allg. Chem. 635(2) (2009) 337-345.
[47] V. Kahlenberg, R. Kaindl, D.M. Toebbens, The crystal structure of the interrupted framework silicate K9.6Ca1.2Si12O30 determined from laboratory x-ray diffraction data, J. Solid State Chem. 179(7) (2006) 1948-1956.
[48] E. Arroyabe, R. Kaindl, D.M. Tobbens, V. Kahlenberg, Synthesis, Crystal Structure, and Vibrational Spectroscopy of K2Ca4Si8O21-An Unusual Single-Layer Silicate Containing Q2 and Q3 Units, Inorg. Chem. 48(24) (2009) 11929-11934.
[49] E. Arroyabe, R. Kaindl, D.M. Toebbens, V. Kahlenberg, K2Ca6Si4O15-structural and spectroscopical studies on a mixed tetrahedral-octahedral framework, J. Solid State Chem. 182(12) (2009) 3254-3261.
[50] V.N. Yung, Y.M. Butt, V.V. Myshlyaeva, Effect of alkalies on the properties of calcium silicates, Tsement 17(No. 6) (1951) 9-13.
[51] F.C. Kracek, N.L. Bowen, G.W. Morey, The system: potassium metasilicate-silica, J. Phys. Chem. 33 (1929) 1857-79.
[52] F.C. Kracek, N.L. Bowen, G.W. Morey, Equilibrium relations and factors influencing their determination in the system K2SiO3-SiO2, J. Phys. Chem. 41 (1937) 1183-93.
[53] M. Sakaguchi, I. Sakamoto, R. Akagi, H. Toraya, Powder data for potassium sodium silicate Na1.3K0.7Si2O5, Powder Diffr. 10(4) (1995) 290-2.
[54] S. Rakic, V. Kahlenberg, Single crystal structure investigation of twinned NaKSi2O5 - a novel single layer silicate, Solid State Sci. 3(6) (2001) 659-667.
[55] S. Rakic, V. Kahlenberg, The crystal structure of a mixed alkali phyllosilicate with composition Na1.55K0.45Si2O5, Eur. J. Mineral. 13(6) (2001) 1215-1221.
[56] S. Rakic, V. Kahlenberg, B.C. Schmidt, Hydrothermal synthesis and structural characterization of κ-Na2Si2O5 and Na1.84K0.16Si2O5, Solid State Sci. 5(3) (2003) 473-480.
[57] A.L. Spek, B.H.W.S. de Jong, Potassium sodium phyllosilicate, K1.33Na0.67Si2O5, Acta Crystallogr., Sect. E: Struct. Rep. Online 61(8) (2005) i188-i190.
[58] U.V. Choudary, D.R. Gaskell, G.R. Belton, Thermodynamics of mixing in molten sodium-potassium silicates at 1100°C: the effect of a calcium oxide addition, Metall. Trans., B 8B(1) (1977) 67-71.
[59] J. Rogez, J.C. Mathieu, Enthalpy of formation in the system sodium oxide-potassium oxide-silica, Phys. Chem. Liq. 14(4) (1985) 259-72.
[60] E.A. Kaibicheva, E.B. Rudnyi, L.N. Sidorov, V.L. Stolyarova, Determination of the activity of alkali metal oxides in sodium oxide-potassium oxide-silica-system melts by an ion-molecular-equilibriums method, Fiz. Khim. Stekla 16(3) (1990) 431-8.
[61] E.B. Rudnyi, M.V. Korobov, O.M. Vovk, E.A. Kaibicheva, L.N. Sidorov, Ion equilibria. A new technique for measurement of low oxygen and alkali partial pressures, High Temp. Sci. 26 (1990) 165-74.
[62] K. Kawamura, A molecular dynamics simulation of na2o-2sio2 - k2o-2sio2 melts - effect of basic, Molecular Simulation 6(4-6) (1991) 245-255.

Tables

Table 8.1 Crystal structures of the ternary compounds in the K_2O-CaO-SiO_2 system.

Phase	Crystal system	Space group	Exp. Technique	Reference
K_2CaSiO_4 (KCS)	hexagonal		OM	30Mor[11]
	cubic		XRD	66Hug[40]
	orthorhombic		XRD, IR-S	76Ber[41]
$K_2Ca_2Si_2O_7$ (KC_2S_2)	tetragonal		XRD, SEM	01Aki[44]
	hexagonal	$P6_3/m$	XRD	10Arr[45]
$K_4CaSi_3O_9$ (K_2CS_3)	cubic		OM	30Mor[11]
	cubic	P---	XRD	75Gun[46]
	cubic	$Pa\bar{3}$	XRD, R-S	09Arr[47]
$K_8CaSi_{10}O_{25}$ (K_4CS_{10})	rhombohedral (hexagonal)		XRD	75Gun[46]
$K_4CaSi_6O_{15}$ (K_2CS_6)			OM	30Mor[11]
$K_{9.6}Ca_{1.2}Si_{12}O_{30}$	trigonal (hexagonal)	R3c	XRD	06Kah[48]
$K_2Ca_3Si_6O_{16}$ (KC_3S_6)				
$K_2Ca_2Si_9O_{21}$ (KC_2S_9)				
$K_2Ca_4Si_8O_{21}$ (KC_4S_8)	triclinic	$P\bar{1}$	XRD, R-S	09Arr[49]
$K_2Ca_6Si_4O_{15}$ (KC_6S_4)	monoclinic	$P12/c1$	XRD, R&FTIR-S	09Arr[50]
$K_2Ca_{23}Si_{12}O_{48}$ ($KC_{23}S_{12}$)			OM, XRD	41Tay[37]

OM: Optical microscopy, XRD: X-ray Diffraction, IR-S: Infrared spectroscopy, SEM: Scanning electron microscope, R-S: Raman spectroscopy, FTIR-S: Fourier transform infrared spectroscopy.

Table 8.2 Optimized thermodynamic properties for the ternary compounds of the K_2O-CaO-SiO_2 system.

Compound	$\Delta H^{o}_{298.15K}$ (kJ·mol^{-1})	$S^{o}_{298.15K}$ (J·mol^{-1}·K^{-1})	C_P (J·mol^{-1}·K^{-1}) Neumann-Kopp rule ($x \cdot K_2O + y \cdot CaO + z \cdot SiO_2$)
K_2CaSiO_4 (KCS)	-2205.00	196.49	$1 \cdot Cp(K_2O) + 1 \cdot Cp(CaO) + 1 \cdot Cp(SiO_2$, Trd) (298-2000 K)
$K_2Ca_2Si_2O_7$ (KC_2S_2)	-3884.00	268.55	$1 \cdot Cp(K_2O) + 2 \cdot Cp(CaO) + 2 \cdot Cp(SiO_2$, Trd) (298-2000 K)
$K_4CaSi_3O_9$ (K_2CS_3)	-4745.00	380.00	$2 \cdot Cp(K_2O) + 1 \cdot Cp(CaO) + 3 \cdot Cp(SiO_2$, Qz(HT)) (298-2000 K)
$K_8CaSi_{10}O_{25}$ (K_4CS_{10})	-12580.00	897.00	$4 \cdot Cp(K_2O) + 1 \cdot Cp(CaO) + 10 \cdot Cp(SiO_2$, Trd) (298-2000 K)
$K_4CaSi_6O_{15}$ (K_2CS_6)	-7509.00	564.00	$2 \cdot Cp(K_2O) + 1 \cdot Cp(CaO) + 6 \cdot Cp(SiO_2$, Trd) (298-2000 K)
$K_2Ca_3Si_6O_{16}$ (KC_3S_6)	-8300.00	512.50	$1 \cdot Cp(K_2O) + 3 \cdot Cp(CaO) + 6 \cdot Cp(SiO_2$, Coe) (298-2000 K)
$K_2Ca_2Si_9O_{21}$ (KC_2S_9)	-10365.00	558.30	$1 \cdot Cp(K_2O) + 2 \cdot Cp(CaO) + 9 \cdot Cp(SiO_2$, Coe) (298-2000 K)
$K_2Ca_6Si_4O_{15}$ (KC_6S_4)	-8555.00	490.49	$1 \cdot Cp(K_2O) + 6 \cdot Cp(CaO) + 4 \cdot Cp(SiO_2$, Coe) (298-2000 K)

Qz: quartz, Trd: tridymite, Coe: coesite.

Table 8.3 Optimized model parameters of the liquid solution ($J \cdot mol^{-1}$).

Liquid solution (MQM)
Coordination numbers:
$Z_{KK}^{K} = 0.6887$, $Z_{CaCa}^{Ca} = 1.3774$, $Z_{SiSi}^{Si} = 2.7549$
Ternary excess Gibbs energy parameters:
$q_{Ca,Si(K)}^{001} = -12552$, $q_{Ca,Si(K)}^{012} = -83680$, $q_{K,Si(Ca)}^{012} = -177820$
α- and α′-Ca_2SiO_4 solid solutions (random mixing model) $(K_2^{2+}, Ca^{2+})_2 SiO_4$
<u>α-Ca_2SiO_4</u>
$g^{o}_{\alpha-K_4SiO_4} = g^{o}_{K_4SiO_4} + 20920$
$q^{11}_{K_2,Ca} = -15062\ .4$
<u>α′-Ca_2SiO_4</u>
$g^{o}_{\alpha'-K_4SiO_4} = g^{o}_{K_4SiO_4} + 20920$
$q^{11}_{K_2,Ca} = -15062\ .4$

Table 8.4 Experimental and calculated invariant points in the K_2O-CaO-SiO_2 system involving liquid phase (see the liquidus projection in Fig. 8.8)

Invariant reactions		Temp. (°C)		Liquid composition (mol %)					
Exp.: Morey *et al*. [11]	R-type			K_2O		CaO		SiO_2	
		Calc.	Exp.	Calc.	Exp.	Calc.	Exp.	Calc.	Exp.
1 C_3S+α′-C_2S+α-C_2S	I	1436.8		0.111		0.557		0.332	
2 C_3S_2+α′-C_2S+α-C_2S	I	1436.8		0.017		0.552		0.431	
3 C_3S+CaO+α′-C_2S	P	1380.3		0.120		0.547		0.333	
4 KCS+CaO+α′-C_2S	P	1332.5		0.129		0.538		0.334	
5 KC_2S_2+KCS+α′-C_2S	E	1258.4		0.166		0.470		0.364	
6 KC_2S_2+KC_6S_4+α′-C_2S	P	1228.8		0.191		0.357		0.452	
7 C_3S_2+KC_6S_4+α′-C_2S	P	1190.1		0.179		0.335		0.486	
8 CS(HT)+CS(LT)+Trd	I	1125.3	1200	0.105	0.064	0.141	0.155	0.756	0.781
9 C_3S_2+CS(HT)+CS(LT)	I	1125.3		0.182		0.250		0.569	
10 KCS+CaO+K_2S	P	1000.9		0.635		0.029		0.336	
11 C_3S_2+KC_6S_4+CS(LT)	P	950.2		0.242		0.176		0.582	
12 KC_3S_6+K_2CS_6+CS(LT)	P	949.5		0.202		0.120		0.677	
13 KC_2S_2+KCS+K_2CS_3	P	937.3		0.444		0.055		0.501	
14 KCS+K_2CS_3+KS	P	933.5		0.447		0.052		0.501	
15 K_2CS_6+K_4CS_{10}+CS(LT)	P	928.6		0.237		0.134		0.629	
16 KC_2S_2+KC_6S_4+CS(LT)	P	912.6		0.254		0.155		0.590	
17 KC_2S_2+K_2CS_3+KS_2(HT)	E	900.8		0.315		0.098		0.587	
18 K_4CS_{10}+CS(LT)+KS_2(HT)	P	895.2		0.259		0.141		0.600	
19 KC_2S_2+CS+KS_2(HT)	E	891.9		0.261		0.143		0.596	
20 KC_2S_9+CS(HT)+Trd	P	886.8		0.153		0.071		0.776	
21 KC_2S_9+Qz+Trd	P	866.9	870	0.160	0.138	0.058	0.060	0.783	0.802

22 KC_2S_9+KC_3S_6+K_2CS_6	P	807.7		0.190		0.042		0.768	
23 K_2CS_3+KS_2(HT)+KS	E	780.0	770	0.419	0.435	0.004	0.003	0.577	0.562
24 KC_2S_9+K_2CS_6+K_4CS_{10}	P	773.3		0.198		0.021		0.781	
25 KC_2S_9+K_S4(HT)+Qz	E	762.7	720	0.187	0.176	0.011	0.022	0.802	0.802
26 KC_2S_9+K_4CS_{10}+KS_4(HT)	E	761.8		0.198		0.016		0.786	
27 K_4CS_{10}+KS_2(HT)+KS_4(HT)	E	752.4		0.228		0.001		0.771	
28 KCS+KS+K_2S	E	712.2		0.585		0.003		0.412	
29 CaO+K_2O+K_2S	E	678.5		0.870		0.002		0.129	

K: K2O, C: CaO, S: SiO2, Qz: quartz, Trd: tridymite, E: eutectic, P: peritectic, I: inversion.

Table 8.5 Optimized model parameters of solutions for the K_2O-Na_2O-SiO_2 system ($J \cdot mol^{-1}$).

Liquid solution (MQM)
Coordination numbers:
$Z_{KK}^{K} = 0.6887$, $Z_{NaNa}^{Na} = 0.6887$, $Z_{SiSi}^{Si} = 2.7549$
K_2O-Na_2O binary excess Gibbs energy parameters:
$\Delta g_{K-Na} = 0$
Ternary excess Gibbs energy parameters:
$q_{K,Si(Na)}^{021} = -20920$
$q_{K,Si(Na)}^{022} = -62760$
$q_{Na,Si(K)}^{022} = -33472$
Metasilicate solid solution (CEF) $(K_2^{2+}, Na_2^{2+})SiO_3$
$G_{K_2SiO_3}^{o} = G_{K_2SiO_3}^{o}$
$G_{Na_2SiO_3}^{o} = G_{Na_2SiO_3}^{o}$
$L_{K,Na:SiO_3} = 35145.6$
${}^1L_{K,Na:SiO_3} = -12552$
Disilicate solid solutions (CEF) $(K_2^{2+}, Na_2^{2+})Si_2O_5$
Low-temperature polymorph
$G_{K_2Si_2O_5}^{o} = G_{K_2Si_2O_5}^{o}$ (LT)
$G_{Na_2Si_2O_5}^{o} = G_{Na_2Si_2O_5}^{o}$ (LT)
$L_{K,Na:Si_2O_5} = 18828$
${}^1L_{K,Na:Si_2O_5} = -8368$
Intermediate-temperature polymorph
$G_{K_2Si_2O_5}^{o} = G_{K_2Si_2O_5}^{o}$ (IT)
$G_{Na_2Si_2O_5}^{o} = G_{Na_2Si_2O_5}^{o}$ (IT)
$L_{K,Na:Si_2O_5} = 37656$
High-temperature polymorph
$G_{K_2Si_2O_5}^{o} = G_{K_2Si_2O_5}^{o}$ (HT)
$G_{Na_2Si_2O_5}^{o} = G_{Na_2Si_2O_5}^{o}$ (HT)
$L_{K,Na:Si_2O_5} = 37656$

Table 8.6 Experimental and calculated invariant points in the K_2O-Na_2O-SiO_2 system involving liquid phase (see the liquidus projection in Fig. 8.13).

Invariant reactions		Temp. (°C)		Liquid composition (mol %)					
Exp.: Kracek *et al*. [16]	R-type			K_2O		Na_2O		SiO_2	
Exp error: ± 10 °C		Calc.	Exp.	Calc.	Exp.	Calc.	Exp.	Calc.	Exp.
1 NS+N_2S+N_3S_2	P	837.3		0.137		0.439		0.424	
2 NS_2(HT)+NS_2(LT)+NS	I	803.3		0.034		0.319		0.648	
3 N_5S+Na_2O(IT)+N_2S	P	767.9		0.062		0.737		0.202	
4 Na_2O(LT)+Na_2O(IT)+N_2S	I	749.9		0.096		0.696		0.209	
5 NS_2(HT)+NS_2(LT)+N_3S_8	I	748.9		0.032		0.214		0.755	
6 NS_2(LT)+N_3S_8+Qz	P	737.8		0.037		0.204		0.759	
7 KS_2(HT)+NS_2(LT)+NS	E	709.9	665	0.180	0.179	0.182	0.185	0.638	0.636
8 KS+NS_2+KS_2	E	653.8	645	0.332	0.300	0.105	0.133	0.563	0.566
9 N_2S+KS+NS_2	P	643.4		0.331		0.236		0.433	
10 KS_2+NS_2+KS_4(HT)	P	612.5		0.167		0.086		0.747	
11 Na_2O(LT)+K_2S+N_2S	E	607.4		0.367		0.347		0.285	
12 NS_2+KS_4(LT)+KS_4(HT)	I	591.9		0.153		0.100		0.747	
13 KS_4(LT)+KS_4(HT)+Qz(HT)	I	591.9		0.127		0.095		0.777	
14 KS_4(LT)+Qz(LT)+Qz(HT)	I	574.9		0.123		0.104		0.773	
15 NS_2(LT)+Qz(LT)+Qz(HT)	I	574.8		0.116		0.112		0.771	
16 NS_2(LT)+KS_4(LT)+Qz(LT)	E	566.7		0.120		0.108		0.772	
17 K_2O+Na_2O(LT)+K_2S	E	547.8		0.693		0.210		0.098	
18 K_2S+KS+N_2S	E	546.9		0.456		0.150		0.394	
Quasi-binary KS+NS	E	737.7	745	0.330	0.327	0.170	0.173	0.500	0.500
Quasi-binary KS_2+NS_2	E	704.9	705	0.180	0.172	0.154	0.160	0.667	0.667

K: K_2O, N: Na_2O, S: SiO_2, Qz: quartz, E: eutectic, P: peritectic, I: inversion.

Figures

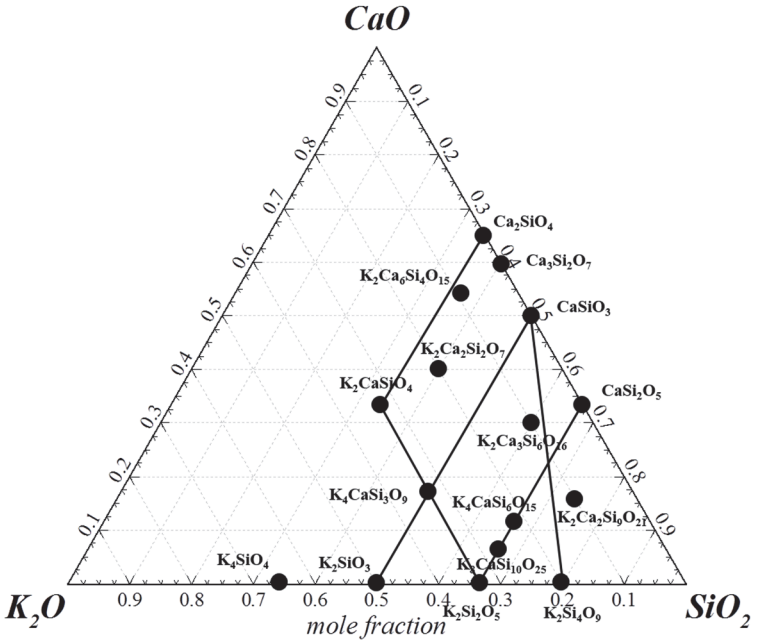

Figure 8.1 Schematic diagram of the K_2O-CaO-SiO_2 system showing all stable compounds and experimentally investigated isoplethal sections.

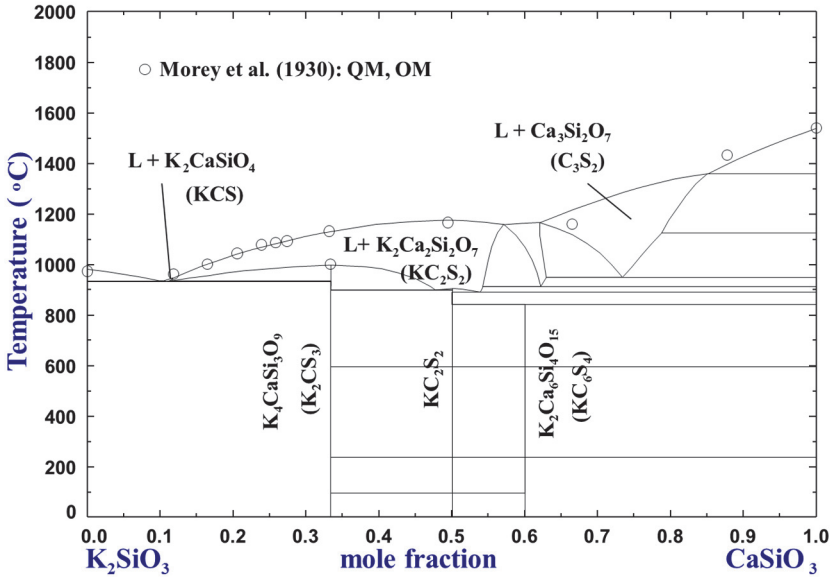

Figure 8.2 Optimized phase diagram of the K_2SiO_3-$CaSiO_3$ section with experimental data.

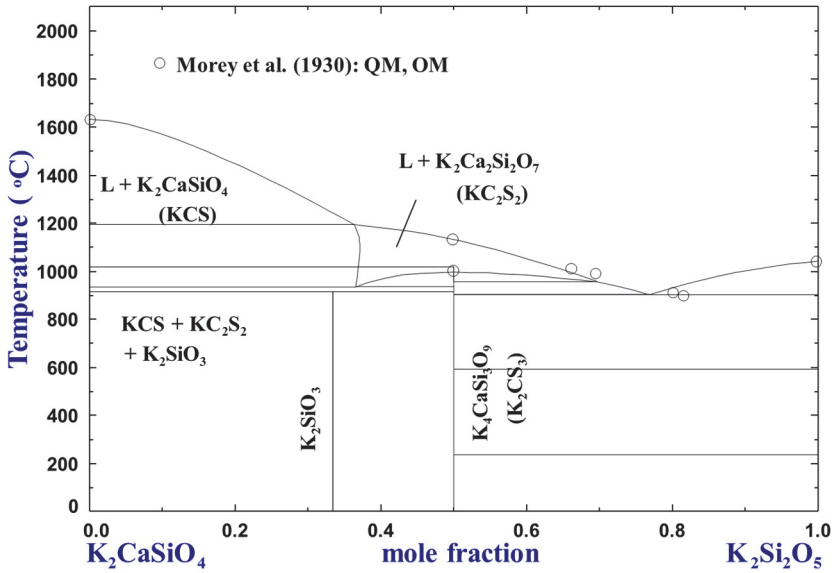

Figure 8.3 Optimized phase diagram of the K_2CaSiO_4-$K_2Si_2O_5$ section with experimental data.

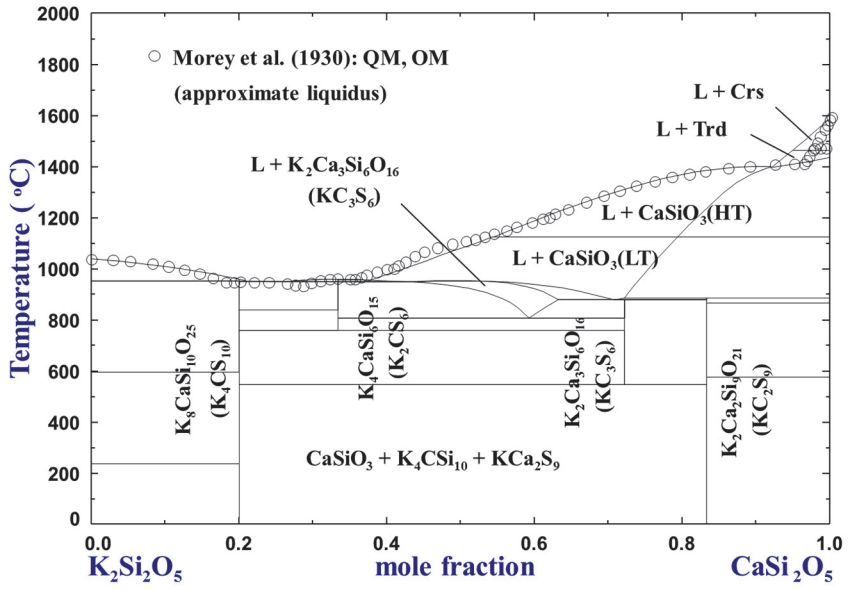

Figure 8.4 Optimized phase diagram of the $K_2Si_2O_5$-$CaSi_2O_5$ section with experimental data.

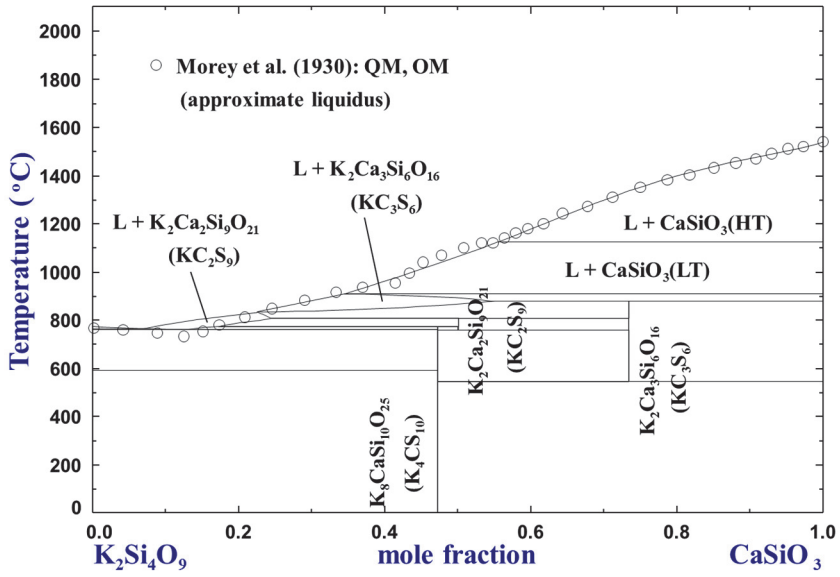

Figure 8.5 Optimized phase diagram of the $K_2Si_4O_9$-$CaSiO_3$ section with experimental data.

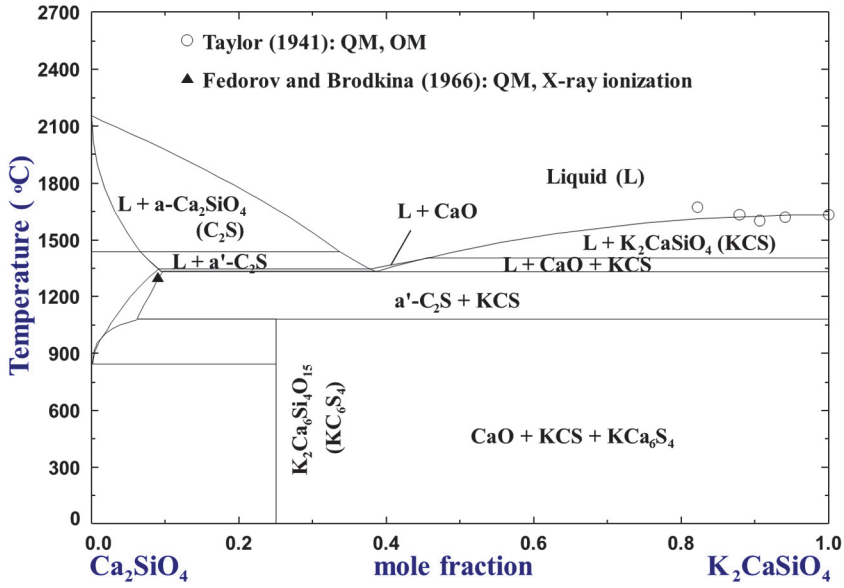

Figure 8.6 Optimized phase diagram of the Ca_2SiO_4-K_2CaSiO_4 section with experimental data.

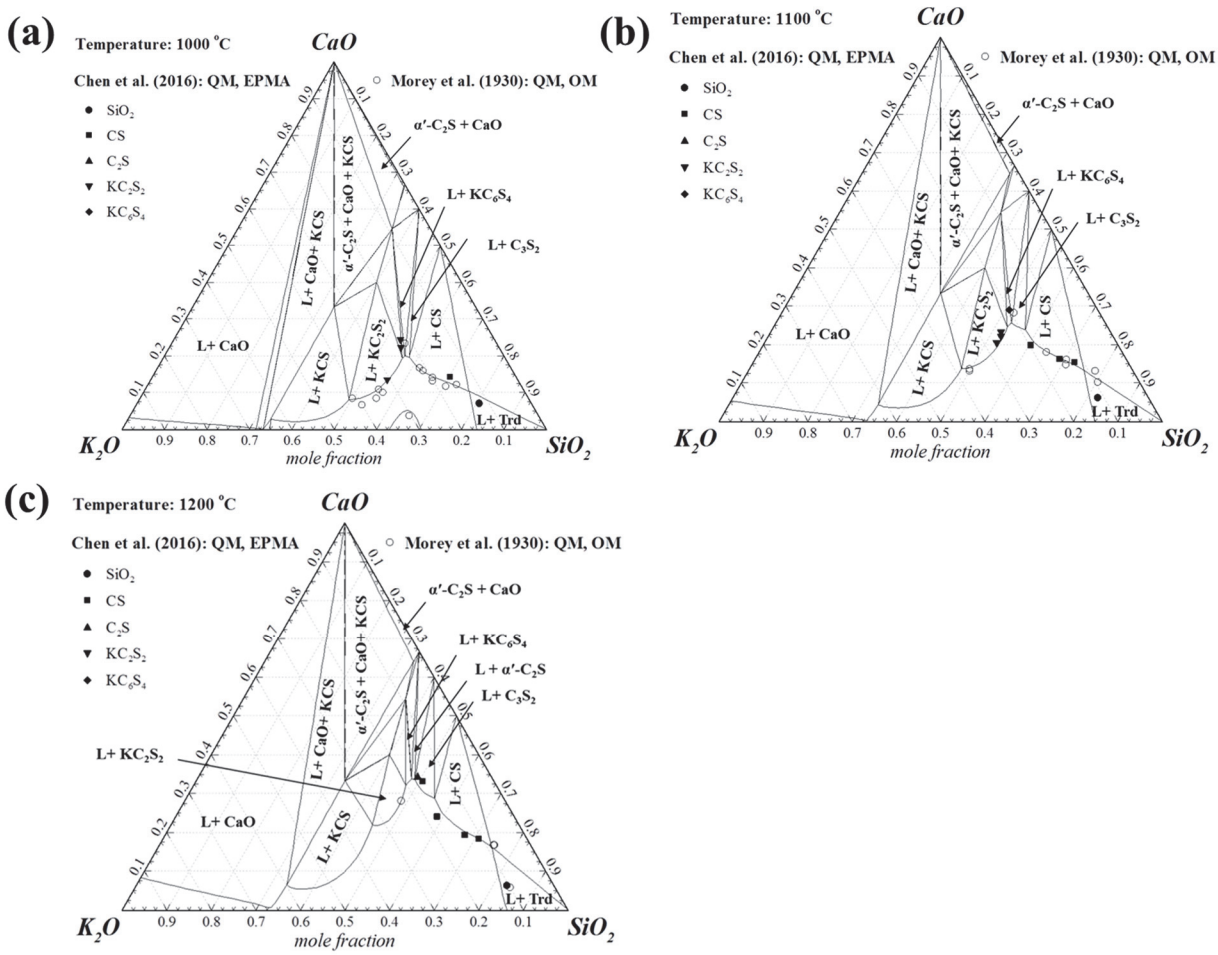

Figure 8.7 Optimized isothermal sections of the K_2O-CaO-SiO_2 system (a) at 1000 °C (b) at 1100 °C, and (c) at 1200 °C with experimental data.

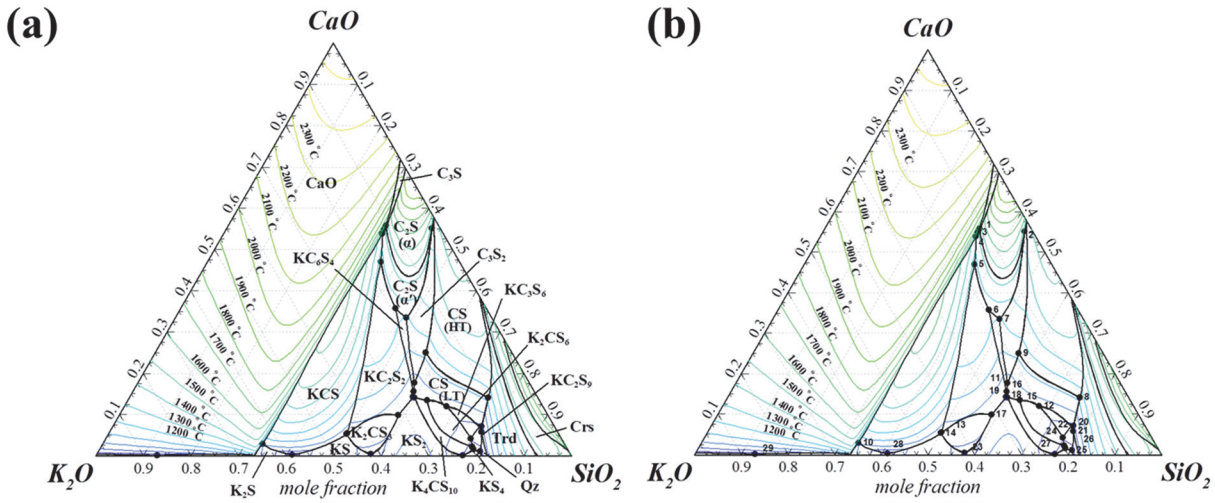

Figure 8.8 Optimized liquidus projection of the K_2O-CaO-SiO_2 system indicating (a) primary phase regions (b) invariant reaction points (for the details of invariant reaction, see Table 8.4).

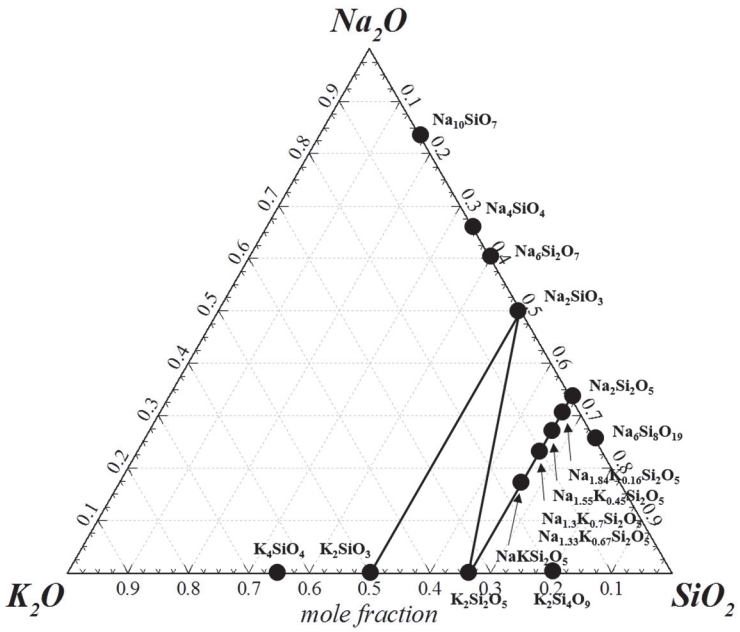

Figure 8.9 Schematic diagram of the K_2O-Na_2O-SiO_2 system showing all ternary compounds reported in the literature and experimentally investigated isoplethal sections.

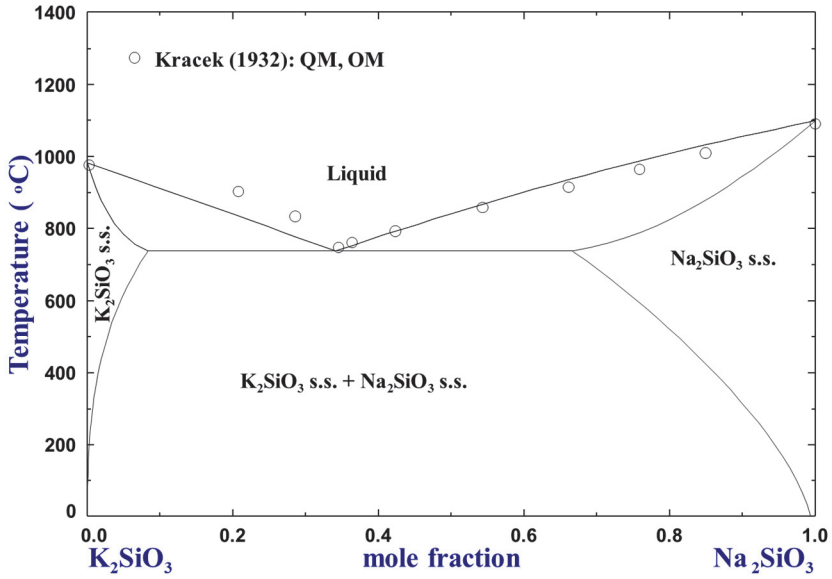

Figure 8.10 Optimized phase diagram of the K_2SiO_3-Na_2SiO_3 section with experimental data.

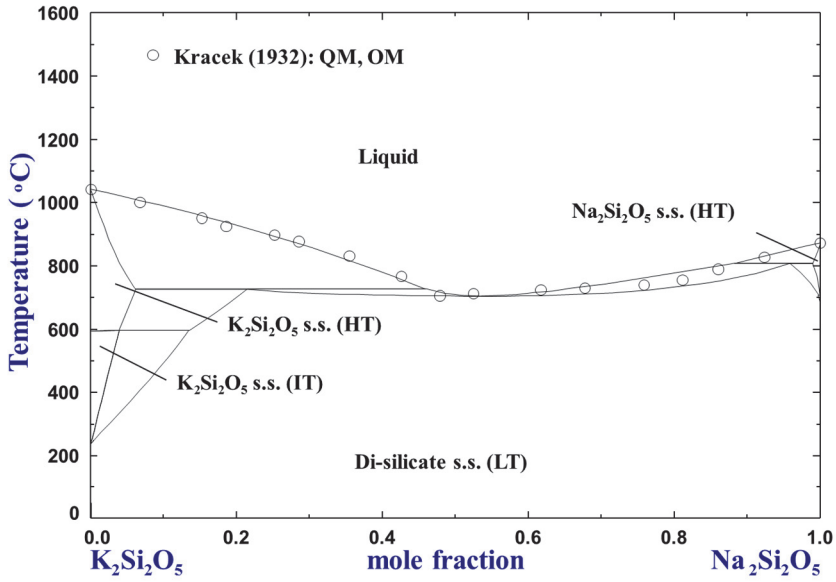

Figure 8.11 Optimized phase diagram of the $K_2Si_2O_5$-$Na_2Si_2O_5$ section with experimental data.

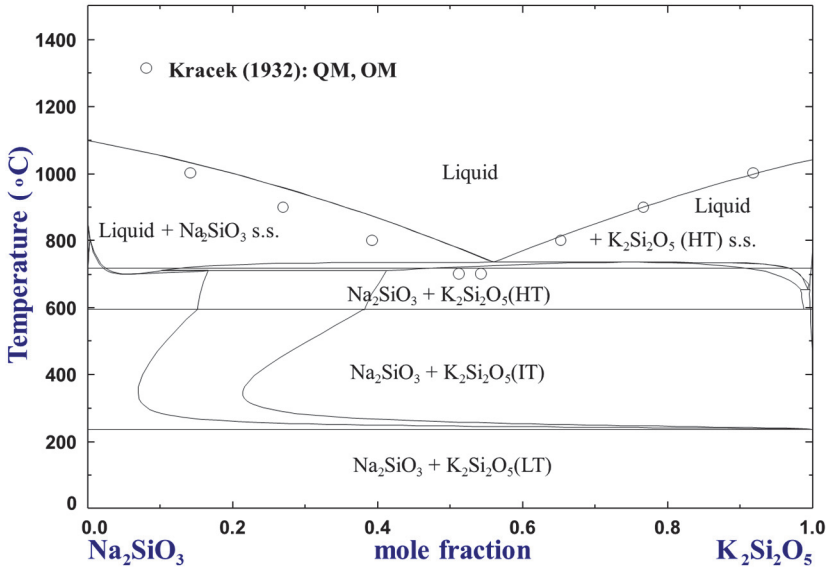

Figure 8.12 Optimized phase diagram of the Na_2SiO_3-$K_2Si_2O_5$ section with experimental data.

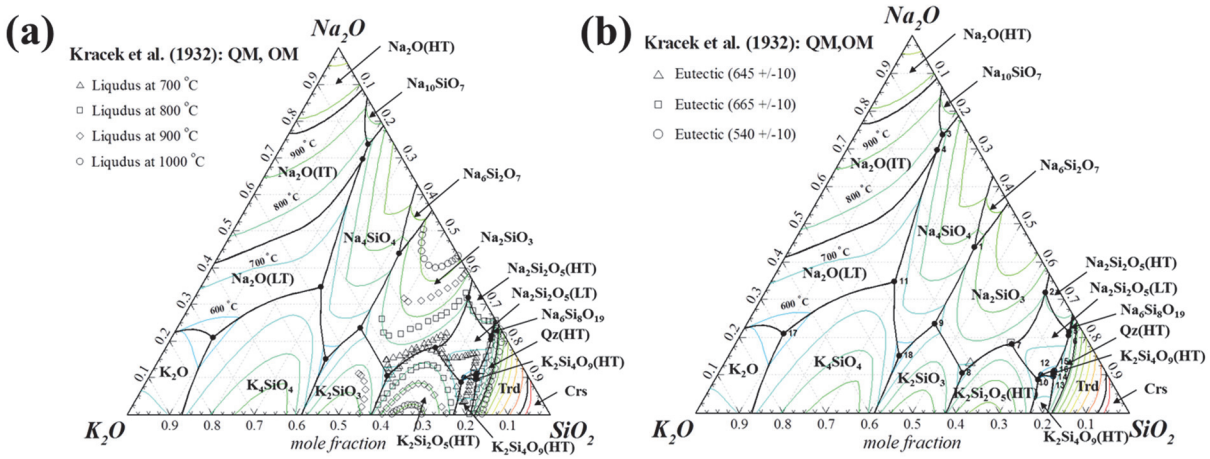

Figure 8.13 Optimized liquidus projection of the K_2O-Na_2O-SiO_2 system indicating (a) primary phase regions and experimental data of isothermal liquidus and (b) invariant reaction points with experimental data (for the details of invariant reaction, see Table 8.6).

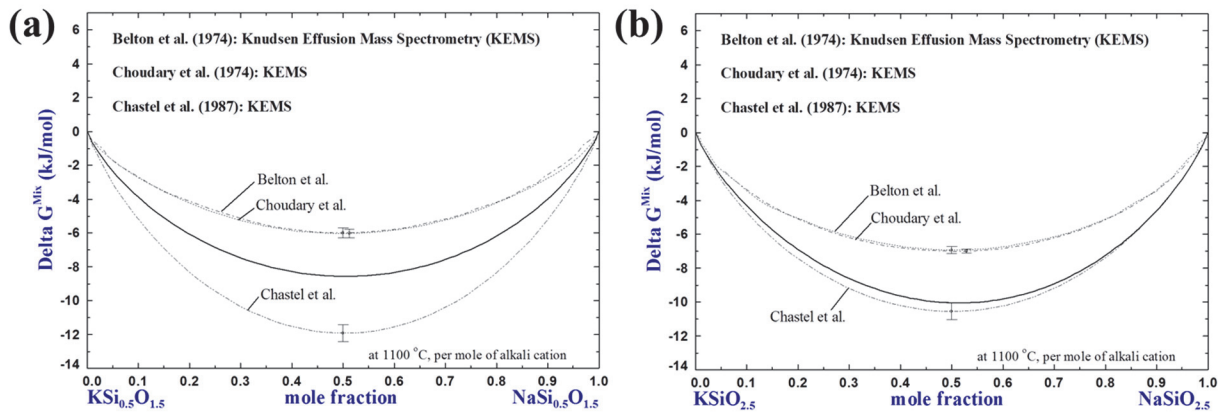

Figure 8.14 Calculated excess Gibbs energy of mixing at 1100 °C (a) along the metasilicate and (b) disilicate compositions with experimental data.

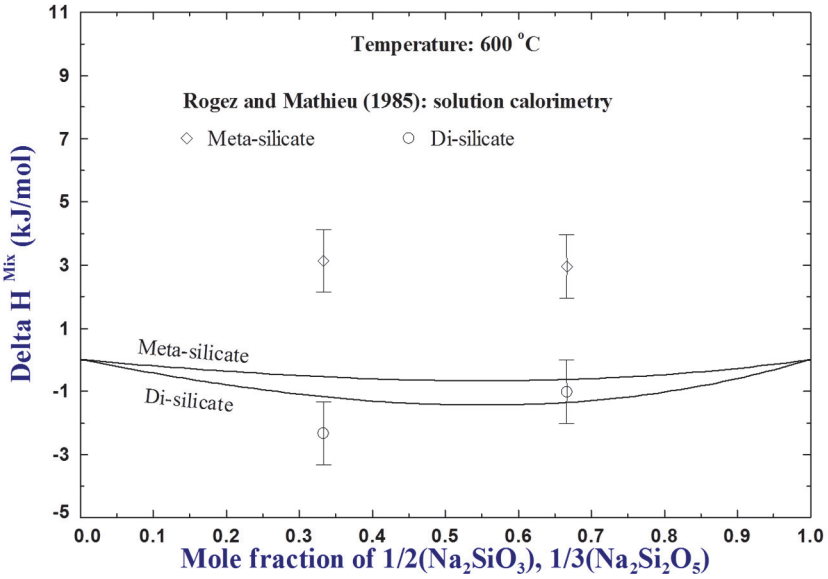

Figure 8.15 Calculated enthalpy of mixing at 600 °C with experimental data.

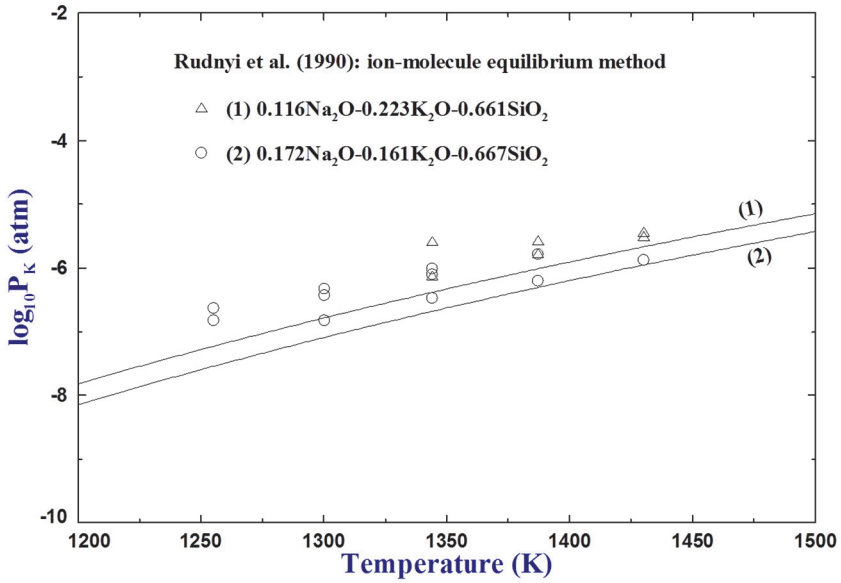

Figure 8.16 Calculated partial pressure of potassium at $0.116Na_2O$-$0.223K_2O$-$0.661SiO_2$ and $0.172Na_2O$-$0.161K_2O$-$0.667SiO_2$ in their mole fractions with experimental data.

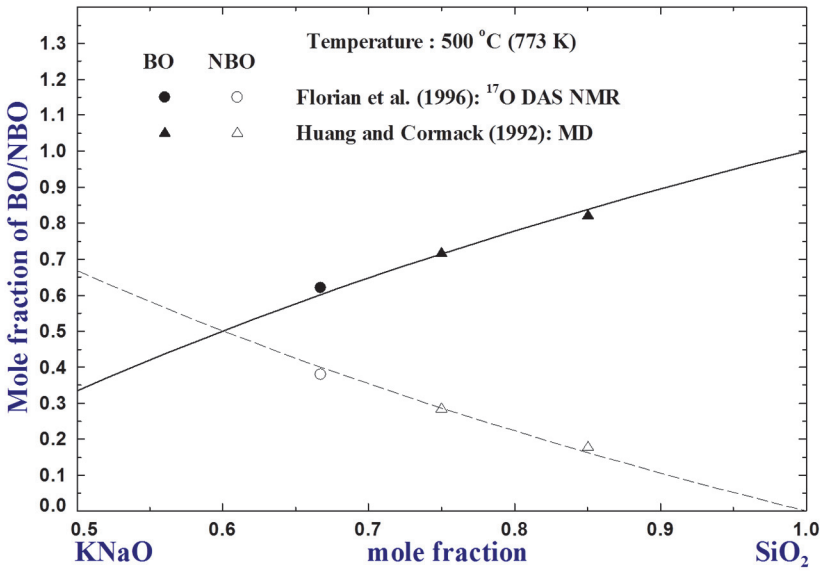

Figure 8.17 Calculated oxygen connectivity at 500 °C (773 K) with experimental data.

Chapter 9 Conclusions and Suggestions for Future Work

9.1 Conclusions

The present study was performed to develop a comprehensive and self-consistent thermodynamic database for the K_2O-Na_2O-MgO-CaO-Al_2O_3-SiO_2 system. Critical evaluations were conducted on all available data in the literature. Key phase diagram experiments were performed to reveal unavailable regions of the phase diagram and resolve discrepancies in the experimental data from the literature. The optimized thermodynamic database for the K_2O-Na_2O-MgO-CaO-Al_2O_3-SiO_2 system is self-consistently built from lower to higher order systems. Thermodynamic optimization of all the K_2O-containing binaries, ternaries, and multi-component systems (including all stoichiometric compounds, solid and liquid solution phases) was performed at 1 atm total pressure. A set of optimized Gibbs energy functions for all stable phases were obtained to reproduce the critically evaluated phase equilibria and thermodynamic properties from 298.15 K to temperatures above liquidus. With interpolations and extrapolations of the Gibbs energy functions, all the calculated results are self-consistent and consistent with thermodynamic principles. In general, the calculated results of the present optimization are in good agreement with the experimental data. Most of the phase diagram data are reproduced within the error range of 5 mol % and ± 50 °C. Several discrepancies and uncertainties in the literature were also resolved through optimizations, and the accuracy of the database was enhanced. The database can be applied to material designs and process optimizations. The conclusions of this thesis are summarized as follows:

In the experimental study of the K_2O-SiO_2 system, the sensitivity of DTA with sealed Pt capsules was assured using pure potassium chromate (K_2CrO_4) and diopside ($CaMgSi_2O_6$). For the first

time, the temperature of eutectic reaction: Liquid → K_4SiO_4 + K_2SiO_3 was successfully measured at 714 ± 6 °C. The phase diagram in K_2O-rich region is well established for the first time using phase diagram experiments and thermodynamic optimization. This optimization can well reproduce all available and reliable thermodynamic properties and phase diagram data in the K_2O-SiO_2 system. Strong short-range ordering structure in the K_2O-SiO_2 melt is also well predicted by the present modeling.

In the experimental study of the K_2O-MgO system, the stability of the K_6MgO_4 compound at 700 and 800 °C was confirmed by equilibration/quenching experiments with up to 167 hours of annealing using sealed Pt capsules. From the results of DSC and quenching experiments, it is concluded that the peritectic reaction of liquid + MgO → K_6MgO_4 occurs at 858 ± 14 °C. In the thermodynamic optimization of the K_2O-MgO-SiO_2 system, the SiO_2 liquidus was well reproduced by introducing the K_2MgSiO_4 associate in the liquid solution.

In the thermodynamic modeling of the K_2O-Al_2O_3 system, the large discrepancies of the eutectic temperature between $KAlO_2$ and K β-alumina were resolved. The stability of K β″-alumina was confirmed up to 1600 °C through equilibration/quenching experiments. β- and β″-alumina solutions were modeled with five-sublattice model under the framework of the compound energy formalism. This model contains structural characteristics of complex ion exchange reactions. Both phase stability region and quantitative ionic site occupations can be calculated as functions of composition and temperature in the K_2O-MgO-Al_2O_3 system.

In the thermodynamic optimization of the K_2O-Al_2O_3-SiO_2 system, the $KAlO_2$ associate species was introduced to describe not only the thermodynamic properties, but also the short-range ordering structure of the liquid solution.

In the thermodynamic optimization of the K_2O-CaO-SiO_2 system, eight stoichiometric compounds were concluded to be the stable phases: K_2CaSiO_4, $K_2Ca_2Si_2O_7$, $K_4CaSi_3O_9$, $K_8CaSi_{10}O_{25}$, $K_4CaSi_6O_{15}$, $K_2Ca_3Si_6O_{16}$, $K_2Ca_2Si_9O_{21}$, and $K_2Ca_6Si_4O_{15}$. Formations of meta- and disilicate solid solutions were suggested in the thermodynamic optimization of the K_2O-Na_2O-SiO_2 system based on the critical evaluation of all experimental data. The stoichiometric compounds, $NaKSi_2O_5$, $K_{1.33}Na_{0.67}Si_2O_5$, $Na_{1.3}K_{0.7}Si_2O_5$, $Na_{1.55}K_{0.45}Si_2O_5$, and $Na_{1.84}K_{0.16}Si_2O_5$ reported along the disilicate compositions, were concluded to be parts of solid solutions.

9.2 Suggestions for Future Work

Although the thermodynamic modeling/optimization was performed in good accordance with the reliable experimental data, some limitations still exist, which can be improved in the future:

- Thermodynamic optimizations in the high concentration regions of alkali oxide (K_2O and Na_2O) were often based on predictions due to the lack of experimental data. Further phase diagram experiments in the alkali-rich regions are suggested to increase the accuracy of thermodynamic optimizations for large composition ranges.
- It is recommended to further investigate the stability and the thermodynamic properties of some critical ternary compounds. For example, $K_{10}Mg_5Si_{11}O_{32}$ and $K_4Mg_2Si_5O_{14}$ in the K_2O-MgO-SiO_2 system; the tetragonal phase with the approximate composition $K_{1.1}Al_{1.1}Si_{0.9}O_4$ in the K_2O-Al_2O_3-SiO_2 system; and the β‴-alumina phase reported in the K_2O-MgO-Al_2O_3 system.
- The meta- and disilicate solid solutions in the K_2O-Na_2O-SiO_2 system were optimized based on the liquidus data, on ternary compounds, and on estimations based on the phase

diagram data of the Li_2O-Na_2O-SiO_2 system. Further experimental investigations of the solid solutions can improve the understanding of the stability region of the solid solutions.

- Addition of the K_2MgSiO_4 associate species in the liquid solution was necessary for the optimization of the K_2O-MgO-SiO_2 system. However, direct experimental observation on this charge compensation effect is not investigated in the literature. It is recommended to perform further structural investigations on the melt of the K_2O-MgO-SiO_2 system.

Chapter 10 Contributions to Original Knowledge

This work is the first attempt to critically evaluate and optimize the thermodynamic properties and phase equilibria of the K_2O-Na_2O-CaO-MgO-Al_2O_3-SiO_2 system under 1 atm pressure using the Modified Quasichemical Model (MQM). A set of self-consistent thermodynamic functions was optimized for this six-component system based on critical evaluations of all K_2O-containing binaries, ternaries, and multi-component systems. Uncertainties in the unexplored and inconsistent regions of the system were resolved by performing key phase diagram experiments and employing the accurate thermodynamic database developed in this study.

- For the first time, the temperature of the eutectic reaction in the K_2O-SiO_2 system: Liquid → K_4SiO_4 + K_2SiO_3 was successfully measured at 714 ± 6 °C using the thermal analysis technique with sealed Pt capsules.
- The peritectic reaction Liquid + MgO → K_6MgO_4 in the K_2O-MgO system was determined to be at 858 ± 14 °C using thermal analysis and equilibration techniques with sealed Pt capsules for the first time.
- The stability of K β″-alumina was confirmed up to 1600 °C using equilibration experiments followed by XRD phase characterizations. The large discrepancies in the literature about the eutectic temperature between $KAlO_2$ and β-alumina were resolved.
- The K β- and β″-alumina solutions were modeled using the compound energy formalism. For the first time, thermodynamic and structural properties of K β and β″-alumina can be successfully obtained from classical thermodynamic calculations. With the present models,

site occupations in K β- and β″-alumina solutions can also be accurately predicted as functions of composition and temperature.

- The thermodynamic database developed in this study can well predict phase diagrams and thermodynamic properties of multi-component systems. It can be used to obtain unexplored phase diagram sections and thermodynamic properties of the six-component system.

Appendix I Multi-Component Calculations

A thermodynamic database for the K_2O-Na_2O-CaO-MgO-Al_2O_3-SiO_2 system is developed in the present study. A set of self-consistent model parameters for each of the K_2O-containing binary and ternary sub-systems was obtained as shown in Chapters 4 to 8. Using the FactSage software with the present database, any phase diagram sections and thermodynamic properties within the six-component system can be calculated with reasonable accuracy. In this part, examples are provided on thermodynamic calculations in four quaternary and the six-component systems using the present database and are compared with the available experimental data in the literature. These calculations are mostly related to geological studies regarding rock-forming minerals.

I-1. The K_2O-Na_2O-Al_2O_3-SiO_2 System

I-1.1 Phase Diagram

The calculated phase diagram of the pseudo-binary section between $NaAlSiO_4$ and $KAlSiO_4$ is shown in Fig. I-1 with the experimental data from the literature. Bowen [1] used the equilibration/quenching method and optical microscopy to investigate this section. The solubility range of $KAlSiO_4$ in $NaAlSiO_4$ was reported with the liquidus in the range of about 30 to 100 mol % $NaAlSiO_4$. Tuttle and Smith [2] also studied this pseudo-binary section using the equilibration/quenching technique and XRD phase analysis. A new phase was found at the composition near $K_3NaAl_4Si_4O_{16}$ at temperatures from 1050 to 1600 °C. This phase separates the complete solid solution between $NaAlSiO_4$ and $KAlSiO_4$ into nepheline ($NaAlSiO_4$)- and kalsilite ($KAlSiO_4$)-type phases. The experimental equilibration time above 1050 °C was short due to a severe volatile loss of the alkali oxides (especially at $KAlSiO_4$-rich compositions). Thus, the reliability of the data at high $KAlSiO_4$ region including the $K_3NaAl_4Si_4O_{16}$ phase can be

questionable. The measured liquidus data, in general, show a reasonable agreement with the calculations. The sub-solidus miscibility gap of nepheline was reproduced simultaneously. Gupta and Edgar [3] studied the pseudo-binary section between leucite ($KAlSi_2O_6$) and Na feldspar ($NaAlSi_3O_8$) using the equilibration/quenching method followed by optical microscopy, XRD, and EPMA. Sealed Au capsules were used to prevent volatile loss of alkali oxides. The calculated phase diagram and the experimental liquidus data are presented in Fig. I-2. Schairer [4] investigated the phase diagram section between K and Na feldspars ($KAlSi_3O_8$ and $NaAlSi_3O_8$) using equilibration/quenching experiments and optical microscopy. Schairer found a complete solid solution between these two alkali feldspars close to their melting points. Since these feldspar compositions are in the SiO_2-rich region of the system, where the liquid is extremely viscous, equilibration experiments were performed up to 35 days to provide reliable results. The calculated phase diagram in this section is compared with the experimental data in Fig. I-3. They are in very good agreement over the entire composition range. Bowen and Tuttle [5] and Smith and MacKenzie [6] reported a miscibility gap between these feldspars using equilibration/quenching experiments and XRD analysis. In their experiments, Bowen and Tuttle used synthetic feldspar, and Smith and MacKenzie used natural sodium-rich feldspar. Although reaction kinetics in this composition and temperature ranges are very slow, experimental results from these two studies are in reasonable agreement with each other. Calculations from the present optimization show a good agreement with Bowen and Tuttle's data.

I-1.2 Thermodynamic Properties

Rogez *et al*. [7] studied the enthalpy of mixing (ΔH^{Mix}) of the melt between K feldspar ($KAlSi_3O_8$) and Na feldspar ($NaAlSi_3O_8$) at 697 ^oC. The dissolution heat of the samples at different compositions was measured in liquid lead borate ($2PbO \cdot B_2O_3$). The calculated ΔH^{Mix} is within

their experimental error ranges as depicted in Fig. I-4. One data point at the $NaAlSi_3O_8$-rich composition was considered to be inaccurate by Rogez *et al.* The ΔH^{Mix} function in Rogez *et al*.'s study was derived without this data point. Rammensee and Fraser [8] also studied the enthalpy of mixing of the melt in this composition range using Knudsen Effusion Mass Spectrometry (KEMS). A small positive deviation from the ideal solution behavior was observed at high $KAlSi_3O_8$ compositions as depicted in Fig. I-4. ΔH^{Mix} calculations from the present study were performed at temperatures of 1200 and 1600 °C. The trend of the experimental data was well reproduced considering the discrepancies between the two sets of experimental data.

I-2. Phase Diagram of the K_2O-MgO-Al_2O_3-SiO_2 System

Schairer [9] investigated two pseudo-ternary systems of $KAlSi_2O_6$-Al_2O_3-$MgAl_2O_4$ and $KAlSi_2O_6$-Mg_2SiO_4-$MgAl_2O_4$ within this quaternary system. The equilibration/quenching method was used followed by petrographic microscopy. Among the regions that the author investigated, the $MgAl_2O_4$-$KAlSi_2O_6$ pseudo binary section is presented in Fig. I-5 compared with calculations using our database. The reported eutectic point is reasonably reproduced in the present calculation.

I-3. Phase Diagram of the K_2O-CaO-Al_2O_3-SiO_2 System

Schairer and Bowen [10] studied the pseudo-ternary system of Ca feldspar ($CaAl_2Si_2O_8$), leucite ($KAlSi_2O_6$), and silica (SiO_2) using the equilibration/quenching method followed by petrographic microscopy. The samples were made as homogeneous glasses at 11 different compositions by melting the crushed quenched glasses more than three times. Equilibrium condition was achieved in a few hours at temperatures above 1550 °C, in a few days for temperatures between 1350 and 1550 °C, and in one or two weeks for temperatures below 1350 °C. All samples were wrapped in tiny Pt envelopes. The weight loss of the samples is negligible (less than 0.05 wt. %). The pseudo-

binary section between $KAlSi_2O_6$ and $CaAl_2Si_2O_8$ is shown in Fig. I-6 with the calculations from this study. The eutectic point and liquidus at all compositions were well reproduced in the present calculations. The calculated K and Ca feldspar section is compared with the experimental data in Fig. I-7. All experimental points are in reasonable agreement with the present calculations.

I-4. Thermodynamic Property of the K_2O-Na_2O-CaO-SiO_2 System

Choudary *et al*. [11] reported the excess Gibbs energy of mixing at metasilicate compositions using Knudsen Effusion Mass Spectrometry (KEMS) as shown in Fig. I-8. The sample composition was at 7.5 mol % CaO, 50 mol % SiO_2, and 42.5 mol % (K_2O + Na_2O) and the temperature was at 1100 °C. Considering the experimental errors of the KEMS technique, the actual error range can be more than ± 2 $kJ \cdot mol^{-1}$. The calculations from this study and the experimental data are in reasonable agreement with each other, showing almost an ideal solution behavior.

I-5. Thermodynamic Property of the K_2O-Na_2O-CaO-MgO-Al_2O_3-SiO_2 system

Hastie and Bonnell [12] investigated the melt properties of this six-component system. Vapor pressure measurements on this alkali oxide containing system are important for coal conversion and combustion processes. The authors measured the partial pressure of alkali components K and Na and O_2 using high temperature mass spectrometry. The overall composition was 12.75% Na_2O, 2.02% K_2O, 10.75% CaO, 0.27% MgO, 2.78% Al_2O_3, 71.39% SiO_2 with only a small amount of Fe_2O_3 (0.04%) in weight percentage. Therefore, it was assumed to be the property of the six-component melt without Fe_2O_3. The calculated results and the experimental data are in good agreement with each other as shown in Fig. I-9.

References

[1] N.L. Bowen, Sodium potassium nephelites, Am. J. Sci. 43 (1917) 115-32.
[2] O.F. Tuttle, J.V. Smith, The nepheline-kalsilite system. II. Phase relations, Am. J. Sci. 256 (1958) 571-89.
[3] A.K. Gupta, A.D. Edgar, Leucite-sodium-feldspar incompatibility, Mineral. Mag. 40(312) (1975) 377-84.
[4] J.F. Schairer, The alkali-feldspar join in the system NaAlSiO4-KAlSiO4SiO2, J. Geol. 58 (1950) 512-17.
[5] N.L. Bowen, O.F. Tuttle, The system NaAlSi3O8-KAlSi3O8-H2O, J. Geol. 58 (1950) 489-511.
[6] J.V. Smith, W.S. MacKenzie, The alkali feldspars. IV. The cooling history of high-temperature sodium-rich feldspars, Am. Mineral. 43 (1958) 872-89.
[7] J. Rogez, R. Chastel, C. Begman, C. Brousse, R. Castanet, J.C. Mathieu, Thermodynamic study of the albite-orthoclase system by dissolution calorimetry and Knudsen cell mass spectrometry, Bull. Mineral. 106(1-2) (1983) 119-28.
[8] W. Rammensee, D.G. Fraser, Determination of activities in silicate melts by Knudsen cell mass spectrometry. I. The system NaAlSi3O8-KAlSi3O8, Geochim. Cosmochim. Acta 46(11) (1982) 2269-78.
[9] J.F. Schairer, The ternary systems leucite-corundum-spinel and leucite-forsterite-spinel, J. Am. Ceram. Soc. 38 (1955) 153-8.
[10] J.F. Schairer, N.L. Bowen, The system anorthite-leucite-silica, Bull. Comm. Geol. Finl. No. 140 (1947) 67-87(also in Compt. rend. soc. geol. Finlande No. 20 (Eskola Vol.)).
[11] U.V. Choudary, D.R. Gaskell, G.R. Belton, Thermodynamics of mixing in molten sodium-potassium silicates at 1100°C: the effect of a calcium oxide addition, Metall. Trans., B 8B(1) (1977) 67-71.
[12] J.W. Hastie, D.W. Bonnell, A predictive phase equilibrium model for multicomponent oxide mixtures. Part II. Oxides of sodium, potassium, calcium, magnesium, aluminum, and silicon, High Temp. Sci. 19(3) (1985) 275-306.

Figures

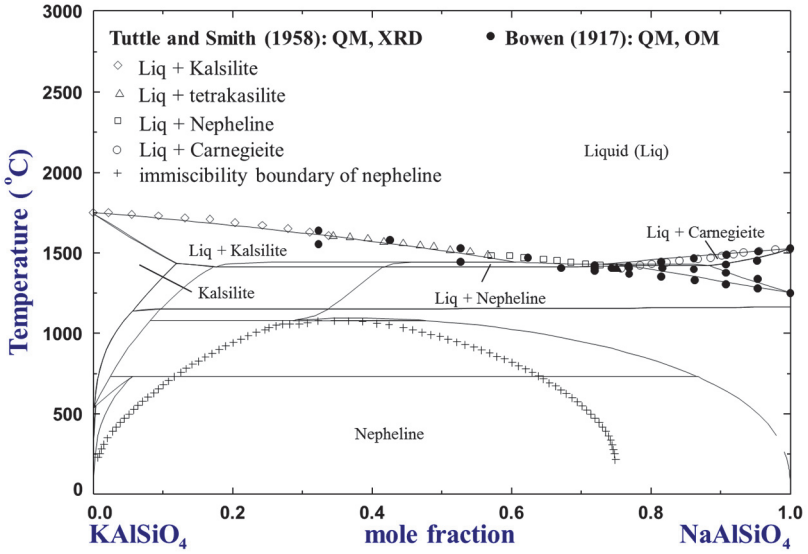

Figure I-1 Phase diagram of kalsilite ($KAlSiO_4$) and nepheline ($NaAlSiO_4$) section with experimental data.

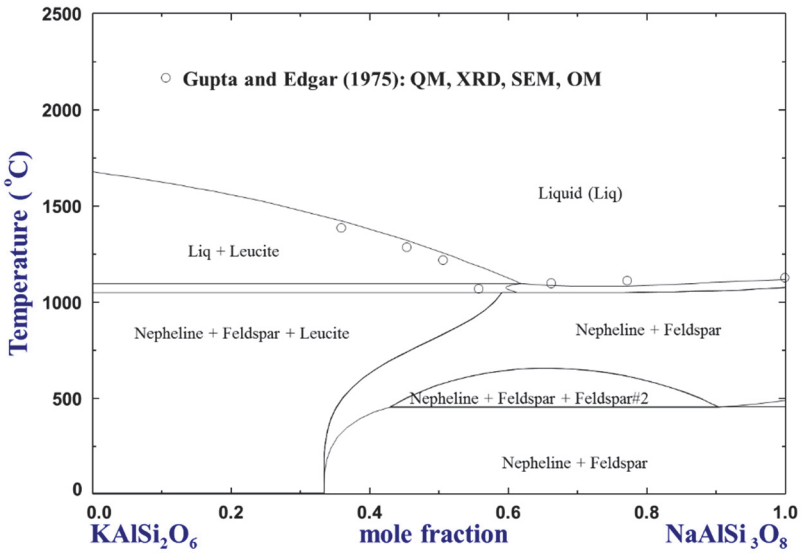

Figure I-2 Phase diagram of leucite ($KAlSi_2O_6$) and Na feldspar ($NaAlSi_3O_8$) section with experimental data.

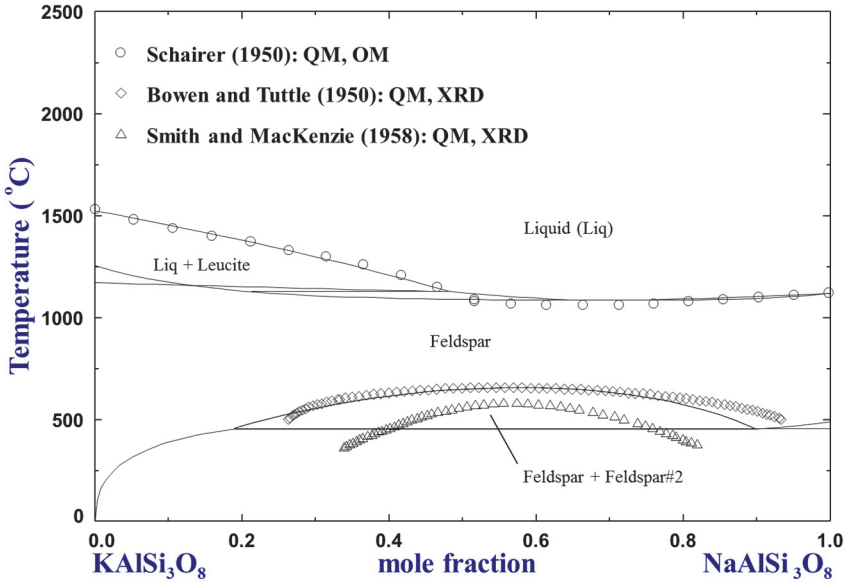

Figure I-3 Phase diagram of feldspars ($KAlSi_3O_8$ and $NaAlSi_3O_8$) section with experimental data.

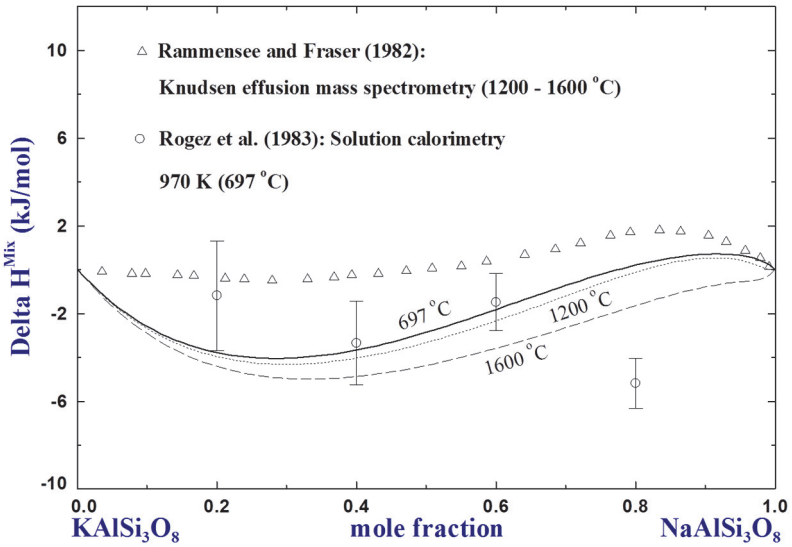

Figure I-4 The enthalpy of mixing of melt at feldspar compositions with experimental data.

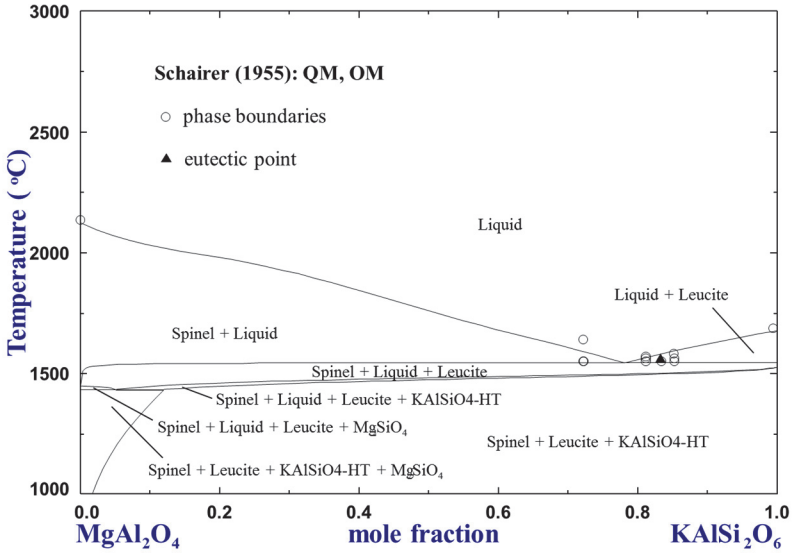

Figure I-5 Phase diagram of spinel ($MgAl_2O_4$) and leucite ($KAlSi_2O_6$) section with experimental data.

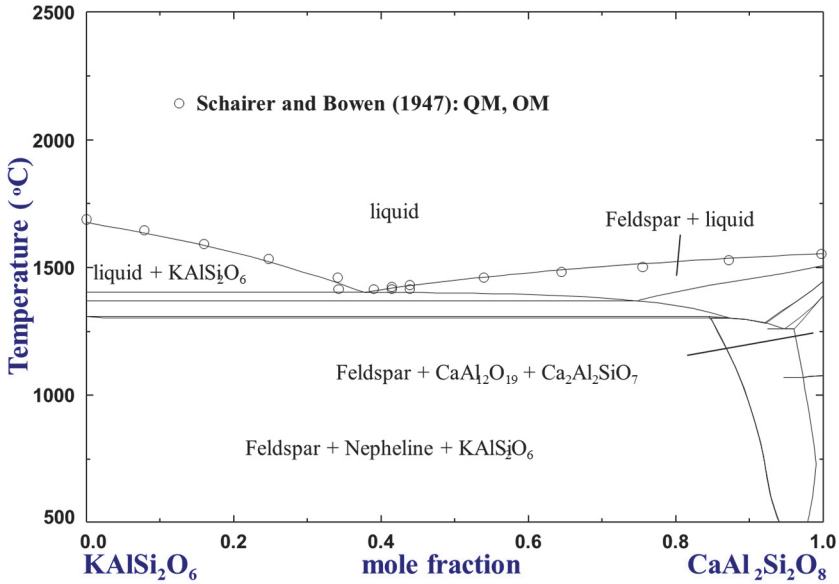

Figure I-6 Phase diagram of leucite ($KAlSi_2O_6$) and Ca feldspar ($CaAl_2Si_2O_8$) section with experimental data.

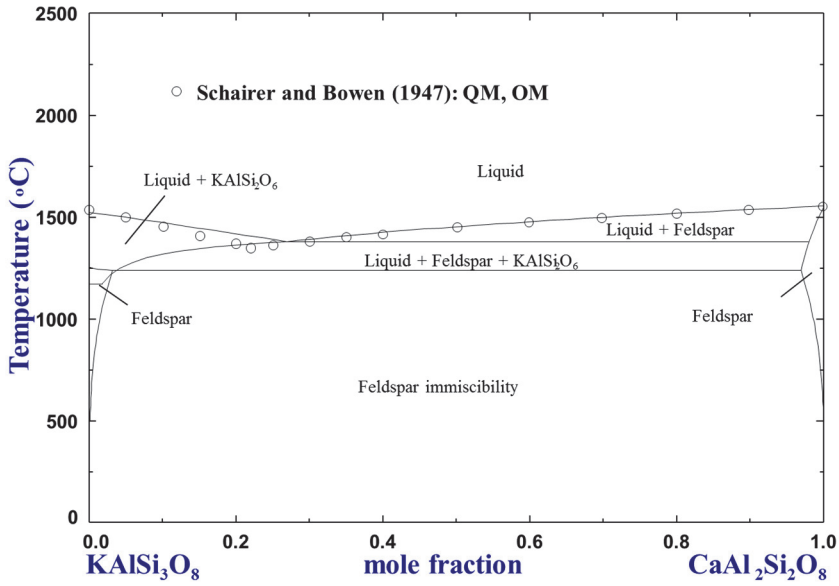

Figure I-7 Phase diagram of K feldspar ($KAlSi_3O_8$) and Ca feldspar ($CaAl_2Si_2O_8$) section with experimental data.

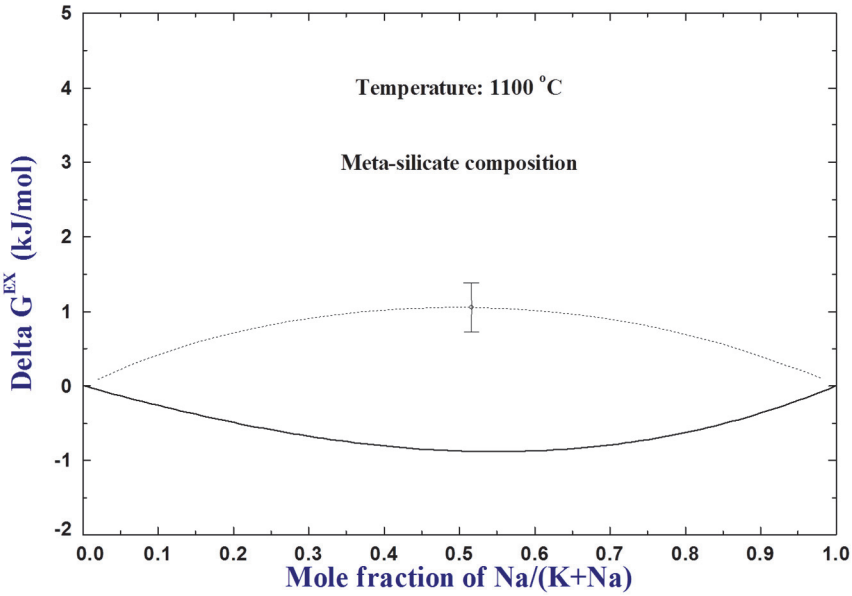

Figure I-8 The excess Gibbs energy at metasilicate compositions at 1100 °C with experimental data.

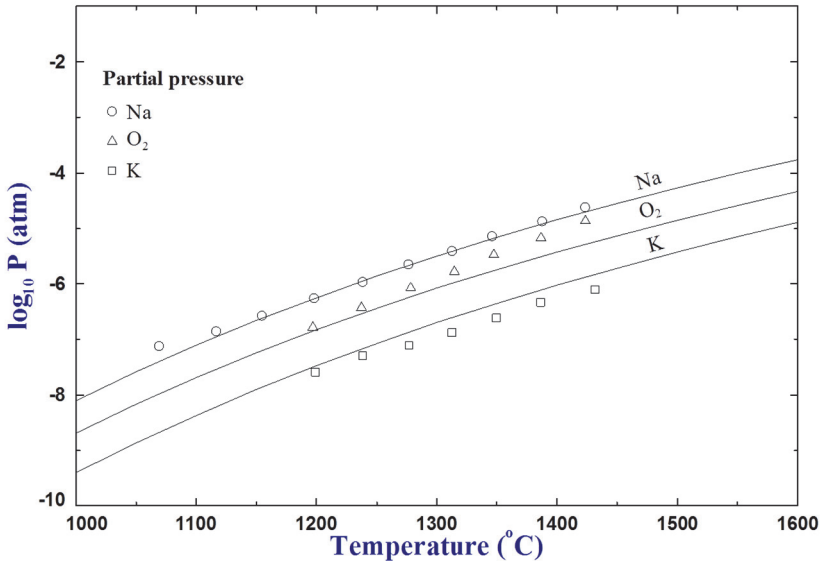

Figure I-9 Vapor pressure of K, Na, and O_2 of the melt with experimental data.

Appendix II Industrial Applications

Several calculations were performed for the industrial applications regarding glass-ceramics production, phase equilibria of biomass ashes, mold flux in steelmaking, refractory corrosion, and β- and β″-alumina in Alkali Metal Thermal to Electric Converter (AMTEC) application.

II-1. Solidification Calculations Related to Glass-Ceramics Production

The K_2O-Na_2O-CaO-MgO-Al_2O_3-SiO_2 system contains major glassmaking components [1]. Leucite ($KAlSi_2O_6$)-based and cordierite ($Mg_2Al_4Si_5O_{18}$)-based glass-ceramics are made by the glass melt of this six-component system [2, 3]. Several studies can be found in the literature regarding dental restoration applications of the glass-ceramics. Leucite-based glass-ceramic is one of the widely used dental restoration materials.

Gonzaga *et al*. [2] investigated the leucite-based glass-ceramics from the glass melt composition at 63 % SiO_2, 17.7 % Al_2O_3, 11.2 % K_2O, 4.6 % Na_2O, and 1.6 % CaO in weight percentage. Minor components of B_2O_3, TiO_2, BaO, and CeO exist, which are less than 1 %. This glass sample was annealed at temperatures in between 920 and 1200 °C for approximately 1 h. In this heat treatment stage, authors found crystalline leucite growing from the base glass. Then, another heat treatment was performed at 1075 °C for 35 min. This heat treatment stage was called maturing process. As a result, 30 to 35 vol. % of tetragonal leucite crystalline was obtained from the base glass.

This experimental observation is compared with equilibrium solidification calculations using the thermodynamic database developed in this study. The calculations were performed using the glass composition reported in Gonzaga *et al*.'s work [2] without considering the minor components. The

calculated results from this study are shown in Fig. II-1 from 500 to 1500 °C. The maturing process of the glass-ceramics at 1075 °C was found to be the temperature close to maximum leucite crystalline fraction in the calculated results. The reason of setting the annealing temperature at 1075 °C was better understood. The newly developed thermodynamic database can well predict phase equilibria for this complex system and it can be used for process design of glass-ceramics fabrication.

II-2. Biomass Combustion/Gasification

Common biomass ashes consist of about 55 to 90 wt. % of K_2O-CaO-SiO_2 with some Na_2O, MgO, Al_2O_3, Fe_2O_3, and P_2O_5 [4]. The mainstream biomass used for combustion/gasification process is phosphorus-poor biomasses. It means, the K_2O-Na_2O-CaO-MgO-SiO_2 system is sufficient to understand the majority of the chemical reactions for the slag formation in the biomass combustion/gasification process [5]. The thermodynamic database of the K_2O-Na_2O-CaO-MgO-Al_2O_3-SiO_2 system developed in this Ph.D. work covers these major ash components of biomass combustion/gasification process. Potassium silicates in the K_2O-CaO-SiO_2 ternary system are known to be the main components of slagging problem. Phase diagram calculations were performed and compared with experimental data regarding this ternary system.

Zevenhoven-Onderwater *et al*. [4] reported approximate compositions of seven biomass fuels in the K_2O-CaO-SiO_2 ternary diagram as shown in Fig. II-2. Two comprehensive phase diagram measurements and one specific liquidus measurement in the K_2O-CaO-SiO_2 system were found in the literature. Morey *et al*. [6, 7] performed phase diagram experiments on the K_2O-CaO-SiO_2 system using the equilibration/quenching method followed by petrographic microscopy and XRD analysis. Liquidus and invariant reactions were measured in the composition range between

metasilicates and pure SiO_2. Pt or Au foils were used to wrap the sample materials. Quenching was performed by taking out the crucible from the furnace. When rapid cooling rate was required, the crucibles were quenched into mercury. Liquidus projection was constructed based on the measurements of 160 compositions. Chen *et al*. [8] investigated isothermal sections from 1000 to 1200 °C using the equilibration/quenching method followed by EPMA. Samples were wrapped in Pt foil to prevent volatile loss of K_2O. Equilibration time was set between 4 and 72 h depending on the target compositions and temperatures. Berjonneau *et al*. [9] studied the liquidus temperature of the samples representing miscanthus and straw ashes using the quenching technique. Sealed capsules were used to prevent volatile loss of K_2O. Slow quenching is expected as the samples were cooled in the furnace.

These experimental data are depicted in Fig. II-3 with the calculated results from this study. The experimental data from Morey *et al*. [6, 7] and Chen *et al*. [8] show reasonable agreement with each other, while the data from Berjonneau *et al*. [9] show large discrepancies. As the experimental data from Berjonneau *et al*. [9] represent the liquidus of 1230 °C, the actual difference at 1200 °C should be even larger. The database developed in this study can well reproduce the reliable experimental data from Morey *et al*. and Chen *et al*. It can be said that the melting points of miscanthus and straw ashes can be better predicted in the present calculations than Berjonneau *et al*.'s study. Liquidus temperature of many different types of biomass can also be calculated with reasonable accuracy.

II-3. Mold Flux in Steelmaking

In the continuous casting process in steelmaking, proper mold flux is essential to control heat transfer, lubrication, and inclusions, etc. Conventional mold flux contains fluorine, which is

harmful for environment. To reduce fluorine in mold flux, alkali oxides are considered as substitutes for fluorine. Lu *et al*. [10] investigated the effect of K_2O addition into mold flux used in high speed continuous casting. From 1 to 5 wt. % of K_2O were added into the mold flux and the corresponding melting temperature was measured. The experimental composition contains some iron and fluorine. However, calculations in this study were performed considering the compositions in the K_2O-Na_2O-CaO-MgO-Al_2O_3-SiO_2 system. That is, 37.72 % SiO_2, 4.93 % Al_2O_3, 30.7 % CaO, 1.922 % MgO, and 6.69 % Na_2O in weight percentage with different amounts of K_2O. The calculated results in Fig. II-4 show a reasonable agreement with the experimental data considering the difference in sample compositions between the calculations and the experiments. More accurate calculations will be possible when the interaction parameters with Fe_2O_3 and CaF_2 are optimized simultaneously with the present database.

II-4. Refractory Corrosion

Potassium vapor is known to be corrosive to refractories in glass-melting furnace [11, 12], kiln for iron ore pellet production [13], and blast furnace [14, 15]. In blast furnace, K_2O vapor from raw materials circulates in the furnace and has reactions with mullite-type refractories. The thermodynamic database can be used to understand and avoid the premature wear of these refractories due to K_2O vapor reactions [11-15].

Scudeller *et al*. [15] studied the reaction between K_2O vapor and the alumina-silica refractory containing 45 and 55 wt. % SiO_2 at 1000 °C. K_2CO_3 was used as a source of K_2O vapor from the coke. Phase and composition of the samples were analyzed using XRD, SEM, atomic absorption spectrometry, and induction coupling plasma spectrometry. It was found that through the reaction time from 0.5 to 32 h, resultant phases from the reactions were analyzed to be the equilibrium

phases from the Al_2O_3-SiO_2 binary system to the K_2O-rich region of the K_2O-Al_2O_3-SiO_2 system as shown in Fig. II-5. SEM analysis showed different phase equilibria from the sample surface area (b in Fig. II-6) to the inner area (c in Fig. II-6). This result was simulated using the present thermodynamic database by varying the amount of gas involved in the calculation. In Fig. II-6, the amount of gas involved in the calculation represents the depth of the reaction area in the sample. Thus, the reacted gas on the sample surface was reasonably calculated. Then, calculations with different amount of K_2CO_3 can elucidate how much K_2CO_3 will effectively avoid the formation of kaliophilite ($KAlSiO_4$) phase on the sample surface. Kaliophilite is responsible for the refractory failures due to significant volume change [15]. Based on the calculations from this study, controlling K_2CO_3 below 15 wt. % / total coke can avoid the formation of the kaliophilite phase as shown in Fig. II-7.

II-5. K β-Alumina for Energy Storage

High ionic conductivity of K β-alumina makes it attractive for many battery-related applications. From 1978, K β-alumina solid electrolytes were developed for Magneto Hydro Dynamic (MHD) power plants [16] and the thermionic energy converters [17]. The Mg-doped K β″-alumina phase was studied for fuel cell applications [18]. More recently, Alkali Metal Thermal Electric Converter (AMTEC) is found to be one of the most promising battery for spacecraft and hybrid electric vehicle systems according to Lodhi *et al*. [19]. AMTEC can reduce 75% of mass of the heat source used in aircraft (plutonium-238), which can save fuel and total cost. One of the main limitations is the time-dependent performance of β″-alumina solid electrolyte (BASE) materials. BASE was found to be responsible for 76% out of 92% power degradation in 100000 h [20]. Therefore, the optimization of the BASE materials is a key issue for the development of AMTEC system. AMTEC generally uses Na β-alumina series. Parasitic heat loss and internal joule loss at high

temperatures can significantly decrease the efficiency of energy conversion. Since the vapor pressure of K is much higher than that of Na at low temperatures, K β″-alumina was extensively studied more recently. The operation temperature of K-BASE was found to be 120 K lower than the Na ones, and the efficiency of K-BASE battery can be 25% higher [21]. K β″-alumina for AMTEC applications was tested by Barkan *et al*. [22]. The results showed that K-BASE improves the lifetime of battery and enhances the energy efficiency.

Using the present thermodynamic database, the partial pressure of potassium (P_K) was calculated as a function of temperature. Different P_K at low- and high-temperature side of electrolyte in AMTEC is the driving force of ionic conduction. The cold side of the AMTEC is about 530 K and the hot side is about 1000-1100 K [21]. Typical compositions of K β-alumina at $K_{1.3}Al_{11}O_{17.15}$ [23] and β″-alumina at $K_{1.67}Mg_{0.67}Al_{10.33}O_{17}$ [24] were used in the calculations. The calculations were performed for a typical composition of K β-alumina at $K_{1.3}Al_{11}O_{17.15}$ [23] and β″-alumina at $K_{1.67}Mg_{0.67}Al_{10.33}O_{17}$ [24] as shown in the Fig. II-8 (a) and (b), respectively. Comparing the two calculated results, β″-alumina is found to have a larger difference of P_K between the cold and hot sides of the AMTEC ($\Delta \log P_K = 18.65$ (atm)) than β-alumina ($\Delta \log P_K = 16.63$ (atm)). This result implies that K β″-alumina can produce higher electric power compared to K β-alumina for this AMTEC application.

References

[1] B.O. Mysen, P. Richet, Silicate glasses and melts properties and structure, Elsevier2005.
[2] C.C. Gonzaga, P.F. Cesar, C.Y. Okada, C. Fredericci, F. Beneduce Neto, H.N. Yoshimura, Mechanical properties and porosity of dental glass-ceramics hot-pressed at different temperatures, Mater. Res. (Sao Carlos, Braz.) 11(3) (2008) 301-306.

[3] L. Song, J. Wu, Z. Li, X. Hao, Y. Yu, Crystallization mechanisms and properties of α-cordierite glass–ceramics from K2O–MgO–Al2O3–SiO2 glasses, Journal of Non-Crystalline Solids 419 (2015) 16-26.
[4] M. Zevenhoven-Onderwater, R. Backman, B.J. Skrifvars, M. Hupa, The ash chemistry in fluidised bed gasification of biomass fuels. Part I: predicting the chemistry of melting ashes and ash-bed material interaction, Fuel 80(10) (2001) 1489-1502.
[5] I.-L. Naezelius, J. Fagerstroem, C. Boman, D. Bostroem, M. Oehman, Slagging in Fixed-Bed Combustion of Phosphorus-Poor Biomass: Critical Ash-Forming Processes and Compositions, Energy Fuels 29(2) (2015) 894-908.
[6] G.W. Morey, F.C. Kracek, N.L. Bowen, The ternary system K2O-CaO-SiO2, J. Soc. Glass Technol. 14 (1930) 149-187.
[7] G.W. Morey, F.C. Kracek, N.L. Bowen, The ternary system: K2O-CaO-SiO2, J. Soc. Glass Technol. 15 (1931) 57-8.
[8] M. Chen, X. Hou, J. Chen, B. Zhao, Phase Equilibria Studies in the SiO2-K2O-CaO System, Metall. Mater. Trans. B 47(3) (2016) 1690-1696.
[9] J. Berjonneau, L. Colombel, J. Poirier, M. Pichavant, F. Defoort, J.-M. Seiler, Determination of the Liquidus Temperatures of Ashes from the Biomass Gasification for Fuel Production by Thermodynamical and Experimental Approaches, Energy Fuels 23(12) (2009) 6231-6241.
[10] Y. Lu, X. Fang, G. Zhang, Effects of K2O on properties of low fluoride content mould flux for high speed continuous casting, Appl. Mech. Mater. 71-78 (2011) 2899-2902.
[11] M.D. Allendorf, K.E. Spear, Thermodynamic analysis of silica refractory corrosion in glass-melting furnaces, J. Electrochem. Soc. 148 (2001) B59-B67.
[12] K.E. Spear, M.D. Allendorf, Thermodynamic analysis of alumina refractory corrosion by sodium or potassium hydroxide in glass melting furnaces, J. Electrochem. Soc. 149(12) (2002) B551-B559.
[13] J. Stjernberg, B. Lindblom, J. Wikstroem, M.L. Antti, M. Oden, Microstructural characterization of alkali metal mediated high temperature reactions in mullite based refractories, Ceram. Int. 36(2) (2010) 733-740.
[14] S.E. McCune, T.P. Greaney, W.C. Allen, R.B. Snow, Reaction between K2O and Al2O3-SiO2 refractories as related to blast-furnace linings, J. Am. Ceram. Soc. 40 (1957) 187-95.
[15] L.A.M. Scudeller, E. Longo, J.A. Varela, Potassium vapor attack in refractories of the alumina-silica system, J. Am. Ceram. Soc. 73(5) (1990) 1413-16.
[16] I. Eliezer, R.A. Howald, High-temperature thermodynamics and phase equilibria in the potassium oxide-aluminum oxide system, High Temp. Sci. 10 (1978) 1-16.
[17] J.A.M. Van Hoek, F.J.J. Van Loo, R. Metselaar, Phase relations in the calcium oxide-potassium oxide-aluminum oxide system, Mater. Sci. Monogr. 66B(Ceram. Today--Tomorrow's Ceram., Pt. B) (1991) 581-90.
[18] G.W. Schaefer, A.P. de Kroon, F. Aldinger, Influence of precursor chemistry on phase evolution and stability range in the potassium-beta alumina system, Mater. Res. Soc. Symp. Proc. 393(Materials for Electrochemical Energy Storage and Conversion-Batteries, Capacitors and Fuel Cells) (1995) 61-6.
[19] M.A.K. Lodhi, P. Vijayaraghavan, A. Daloglu, An overview of advanced space/terrestrial power generation device: AMTEC, J. Power Sources 103(1) (2001) 25-33.
[20] M.A.K. Lodhi, P. Vijayaraghavan, A. Daloglu, Time-dependent BASE performance and power degradation in AMTEC, J. Power Sources 93(1-2) (2001) 41-49.

[21] M.S. El-Genk, J.-M.P. Tournier, AMTEC/TE static converters for high energy utilization, small nuclear power plants, Energy Convers. Manage. 45(4) (2004) 511-535.
[22] A. Barkan, T.K. Hunt, B. Thomas, Potassium AMTEC Cell Performance, SAE International, 1999.
[23] G. Collin, J.P. Boilot, A. Kahn, J. Thery, R. Comes, Structural investigation of potassium(+) and thallium(+) β-aluminas, J. Solid State Chem. 21(4) (1977) 283-92.
[24] J.P. Boilot, G. Collin, P. Colomban, R. Comes, X-ray-scattering study of the fast-ion conductor β″-alumina, Phys. Rev. B: Condens. Matter 22(12) (1980) 5912-23.

Figures

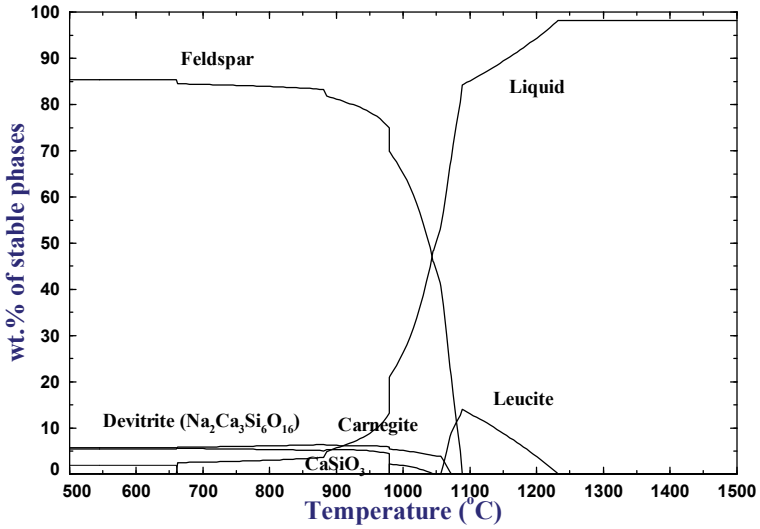

Figure II-1. Crystallization of leucite-type glass-ceramic (63 % SiO_2, 17.7 % Al_2O_3, 11.2 % K_2O, 4.6 % Na_2O, and 1.6 % CaO in weight percentage).

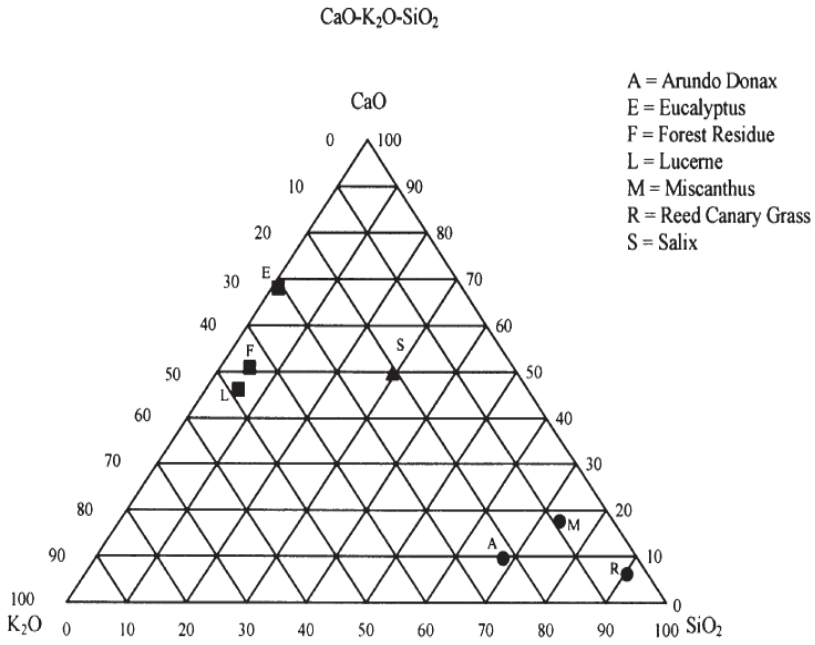

Figure II-2. Typical biomass ash compositions

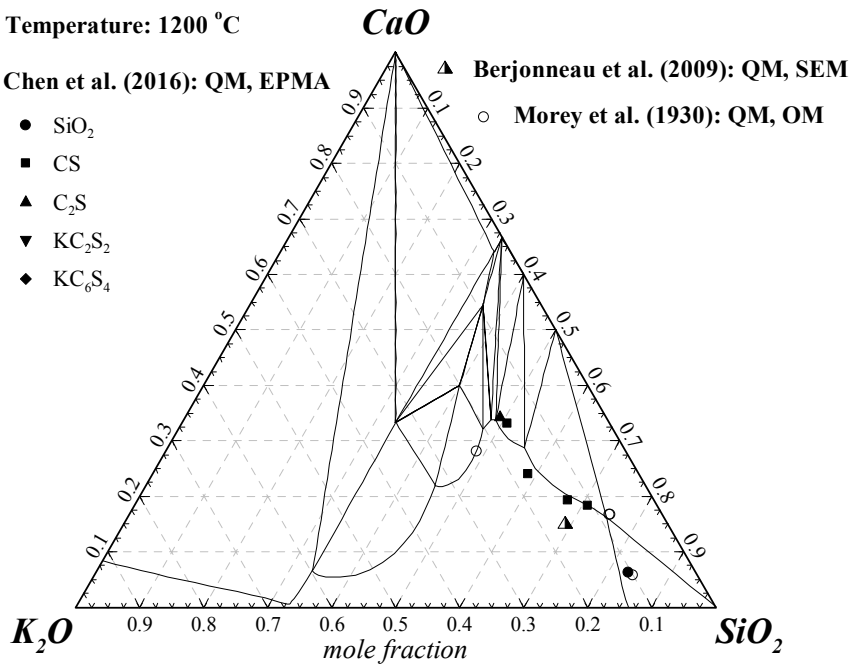

Figure II-3. Calculated phase diagram of the K_2O-CaO-SiO_2 system with experimental data (K: K_2O, C: CaO, S: SiO_2).

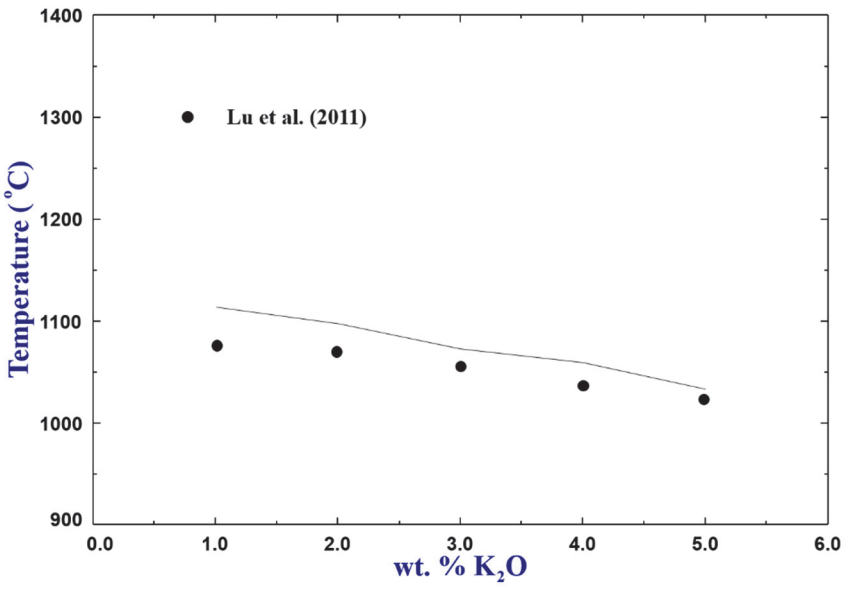

Figure II-4. Melting temperature of mold flux with experimental data (37.72 % SiO_2, 4.93 % Al_2O_3, 30.7 % CaO, 1.922 % MgO, and 6.69 % Na_2O in weight percentage).

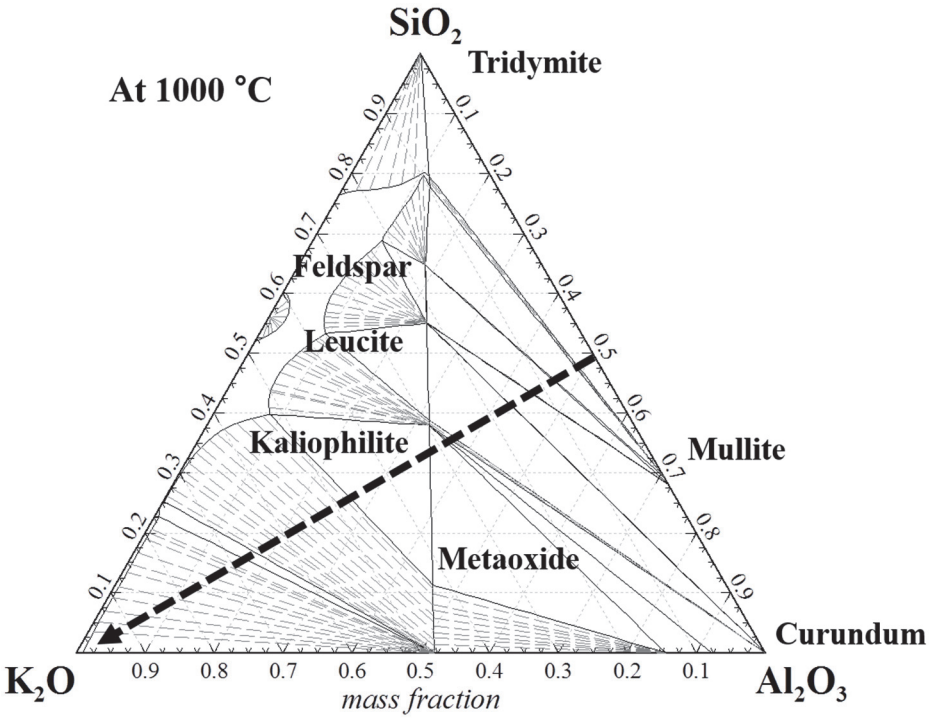

Figure II-5. The K_2O-Al_2O_3-SiO_2 ternary isothermal section at 1000 °C.

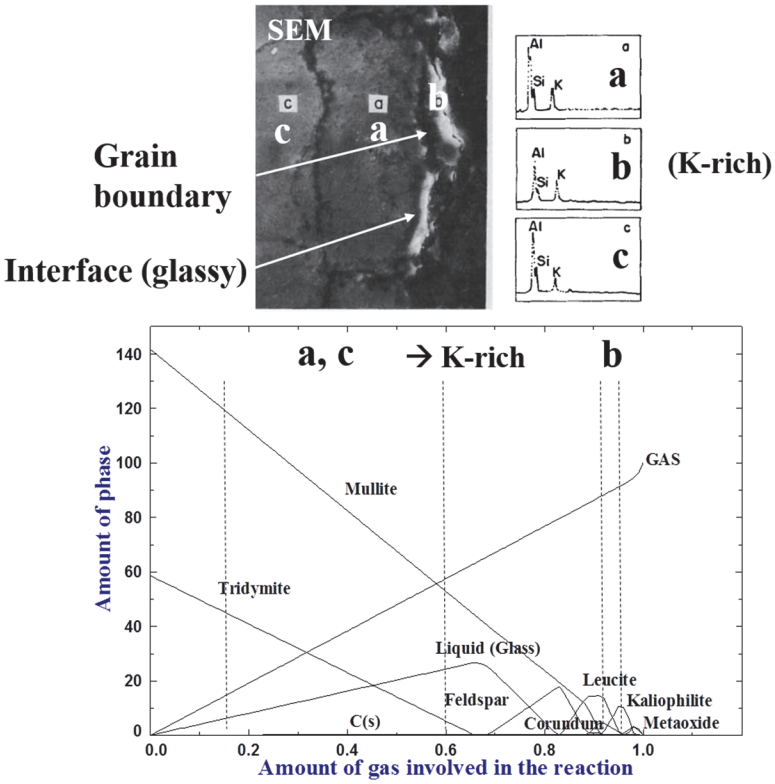

Figure II-6. Equilibrium calculations between refractory and gas phases at 1000 °C with experimental data.

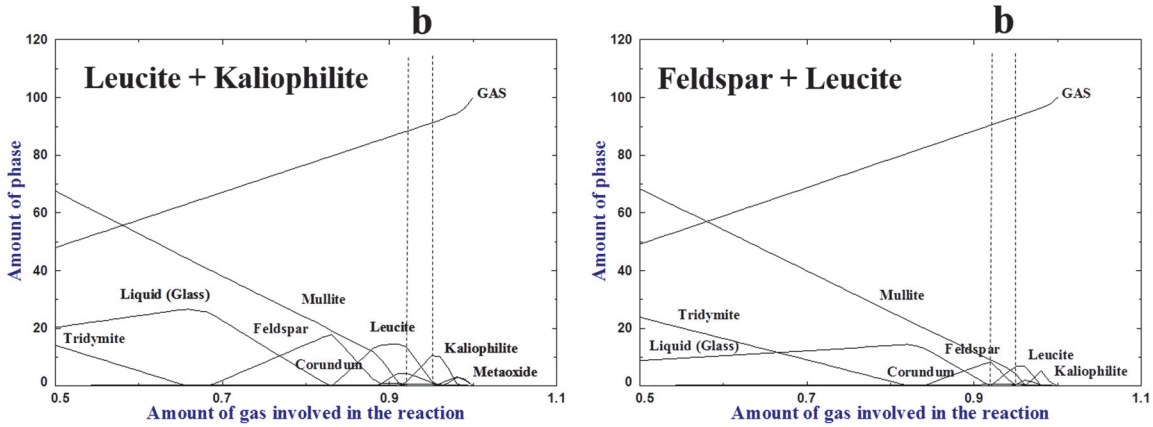

<100 wt.%K_2CO_3 / total Coke> (K_2CO_3 unlimited)

<15 wt.%K_2CO_3 / total Coke>

Figure II-7. Equilibrium calculations with 100 and 15 wt. % K_2CO_3 per total coke.

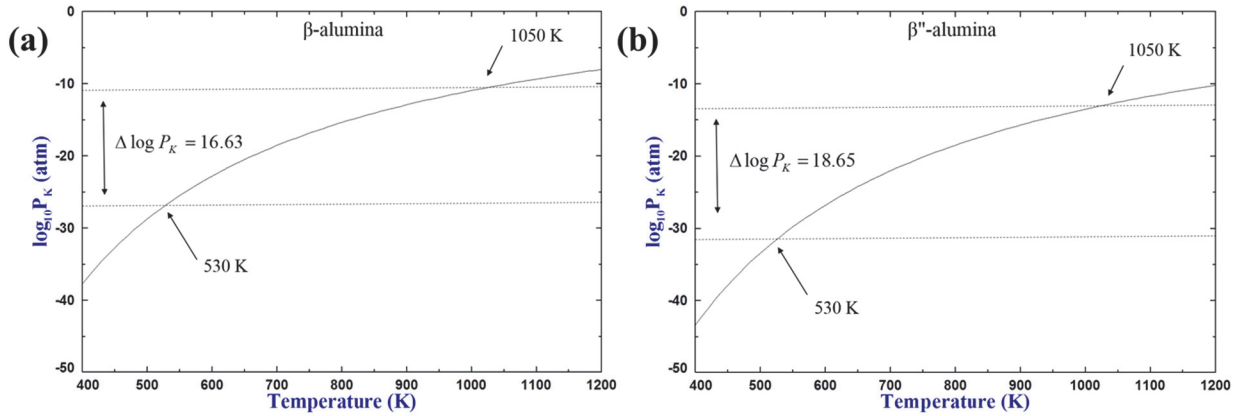

Figure II-8. Partial pressure of potassium of (a) β-alumina and (b) β″-alumina as a function of temperature.